

# **Design and Analysis of Extremely Low-Noise MEMS Gyroscopes for Navigation**

by

Ali Darvishian

A dissertation submitted in partial fulfillment  
of the requirements for the degree of  
Doctor of Philosophy  
(Electrical and Computer Engineering)  
in the University of Michigan  
2018

Doctoral Committee:

Professor Khalil Najafi, Chair  
Assistant Research Scientist Jae Yoong Cho  
Professor Yogesh Gianchandani  
Professor Kenn Oldham

Ali Darvishian

darvishi@umich.edu

ORCID iD: 0000-0002-1761-0417

© Ali Darvishian 2018

## **Dedication**

Dedicated to people who encourage others to question everything, think differently and critically!

## Acknowledgements

I would like to thank my thesis advisor Prof. Khalil Najafi for his patience, support, and guidance, throughout my PhD. I have learned great deal from him, especially how to write and present effectively.

I would like to express my sincere appreciation to Dr. Jae Yoong Cho. I feel very lucky to work in the same group as him. I got great deals of helps from him about fabrication process, simulation, and modeling of MEMS gyroscopes.

I would like to thank my committee members Prof. Ken Oldham, and Prof. Yogesh Gianchandani for their time, support, and valuable comments on my thesis.

I would like to appreciate Dr. Guohong He for his help, assistance, and advices. He is a very kind, smart, and knowledgeable mentor and friend. I also would like to thank him for encouraging me to design novel inertial sensors, which resulted in several interesting ideas.

I would like to express my sincere gratitude to Robert Gordenker and Trasa Burkhardt for providing the perfect environment in which to research. I would like to specially thank Robert for his advices on preparing academic publications and keeping the laboratory safe.

I would like to thank **Mr. Sajal Singh** for being extremely kind, helpful and understanding friend. I am grateful to him for lending his keyboard and monitor while I was writing my thesis (to encourage me to write), as well as his help on characterization of resonators using LDV. Furthermore, I would like to thanks him for reviewing this thesis. Thanks Bhai!

I would like to appreciate **Mr. Amin Sandoughsaz** for his friendship, advices, and technical help. He is a very nice, considerate, and helpful friend. Thanks Seyed!

I would like to express my gratitude to Prof. Durali for showing me the beauty, joyfulness, and fulfillment of “design”. He taught me that design is not what it looks like. Design is understanding, analyzing, finding solutions, and finally and most importantly solving the problem to make life better for others. I also want to appreciate Prof. Moeenfard who introduced me MEMS.

I would like to thank Dr. Jong Kwan Woo and Mr. Christopher Boyd for designing circuits, testing gyroscopes, all the technical discussions, and friendship. I also would like to thank Dr. Behrouz Shiari and Mr. Farzad Asgarian for technical helps, discussions, and being good friends. I would like to acknowledge Dr. Tal Nagourney for taking amazing photos, both technical and personal. I would like to appreciate Mr. Donguk Yang, Mr. Yi Yuan, Dr. Stacey Yemin Tang, and Dr. Mehdi Sadeghi for technical helps and friendship. I also thank my previous group mates Zongliang, Jialiang, Seowyuen, Prof. Becky Peterson, Ali B., Daniel, Erkan, Seowyuen, and Dariush.

I would like to express my appreciation to all the staff at Lurie Nanofabrication Facility (LNF). Specially, Mr. James Ricker who always tried his best to support students.

I would like to thank my Iranian friends in Ann Arbor, Milad Z., Morteza S., Mahdi A., Nazanin, Arbab, Kate, Shahab, Mohamadreza, Amin Ra., Kazem, Hussein M., Maryam, Hussein K., Mina, Morteza N., Javad, Morteza F., Morteza T., Mohamad R., Amin Re., Shadi, Mahdi S., Amir R., Amirreza, Mohsen, Mehrdad, Ahmad A., Heidar, Yaser, Alireza, Navid B., Navid A., Milad M., Behnoosh, MohamadMahdi, Houtan, Ashkan, Amir N., Farzad, Ali A., Ali R., Behzad, Ali M., HamidReza, Reza, Shima, Ali T., Salar, Ahmad S., Enayat, Rasool, Ali P., Vahid, Saman, Shayan, Javid, Omid, Ali K., Mohamad K., Ehsan, and Hamed, for all the fun we have had in the past years.

Finally and most importantly, I would like to thank my parents, Baba and Maman, and my sister, Khanoom Doktor, who deserve the biggest appreciation of all. I will be forever indebted to them for the sacrifices they made for my education as well as my well-being.

# Table of Contents

Dedication .....	ii
Acknowledgements .....	iii
List of Tables.....	viii
List of Figures .....	x
Abstract .....	xxx
<b>Chapter 1: Introduction.....</b>	<b>1</b>
1.1 Introduction to Navigation .....	1
1.2 Inertial Navigation.....	3
1.3 MEMS Gyroscopes .....	8
1.4. Thesis Contributions and Organization.....	15
<b>Chapter 2: Important Parameters for Performance of Vibratory Gyroscopes .....</b>	<b>20</b>
2.1 Operational Principles of Vibratory Gyroscopes .....	20
2.2. Errors .....	32
2.3 How to Design Low-Noise Vibratory Gyroscopes .....	45
2.4 Conclusion.....	47
<b>Chapter 3: Conceptual Designs for Measuring Angular Rotation Around Different     Directions .....</b>	<b>50</b>
3.1. Shell Gyroscopes.....	50
3.2. Super Sensitive Stacked ( $S^3$ ) Gyroscopes .....	58
3.3. Summary .....	65
<b>Chapter 4: Design and Analysis of Extremely High-Performance MEMS Shell Gyroscopes     .....</b>	<b>67</b>

4.1 Sensing Quality Factor .....	68
4.2 Effective Mass .....	148
4.3 Angular Gain .....	155
4.4 Resonant Frequency .....	158
4.5 Frequency Split.....	169
4.6 Gyroscope Operation.....	175
4.7 Conclusion.....	179
<b>Chapter 5: Design and Analysis of Extremely High-Performance Pitch or Roll Gyroscopes</b> .....	<b>181</b>
5.1 Sensing Quality Factor .....	182
5.2 Effective Mass .....	219
5.3 Angular Gain .....	220
5.4. Resonant Frequency .....	221
5.5 Frequency Split.....	232
5.6 Gyroscopic Operation.....	237
5.7 Conclusion.....	240
<b>Chapter 6: Summary, Conclusions, and Future Works</b> .....	<b>241</b>
6.1 Summary .....	241
6.2 Conclusion.....	243
6.3 Future Work .....	244
<b>Appendix A: Fabrication of Birdbath Shell Structures</b> .....	<b>246</b>
<b>References</b> .....	<b>250</b>



## List of Tables

<b>Table 1.1:</b> Summary of contribution .....	19
<b>Table 2.1:</b> Reducing the effect of temperature change in bias drift/instability using a temperature controlled package [31] .....	35
<b>Table 2.2:</b> Reducing the effect of stress in bias drifts using a stress isolation platform [32]....	36
<b>Table 2.3:</b> Effect of increasing different parameters on noises of CVGs.....	49
<b>Table 3.1:</b> Summary of MEMS shell resonators performances.....	57
<b>Table 4.1:</b> Summary of the effects of different parameters on anchor loss of HSRs.....	102
<b>Table 4.2:</b> $Q_{TED}$ of BSRs with different materials.....	123
<b>Table 4.3:</b> Normalized $Q_{TED}$ of chipped edge shells .....	126
<b>Table 4.4:</b> Summary of the effects of different parameters on TED of BSRs.....	136
<b>Table 4.5:</b> Akhiezer $Q$ for shell resonators with resonant frequency of 10,000Hz.....	139
<b>Table 4.6:</b> Comparing analytical model, numerical simulation and experimental data values for resonant frequency .....	164
<b>Table 4.7:</b> Tested BSR gyroscope parameters.....	177
<b>Table 5.1:</b> Effect of substrate thickness on $Q$ (Experimental data and FEM simulation show an excellent agreement).....	189

**Table 5.2:** Summary of the effects of different parameters on anchor loss of stacked resonators.  
..... 209

**Table 5.3:** Dimensions used for simulating TED in SMFB resonators ..... 211

**Table 5.4:**  $Q_{TED}$  of SMFB resonators with Different Materials..... 214

**Table 5.5:** Estimated values for  $Q_s$  of stacked SMFB resonators in out-of-plane mode ..... 218

**Table 5.6:** Estimated ARW of  $S^3$  gyroscope ..... 239

## List of Figures

<b>Figure 1.1:</b> Finding the position using celestial navigation technique. In this technique, angular measurements taken between a celestial body such as, the Sun, the Moon, a planet, or a star, and the visible horizon are used to find observer’s position. ....	2
<b>Figure 1.2:</b> Fundamentals of inertial navigation. This technique determines current position by using a previously determined position and advancing that position by measuring displacements and orientations in each time-step. ....	4
<b>Figure 1.3:</b> Noise versus size of different type of gyroscopes. Angle random walk (ARW) shows the noise in gyroscopes. As noise is smaller in a gyroscope, the accumulative error of inertial navigation decreases. ....	7
<b>Figure 1.4:</b> Schematic of a beam gyroscope [1]. ....	9
<b>Figure 1.5:</b> Schematic of a single mass gyroscope [2]. ....	9
<b>Figure 1.6:</b> A tuning fork gyroscope developed at Georgia Institute of Technology [3]. ....	10
<b>Figure 1.7:</b> Driving and sensing modes of a quad mass gyroscope [4]. ....	11
<b>Figure 1.8:</b> $n = 2$ WG modes in a shell gyroscope. ....	11
<b>Figure 1.9:</b> Shell resonators with different shapes that are shown in this figure, can be used as MEMS gyroscopes. ....	12
<b>Figure 1.10:</b> Two main structures of circular gyroscopes. ....	12

**Figure 1.11:** A square BAW gyroscope [8]..... 13

**Figure 1.12:** Schematic of a torsional gyroscope [9]. ..... 14

**Figure 1.13:** Noise performance in the best MEMS gyroscopes. None of them shows required performance for navigation. .... 14

**Figure 1.14:** Questions that will be answered in this research. .... 16

**Figure 2.1:** Dynamics diagram of a vibratory gyroscope inside a mobile object..... 21

**Figure 2.2:** A mass spring damper system. .... 37

**Figure 2.3:** Schematic of sensing circuit for capacitive detection of proof mass movement in the sensing direction..... 40

**Figure 2.4:** Dependency of the noise floor in mechanical gyroscopes on frequency mismatch. 44

**Figure 2.5:** Design checklist of CVGs. .... 47

**Figure 3.1:** A schematic of a shell gyroscope including a shell resonator and electrodes. .... 51

**Figure 3.2:** Deformation pattern in an axisymmetric shell structure in the  $n = 2$  WG modes. Color legend in shows normalized displacement. For a perfectly symmetric shell, resonant frequencies and vibrational behavior of the first and second  $n = 2$  WG modes have the same shape, but deformation pattern shifts by  $45^\circ$ ..... 52

**Figure 3.3:** A schematic of driving a shell structure in one of its WG modes using electrostatic force and measuring the deflection of the shell using capacitive sensing. .... 53

**Figure 3.4:** Configuration of driving electrodes around a shell. .... 54

**Figure 3.5:** Configuration of sensing electrodes around a shell when operating in an open loop system..... 55

**Figure 3.6:** Configuration of sensing electrodes around a shell when operating in a force-to-rebalance system..... 55

**Figure 3.7:** Configuration of tuning electrodes around a shell to match resonant frequencies of an imperfect shell. .... 56

**Figure 3.8:** Schematic of  $S^3$  gyroscopes for (a) pitch and (b) roll measurements..... 59

**Figure 3.9:** Schematic of different part of a  $S^3$  gyroscope. .... 60

**Figure 3.10:** Operating mode shapes of a  $S^3$  gyroscope..... 61

**Figure 3.11:** A schematic of driving a  $S^3$  gyroscope using comb-drive actuators and measuring the deflection of the resonant masses using capacitive sensing. .... 62

**Figure 3.12:** Configuration of driving mode operation of a  $S^3$  gyroscope. .... 63

**Figure 3.13:** Configuration of sensing electrodes on top and bottom of resonant masses when system operating in an open loop readout. .... 64

**Figure 3.14:** Configuration of sensing electrodes around a shell when operating in a force-to-rebalance system..... 64

**Figure 3.15:** Configuration of tuning electrodes to match resonant frequencies of a  $S^3$  gyroscope. .... 65

**Figure 3.16:** Shape of considered MEMS gyroscopes for inertial navigation. .... 66

**Figure 4.1:** Design checklist for CVGs. .... 67

**Figure 4.2:** Illustration of the major dissipation mechanisms in shell resonators. These dissipation mechanisms are anchor loss, surface loss, fluidic damping, phonon interaction, internal dissipation, and TED. .... 69

**Figure 4.3:** Normalized deformation distribution inside the substrate beneath an HSR when the shell is vibrating in one of the WG modes—the shell is located in the upper right corners of these figures. .... 71

**Figure 4.4:** Micromachined HSRs fabricated from different materials. Different configurations can be used to attach the shell to the substrate. Usually, a stem is utilized to connect the shell and substrate together. As shown in this figure, the size, shape, and configuration of these stems can be different..... 72

**Figure 4.5:** Cross sectional view of an HSR with a stem (left), and geometrical parameters and nominal dimensions used in this subsection (right). .... 72

**Figure 4.6:** Schematic of wave propagation into an absorbing layer. As waves enter the absorbing layer, they start decaying. If the thickness of the absorbing layer is large enough, waves are damped before reaching the boundary of the layer; therefore, there is not any wave reflection from the absorbing layer to the wave source. .... 73

**Figure 4.7:** One of mesh configurations used to simulate  $Q_{Anchor}$  in HSRs. To create this mesh, quadrilateral elements are generated in a 2D plane and then these elements are revolved to generate a 3D mesh distribution. It is important that the PML meshed such that there are more than 12 nodes per wavelength across the PML. .... 76

**Figure 4.8:** Classification of important parameters affecting anchor loss in HSRs. The anchor loss depends on the shell, stem, substrate properties, and the external motion of an HSR. The effects of all of these properties are investigated in this subsection. .... 79

**Figure 4.9:** Effect of shell material properties on  $Q_{Anchor}$ . By increasing the shell’s Young’s modulus and density,  $Q_{Anchor}$  changes. However, the shell’s Poisson’s ratio has a negligible effect on  $Q_{Anchor}$ . .... 81

**Figure 4.10:** Effect of shell radius and thickness on  $Q_{Anchor}$ . By increasing the shell radius,  $Q_{Anchor}$  increases. However, by increasing the shell thickness,  $Q_{Anchor}$  decreases. .... 82

**Figure 4.11:** Contours of the normalized deformation distribution in the cross section for the thin (left) and thick (right) shells. Upper shells have a smaller radius ( $R = 1250 \mu\text{m}$ ) than lower shells ( $R = 5000 \mu\text{m}$ ). In each case, the largest normalized deformation is fixed to one. In this figure, the minimum amount of normalized deformation in the substrate,  $D_m$ , is shown for each case. The deformation in the substrate of the thicker shells is larger than the thin ones. It is also observed that the shells with smaller radii cause larger deformations in the substrate..... 83

**Figure 4.12:** Effect of an imbalanced mass on  $Q_{Anchor}$ . Mass imperfection, which is modeled as an extra point mass at the rim of a shell, reduces the  $Q_{Anchor}$  of both WG modes; however, it reduces the  $Q_{Anchor}$  of the first mode more than the second one. .... 84

**Figure 4.13:** Effect of non-circularity imperfection on  $Q_{Anchor}$ . Non-circularity reduces  $Q_{Anchor}$  of both WG modes; however, it reduces the  $Q_{Anchor}$  of the second mode more than the first one. .... 86

**Figure 4.14:** Effect of imperfect cutting on  $Q_{Anchor}$ . Imperfect cutting reduces the  $Q_{Anchor}$  of both WG modes similarly..... 86

**Figure 4.15:** Effect of stem material properties on  $Q_{Anchor}$ . By increasing the stem’s Young’s modulus and Poisson’s ratio,  $Q_{Anchor}$  changes. However, the stem’s density has a negligible effect on  $Q_{Anchor}$ . ..... 88

**Figure 4.16.** Effect of stem radius and height on  $Q_{Anchor}$ . By increasing the stem radius,  $Q_{Anchor}$  decreases. However, by increasing the stem height,  $Q_{Anchor}$  increases..... 89

**Figure 4.17:** Contours of the normalized deformation distribution in the cross section for systems with thin stems (left) and thick stems (right). In each case, the largest normalized deformation is fixed to one. Upper shells have shorter stems ( $h = 50 \mu\text{m}$ ) than lower shells ( $h = 400 \mu\text{m}$ ). The deformation in the substrate of the thicker stems is larger than the thin ones. It is also observed that the shells with shorter stem cause larger deformations in the substrate..... 90

**Figure 4.18:** Schematic of the wave propagation from shells with different stem sizes: (a) thin and short, (b) thin and tall, (c) thick and short, and (d) thick and tall. .... 90

**Figure 4.19:** Experimental data reported in [44] about the effect of the stem radius on  $Q$ . In this experiment,  $Q$  of a shell is measured when it is on top of a thick stem, then again when the radius of the stem is reduced from  $7 \mu\text{m}$  to  $3 \mu\text{m}$ . The results show that  $Q$  improves more than 5 times for the case with the thinner stem. .... 91

**Figure 4.20:** Effect of radius of a cylindrical hole in the stem on  $Q_{Anchor}$ . The results show that shells with a solid stem have higher  $Q_{Anchor}$  s than shells with a hollow stem when the stem



wall thickness is not very small. If the stem wall thickness becomes very small  $Q_{Anchor}$  starts to improve. .... 92

**Figure 4.21:** Schematic of the wave propagation from shells with different stems: (a) solid stem, (b) stem with a small hole, (c) stem with a large hole, and (d) stem with a very large hole. .... 92

**Figure 4.22:** Effect of stem shape on  $Q_{Anchor}$ . A shell with a stem with hourglass shape shows the highest  $Q_{Anchor}$ . .... 93

**Figure 4.23:** (a) Effect of an axial misalignment on  $Q_{Anchor}$ . (b) Effect of an angular misalignment on  $Q_{Anchor}$ . These misalignments reduce  $Q_{Anchor}$  significantly. .... 95

**Figure 4.24:** Effect of substrate material properties on  $Q_{Anchor}$ . By changing substrate's Young's modulus and density  $Q$  changes. However, substrate's Poisson's ratio has a negligible effect on  $Q_{Anchor}$ . .... 96

**Figure 4.25:** Effect of radius of the adhesive material on  $Q_{Anchor}$ . Utilizing an adhesive material between the stem and substrate increases  $Q_{Anchor}$ ; however, as the radius of this material increases  $Q_{Anchor}$  decreases and converges to the case that there is not any adhesive material. .... 97

**Figure 4.26:** (a) Different configurations for attaching the stem to the substrate. The best configuration is using a stem inside the shell. (b) Effect of the holding height on  $Q_{Anchor}$  when the stem is held from its edge. By increasing the holding height,  $Q_{Anchor}$  increases; however,  $Q_{Anchor}$  is smaller than the case where the stem is directly attached to the substrate. .... 99

**Figure 4.27:** Effect of vertical and horizontal shocks on  $Q_{Anchor}$ . Horizontal shocks have larger impact on  $Q_{Anchor}$ . ..... 100

**Figure 4.28:** Effect of rotation rate on  $Q_{Anchor}$ . ..... 101

**Figure 4.29:** Schematic of a low anchor loss shell. This shell has the shape of a birdbath with thickness varying along its curvature. .... 103

**Figure 4.30:** Left: dimensions used for anchor loss simulation in BSR. Right: normalized deformation in BSR and the substrate beneath it. .... 104

**Figure 4.31:** Left: schematic of wave propagation in the HSR and BSR. Right: normalized deformation in the substrate of these shells for different amount of deformation. .... 105

**Figure 4.32:** Top: an axisymmetric birdbath shell that is made out of fused silica using blowtorch reflow process. Bottom: cross section of a fabricated shell is shown in right-hand side of this figure..... 106

**Figure 4.33:** Effect of frequency split on  $Q$  of BSRs with 5 mm diameter. Different colors indicate different fabrication batches. No correlation between frequency split and  $Q$ s, suggests that anchor loss is not a major dissipation mechanism in the designed shell structure..... 107

**Figure 4.34:**  $Q_{TED}$  versus resonant frequency of beam resonators with different thicknesses. All beams have a same minimum  $Q_{TED}$ . This minimum occurs in lower resonant frequencies for thicker beams. .... 113

**Figure 4.35:** Cross sectional view of a micro-birdbath shell. Important geometrical parameters for this shell are designated as shown. Nominal dimensions are used as the reference geometry in this subsection. .... 114

**Figure 4.36:** Mesh configuration of a birdbath shell structure. To produce this mesh, quadrilateral elements have been created in the cross section of the shell, and then these 2D elements are revolved. .... 115

**Figure 4.37:** (a) Temperature distribution of a shell resonator in a WG mode. Large temperature gradients are found at the rim and top part of the shell. (b) Thermal paths in a shell when it is vibrating in a WG mode. These paths are across the rim, across the top of the shell, in the polar direction between the rim and top part, in the azimuthal direction between the hot and cold regions in the rim, and in the azimuthal direction between the hot and cold regions in the top part. .... 116

**Figure 4.38:** Amount of elastic strain energy in different parts of the shell. Strain energy in the stem is very small compared to the other parts. .... 117

**Figure 4.39:** Important parameters in TED of shell resonators. TED depends on material properties, geometry, rim conditions, operating temperature, and metal coating. .... 120

**Figure 4.40:** Effect of shell’s material properties on its  $Q_{TED}$ . Increasing  $\alpha$ ,  $k$ ,  $E$ , or  $\nu$  decreases  $Q_{TED}$ , while increasing  $C_{SP}$  or  $\rho$  increases  $Q_{TED}$  of a shell that operates in the quasi-adiabatic regime. .... 121

**Figure 4.41:** Effect of geometrical parameters on  $Q_{TED}$ . Simulation results show that by increasing the rim thickness,  $Q_{TED}$  increases. The results also reveal that other geometrical parameters do not have a significant effect on  $Q_{TED}$ . .... 124

**Figure 4.42:** (a) SEM image of the birdbath resonator rim. As shown in this figure, polishing may cause some chips around the rim edges. (b) A model for a chipped rim. In this model, the

chips are considered to be triangular prisms. The length of base triangle's sides and the prism height are assumed to be  $10 \mu\text{m}$ . ..... 126

**Figure 4.43:** Schematic view of a shell with rounded rim edges. .... 127

**Figure 4.44:** (a) Schematic view of a shell with cutouts from its rim. This method was used to rebalance imperfect shell resonators in [5]. Here, it is considered that the removed masses have a height of  $200 \mu\text{m}$  and arc length calculated from the central angle  $\theta$ . (b) von Mises stress in a shell with rectangular cutouts from its rim. It is found that cutting out some areas from the rim creates concentration of stress at the trimmed corners, which reduces  $Q_{TED}$ . ..... 128

**Figure 4.45:** Normalized  $Q_{TED}$  as a function of arc length for different number of rectangular cutouts around the rim. In this figure,  $Q_{FS}$  is  $Q_{TED}$  of a shell without any rectangular cutouts. As the number of cutouts increases,  $Q_{TED}$  decreases. .... 129

**Figure 4.46:** (a) Schematic view of a grooved rim. (b) Heat transfer across the rim with different groove dimensions..... 130

**Figure 4.47:** Effect of dimension of a groove in the rim on  $Q_{TED}$ . ..... 131

**Figure 4.48:** Normalized  $Q_{TED}$  versus temperature. By increasing the temperature, coupling between the thermal and mechanical domains, also  $\alpha_{FS}$  increases; therefore,  $Q_{TED}$  decreases..... 132

**Figure 4.49:**  $Q_{TED}$  versus thickness of metal coating, normalized to an uncoated resonator. Metal coating has a huge effect on  $Q_{TED}$ . However, as coating thickness becomes very small, the  $Q_{TED}$  of a coated resonator approaches that of an uncoated resonator. .... 134

**Figure 4.50:** Effect of coating material properties on  $Q_{TED}$ . Increasing  $E$ ,  $\alpha$ , or  $\nu$  decreases  $Q_{TED}$ , while  $k$ ,  $\rho$ , and  $C_{SP}$  do not have a remarkable effect. .... 135

**Figure 4.51:** Effect of operating pressure on the  $Q$  of a fused silica BSR. When the pressure is larger than 100  $\mu$ Torr, fluidic damping is the  $Q$ -limiting mechanism. As pressure goes below 10  $\mu$ Torr, other dissipation mechanisms limit  $Q$ . .... 137

**Figure 4.52:** Different sources of surface loss in fused silica shell resonators. Energy might dissipate in surface of fused silica resonators due to the contaminants, intrinsic fused silica dissipation and conductive coating. .... 140

**Figure 4.53:** A summary of several testing steps regarding the effect of surface rinsing on  $Q$  of a fused silica BSR. The results show that surface rinsing has an impact on  $Q$ . Data is provided by Dr. Tal Nagourney. .... 141

**Figure 4.54:** Dependency of fused silica resonators  $Q$  on their V/S (original plot is from [98]). As V/S increases in fused silica resonators  $Q$  improves. .... 143

**Figure 4.55:** Normalized  $Q$  versus V/S of fabricated fused silica BSRs. It appears that increasing V/S increases  $Q$  limit in BSRs.  $Q$  values are provided by Dr. Jae Young Cho, Dr. Tal Nagourney, and Mr. Sajal Singh. .... 144

**Figure 4.56:** Effect of coating thickness on  $Q$  of shell resonators. For both samples,  $Q$  decreases significantly with the first metal deposition of Cr/Au 15/20 Å, then approximately linearly for each additional 40 Å of Au deposited. The results show a good agreement with theoretical value for internal dissipation in metal films. .... 146

**Figure 4.57:** An arbitrary point  $p$  in a shell structure. .... 149

**Figure 4.58:** Reduced order model of vibration of a resonator in the WG modes. The dynamical behavior of a resonator when it is oscillating in the WG modes can be simplified to the vibration of two coupled masses. .... 153

**Figure 4.59:** Effect of geometric properties of the resonator on effective mass. Increasing the rim thickness, shell radius, or height increases the effective mass, while the top and stem wall thicknesses and anchor radius have very small effect. .... 154

**Figure 4.60:** Schematic of a large effective mass shell. This shell is tall and has a large radius and thick rim. .... 155

**Figure 4.61:** Effect of geometric properties of the resonator on angular gain. Increasing the aspect ratio ( $h/R$ ) of shell increases angular gain. .... 157

**Figure 4.62:** Deformation vectors in large and small aspect ratio shells. Majority of movement in small aspect ratio shells is in vertical direction that does not play a role for rotation around vertical axis..... 158

**Figure 4.63:** Birdbath structure is divided to the resonant and non-resonant parts for  $n = 2$  WG modes..... 159

**Figure 4.64:** A ring and a curved beam that cause the deformation of resonant part of the birdbath shell. .... 160

**Figure 4.65:** Effect of geometric properties of the resonator on resonant frequency. Increasing the shell radius and height decreases the resonant frequency, while increasing the rim thickness increases the resonant frequency. The top and stem wall thicknesses and anchor radius have very small effect on resonant frequency. .... 162

**Figure 4.66:** Frequency sweeps of  $n = 2$  WG modes for a BSR. Because of imperfections in the shell, the two modes have an 85 Hz frequency difference. .... 164

**Figure 4.67:** Effect of temperature on material properties of fused silica, which is reported in [89]. (a) Effect of temperature on Young’s modulus. (b) Effect of temperature on Poisson’s ratio. .... 165

**Figure 4.68:** Effect of operating temperature of the fused silica shell resonator on its resonant frequency. Experimental data and simulation results matched together very well. .... 166

**Figure 4.69:** von Mises stress in birdbath structure under 1,000g shock. Horizontal and vertical shocks cause a large stress in the bottom part of the shell. Horizontal shock creates larger stress in resonant parts of the structure comparing to the vertical shock. .... 167

**Figure 4.70:** Effect of vertical shock on resonant frequencies. This shock has a small effect on the resonant frequencies. Additionally, it does not cause any frequency split. .... 168

**Figure 4.71:** Effect of horizontal shock on resonant frequencies. This shock has a large effect on the resonant frequencies. Furthermore, it can create frequency split because it makes the system non-axisymmetric. .... 168

**Figure 4.72:** Normalized  $\Delta f$ , versus normalized extra mass.  $\Delta f$  increases linearly with respect to increasing amount of point mass at the rim of the shell. .... 170

**Figure 4.73:** Effect of edge imperfection on  $\Delta f$ . The results show that the edge imperfection play a key role in  $\Delta f$  between the WG modes. .... 172

**Figure 4.74:** Effect of height imperfection on  $\Delta f$ . The frequency split is not very sensitive to height imperfections less than  $40 \mu\text{m}$ , but for larger height imperfections, it can increase rapidly..... 172

**Figure 4.75:** Effect of electrostatic tuning on normalized change in resonant frequency. The resonant frequency decreases linearly with respect to the tuning signal,  $V^2$ . Here, absolute value of change in resonant frequency is depicted..... 174

**Figure 4.76:** A shell integrated with silicon electrodes. Photos used in this figure are courtesy of Dr. Jae Yoong Cho. .... 176

**Figure 4.77:** Allan deviation plot for a BSR gyroscope. This device achieved one the best ARW and bias instability in MEMS gyroscopes. Test is done by Mr. Christopher Boyd and Dr. Jong Kwan Woo (the detail can be found in [103]). .... 177

**Figure 4.78:** Effect of driving amplitude on ARW in a BSR gyroscope. Experiment is done by Mr. Christopher Boyd and Dr. Jong Kwan Woo..... 178

**Figure 4.79:** Checking BSR gyroscopes design parameters. BSR gyroscopes satisfy majority of the design parameters. .... 180

**Figure 5.1:** Design checklist for CVGs that should be satisfied for  $S^3$  gyroscopes. .... 181

**Figure 5.2:** Operation principle of a roll gyroscope. A mass is driven in the in-plane mode and it will be moved in out-of-plane mode due to Coriolis acceleration. .... 183

**Figure 5.3:** First generation of fused silica resonators in out-of-plane mode and their frequency responses. These resonators show extremely low  $Q$  in the out-of-plane mode (the



fabrication was done by Dr. Zongliang Cao and Mr. Yi Yuan and testing was done by Dr. Gouhonhg He). ..... 184

**Figure 5.4:** Second generation of fused silica resonators in out-of-plane mode and their frequency responses. These resonators show low  $Q$  in the out-of-plane mode. .... 185

**Figure 5.5:** Difference between the first and second generations of fused silica out-of-plane resonators. In general, the second-generation devices tend to produce larger  $Q$ s in the out-of-plane mode..... 186

**Figure 5.6:** Visual representation of deformation in substrate of a single mass resonator as vibrating in out-of-plane mode. When the substrate and resonator have the same thickness, resonator movement causes a large deformation in the substrate. .... 187

**Figure 5.7:** A simple model for the interaction of the resonator and substrate. Decreasing ratio of the substrate to resonator stiffness, increases the deformation in the substrate, leading to a large anchor loss. .... 188

**Figure 5.8:** Effect of substrate thickness on  $Q_{Anchor}$  of in-plane and out-of-plane modes of a single mass resonator. Substrate thickness affects  $Q_{Anchor}$  of out-of-plane mode largely..... 190

**Figure 5.9:** Schematic of force balancing in rope-pulling. Since equal forces pull the rope in opposite direction, there is no movement..... 190

**Figure 5.10:** A simple model for the force balanced out-of-plane resonator. Based on this model, there should not be any motion in the substrate of this resonator. .... 191

**Figure 5.11:** Left: dimensions used for anchor loss simulation in stacked force-balanced resonator. Right: normalized deformation in cross section of this resonator and the substrate beneath it. .... 192

**Figure 5.12:** Left: schematic of wave propagation in the 1 layer and stacked force-balanced resonators. Right: normalized deformation in the substrate of these resonators for different amount of deformation. .... 193

**Figure 5.13:** Classification of important parameters affecting anchor loss in stacked resonators. The anchor loss depends on the device, bonding, and cap layers properties. .... 194

**Figure 5.14:** Effect of device layer material properties on  $Q_{Anchor}$ . By increasing the Young’s modulus and Poisson’s ratio,  $Q_{Anchor}$  decreases. However, increasing the density increases  $Q_{Anchor}$ . .... 195

**Figure 5.15:** Effect of device layer geometric properties on  $Q_{Anchor}$ . Increasing device thickness and suspension width reduces  $Q_{Anchor}$ . While, increasing suspension beam length increases  $Q_{Anchor}$ . .... 196

**Figure 5.16:** Effect of imperfections in geometry of device layers on  $Q_{Anchor}$ . Difference between the geometry of two layers reduces  $Q_{Anchor}$  significantly. .... 197

**Figure 5.17:** Effect of bonding material properties on  $Q_{Anchor}$ . Increasing the bonding Poisson’s ratio decreases  $Q_{Anchor}$  changes. However, the bonding Young’s modulus and density have negligible effects on  $Q_{Anchor}$ ..... 198

**Figure 5.18.** Effect of bonding layer length and thickness on  $Q_{Anchor}$ . By increasing the bonding length,  $Q_{Anchor}$  increases. However, by increasing the bonding thickness,  $Q_{Anchor}$  decreases. .... 199

**Figure 5.19:** Effect of misalignment on  $Q_{Anchor}$ . Misalignments decreases  $Q_{Anchor}$  moderately. .... 199

**Figure 5.20:** Effect of cap material properties on  $Q_{Anchor}$ . By changing cap’s Young’s modulus  $Q_{Anchor}$  changes. However, cap’s density and Poisson’s ratio have negligible effects on  $Q_{Anchor}$ . .... 200

**Figure 5.21:** Effect of cap thickness on  $Q_{Anchor}$ . Increasing cap thickness increases  $Q_{Anchor}$ .... 201

**Figure 5.22:** (a) Exploded view of various part of the tested structure and their dimensions. (b) Assembled structure. .... 202

**Figure 5.23:** a) Frequency response of one layer and two stacked layers resonators. Stacking increases  $Q_{Anchor}$  more than 50×. b) Measured ring-down plot of the one layer and two stacked layers resonators. Stacked resonators shows much larger ring-down time. .... 204

**Figure 5.24:** Effect of mass imbalance between two layers on  $Q$  of a stacked resonator. Mass imbalance between layers decreases  $Q$  slightly. .... 205

**Figure 5.25:** Normalized  $Q$  versus normalized thickness of material between layers. It is found that increasing thickness reduces coupling between layers and increases anchor loss. Using a material like sponge that disconnects acoustic coupling between devices increases anchor loss significantly. Intrinsic damping of plastic layer causes that the larger amount of the device energy dissipates in the stacked resonators. .... 206

**Figure 5.26:** Effect of linear misalignments on  $Q$  of a stacked resonator. Misalignment values are normalized relative to the length (for longitudinal misalignment) and width (for lateral misalignment) of contact area. It is found that improvement due to the stacking is so good

that even with 15% misalignment anchor loss is not dominant dissipation mechanism.  
..... 207

**Figure 5.27:** Effect of angular misalignment on  $Q$  of a stacked resonator. It is found that angular misalignment decreases  $Q$  significantly. .... 208

**Figure 5.28:** One layer SMFB resonator that is used for the TED simulation. .... 210

**Figure 5.29:** Temperature deviation distribution of an SMFB resonator in out-of-plane mode.  
..... 211

**Figure 5.30:** Thermal paths in a folded beam of an SMFB resonator when it is vibrating in sensing mode. These paths are across the thicknesses and lengths of beams  $a$  and  $b$ . .... 212

**Figure 5.31:**  $Q_{TED}$  versus resonant frequency of SMFB resonators made from silicon with different thicknesses. All resonators have a same minimum  $Q_{TED}$ . This minimum occurs in lower resonant frequencies for thicker structures. .... 216

**Figure 5.32:** Effect of silicon resonators dimension on their  $Q$  (original plot is from [95]).... 217

**Figure 5.33:** Schematic of the driving and sensing motion in a  $S^3$  gyroscope. For this schematic, directions of motion in driving and sensing modes are perpendicular to each other as well as to the rotation direction; therefore, angular gain is one. .... 220

**Figure 5.34:** A folded beam assumed as two guided-end beams. .... 221

**Figure 5.35:** Normalized resonant frequencies of driving and sensing mode of a  $S^3$  gyroscope versus its geometrical properties. (b) Effect of thickness of the structure on resonant frequencies. (c) Effect of width of central mass on resonant frequencies. (d) Effect of length of central mass on resonant frequencies. (e) Effect of width of beam  $a$  on resonant

frequencies. (f) Effect of width of beam  $b$  on resonant frequencies. (g) Effect of length of beam  $a$  on resonant frequencies. (h) Effect of length of beam  $b$  on resonant frequencies. .... 226

**Figure 5.36:** Effect of operating temperature of the silicon  $S^3$  gyroscope on its resonant frequencies..... 227

**Figure 5.37:** von Mises stress in one layer of a  $S^3$  structure under 1,000g shock in different directions. These shocks create a large stress in the folded beams. .... 228

**Figure 5.38:** Effect of shock in the  $x$  direction on resonant frequencies. This shock has a significant impact on the resonant frequencies. Additionally, it creates a large frequency split. .... 229

**Figure 5.39:** Effect of shock in the  $y$  direction on resonant frequencies. This shock has a small effect on the resonant frequencies. Furthermore, it does not create a large frequency split. .... 230

**Figure 5.40:** Effect of shock in the  $z$  direction on resonant frequencies. This shock has a significant impact on resonant frequencies. Additionally, it creates a large frequency split. .... 231

**Figure 5.41:** Effect of location of the  $S^3$  gyroscope on a silicon wafer on its resonant frequencies. This figure also shows a wafer with miller indices in a cubic crystal..... 232

**Figure 5.42:** Effect of imperfections in fabrication of geometric properties of the resonator on split on frequencies. Among all of the parameters, variation in the thickness of the resonator has the largest impact. .... 234

**Figure 5.43:** Effect of location of the  $S^3$  gyroscope on the silicon wafer on its frequency split. It is considered that when  $\Theta$  is zero there is no frequency split. .... 235

**Figure 5.44:** Schematic of the  $S^3$  gyroscope and a lumped model for the lower mass and tuning electrodes..... 236

**Figure 5.45:** Schematic of a  $S^3$  gyroscope with extremely small sensing gap and large driving gap. This structure could produce a large driving amplitude and a large sensitivity. .... 238

**Figure 5.46:** Checking the  $S^3$  gyroscope design parameters. This novel design structure can satisfy all the required parameters for high performance gyroscopes..... 240

**Figure 6.1:** Summary of the noise performance of the best MEMS gyroscopes. BSR and  $S^3$  gyroscopes could provide required performance for navigation..... 243

**Figure A1:** First step in fabrication of micro-scale self-aligned shells. (a) A meltable substrate is placed on a machined mold (in this case graphite). (b) Blowtorch is lowered to heat and soften the substrate until it reflows..... 247

**Figure A2:** Second step in fabrication of micro-scale self-aligned shells. (a) Molded structures which are coated with a sacrificial protective metal set into a thick silicon wafer using thermoplastic. (b) The flat portion of the molded substrate is lapped, and the shell rims are polished using CMP. Figures are from [30] and [39]..... 248

**Figure A3:** Birdbath shell structures with different sizes that are made from fused silica using blowtorch reflow process. Photo used in this figure is courtesy of Dr. Tal Nagourney. .... 249

## Abstract

Inertial measurement sensors that include three gyroscopes and three accelerometers are key elements of inertial navigation systems. Miniaturization of these sensors is desirable to achieve low manufacturing cost, high durability, low weight, small size, and low energy consumption. However, there is a tradeoff between miniaturization of inertial sensors and their performance. Developing all the necessary components for navigation using inertial sensors in a small volume requires major redesign and innovation in these sensors.

The main goal of this research is to identify, analyze and optimize parameters that limit the performance of miniaturized inertial gyroscopes and provide comprehensive design guidelines for achieving multi-axis navigation-grade MEMS gyroscopes.

It is shown that the fundamental performance limit of inertial gyroscopes is angle random walk (ARW) due to thermo-mechanical and electronic noises. Theoretical models show that resonant frequency, frequency mismatch between sensing and driving modes, effective mass, quality factor ( $Q$ ), driving amplitude, sensing gap, sensing area and angular gain are the most important parameters that need to be optimized for best noise and most practical device design.

In this research, two different structures are considered for low-noise MEMS gyroscopes: 1) shell gyroscopes in yaw direction, and 2) a novel super sensitive stacked ( $S^3$ ) gyroscope for pitch/roll directions.

Extensive analytical and FEM numerical modeling was conducted throughout this research to investigate the mechanisms that affect  $Q$  and noise in shell resonators used in yaw-rate

gyroscopes. These models provided insight into ways to significantly improve resonator design, structure, fabrication, and assembly and helped fabricate fused silica shells with  $Q$ s as high as 10 million (at least an order of magnitude larger than other similar shells). Noise performance of these fused silica shell gyroscopes with 5 mm diameter improved by about two orders of magnitude ( $<5 \times 10^{-3} \text{ }^\circ / \sqrt{hr}$ ), representing one of the best noise performances reported for a MEMS gyroscope.

To build a high-performance MEMS-based planar vibratory pitch/roll gyroscope, it is critical to have a resonator with high  $Q$  in the out-of-plane resonant mode. Existing out-of-plane resonators suffer from low  $Q$  due to anchor loss or/and thermoelastic dissipation (TED). Increasing the thickness of the out-of-plane resonator reduces TED, but this increases the anchor loss. To reduce anchor loss significantly, a novel structure called  $S^3$  is designed. In this structure, two similar resonators are stacked on top of each other and move in opposite directions, thus providing a balanced stacked resonator with reduced anchor loss. The reduction of anchor loss allows larger thickness of silicon  $S^3$  gyroscopes, leading to a very low TED. A large-scale model of a stacked balanced resonator is fabricated and tested. The initial results show more than 50 times improvement in  $Q$  (measured in air) when resonators are stacked. It is expected that by testing this device in vacuum,  $Q$  would improve by more than three orders of magnitude.

The  $S^3$  design also has an extremely large effective mass, a very large angular gain, a large driving amplitude, a very small sensing gap, and a large sensing area. It is estimated that a 500  $\mu\text{m}$  thick silicon  $S^3$  gyroscope provides ARW of about  $1.5 \times 10^{-5} \text{ }^\circ / \sqrt{hr}$  (more than two orders of magnitude better performance than a navigation-grade gyroscope). This extraordinary small value can be improved for 1mm thick fused silica to  $7.6 \times 10^{-7} \text{ }^\circ / \sqrt{hr}$  if the technology for etching fused silica could be developed in the future.



# Chapter 1: Introduction

## 1.1 Introduction to Navigation

People have moved from one place to another for a long time. To find their destination, they need a tool to guide them in their path. Navigation is the science of guiding movable objects between two points. Majority of navigational techniques include locating the moving object position compared to a known location and then providing direction for the next movement. Currently, there are several navigation approaches:

**-Celestial navigation:** Celestial navigation involves measuring the angle between celestial bodies, which include the sun, the moon, a star, or a planet, and the visible horizon to locate one's position. A celestial body is located directly over one point on the Earth's surface at a given time. The location of this point is known and can be determined from tables. By measuring the angle between the celestial body and the visible horizon the distance between the celestial body's geographic position and the observer's position can be determined. By computing this distance, the point of position of the observer lies on a circle around celestial body's geographic position. Using this method for another celestial body generates another set of points of position for the observer. These two curves intersect in the observer location (as these curves are circles, there are two intersection points, but one of them can be discarded because it is far from the estimated position). An example for this technique is shown in Figure 1.1.

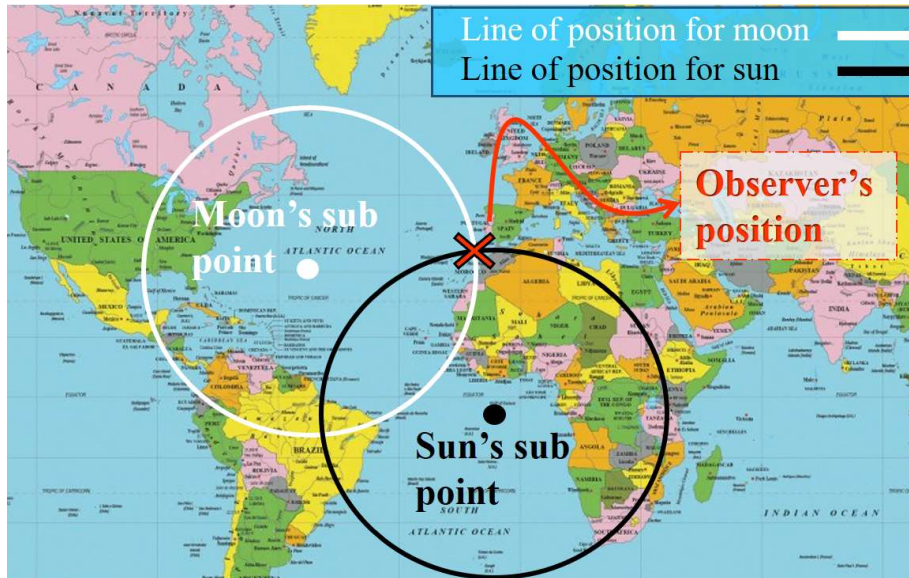


**Figure 1.1:** Finding the position using celestial navigation technique. In this technique, angular measurements taken between a celestial body such as, the Sun, the Moon, a planet, or a star, and the visible horizon are used to find observer's position.

- **Inertial navigation:** Inertial navigation systems determine position by integrating the motion of an object over time. This system needs to know the initial position, direction and magnitude of movement. Inertial sensors such as accelerometers and gyroscopes are used to measure the magnitude and direction of motion. This technique is discussed in detail in subsection 1.2.

- **Radio navigation:** Radio navigation uses a radio direction finder to find the direction to a radio source. A radio direction finder operates by rotating a directional antenna and listening to the signals from a known station and finding which direction has the strongest signal. By measuring second direction from another station and using triangulation the position of moving object can be calculated.

- **Radar navigation:** When a moving object is within the range of navigation radars, the angular bearings and distances can be found from the radar. These data can be used to find the position.

- **Satellite navigation:** A satellite navigation system uses satellites and small electronic receivers to provide the location of moving object (containing receivers). In this system, the satellite broadcasts a signal that contains data about the position of the satellite and the timestamp of the signal. By comparing the time of broadcast from several satellites, the time-of-flight to each satellite can be measured by a receiver, thereby calculating the distance from each satellite, which can lead to the position of the receiver using trilateration process. The Global Positioning System (GPS) uses this technique with accuracy of about a few meters. In fact, United States government commits to broadcasting the GPS signal in space with an average error of  $\leq 7.8$  m, with 95% probability; and the majority of the times, the actual performance is better than this value.

Except inertial navigation system, all other systems need external information. Therefore, they are vulnerable to external conditions, such as weather. Furthermore, the signal is not well transmitted inside buildings, in tunnels, underwater, and underground locations. Additionally, the external signal can be jammed by enemies that might cause problems especially in battle fields. As a result, more reliable navigation technique should be used in these cases. Inertial navigation could potentially be a good candidate for this.

## **1.2 Inertial Navigation**

As shown in Figure 1.2, inertial navigation is a technique that calculates one's current position by using a previously determined position and advancing that position by measuring displacements and orientations in each time-step. Displacement can be measured by double integrating the acceleration information. To measure the actual displacement there is a need for three accelerometers each placed in a mutually perpendicular direction.

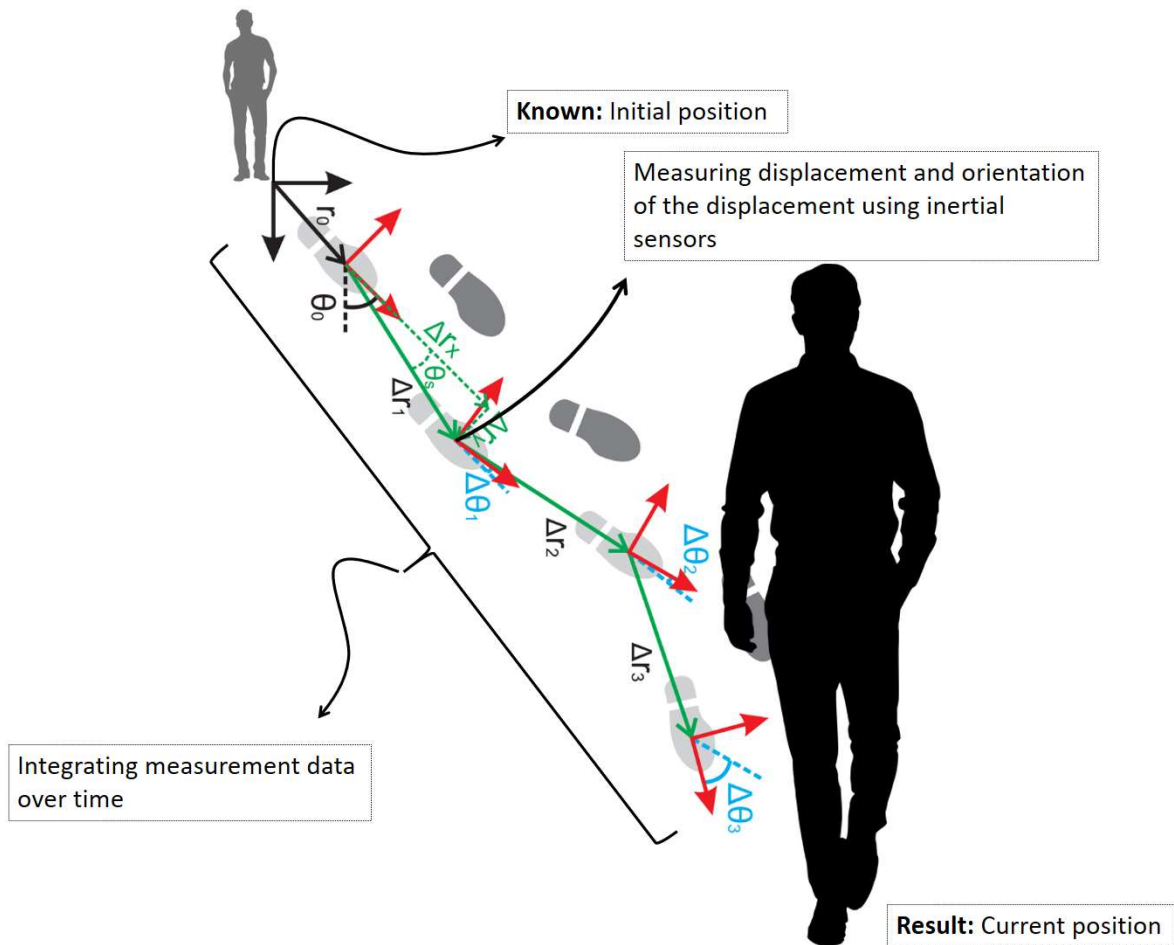


**Figure 1.2:** Fundamentals of inertial navigation. This technique determines current position by using a previously determined position and advancing that position by measuring displacements and orientations in each time-step.

Different types of accelerometers have been developed some of which are listed:

- **Piezoresistive accelerometers:** In these types of accelerometers, piezoresistors are incorporated in the suspension beams that are connected to a proof mass. When there is an acceleration in the system, the proof mass moves relative to the support frame that causes the suspension beams to elongate or shorten, which changes their stress and hence the resistivity of the embedded piezoresistors. This change in resistivity can be measured and calibrated using electronic circuitry.

- **Optical accelerometers:** In these accelerometers, different optical phenomena are used for measuring acceleration. Fiber Bragg grating accelerometer is one of them. In this type of accelerometer, a distributed Bragg reflector that is created within segments of an optical fiber is connected to a proof mass. Fiber Bragg grating reflects unique wavelengths of light, and it transmits all other wavelengths. The refractive index of the optical fiber core varies with changes in strain, so that the Bragg wavelength shifts to higher or lower wavelengths in response to applied stress in the fiber. When there is an acceleration in the system, the proof mass moves relative to the support frame and hence changes the stress inside the connected fiber, which results in wavelength shift.

- **Capacitive accelerometers:** These accelerometers usually consist of a proof mass that is suspended in a support frame. When there is an acceleration in the system, the proof mass moves relative to the support frame, which changes the capacitance between the proof mass and a fixed conductive electrode separated by a narrow gap. This change in capacitance can be measured and calibrated using electronic circuitry.

- **Resonant accelerometers:** In these accelerometers, a proof mass is connected to resonant beams. As there is an acceleration in the system, the proof mass inertial force is transferred to axial force on the resonant beams that changes their resonant frequencies. By measuring and calibrating these shifts in resonant frequencies using electronic circuitry, acceleration can be calculated.

- **Tunneling accelerometers:** These accelerometers use a constant tunneling current between a tunneling tip that is attached to a movable microstructure and its counter-electrode to sense displacement. When the tip is sufficiently close to its counter-electrode, a tunneling current is established and remains constant if the tunneling voltage and distance between the tip and counter-electrode are unchanged. As there is a displacement in the proof mass due to acceleration,

the readout circuit responds to the change of current and adjusts the bottom deflection voltage to move the proof mass back to its original position using electrostatic force generated by the bottom deflection electrode, thus maintaining a constant tunneling current. In this closed loop system, acceleration can be measured by reading out the voltage.

In addition to aforementioned accelerometers, there are other types of accelerometers including thermal, electromagnetic, and piezoelectric accelerometers.

Other than accelerometers, there is a need for three gyroscopes for measuring rotation, that can be used to calculate the orientation of displacements measured by the accelerometer. Several different types of high-performance gyroscopes are also developed, including:

- **Mechanical gyroscopes:** Mechanical gyroscopes operate based on the Coriolis effect. When a mass vibrates in a rotating frame, Coriolis force is exerted to the mass in the perpendicular direction to both the movement and the rotation directions. The magnitude of this force is proportional to the velocity of the mass and the rotation rate.

- **Optical gyroscopes:** These gyroscopes operate based on the Sagnac effect. According to this effect, there are rotation-induced path-length differences for oppositely-traveling lights through an optical loop. Ring laser gyroscopes (RLG) and fiber optic gyroscopes (FOG) are the main types of optical gyroscopes.

- **Nuclear magnetic resonance (NMR) gyroscopes:** These gyroscopes operate based on the change in the Larmor precession frequency of nuclear spins in an applied magnetic field due to rotation.

- **Cold atom gyroscopes:** These gyroscopes operate based on path-length change for two oppositely-traveling atomic waves at extremely low temperature due to rotation (the fundamental principle of cold atom gyroscopes is similar to optical gyroscopes).

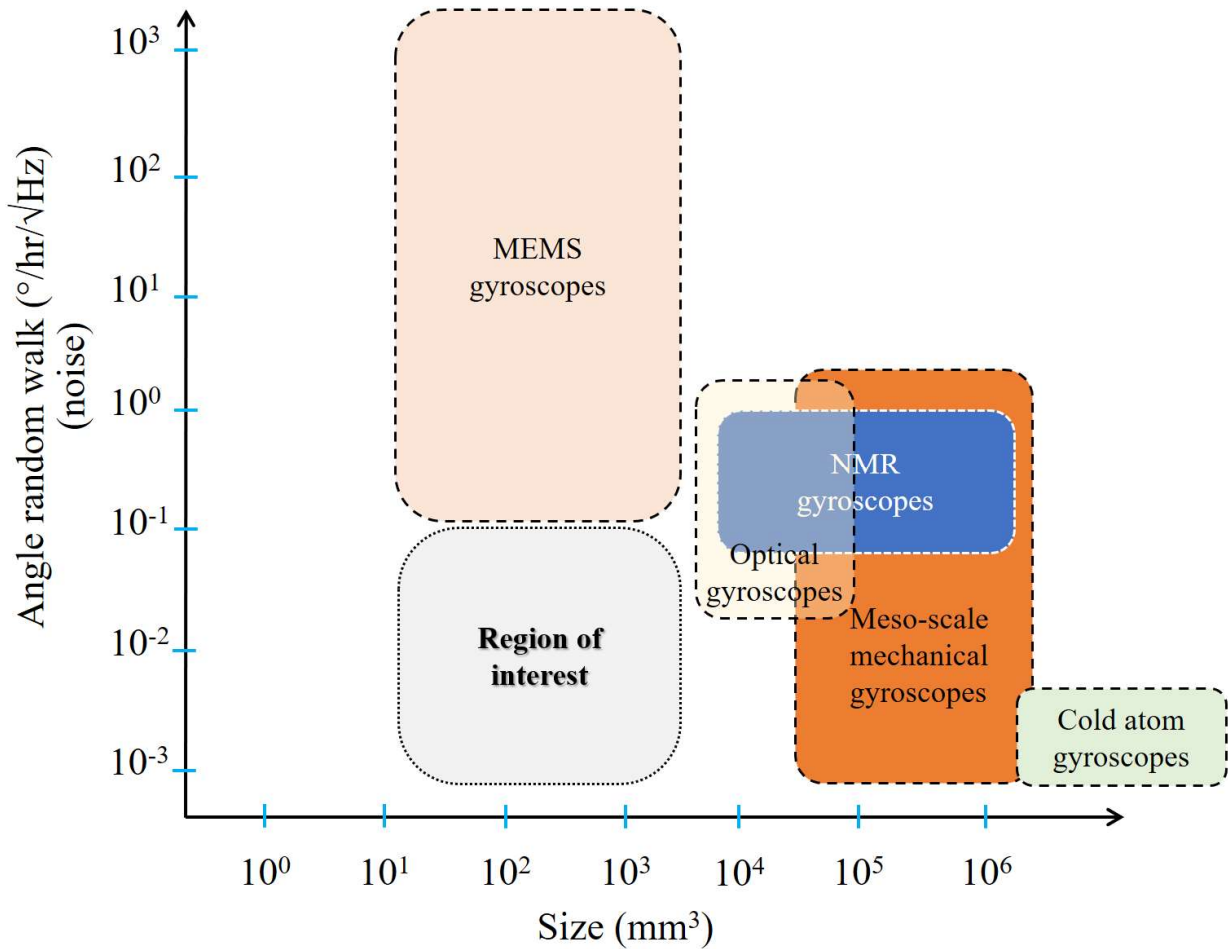


**Figure 1.3:** Noise versus size of different type of gyroscopes. Angle random walk (ARW) shows the noise in gyroscopes. As noise is smaller in a gyroscope, the accumulative error of inertial navigation decreases.

Figure 1.3 shows noise versus size of different type of gyroscopes. In this figure, different boxes show general trend for size and performance of gyroscopes (not exact values). Inertial navigation is subject to cumulative errors; therefore, it is crucial for gyroscopes to have very low noise. Although several high-precision gyroscopes have been already developed, they are very **expensive** and **large** for many applications and still need improvement to overcome price and size issues. A promising approach to overcome these issues is using Microelectromechanical system

(MEMS) technology. MEMS technology is attractive for its low manufacturing cost, light weight, small size, low energy consumption and compatibility with integrated circuits. These features make it extremely attractive for inertial navigation. Unfortunately, existing MEMS gyroscopes have bad performance in terms of noise, limiting their usage for inertial navigation. The aim of this research is to design and develop extremely low-noise MEMS gyroscopes for navigation. In the next section, an overview of MEMS gyroscopes is presented.

### 1.3 MEMS Gyroscopes

Most MEMS gyroscopes are Coriolis Vibratory Gyroscope (CVG). These gyroscopes use the Coriolis acceleration that arises in a moving mass when it is located in a rotating reference frame to measure rotation. In chapter 2, the principles of CVGs will be discussed comprehensively.

Achieving low-noise MEMS gyroscopes to navigate inertially has been a big challenge since the introduction of micromachining technology. Different types of MEMS gyroscopes have been made in the past few decades. They are categorized as follows:

- **Beam gyroscopes:** These gyroscopes consist of a beam, which is vibrating in drive direction as shown in Figure 1.4 [1]. When there is a rotation in the system, the beam starts to vibrate in the sensing direction, which is perpendicular to the rotation and driving axes. To drive these gyroscopes both piezoelectric and electrostatic actuation can be used. For sensing, capacitive and piezoelectric sensing have been used. These gyroscopes usually show a very low performance.



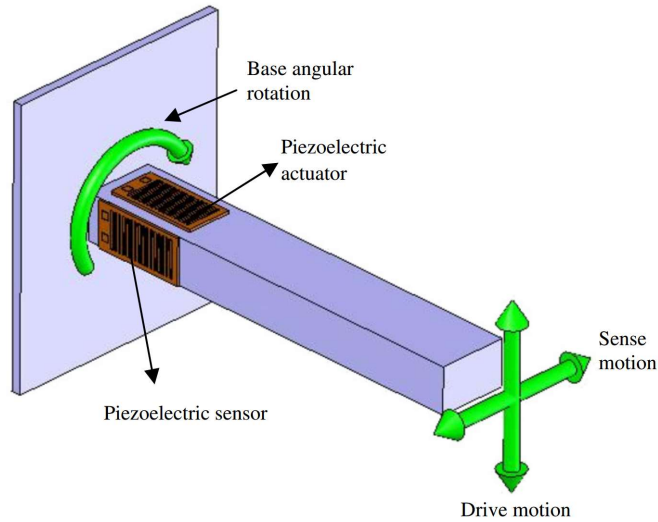


Figure 1.4: Schematic of a beam gyroscope [1].

- **Single mass gyroscopes:** Typically, single mass gyroscopes have a suspended mass and multiple springs that support the mass. This mass vibrates in driving direction and when there is a rotation in the system, it starts to vibrate in a direction that is perpendicular to the driving and rotation axes. To measure this vibration, usually capacitive sensing is used. These gyroscopes usually show low performance. Figure 1.5 shows schematic of a single-mass gyroscope [2].

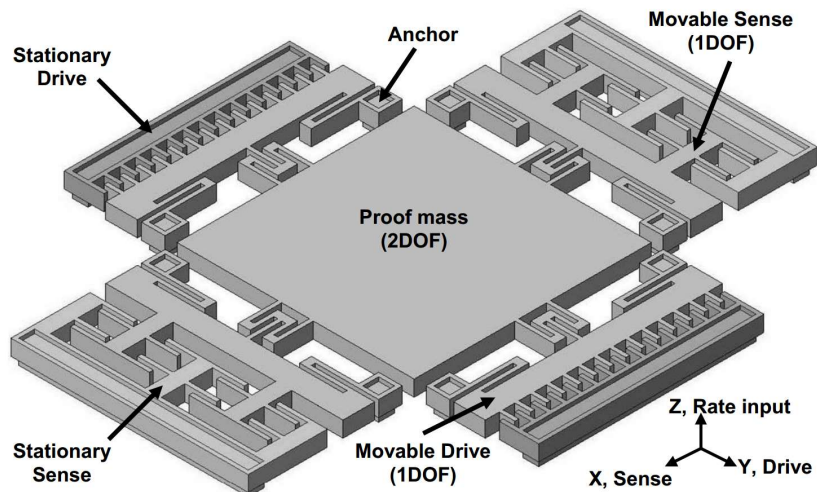
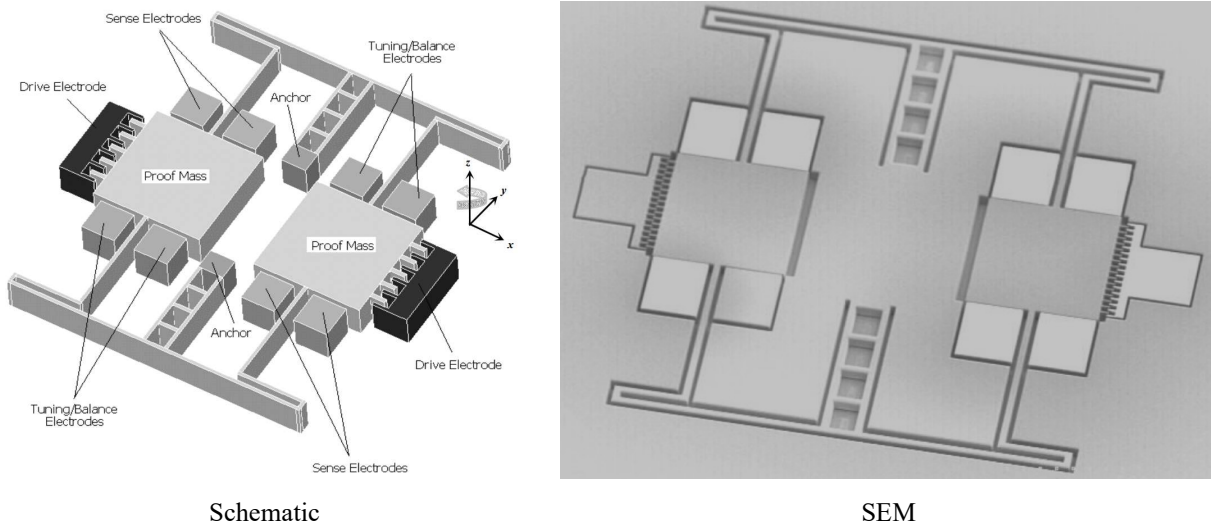


Figure 1.5: Schematic of a single mass gyroscope [2].

- **Dual mass gyroscopes:** These gyroscopes consist of two identical masses that are vibrated in opposite directions. These gyroscopes are basically tuning forks with concentrated masses. They typically use electrostatic driving and capacitive detection methods and have relatively high performance. Figure 1.6 shows one of these gyroscopes that is developed at Georgia Institute of Technology [3].



**Figure 1.6:** A tuning fork gyroscope developed at Georgia Institute of Technology [3].

- **Quad mass gyroscopes:** These gyroscopes consist of four identical suspended masses, coupling springs and levers, and supporting springs. Figure 1.7 shows the driving and sensing modes in a quad mass gyroscope [4]. All the quad mass gyroscopes that are developed until now use electrostatic driving and capacitive sensing. It is shown that these types of gyroscopes can achieve high performance.

- **Shell gyroscopes:** Shell gyroscopes consist of a thin three-dimensional (3D) axisymmetric structure. This structure can vibrate in wine-glass (WG) modes. These modes can be used as driving and sensing modes of a gyroscope as shown in Figure 1.8. These resonance modes occur at the same frequency and have indistinguishable mode shapes.

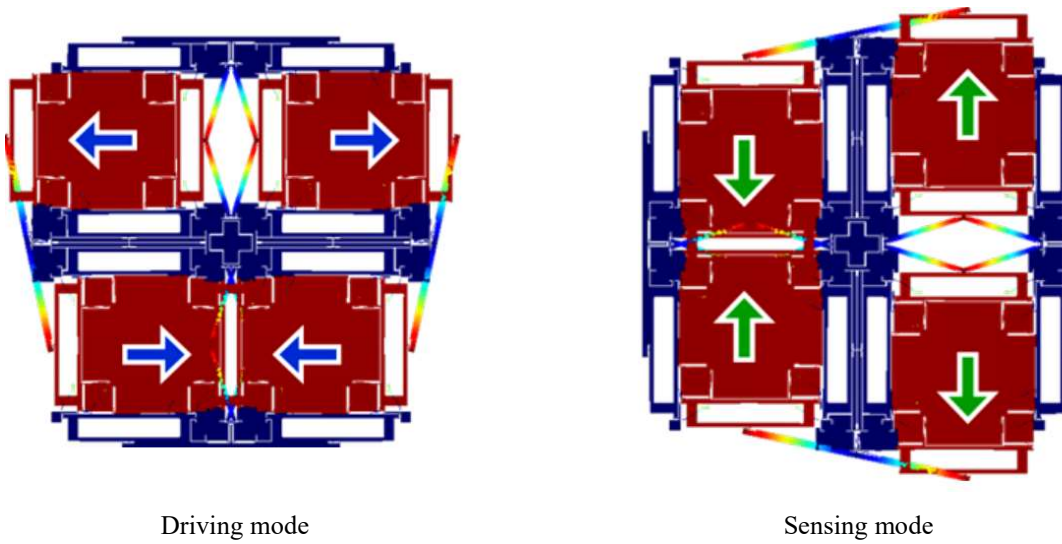


**Figure 1.7:** Driving and sensing modes of a quad mass gyroscope [4].

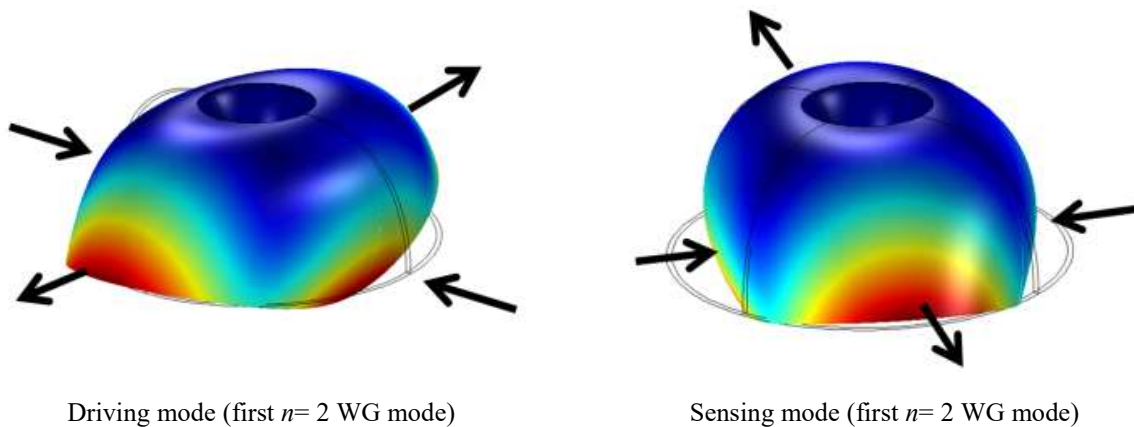


**Figure 1.8:**  $n=2$  WG modes in a shell gyroscope.

These kind of gyroscopes can be fabricated in different shapes as shown in Figure 1.9. It is shown that shell resonators can achieve extremely high performance when they are in meso-scale [5]; however, for micromachined shell gyroscopes the performance is yet below inertial navigation requirement and there is need for more improvement.

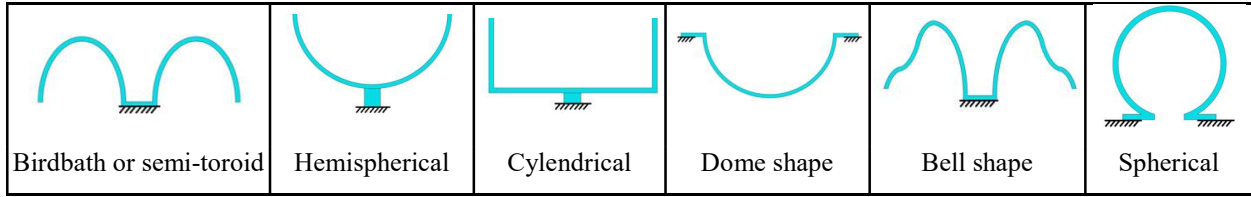


**Figure 1.9:** Shell resonators with different shapes that are shown in this figure, can be used as MEMS gyroscopes.

- **Circular gyroscopes:** These gyroscopes also operate in WG modes. The difference between these and shell gyroscopes is that circular gyroscopes have flat structure as opposed to 3D structure of shell gyroscopes. As shown in Figure 1.10, these gyroscopes can be fabricated in the shape of a ring or disk [6, 7].

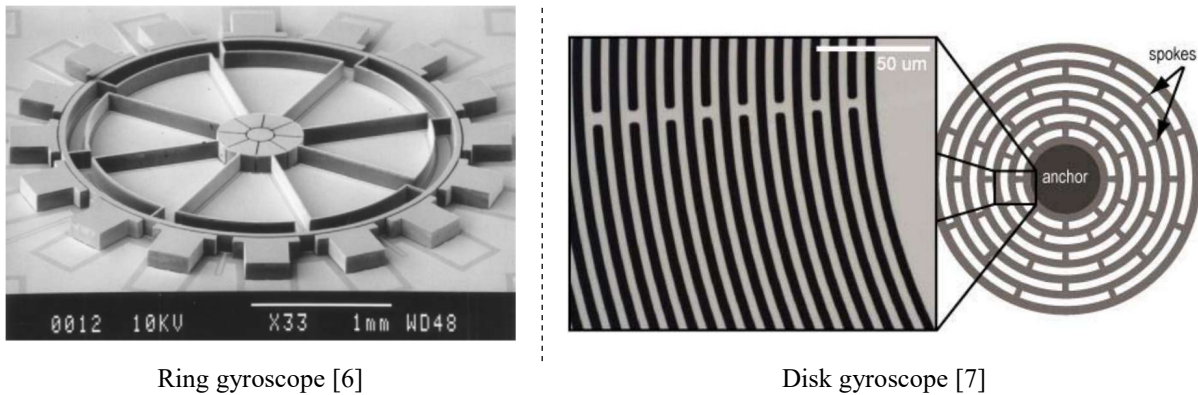


**Figure 1.10:** Two main structures of circular gyroscopes.

- **Bulk acoustic wave (BAW) gyroscopes:** These gyroscopes use acoustic wave motion instead of vibration of proof masses; when there is a rotation in the system, Coriolis effect causes acoustic wave motion in the sensing direction. Both piezoelectric and electrostatic driving and piezoelectric and capacitive sensing have been used in these gyroscopes. Because these gyroscopes operate at very high resonant frequencies, they are very robust to shock and vibration, which makes them promising candidates for navigation in harsh environments; however, because

it is hard to drive them with large amplitude, their performance is not good enough. Figure 1.11 shows one of these gyroscopes [8].

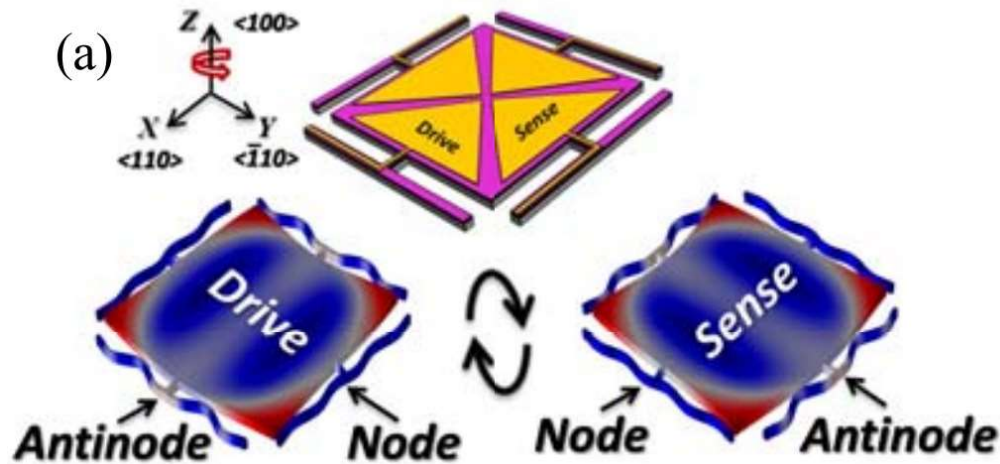


Figure 1.11: A square BAW gyroscope [8].

- **Torsional gyroscopes:** these gyroscopes typically consist of a mass with large moment of inertia which can rotate in different direction. The difference between these gyroscopes and single mass gyroscope is that the proof mass is oscillating torsionally around the driving axis instead of vibrating linearly. When there is a rotation in this system, the mass starts to rotate around the sensing axis, which is perpendicular to the driving and rotation axes. Figure 1.12 shows a schematic of this type of gyroscopes.

Figure 1.13 shows a summary of the noise performance (ARW) of some MEMS gyroscopes in the past 20 years.

Even though there was a good improvement in the performance of these gyroscopes, they are not good enough for navigation, especially for the pitch/roll directions. A gyroscope with ARW less than  $2 \times 10^{-3} \text{ }^\circ/\sqrt{hr}$  ( $1.2 \times 10^{-1} \text{ }^\circ/hr/\sqrt{Hz}$ ) is considered navigation-grade gyroscope [29, 30]. Therefore, there is a need for developing high performance MEMS gyroscopes for all three axes (yaw, pitch, and roll).

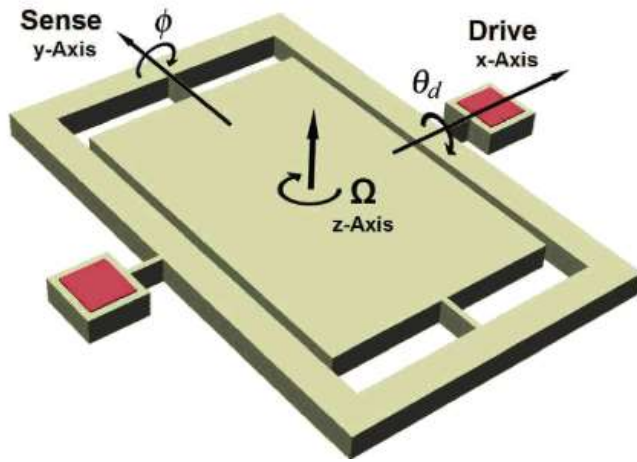


Figure 1.12: Schematic of a torsional gyroscope [9].

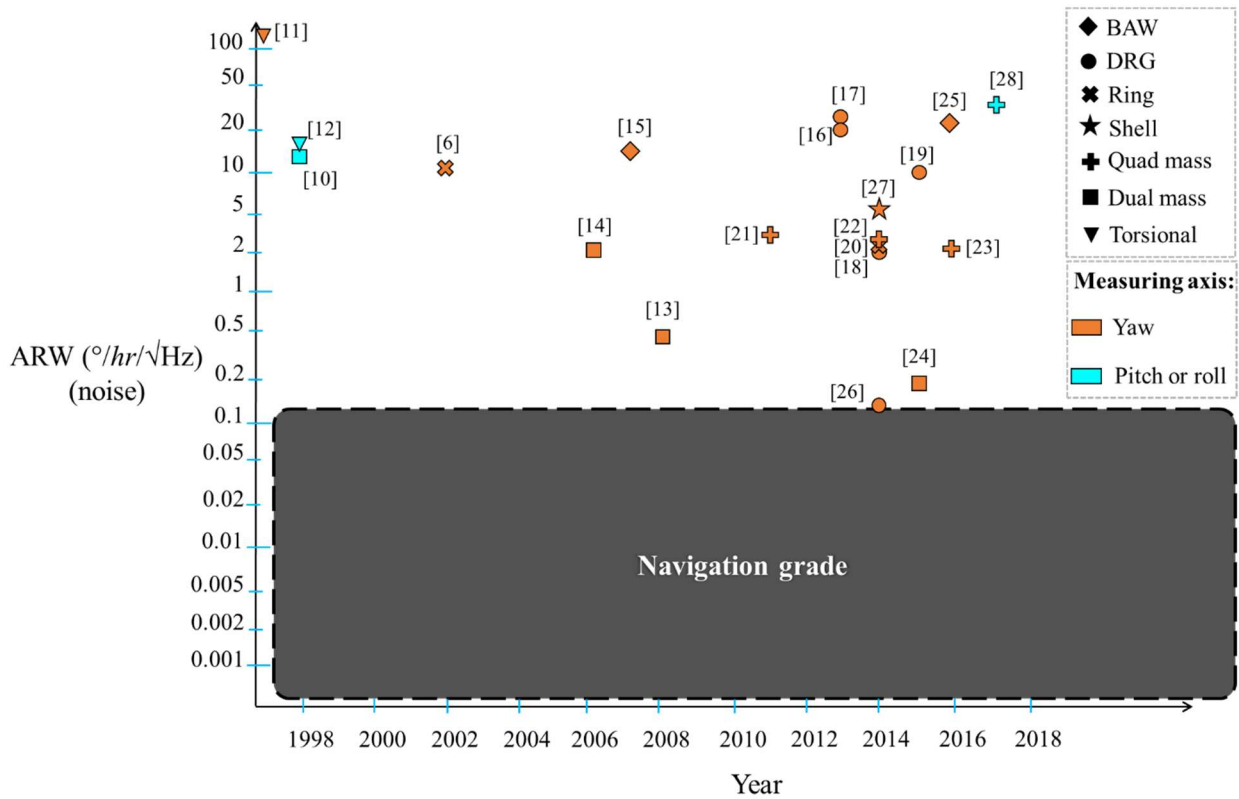


Figure 1.13: Noise performance in the best MEMS gyrosopes. None of them shows required performance for navigation.

## 1.4. Thesis Contributions and Organization

### Research objective:

The main goal of this research is to identify, analyze and optimize parameters that limit the performance of miniaturized inertial gyroscopes and provide design guidelines for achieving navigation grade gyroscopes for all three axes in a small size. Figure 1.14 shows the overview of this research.

As it will be shown in chapter 2, the main source of error in inertial gyroscopes is noise, including thermos-mechanical and electronic noises. Theoretical models are developed to quantify the effect of different parameters on these noises. It is found that resonant frequency, frequency mismatch between sensing and driving modes, effective mass, quality factor, driving amplitude, sensing gap, sensing area and angular gain are the most important parameters for noise in inertial gyroscopes.

To achieve the required noise performance for inertial navigation, two different structures are considered: 1) shell gyroscopes, and 2) super sensitive stacked ( $S^3$ ) gyroscope.

Shell gyroscopes are considered for measuring rotation rate in yaw direction. This type of gyroscope has been utilized in the meso-scale. But miniaturization of these devices reduces their quality factor and effective mass, which leads to a larger noise. This research analyzes all the factors that affect noise of these devices to find new design for these structures, which could provide navigation grade performance in miniaturized shell structures. This includes investigation of loss mechanisms in miniaturized shell structures that could provide guidelines for increasing their quality factor, investigating the sources of frequency mismatch to eliminate them, and some design guidelines for increasing effective mass and angular gain.

This research is about answering the following questions:

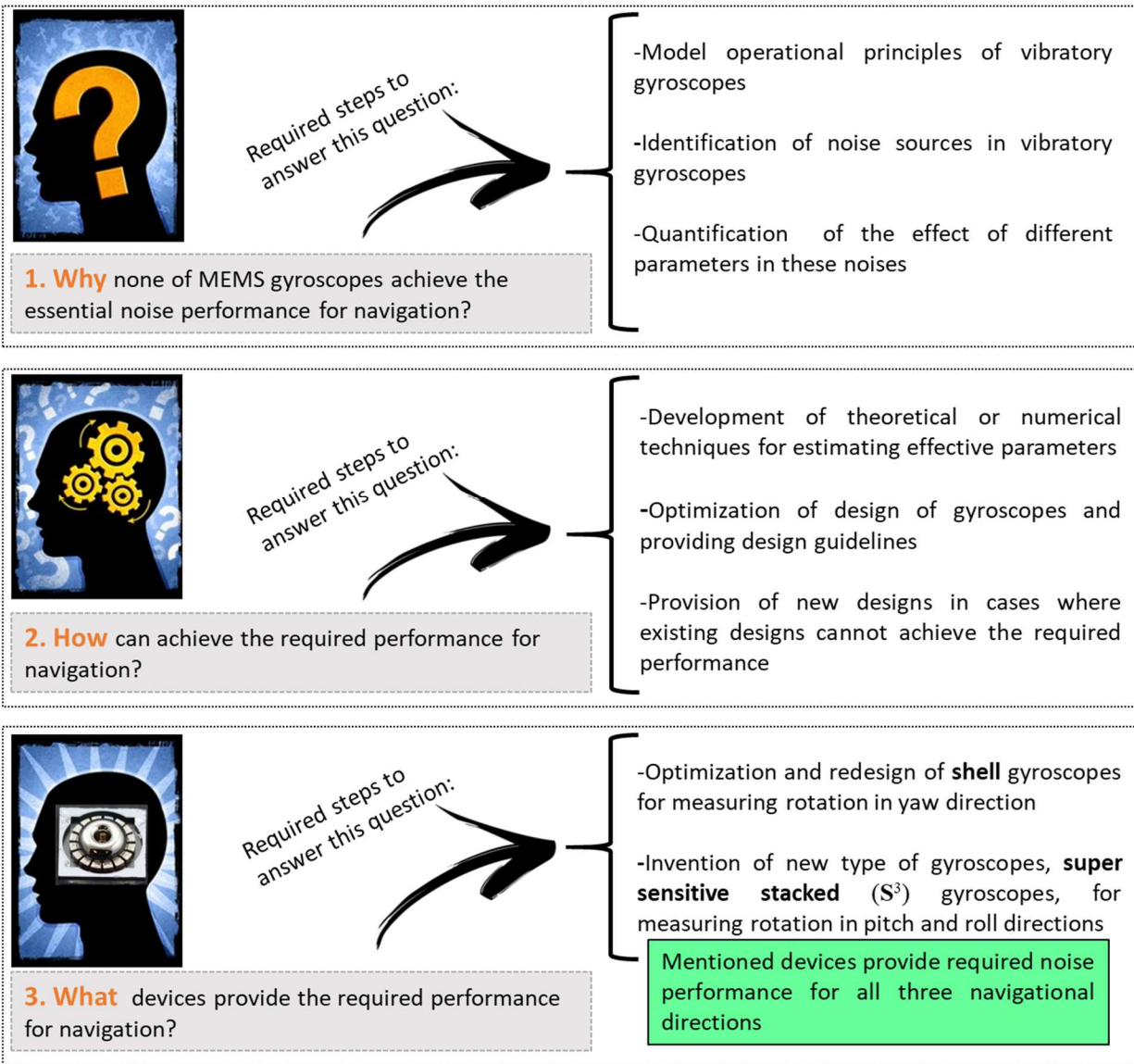


**Figure 1.14:** Questions that will be answered in this research.

In order to measure rotation rate in pitch and roll directions,  $S^3$  gyroscopes are designed. This is the first time that this type of gyroscopes is introduced. The main problem of existing pitch and roll gyroscopes is their low quality factor that is mainly limited by anchor loss and/or thermoelastic dissipation (TED). Increasing the thickness of gyroscopes (for out-of-plane mode)



can reduce TED, but this increases anchor loss. Therefore, the quality factor cannot be increased more than a certain amount. To overcome this problem, the idea of tuning forks is reinvented by stacking two similar resonators in  $S^3$  gyroscopes. In this case, TED can be minimized by increasing the thickness of the gyroscope's layers and anchor loss can be eliminated by preventing wave propagation through balancing of two stacked layers.

Besides improving quality factor, the idea of  $S^3$  gyroscope provides a structure that allows optimization of all other effective parameters in noise of gyroscopes. This includes extremely large effective mass, large angular gain, very small sensing gap, and very large sensing area. In this research, the effect of all design variables on the noise of  $S^3$  gyroscope is analyzed and sets of design guidelines are provided for extremely low noise pitch and roll gyroscopes.

In order to provide the mentioned design guidelines for shell and  $S^3$  gyroscopes, some numerical simulation approaches are developed for the current devices. In some cases, theoretical models are used or developed for better understanding of the behavior of the gyroscopes. Some experimental data are also used for verifying and comprehending some physical phenomena, especially energy dissipation mechanisms in these gyroscopes.

This thesis contributes in several areas, including theoretical modeling, design, and analysis of low-noise gyroscopes and the factors that affect performance. A list of these contributions is provided in Table 1.1. A summary of the main contributions of this research are:

- Identification, modeling, and analysis of parameters that limit the performance of inertial vibratory gyroscopes.
- A comprehensive analysis of critical parameters contributing to noise and step-by-step design guidelines for low-noise MEMS gyroscopes.

- Extensive design, modeling, characterization, and optimization of 3D shell structures for use as high-performance yaw gyroscopes.
- Fabrication and characterization of large-scale stacked balanced resonators, demonstrating significant reduction in anchor loss and improvement in quality factor.
- Design, modeling, and analysis of a novel high-performance MEMS-based planar vibratory pitch/roll gyroscope (the  $S^3$  gyroscope), taking advantage of anchor loss reduction in these out-of-plane stacked balanced resonators.

**Organization of this dissertation:**

This dissertation is organized in six chapters:

**Chapter 1** introduces inertial navigation method and MEMS gyroscopes.

**Chapter 2** analyzes essential design parameters for high-performance gyroscopes.

**Chapter 3** introduces shell and  $S^3$  gyroscopes.

**Chapter 4** investigates and optimizes design parameters for shell gyroscopes.

**Chapter 5** investigates and optimizes design parameters for  $S^3$  gyroscopes.

**Chapter 6** summarizes this research and gives recommendations for improvement in gyroscopes performance.

TABLE 1.1: SUMMARY OF CONTRIBUTION

Area of research	Contribution
<b>Theoretical modeling</b>	<ul style="list-style-type: none"> <li>• Introducing a three degrees of freedom model for dynamics of vibratory gyroscopes</li> <li>• Theoretical modeling of noise sources in gyroscopes with considering the effect of mismatch between driving and sensing frequencies</li> <li>• Providing a reduced order model for dynamics of shell structure</li> <li>• Introducing a theoretical model for predication of resonant frequency of shell resonators in <math>n = 2</math> WG mode</li> <li>• Introducing a theoretical model for predication of quality factor (<math>Q</math>) due to TED of shell resonators in <math>n = 2</math> WG mode</li> <li>• Providing a reduced order model for dynamics of <math>S^3</math> structures when operating as a gyroscope</li> <li>• Introducing a theoretical model for predication of <math>Q</math> due to TED in <math>S^3</math> resonators</li> </ul>
<b>Design and analysis</b>	<ul style="list-style-type: none"> <li>• A comprehensive analysis of critical design parameters for low noise MEMS gyroscopes</li> <li>• Investigating resonant behavior (resonant frequency, frequency split between sensing and driving modes, and mode shapes) of shell structures</li> <li>• Calculating and optimization of effective mass of shell structures</li> <li>• Calculating and optimization of angular gain of shell structures</li> <li>• Comprehensive study in anchor loss of shell resonators</li> <li>• Comprehensive investigation of TED in shell resonators</li> <li>• Analyzing the effect of surface loss, fluidic damping and metal coating on <math>Q</math> of shell resonators</li> <li>• Introducing a novel design for high performance pitch/roll gyroscopes (<math>S^3</math> gyroscopes)</li> <li>• Investigating resonant behavior (resonant frequency, frequency split between sensing and driving modes, and mode shapes) of <math>S^3</math> gyroscopes</li> <li>• Studying anchor loss in <math>S^3</math> gyroscopes</li> <li>• Investigating TED in <math>S^3</math> gyroscopes</li> </ul>
<b>Fabrication and achievements</b>	<ul style="list-style-type: none"> <li>• Fabrication and testing of stacked balanced resonators</li> <li>• Achieved the highest reported <math>Q</math> in MEMS resonators</li> <li>• Achieved 50 times improvement in <math>Q</math> of stacked balanced resonators comparing to non-stacked resonators</li> </ul>

## Chapter 2: Important Parameters for Performance of Vibratory Gyroscopes

To find important parameters in design of vibratory gyroscopes, their physics of operation should be analyzed. In this chapter, dynamics of vibratory gyroscopes will be modeled and then important parameters that determine performance of gyroscopes will be investigated.

### 2.1 Operational Principles of Vibratory Gyroscopes

Here, the operation of a vibratory gyroscope is explained when it is considered as a concentrated mass. To model the dynamical behavior of a vibratory gyroscope, a dynamic system diagram shown in Figure 2.1 is considered. In this system, the gyroscope's proof mass is suspended in a sensors package, which is located in a mobile platform. The mobile platform can move with respect to the inertial frame,  $O_A$ . In Figure 2.1,  $O_S$ ,  $O_P$ , and  $O_m$  are frames that are attached to the mobile platform, the sensors package, and the proof mass, respectively.

Newton's second law of motion can be used to model dynamic behavior of this mass. According to this law,

$$\sum \vec{F} = m\vec{a} \quad (2.1)$$

where,  $\vec{F}$  is force on the mass,  $m$  is the mass of the object, and  $\vec{a}$  is its acceleration in an inertial frame.

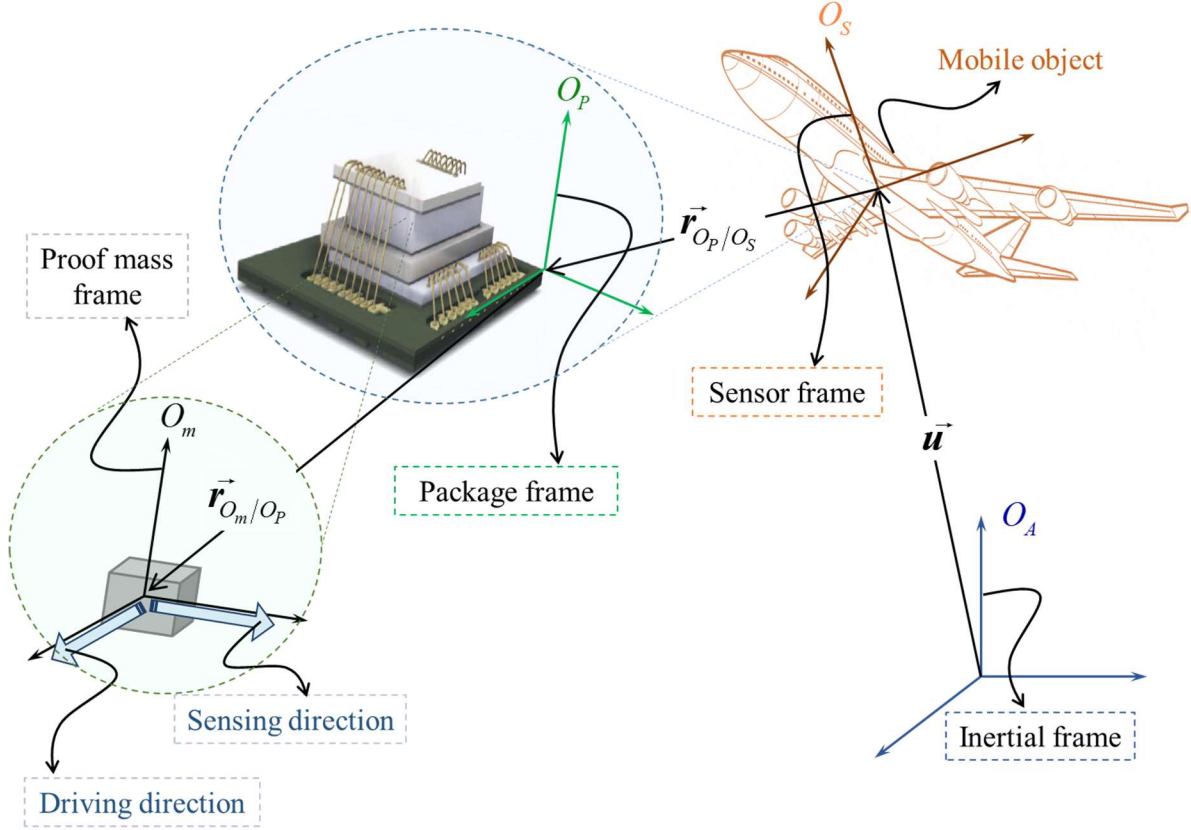


**Figure 2.1:** Dynamics diagram of a vibratory gyroscope inside a mobile object.

It can be shown that the acceleration in the inertial frame equals:

$$\vec{a}_{m/O_A/A} = \vec{a}_{m/O_S/S} + 2\vec{\Omega}_{S/A} \times \vec{v}_{m/O_S/S} + \vec{\Omega}_{S/A} \times \vec{r}_{m/O_S} + \vec{\Omega}_{S/A} \times (\vec{\Omega}_{S/A} \times \vec{r}_{m/O_S}) + \vec{a}_{O_S/O_A/A} \quad (2.2)$$

where:

- $\vec{a}_{m/O_A/A}$ : acceleration of  $m$  relative to the origin of inertial frame in respect to the inertial frame.
- $\vec{a}_{m/O_S/S}$ : acceleration of  $m$  relative to the origin of sensor frame in respect to the sensor frame.
- $\vec{a}_{O_S/O_A/A}$ : acceleration of origin of the sensor frame relative to the origin of the inertial frame in respect to the inertial frame.

- $\vec{v}_{m/O_S/S}$ : velocity of  $m$  relative to the origin of sensor frame in respect to the sensor frame.
- $\vec{\Omega}_{S/A}$ : angular velocity of sensor frame relative to the inertial frame.
- $\vec{\Omega}_{S/A}$ : angular acceleration of sensor frame relative to the inertial frame.
- $\vec{r}_{m/O_S}$ : is position of  $m$  relative to the origin of the sensor frame.

In (2.2), the second, third and fourth terms on the right hand side of the equation are Coriolis, angular acceleration, and centrifugal accelerations, respectively.  $\vec{r}_{m/O_S}$  can be defined as:

$$\vec{r}_{m/O_S} = \vec{r}_{m/O_p} + \vec{r}_{O_p/O_S} \quad (2.3)$$

where  $\vec{r}_{m/O_p}$  is vector of position of  $m$  relative to the origin of the package frame and  $\vec{r}_{O_p/O_S}$  is vector of position of origin of package's frame relative to the origin of sensor's frame. They can be written as:

$$\vec{r}_{m/O_p} = \vec{r}_{0_{m/O_p}} + \vec{X}_m = \left( r_{0_{x_{m/O_p}}} \hat{i} + r_{0_{y_{m/O_p}}} \hat{j} + r_{0_{z_{m/O_p}}} \hat{k} \right) + \left( x_m \hat{i} + y_m \hat{j} + z_m \hat{k} \right) \quad (2.4)$$

$$\vec{r}_{O_p/O_S} = \vec{r}_{0_{O_p/O_S}} + \vec{X}_p = \left( r_{0_{x_{p/O_S}}} \hat{i} + r_{0_{y_{p/O_S}}} \hat{j} + r_{0_{z_{p/O_S}}} \hat{k} \right) + \left( x_p \hat{i} + y_p \hat{j} + z_p \hat{k} \right) \quad (2.5)$$

where  $\vec{r}_{0_{m/O_p}}$  is vector of initial position of  $m$  relative to the origin of the package's frame,  $\vec{r}_{0_{O_p/O_S}}$  is vector of initial position of origin of package's frame relative to the origin of the sensor's frame, and  $\vec{X}_m$  and  $\vec{X}_p$  are the vectors of change in these initial positions, respectively.  $r_{0_{x_{m/O_p}}}$ ,  $r_{0_{y_{m/O_p}}}$ , and  $r_{0_{z_{m/O_p}}}$ ;  $r_{0_{x_{p/O_S}}}$ ,  $r_{0_{y_{p/O_S}}}$ , and  $r_{0_{z_{p/O_S}}}$ ;  $x_m$ ,  $y_m$ , and  $z_m$ ; and  $x_p$ ,  $y_p$ , and  $z_p$  are the components of these vectors. In addition, the components of the  $\vec{\Omega}_{S/A}$  can be represented by  $\Omega_x$ ,  $\Omega_y$ , and  $\Omega_z$ . Therefore,

$$\bar{\mathbf{v}}_{m/O_S/S} = \bar{\mathbf{v}}_{m/O_p/S} + \bar{\mathbf{v}}_{O_p/O_S/S} = \dot{x}_p \hat{i} + \dot{y}_p \hat{j} + \dot{z}_p \hat{k} + \dot{x}_m \hat{i} + \dot{y}_m \hat{j} + \dot{z}_m \hat{k} \quad (2.6)$$

$$\bar{\mathbf{a}}_{m/O_S/S} = \bar{\mathbf{a}}_{m/O_p/S} + \bar{\mathbf{a}}_{O_p/O_S/S} = \ddot{x}_p \hat{i} + \ddot{y}_p \hat{j} + \ddot{z}_p \hat{k} + \ddot{x}_m \hat{i} + \ddot{y}_m \hat{j} + \ddot{z}_m \hat{k} \quad (2.7)$$

$$\bar{\mathbf{a}}_{O_S/O_A/A} = \ddot{u}_x \hat{i} + \ddot{u}_y \hat{j} + \ddot{u}_z \hat{k} \quad (2.8)$$

$$\bar{\boldsymbol{\Omega}}_{S/A} = \Omega_x \hat{i} + \Omega_y \hat{j} + \Omega_z \hat{k} \quad (2.9)$$

where  $u_x$ ,  $u_y$ , and  $u_z$  are the components of the vector  $\bar{\mathbf{u}}$  that represents the position of the origin of the sensor frame relative to the origin of the inertial frame. Hence, the mass acceleration relative to the inertial frame's origin in respect to the inertial frame can be written as:

$$\begin{aligned} \bar{\mathbf{a}}_{m/O_A/A} = & \ddot{x}_p \hat{i} + \ddot{y}_p \hat{j} + \ddot{z}_p \hat{k} + \ddot{x}_m \hat{i} + \ddot{y}_m \hat{j} + \ddot{z}_m \hat{k} + \ddot{u}_x \hat{i} + \ddot{u}_y \hat{j} + \ddot{u}_z \hat{k} \\ & + 2 \left\{ \left[ \Omega_y (\dot{z}_p + \dot{z}_m) - \Omega_z (\dot{y}_p + \dot{y}_m) \right] \hat{i} + \left[ -\Omega_x (\dot{z}_p + \dot{z}_m) + \Omega_z (\dot{x}_p + \dot{x}_m) \right] \hat{j} \right. \\ & \left. + \left[ \Omega_x (\dot{y}_p + \dot{y}_m) - \Omega_y (\dot{x}_p + \dot{x}_m) \right] \hat{k} \right\}_{\text{Coriolis}} \\ & + \left\{ \left[ \dot{\Omega}_y (r_{0z_p/O_S} + r_{0z_m/O_p} + z_p + z_m) - \dot{\Omega}_z (r_{0y_p/O_S} + r_{0y_m/O_p} + y_p + y_m) \right] \hat{i} \right. \\ & + \left[ -\dot{\Omega}_x (r_{0z_p/O_S} + r_{0z_m/O_p} + z_p + z_m) + \dot{\Omega}_z (r_{0x_p/O_S} + r_{0x_m/O_p} + x_p + x_m) \right] \hat{j} \\ & \left. + \left[ \dot{\Omega}_x (r_{0y_p/O_S} + r_{0y_m/O_p} + y_p + y_m) - \dot{\Omega}_y (r_{0x_p/O_S} + r_{0x_m/O_p} + x_p + x_m) \right] \hat{k} \right\}_{\text{Angular Acceleration}} \\ & + \left\{ \left[ \Omega_y \left[ \Omega_x (r_{0y_p/O_S} + r_{0y_m/O_p} + y_p + y_m) - \Omega_y (r_{0x_p/O_S} + r_{0x_m/O_p} + x_p + x_m) \right] \right. \right. \\ & - \Omega_z \left[ -\Omega_x (r_{0z_p/O_S} + r_{0z_m/O_p} + z_p + z_m) + \Omega_z (r_{0x_p/O_S} + r_{0x_m/O_p} + x_p + x_m) \right] \left. \right] \hat{i} \\ & + \left[ -\Omega_x \left[ \Omega_x (r_{0y_p/O_S} + r_{0y_m/O_p} + y_p + y_m) - \Omega_y (r_{0x_p/O_S} + r_{0x_m/O_p} + x_p + x_m) \right] \right. \\ & + \Omega_z \left[ \Omega_y (r_{0z_p/O_S} + r_{0z_m/O_p} + z_p + z_m) - \Omega_z (r_{0y_p/O_S} + r_{0y_m/O_p} + y_p + y_m) \right] \left. \right] \hat{j} \\ & + \left[ \Omega_x \left[ -\Omega_x (r_{0z_p/O_S} + r_{0z_m/O_p} + z_p + z_m) + \Omega_z (r_{0x_p/O_S} + r_{0x_m/O_p} + x_p + x_m) \right] \right. \\ & \left. - \Omega_y \left[ \Omega_y (r_{0z_p/O_S} + r_{0z_m/O_p} + z_p + z_m) - \Omega_z (r_{0y_p/O_S} + r_{0y_m/O_p} + y_p + y_m) \right] \right] \hat{k} \left. \right\}_{\text{Centrifugal}} \end{aligned} \quad (2.10)$$

This equation should be used for right hand side of (2.1). Left hand side of (2.1) equals:

$$\sum \vec{F} = -[\mathbf{K}] \begin{bmatrix} x_m \\ y_m \\ z_m \end{bmatrix} - [\mathbf{C}] \begin{bmatrix} \dot{x}_m \\ \dot{y}_m \\ \dot{z}_m \end{bmatrix} + \vec{f} \quad (2.11)$$

where  $[\mathbf{K}]$  and  $[\mathbf{C}]$  are stiffness and damping matrices, respectively. And  $\vec{f}$  is vector of external forces.  $[\mathbf{K}]$ ,  $[\mathbf{C}]$ , and  $\vec{f}$  can be shown as (2.12), (2.13), and (2.14).

$$[\mathbf{K}] = \begin{bmatrix} k_{xx} & k_{xy} & k_{xz} \\ k_{yx} & k_{yy} & k_{yz} \\ k_{zx} & k_{zy} & k_{zz} \end{bmatrix} \quad (2.12)$$

$$[\mathbf{C}] = \begin{bmatrix} c_{xx} & c_{xy} & c_{xz} \\ c_{yx} & c_{yy} & c_{yz} \\ c_{zx} & c_{zy} & c_{zz} \end{bmatrix} \quad (2.13)$$

$$\vec{f} = \begin{bmatrix} f_x \\ f_y \\ f_z \end{bmatrix} \quad (2.14)$$

To simplify equations, new variable that are shown in (2.15)–(2.31) are defined as:

$$\omega_{xx} = \sqrt{\frac{k_{xx}}{m}} \quad (2.15)$$

$$\omega_{xy} = \sqrt{\frac{k_{xy}}{m}} \quad (2.16)$$

$$\omega_{xz} = \sqrt{\frac{k_{xz}}{m}} \quad (2.17)$$

$$\omega_{yx} = \sqrt{\frac{k_{yx}}{m}} \quad (2.18)$$



$$\omega_{yy} = \sqrt{\frac{k_{yy}}{m}} \quad (2.19)$$

$$\omega_{yz} = \sqrt{\frac{k_{yz}}{m}} \quad (2.20)$$

$$\omega_{zx} = \sqrt{\frac{k_{zx}}{m}} \quad (2.21)$$

$$\omega_{zy} = \sqrt{\frac{k_{zy}}{m}} \quad (2.22)$$

$$\omega_{zz} = \sqrt{\frac{k_{zz}}{m}} \quad (2.23)$$

$$\frac{1}{\tau_{xx}} = \frac{c_{xx}}{2m} \quad (2.24)$$

$$\frac{1}{\tau_{xy}} = \frac{c_{xy}}{2m} \quad (2.25)$$

$$\frac{1}{\tau_{xz}} = \frac{c_{xz}}{2m} \quad (2.26)$$

$$\frac{1}{\tau_{yx}} = \frac{c_{yx}}{2m} \quad (2.27)$$

$$\frac{1}{\tau_{yy}} = \frac{c_{yy}}{2m} \quad (2.28)$$

$$\frac{1}{\tau_{yz}} = \frac{c_{yz}}{2m} \quad (2.29)$$

$$\frac{1}{\tau_{zx}} = \frac{c_{zx}}{2m} \quad (2.30)$$

$$\frac{1}{\tau_{zy}} = \frac{c_{zy}}{2m} \quad (2.31)$$

$$\frac{1}{\tau_{zz}} = \frac{c_{zz}}{2m} \quad (2.32)$$

$$F_x = \frac{f_x}{m} \quad (2.33)$$

$$F_y = \frac{f_y}{m} \quad (2.34)$$

$$F_z = \frac{f_z}{m} \quad (2.35)$$

Using (2.1) and (2.10)–(2.35), dynamical behavior of a vibratory gyroscope can be expressed as (2.36)–(2.38).

$$\begin{aligned} F_x = & \ddot{x}_m + \ddot{x}_p + \ddot{u}_x + \omega_{xx}^2 x_m + \omega_{xy}^2 y_m + \omega_{xz}^2 z_m + \frac{2}{\tau_{xx}} \dot{x}_m + \frac{2}{\tau_{xy}} \dot{y}_m + \frac{2}{\tau_{xz}} \dot{z}_m \\ & + 2\left(\Omega_y (\dot{z}_p + \dot{z}_m) - \Omega_z (\dot{y}_p + \dot{y}_m)\right) + \dot{\Omega}_y \left(r_{0z_p/O_s} + r_{0z_m/O_p} + z_p + z_m\right) \\ & - \dot{\Omega}_z \left(r_{0y_p/O_s} + r_{0y_m/O_p} + y_p + y_m\right) + \Omega_y \left(\Omega_x \left(r_{0y_p/O_s} + r_{0y_m/O_p} + y_p + y_m\right)\right) \\ & - \Omega_y \left(r_{0x_p/O_s} + r_{0x_m/O_p} + x_p + x_m\right) - \Omega_z \left(-\Omega_x \left(r_{0z_p/O_s} + r_{0z_m/O_p} + z_p + z_m\right)\right) \\ & + \Omega_z \left(r_{0x_p/O_s} + r_{0x_m/O_p} + x_p + x_m\right) \end{aligned} \quad (2.36)$$

Considering the package and sensor's frames are located in the same place without any movement relative to each other and also considering the origin of mass is initially located at the origin of package's frame, and furthermore ignoring movement in z-direction for a yaw gyroscope (for a yaw gyroscope, which measures rotation in the z-axis, gyroscope should be designed in a way that mass does not move in the z-direction.), the dynamical behavior of gyroscope is simplified in (2.39) and (2.40).

$$\begin{aligned}
F_y = & \ddot{y}_m + \ddot{y}_p + \ddot{u}_y + \omega_{yx}^2 x_m + \omega_{yy}^2 y_m + \omega_{yz}^2 z_m + \frac{2}{\tau_{yx}} \dot{x}_m + \frac{2}{\tau_{yy}} \dot{y}_m + \frac{2}{\tau_{yz}} \dot{z}_m \\
& + 2\left(-\Omega_x \left(\dot{z}_p + \dot{z}_m\right) + \Omega_z \left(\dot{x}_p + \dot{x}_m\right)\right) - \dot{\Omega}_x \left(r_{0z_p/O_s} + r_{0z_m/O_p} + z_p + z_m\right) \\
& + \dot{\Omega}_z \left(r_{0x_p/O_s} + r_{0x_m/O_p} + x_p + x_m\right) - \Omega_x \left(\Omega_x \left(r_{0y_p/O_s} + r_{0y_m/O_p} + y_p + y_m\right)\right. \\
& \left. - \Omega_y \left(r_{0x_p/O_s} + r_{0x_m/O_p} + x_p + x_m\right)\right) + \Omega_z \left(\Omega_y \left(r_{0z_p/O_s} + r_{0z_m/O_p} + z_p + z_m\right)\right. \\
& \left. - \Omega_z \left(r_{0y_p/O_s} + r_{0y_m/O_p} + y_p + y_m\right)\right)
\end{aligned} \tag{2.37}$$

$$\begin{aligned}
F_z = & \ddot{z}_m + \ddot{z}_p + \ddot{u}_z + \omega_{zx}^2 x_m + \omega_{zy}^2 y_m + \omega_{zz}^2 z_m + \frac{2}{\tau_{zx}} \dot{x}_m + \frac{2}{\tau_{zy}} \dot{y}_m + \frac{2}{\tau_{zz}} \dot{z}_m \\
& + 2\left(\Omega_x \left(\dot{y}_p + \dot{y}_m\right) - \Omega_y \left(\dot{x}_p + \dot{x}_m\right)\right) + \dot{\Omega}_x \left(r_{0y_p/O_s} + r_{0y_m/O_p} + y_p + y_m\right) \\
& - \dot{\Omega}_y \left(r_{0x_p/O_s} + r_{0x_m/O_p} + x_p + x_m\right) + \Omega_x \left(\Omega_z \left(r_{0x_p/O_s} + r_{0x_m/O_p} + x_p + x_m\right)\right. \\
& \left. - \Omega_x \left(r_{0z_p/O_s} + r_{0z_m/O_p} + z_p + z_m\right)\right) - \Omega_y \left(\Omega_y \left(r_{0z_p/O_s} + r_{0z_m/O_p} + z_p + z_m\right)\right. \\
& \left. - \Omega_z \left(r_{0y_p/O_s} + r_{0y_m/O_p} + y_p + y_m\right)\right)
\end{aligned} \tag{2.38}$$

$$\begin{aligned}
F_x = & \ddot{x}_m + \ddot{u}_x + \omega_{xx}^2 x_m + \omega_{xy}^2 y_m + \frac{2}{\tau_{xx}} \dot{x}_m + \frac{2}{\tau_{xy}} \dot{y}_m \\
& - 2\Omega_z \dot{y}_m - \dot{\Omega}_z y_m + \Omega_y \Omega_x y_m - \Omega_y^2 x_m - \Omega_z^2 x_m
\end{aligned} \tag{2.39}$$

$$\begin{aligned}
F_y = & \ddot{y}_m + \ddot{u}_y + \omega_{yx}^2 x_m + \omega_{yy}^2 y_m + \frac{2}{\tau_{yx}} \dot{x}_m + \frac{2}{\tau_{yy}} \dot{y}_m \\
& + 2\Omega_z \dot{x}_m + \dot{\Omega}_z x_m - \Omega_x^2 y_m + \Omega_x \Omega_y x_m - \Omega_z^2 y_m
\end{aligned} \tag{2.40}$$

Ignoring the acceleration of moving object and rotations in other axes, the model simplifies to:

$$\ddot{x}_m + \frac{2}{\tau_{xx}} \dot{x}_m + \left(\omega_{xx}^2 - \Omega_z^2\right) x_m = F_x + \left(2\Omega_z - \frac{2}{\tau_{xy}}\right) \dot{y}_m + \left(\dot{\Omega}_z - \omega_{xy}^2\right) y_m \tag{2.41}$$

$$\ddot{y}_m + \frac{2}{\tau_{yy}} \dot{y}_m + \left(\omega_{yy}^2 - \Omega_z^2\right) y_m = F_y - \left(\frac{2}{\tau_{yx}} + 2\Omega_z\right) \dot{x}_m - \left(\omega_{yx}^2 + \dot{\Omega}_z\right) x_m \tag{2.42}$$

This equation is valid for single mass vibratory gyroscopes, where the entire proof mass experiences Coriolis acceleration during rotation. However, it can be shown that for other types of gyroscopes, such as shell and circular gyroscopes, the same equations can be used for dynamical behavior of the gyroscope with a small modification. In fact, other types of gyroscopes operates exactly as a single mass gyroscope while not all of their structural mass have kinetic energy and the parts that have kinetic energy do not fully contribute to the Coriolis force. To make these equations appropriate for all resonant gyroscopes, two terms can be defined:

**-Effective mass:** this term is defined as the amount of the mass that has the exact same kinetic energy as the real gyroscope when the mass is resonating with the amplitude equal to the largest deflection of the real gyroscope structure.

**-Angular gain:** is defined as the ratio of Coriolis force generated in the resonating structure to a single mass gyroscope with the same effective mass.

The value of these parameters depends on the gyroscope material, structure, resonant mode shapes, etc. These will be discussed comprehensively in chapter 4.

Using these definitions, simplified dynamical behavior of all vibratory gyroscopes can be represented by:

$$\ddot{x}_m + \frac{2}{\tau_{xx}} \dot{x}_m + (\omega_{xx}^2 - \Omega_z^2) x_m = F_x + \left( 2A_g \Omega_z - \frac{2}{\tau_{xy}} \right) \dot{y}_m + (\dot{\Omega}_z - \omega_{xy}^2) y_m \quad (2.43)$$

$$\ddot{y}_m + \frac{2}{\tau_{yy}} \dot{y}_m + (\omega_{yy}^2 - \Omega_z^2) y_m = F_y - \left( \frac{2}{\tau_{yx}} + 2A_g \Omega_z \right) \dot{x}_m - (\omega_{yx}^2 + \dot{\Omega}_z) x_m \quad (2.44)$$

Ideally, a harmonic force is exerted to the mass (in driving direction) such that the mass oscillates harmonically with a constant amplitude (a closed loop control system is used).

Considering force has frequency of  $\omega_{dxx}$ , the oscillation of mass in driving direction has the form of:

$$x_m = d \cos(\omega_{dxx} t) \quad (2.45)$$

where  $d$  is driving amplitude of the mass. Therefore, the sensing equation becomes:

$$\ddot{y}_m + \frac{2}{\tau_{yy}} \dot{y}_m + (\omega_{yy}^2 - \Omega_z^2) y_m = F_y + \omega_{dxx} \left( \frac{2}{\tau_{yx}} + 2A_g \Omega_z \right) d \sin(\omega_{dxx} t) - (\omega_{yx}^2 + \dot{\Omega}_z) d \cos(\omega_{dxx} t) \quad (2.46)$$

To measure rotation rate two approaches can be used:

**-Open-loop:** mass freely vibrates in response to the Coriolis acceleration and amplitude of this oscillation is used to measure amount of rotation rate (force in sensing direction is zero.). Since the amplitude of this oscillation is proportional to the Coriolis acceleration, which is itself proportional to the rotation rate, measuring the amplitude of sensing direction can be used to measure rotation rate.

**-Force-to-rebalance:** a force in the sensing direction exerted to the mass in order to cancel the motion of the mass in this direction. This happens in a closed-loop system, where usually electrostatic force is utilized to prevent the movement of the mass in the sensing direction. This force is proportional to the Coriolis acceleration; therefore, by measuring this force, the rotation rate can be measured.

In an open-loop system, the sensing equation becomes:

$$\ddot{y}_m + \frac{2}{\tau_{yy}} \dot{y}_m + (\omega_{yy}^2 - \Omega_z^2) y_m = \omega_{dxx} \left( \frac{2}{\tau_{yx}} + 2A_g \Omega_z \right) d \sin(\omega_{dxx} t) - (\omega_{yx}^2 + \dot{\Omega}_z) d \cos(\omega_{dxx} t) \quad (2.47)$$

Therefore, the steady-state response is:

$$\begin{aligned}
y_m = & \frac{\omega_{dxx} \left( \frac{2}{\tau_{yx}} + 2A_g \Omega_z \right) d}{\sqrt{\left( \omega_{yy}^2 - \Omega_z^2 - \omega_{dxx}^2 \right)^2 + \left( \frac{2\omega_{dxx}}{\tau_{yy}} \right)^2}} \sin(\omega_{dxx}t + \phi) \\
& - \frac{\left( \omega_{yx}^2 + \Omega_z \right) d}{\sqrt{\left( \omega_{yy}^2 - \Omega_z^2 - \omega_{dxx}^2 \right)^2 + \left( \frac{2\omega_{dxx}}{\tau_{yy}} \right)^2}} \cos(\omega_{dxx}t + \phi)
\end{aligned} \tag{2.48}$$

where

$$\phi = \arctan \left( \frac{-2\omega_{dxx}}{\tau_{yy} (\omega_{yy}^2 - \omega_{dxx}^2)} \right) \tag{2.49}$$

Considering rotation rate is small, the sensing motion becomes:

$$y_m = Y_{m_s} \sin(\omega_{dxx}t + \phi) + Y_{m_c} \cos(\omega_{dxx}t + \phi) \tag{2.50}$$

where

$$Y_{m_s} = \frac{\omega_{dxx} \left( \frac{2}{\tau_{yx}} + 2A_g \Omega_z \right) d}{\sqrt{\left( \omega_{yy}^2 - \omega_{dxx}^2 \right)^2 + \left( \frac{2\omega_{dxx}}{\tau_{yy}} \right)^2}} \tag{2.51}$$

$$Y_{m_c} = - \frac{\left( \omega_{yx}^2 + \Omega_z \right) d}{\sqrt{\left( \omega_{yy}^2 - \omega_{dxx}^2 \right)^2 + \left( \frac{2\omega_{dxx}}{\tau_{yy}} \right)^2}} \tag{2.52}$$

Driving frequency is much higher than one, so the input rate can be estimated by demodulating  $y_m$  signal with  $\sin(\omega_{dxx}t + \phi)$  as the reference. As a result, rotation rate is estimated by:

$$\Omega_z = \frac{1}{2A_g d \omega_{dxx}} \sqrt{\left(\omega_{yy}^2 - \omega_{dxx}^2\right)^2 + \left(\frac{2\omega_{dxx}}{\tau_{yy}}\right)^2} dem(y_m) \Big|_{\sin(\omega_{xx}t + \phi)} - \frac{1}{A_g \tau_{yx}} \quad (2.53)$$

where  $dem(y_m) \Big|_{\sin(\omega_{xx}t + \phi)}$  shows demodulating  $y_m$  signal with  $\sin(\omega_{dxx}t + \phi)$  as the reference. This estimate can be written in the form of :

$$\Omega_z = SF \times dem(y_m) \Big|_{\sin(\omega_{xx}t + \phi)} + B \quad (2.54)$$

where

$$SF = \frac{1}{2A_g d \omega_{dxx}} \sqrt{\left(\omega_{yy}^2 - \omega_{dxx}^2\right)^2 + \left(\frac{2\omega_{dxx}}{\tau_{yy}}\right)^2} \quad (2.55)$$

$$B = -\frac{1}{A_g \tau_{yx}} \quad (2.56)$$

$SF$  is called scale factor and  $B$  is the bias in the system.

In a force-rebalance system, the control loop exerts  $F_y$  such that there is no motion in sensing direction; therefore:

$$F_y = -\omega_{dxx} \left( \frac{2}{\tau_{yx}} + 2A_g \Omega_z \right) d \sin(\omega_{dxx}t) + \left( \omega_{yx}^2 + \dot{\Omega}_z \right) d \cos(\omega_{dxx}t) \quad (2.57)$$

Using the demodulation technique, rotation rate is estimated by:

$$\Omega_z = -\frac{1}{2A_g d \omega_{dxx}} dem(F_y) \Big|_{\sin(\omega_{xx}t)} - \frac{1}{A_g \tau_{yx}} \quad (2.58)$$

where  $dem(F_y) \Big|_{\sin(\omega_{xx}t)}$  shows demodulating  $F_y$  signal with  $\sin(\omega_{dxx}t)$  as the reference. Similar to an open-loop system, rotation rate can be written as

$$\Omega_z = SF \times dem(F_y) \Big|_{\sin(\omega_{dxx}t)} + B \quad (2.59)$$

where scale factor and bias are given by:

$$SF = -\frac{1}{2A_g d\omega_{dxx}} \quad (2.60)$$

$$B = -\frac{1}{A_g \tau_{yx}} \quad (2.61)$$

Therefore, using any of these approaches, rotation rate equals a constant times demodulation of the read-out signal adding to another constant. These constants can be easily calculated using calibration. So, one can measure the rotation rate of the system. By integrating the rotation rate over time, the rotation of the system around the desired axis can be calculated. However, inherent errors in rotation rate measurements using vibratory gyroscopes, if not correctly dealt with, can cause significant problems in navigation. In the following section, errors in the vibratory gyroscopes are investigated.

## 2.2. Errors

Errors in CVGs come from different sources. This section talks about the different categories of errors and identifies the limiting errors in the performance of CVGs.

### 2.2.1 Categories of errors

These errors are categorized in the following terms:

- a) Dynamical (inertial) or cross-axis errors
- b) Scale factor non-linearity
- c) Bias and scale factor drift/instability
- d) Earth's rotation



e) Noise (ARW)

These errors will be discussed in the following parts.

**a) Dynamical (inertial) or cross-axis errors:**

As shown in (2.36) to (2.38), rotations around other axes and accelerations in the system have influences on the movement in the sensing direction. To reduce or eliminate this error, the following steps should be taken:

- The package's and sensor's frames should be located in the same place without any movement relative to each other.

- Movement in z-direction should be nulled; either by proper mechanical structure design or by using some closed-loop force-rebalance system. This is for a yaw gyroscope, which measures rotation around the z-axis. For measuring rotation around other axes, gyroscopes should be designed in a way that the mass does not move in the measurement axes.

- Compensating unwanted terms that are calculated in (2.39) and (2.40), by utilizing other inertial sensors that measure other inertial terms.

**b) Scale factor non-linearity:**

As shown in (2.48), the steady-state response of a gyroscope has a nonlinear dependency to rotation rate with reference to sinusoidal signal. By considering rotation rate is small enough, we ignored non-linear term in (2.51). While for large rotation rates this term cannot be ignored.

To solve this problem, one can use (2.48) instead of (2.51), to calculate rotation rate; however, this increases computation costs.

**c) Bias and scale factor drift/instability:**

The initial bias and scale factor may change over time. In fact, as shown in (2.55), (2.56), and (2.60), bias and scale factor depend on physical and driving properties of a gyroscope. These characteristics can change over time, which results in bias and scale factor drift/instability.

Using (2.56), the bias drift/instability,  $\delta B$ , can be calculated as:

$$\begin{aligned}\delta B &= \frac{\partial B}{\partial A_g} \delta A_g + \frac{\partial B}{\partial \tau_{yx}} \delta \tau_{yx} \\ &= \frac{1}{A_g^2 \tau_{yx}} \delta A_g + \frac{1}{A_g \tau_{yx}^2} \delta \tau_{yx}\end{aligned}\tag{2.62}$$

where  $\delta A_g$  and  $\delta \tau_{yx}$  are change in  $A_g$  and  $\tau_{yx}$ , respectively. Since  $A_g$  and  $\tau_{yx}$  are structural properties of a gyroscope, any change in temperature ( $T$ ), mechanical stress ( $P$ ), and other environmental factors can change them and causes bias drift/instability on the system. Equation (2.63) shows the impact of these factors in bias drift/instability:

$$\begin{aligned}\delta B &= \frac{1}{A_g^2 \tau_{yx}} \left( \frac{\partial A_g}{\partial T} \delta T + \frac{\partial A_g}{\partial P} \delta P + \dots \right) + \frac{1}{A_g \tau_{yx}^2} \left( \frac{\partial \tau_{yx}}{\partial T} \delta T + \frac{\partial \tau_{yx}}{\partial P} \delta P + \dots \right) \\ &= -B \left( \left( \frac{1}{A_g} \frac{\partial A_g}{\partial T} + \frac{1}{\tau_{yx}} \frac{\partial \tau_{yx}}{\partial T} \right) \delta T + \left( \frac{1}{A_g} \frac{\partial A_g}{\partial P} + \frac{1}{\tau_{yx}} \frac{\partial \tau_{yx}}{\partial P} \right) \delta P + \dots \right) \dots\end{aligned}\tag{2.63}$$

This drift/instability can cause a huge inaccuracy in navigation. In fact, a bias drift/instability in attitude rate, if not compensated, becomes a quadratic error in velocity and a cubic error in position. Therefore, it is extremely important to eliminate or compensate bias drift/instability in gyroscopes. To reduce or eliminate this error the following approaches can be used:

- Compensating the effect of environmental changes. For example, using a temperature sensor inside the gyroscope package and compensating for the effect of temperature fluctuations on the bias.

-Reducing change in environmental parameters. For example, keep the temperature of gyroscope constant by using a closed-loop oven-control system and/or reducing stress in the system using stress isolation platform. Several experiments that are done in our group [31, 32] validated this idea. The results of these experiments are briefly presented in the next paragraphs.

To do these experiments commercial inertial measurement units (IMUs), Invensense MPU-6050, are utilized.

The effect of temperature on the bias drift/instability of the gyroscopes are measured by changing ambient temperature from -40C to 85C. This temperature change is performed for two configurations: 1) No temperature control in system. 2) IMU inside a temperature-controlled package, where the temperature of the IMU is kept around 92C. The results are shown in Table 2.1:

**TABLE 2.1:** REDUCING THE EFFECT OF TEMPERATURE CHANGE IN BIAS DRIFT/INSTABILITY USING A TEMPERATURE CONTROLLED PACKAGE [31]

Configuration	Bias drift/instability ( $^{\circ}/hr$ )		
	x-axis gyroscope	y-axis gyroscope	z-axis gyroscope
No temperature control	20610	6486	1288
Temperature controlled package	136.7	144.6	30.53

The results of this experiment show extreme reductions in bias drifts/instabilities (more than 40 times) for a system with temperature fluctuations.

The effect of stress on bias drift/instabilities of gyroscopes is measured by putting the IMU package on top of a PCB board including strain gages and producing about 20 MPa stress in the board [32]. These experiments are performed in two configurations for eight different IMUs. These configurations are:

- No stress isolation platform
- IMU on top of a stress isolation platform

The averaged bias drifts/instabilities for eight IMUs are shown in Table 2.2:

**TABLE 2.2: REDUCING THE EFFECT OF STRESS IN BIAS DRIFTS USING A STRESS ISOLATION PLATFORM [32]**

Configuration	Bias drift/instability ( $^{\circ}/hr$ )		
	x-axis gyroscope	y-axis gyroscope	z-axis gyroscope
No stress isolation platform	4930	2420	4274
IMU on top of a stress isolation platform	134	135	46.7

The results of this experiment also show substantial reductions in bias drifts (more than 18 times) for gyroscopes under fluctuating stresses.

Therefore, reducing the changes in environmental parameters significantly improves bias drift/instability.

Equations (2.55) and (2.60) show that scale factor depends on physical and driving characteristics of a gyroscope. The effect of physical characteristics of the gyroscope on the scale factor drift/instability can be reduced or eliminated using the same approach that is explained for the bias drift. For the driving characteristics of a gyroscope, the driving amplitude and driving frequency must be constant. This can be easily achieved using some closed-looped control systems for driving force.

**d) Earth’s rotation:**

Earth revolves 360.9856 degrees per day and this rotation can be seen by gyroscopic measurements. The measurement results depend on the location and direction of the gyroscope. For example, a pitch or roll gyroscope, located at the equator and pointed north or south, measures

the full amount of the Earth's rotation with the rate of 15.04 °/hr, but the same gyroscope, located at a pole, measures zero.

To remove this effect, the amount of Earth's rotation seen by the gyroscope should be calculated and removed from the measurements.

**e) Noise (ARW)**

The performance of mechanical gyroscopes is physically limited by noises including thermomechanical (Brownian) and electronic. In the following part, these two sources of noise, which are the dominant noise sources in gyroscopes are discussed.

**1) Thermomechanical (Brownian) noise:** This noise is resulted from the Brownian motion of the gyroscopes proof mass. For a mass spring damper system, which is shown in Figure 2.2 the spectral density of the fluctuating force equals:

$$F_n = \sqrt{\frac{4k_B TK}{Q\omega_0}} \quad N / \sqrt{Hz} \quad (2.64)$$

where  $k_B$  is Boltzmann's constant,  $T$  is the absolute temperature,  $\omega_0$  is the resonant frequency,  $K$  is the stiffness, and  $Q$  is the quality factor (equals  $Q = \sqrt{Km}/C$ , where  $C$  is the damping constant and  $m$  is the mass).

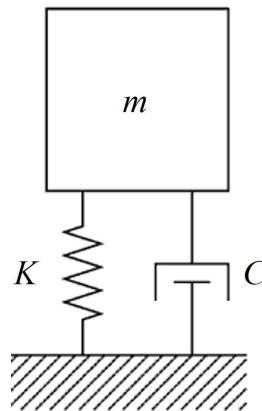


**Figure 2.2:** A mass spring damper system.

As proven in previous subsection, the dynamical behavior of a mechanical gyroscope in the sensing mode has the same model as a second-order mass-spring-damper-system. Displacement to force transfer function for this second-order system equals:

$$G(\omega) = \frac{1}{K \cdot \sqrt{\left(1 - \left(\frac{\omega}{\omega_0}\right)^2\right)^2 + \left(\frac{\omega}{Q\omega_0}\right)^2}} \quad (2.65)$$

where  $\omega$  is the force frequency. Therefore, the Brownian noise displacement,  $\delta_{Brownian}$ , corresponding to the fluctuating force equals:

$$\delta_{Brownian} = \frac{F_n}{K \cdot \sqrt{\left(1 - \left(\frac{\omega}{\omega_0}\right)^2\right)^2 + \left(\frac{\omega}{Q\omega_0}\right)^2}} \quad (2.66)$$

The Brownian noise displacement has its peak where the noise force frequency is the same as the resonant frequency of the system. By considering that the force noise has the resonant frequency component, the displacement noise peak becomes:

$$\delta_{Brownian} = \sqrt{\frac{4k_B T Q}{m\omega_0^3}} \quad (2.67)$$

Amplitude of the response of a mechanical gyroscope to the Coriolis acceleration in the sensing direction equals:

$$Y = \frac{2(A_g)q\Omega_z}{\omega_0 \cdot \sqrt{\left(1 - \left(\frac{\omega}{\omega_0}\right)^2\right)^2 + \left(\frac{\omega}{Q\omega_0}\right)^2}} \quad (2.68)$$

where  $q$  is driving amplitude (that is usually constant) and  $A_g$  is the angular gain. Angular gain is a parameter that shows ability of a gyroscope to transfer motion from the driving direction to the

sensing direction using Coriolis acceleration. This parameter is one for single mass gyroscope and it can be ignored in this equation. However, this parameter decreases to lower values for gyroscopes with distributed mass such as shell gyroscopes and its value should be calculated numerically.

Using (2.67) and (2.68), signal-to-noise ratio,  $SNR$ , in a bandwidth of  $BW$  equals:

$$SNR = \frac{(A_g)q\Omega_z}{\sqrt{\left(1 - \left(\frac{\omega}{\omega_0}\right)^2\right)^2 + \left(\frac{\omega}{Q\omega_0}\right)^2}} \cdot \frac{1}{\sqrt{\frac{k_B T Q}{m\omega_0}} \cdot \sqrt{BW}} \quad (2.69)$$

To calculate the Brownian noise floor, we consider  $SNR = 1$ ; therefore,

$$\Omega_{z(Brownian)} = \frac{1}{(A_g)q} \cdot \sqrt{\frac{k_B T Q}{m\omega_0}} \cdot \sqrt{\left(1 - \left(\frac{\omega}{\omega_0}\right)^2\right)^2 + \left(\frac{\omega}{Q\omega_0}\right)^2} \cdot \sqrt{BW} \quad rad/s \quad (2.70)$$

In the case that sensing resonant frequency is the same as the working frequency (the driving resonant frequency) of the gyroscope, the Brownian noise floor of a gyroscope without frequency split is simplified to:

$$\Omega_{z(Brownian)}^m = \frac{1}{(A_g)q} \cdot \sqrt{\frac{k_B T}{m\omega_0 Q}} \cdot \sqrt{BW} \quad rad/s \quad (2.71)$$

**2) Electronic noise:** This noise is usually the result of the sensing circuit. To detect motion of the proof mass in the sensing direction several approaches can be used. The most common approach is capacitive sensing. As shown in Figure 2.3, in this approach the movement of the proof mass changes the gap between a parallel plate capacitor in a sensing circuit that causes changes in the amount of capacitance ( $C_s$ ).

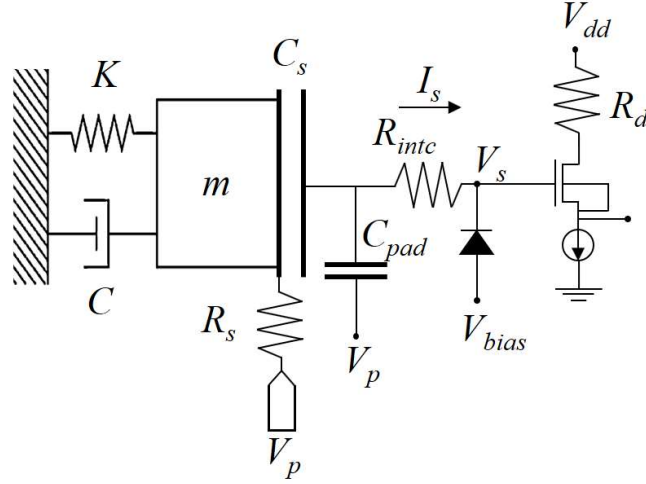


**Figure 2.3:** Schematic of sensing circuit for capacitive detection of proof mass movement in the sensing direction.

In this scheme, the proof mass is set at a polarization voltage,  $V_p$ , a simple source follower is used as the buffer amplifier, the input bias of the amplifier,  $V_{bias}$ , is set by an isolated diode. The capacitance associated with the output pad to the substrate is  $C_{pad}$ , and it is assumed that the substrate is at the polarization voltage.

In this circuit, the ac voltages,  $v_s$ , is developed at the sense electrode due to the movement of the proof mass. Therefore,  $V_s = V_{bias} + v_s$ . The current that flowing through the  $C_s$  and  $C_{pad}$  and injected to the gate of the source follower,  $I_s$ , can be found from (2.72):

$$I_s = \frac{d}{dt}(Q) = \frac{d}{dt}((C_s + C_{pad})(V_p - V_{bias} - v_s)) \quad (2.72)$$

By considering that sensing capacitance has an initial capacitance of  $C_{s_0}$  and varying capacitance of  $\delta C_s$ , (2.72) leads to:

$$I_s = \frac{d}{dt}(C_s) \cdot (V_p - V_{bias} - v_s) - (C_s + C_{pad}) \cdot \frac{d}{dt}(v_s) \quad (2.73)$$



Assuming  $(V_p - V_{bias}) \gg v_s$  and  $(C_{s_0} + C_{pad}) \gg \delta C_s$  simplifies this equation to:

$$I_s \approx \frac{d}{dt}(\delta C_s) \cdot (V_p - V_{bias}) - (C_{s_0} + C_{pad}) \cdot \frac{d}{dt}(v_s) \quad (2.74)$$

The series resistance associated with the path connecting the proof mass to the polarization voltage,  $R_s$ , is negligible compared to the impedance of the sensing capacitance. Considering  $C_{inp}$  is the input capacitance of the buffer amplifier,  $v_s$  can be found from (2.75):

$$v_s = \frac{1}{C_{inp}} \int I_s dt \quad (2.75)$$

Substituting (2.74) to (2.75) results in:

$$v_s = \frac{1}{C_{inp}} \int \left[ \frac{d}{dt}(\delta C_s) \cdot (V_p - V_{bias}) - (C_{s_0} + C_{pad}) \cdot \frac{d}{dt}(v_s) \right] dt \quad (2.76)$$

Therefore,

$$v_s = \frac{\delta C_s}{(C_{s_0} + C_{pad} + C_{inp})} \cdot (V_p - V_{bias}) \quad (2.77)$$

The sensing capacitance can be found from (2.78):

$$C_s = \frac{\varepsilon A}{d_0 + \delta d} \quad (2.78)$$

where  $d_0$  and  $\delta d$  are the initial gap and change in the initial gap of the sensing capacitor, respectively.  $A$  is the area of the sensing capacitor and  $\varepsilon$  is permittivity of the material between sensing capacitor electrodes. Therefore,

$$C_{s_0} = \frac{\varepsilon A}{d_0} \quad (2.79)$$

$$\delta C_s = -\frac{\varepsilon A}{d_0^2} \cdot \delta d \quad (2.80)$$

The amplitude of  $\delta d$  equals the amplitude of the vibration of the proof mass in the sensing direction. As a result:

$$|y_s| = \frac{V_p - V_{bias}}{C_{s_0} + C_{pad} + C_{inp}} \cdot \frac{\varepsilon A}{d_0^2} \cdot Y \quad (2.81)$$

Substituting (2.68) to (2.81), results in the (2.82) for the open loop sensitivity of the gyroscopes:

$$|y_s| = \frac{V_p - V_{bias}}{C_{s_0} + C_{pad} + C_{inp}} \cdot \frac{\varepsilon A}{d_0^2} \cdot \frac{2(A_g)q\Omega_z}{\omega_0 \cdot \sqrt{\left(1 - \left(\frac{\omega}{\omega_0}\right)^2\right)^2 + \left(\frac{\omega}{Q\omega_0}\right)^2}} \quad (2.82)$$

Considering the output power has a noise of  $V_n$  with white spectrum and the bandwidth of the detection circuit is  $BW$ , then  $SNR$  for electronic noise is:

$$SNR = \frac{V_p - V_{bias}}{C_{s_0} + C_{pad} + C_{inp}} \cdot \frac{\varepsilon A}{d_0^2} \cdot \frac{2(A_g)q\Omega_z}{\omega_0 \cdot \sqrt{\left(1 - \left(\frac{\omega}{\omega_0}\right)^2\right)^2 + \left(\frac{\omega}{Q\omega_0}\right)^2}} \cdot \frac{1}{V_n \sqrt{BW}} \quad (2.83)$$

By considering  $SNR = 1$ , the electronic noise floor is calculated to be:

$$\Omega_{z(electronic)} = \frac{C_{s_0} + C_{pad} + C_{inp}}{V_p - V_{bias}} \cdot \frac{\omega_0}{2(A_g)q} \cdot \sqrt{\left(1 - \left(\frac{\omega}{\omega_0}\right)^2\right)^2 + \left(\frac{\omega}{Q\omega_0}\right)^2} \cdot \frac{d_0^2}{\varepsilon A} \cdot V_n \cdot \sqrt{BW} \quad (2.84)$$

For the case that sensing resonant frequency is the same as the working frequency (the driving resonant frequency) of the gyroscope, the electronic noise floor is simplified to:

$$\Omega_z^{m_{z(\text{electronic})}} = \frac{C_{s_0} + C_{pad} + C_{inp}}{V_p - V_{bias}} \cdot \frac{d_0^2}{\varepsilon A} \cdot \frac{\omega_0}{2Q(A_g)q} \cdot V_n \cdot \sqrt{BW} \quad (2.85)$$

**Total noise:** is combination of thermomechanical and electronic noises and can be calculated using the following equation:

$$\begin{aligned} \Omega_z &= \sqrt{\Omega_z^2_{(Brownian)} + \Omega_z^2_{(electronic)}} \\ &= \Omega_z^m \cdot Q \cdot \sqrt{\left(1 - \left(\frac{\omega}{\omega_0}\right)^2\right)^2 + \left(\frac{\omega}{Q\omega_0}\right)^2} \quad \text{rad/s} \end{aligned} \quad (2.86)$$

where  $\Omega_z^m$  is the minimum noise and occurs for the matched gyroscope. This value equals to:

$$\Omega_z^m = \sqrt{\left(\frac{C_{s_0} + C_{pad} + C_{inp}}{V_p - V_{bias}} \cdot \frac{d_0^2}{\varepsilon A} \cdot \frac{\omega_0}{2Q(A_g)q} \cdot V_n\right)^2 + \left(\frac{1}{(A_g)q} \cdot \sqrt{\frac{k_B T}{m\omega_0 Q}}\right)^2} \cdot \sqrt{BW} \quad (2.87)$$

Since the dependency of the Brownian and electronic noises on the frequency mismatch is not clear, this dependency is calculated using the noise floor equations for matched and unmatched gyroscopes. Figure 2.4 shows the results of the numerical calculation of this tendency for different  $Q$ s.

This figure shows that for the operating gyroscopes without mode matching can reduce the performance of the device several times, especially for the devices with high  $Q$ . Therefore, it is extremely important to match the devices to achieve a high performance gyroscope for navigating.

Noise floor for bandwidth of 1 Hz is considered angle random walk (ARW) and it can be calculated using following equation:

$$\text{ARW} = \frac{1}{\sqrt{QqA_g}} \cdot \left( \sqrt{\left( \frac{C_{s_0} + C_{pad} + C_{inp}}{V_p - V_{bias}} \cdot \frac{d_0^2}{\varepsilon A} \cdot \frac{\omega_0}{2\sqrt{Q}} \cdot V_n \right)^2 + \frac{k_B T}{m\omega_0}} \right) \times$$

$$Q \cdot \sqrt{\left( 1 - \left( \frac{\omega}{\omega_0} \right)^2 \right)^2 + \left( \frac{\omega}{Q\omega_0} \right)^2} \quad \text{rad/s}/\sqrt{\text{Hz}} \quad (2.88)$$

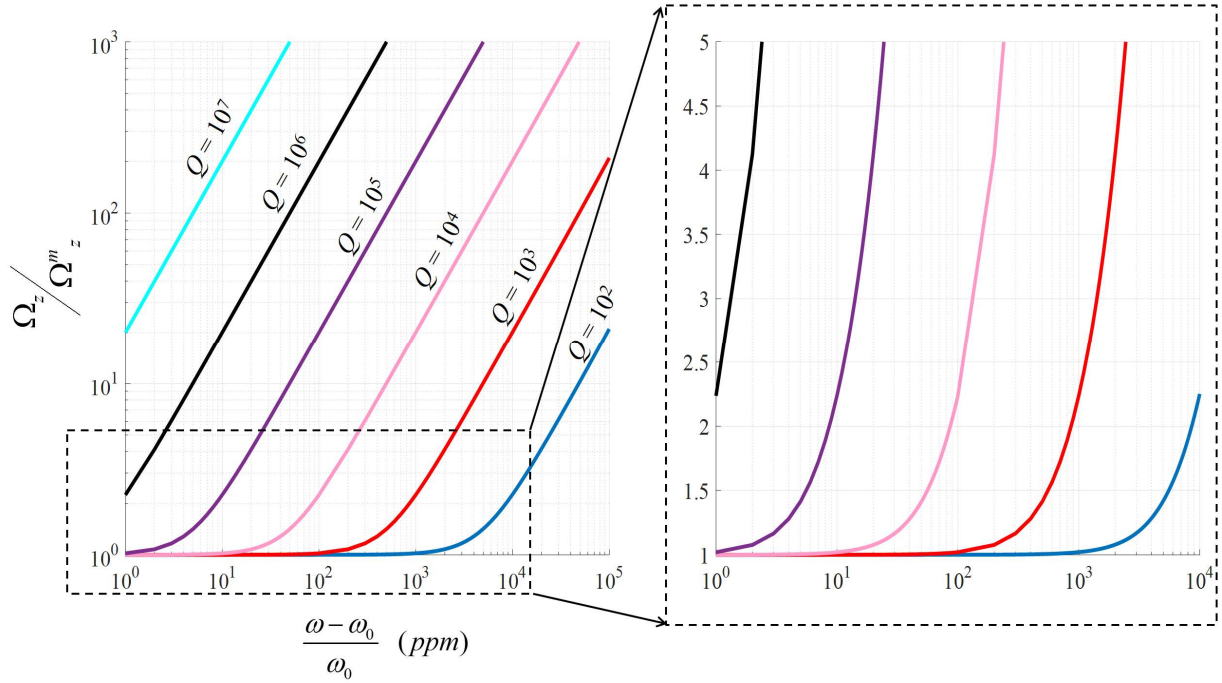


**Figure 2.4:** Dependency of the noise floor in mechanical gyroscopes on frequency mismatch.

## 2.2.2 Fundamental error in CVGs

As explained in this subsection, ARW is the only physical limit for the performance of gyroscopes and other sources of errors can be eliminated and/or compensated; therefore, ARW can be considered as the main characteristic of a vibratory gyroscope. ARW usually is reported with different units. One can use the following equation for converting units:

$$\begin{aligned}
& 1 \text{ rad/s}/\sqrt{\text{Hz}} \\
& = 57.2958 \text{ }^\circ/\text{s}/\sqrt{\text{Hz}} \\
& = 206264.8062 \text{ }^\circ/\text{hr}/\sqrt{\text{Hz}} \\
& = 3437.7467 \text{ }^\circ/\sqrt{\text{hr}}
\end{aligned} \tag{2.89}$$

As discussed in chapter 1, a gyroscope with ARW less than  $2 \times 10^{-3} \text{ }^\circ/\sqrt{\text{hr}}$  ( $1.2 \times 10^{-1} \text{ }^\circ/\text{hr}/\sqrt{\text{Hz}}$ ) is considered navigation grade [29, 30]. While several large vibratory gyroscopes achieve ARW less than  $2 \times 10^{-3} \text{ }^\circ/\sqrt{\text{hr}}$ , no MEMS gyroscopes could achieve this value.

To find out why MEMS gyroscope shows larger ARW compared to larger gyroscopes, (2.88) is analyzed. When the size of a gyroscope is larger, its **effective mass**, **sensing area**, and **driving amplitude** could be larger. Furthermore, experimental data showed that  $Q$  in larger resonators is generally larger and this is because of their smaller surface to volume ratio (in chapter 4, it will be explained why larger surface to volume ratio reduces  $Q$ ). In addition, it is easier to precisely fabricate larger resonators, which leads to **matched resonant frequencies** (no frequency split). Equation (2.88) shows that when a gyroscope has larger effective mass, sensing area, driving amplitude, and  $Q$ , and at the same time has matched frequencies it should produce lower ARW. Therefore, it is completely reasonable to achieve lower noise in larger vibratory gyroscopes.

### 2.3 How to Design Low-Noise Vibratory Gyroscopes

To design a low-noise vibratory gyroscope thermomechanical and electronic noises should be reduced. Theoretical models for these noises were developed in previous subsection. A gyroscope designer can use them to reduce noise in gyroscopes.

Equation (2.70) shows that to reduce thermomechanical noise:

- The effective mass of the gyroscope,  $m$ , should be increased.

- The resonant frequency of the gyroscope,  $\omega_0$ , should be increased.
- The quality factor of sensing mode,  $Q$ , should be increased.
- The amplitude of the driving mode,  $q$ , should be increased.
- The angular gain of the gyroscope,  $A_g$ , should be increased.
- The mismatch frequency between sensing and driving mode,  $|\omega - \omega_0|$ , should be decreased.
- The operating temperature,  $T$ , should be decreased.

Furthermore, (2.84) suggests that for reducing the electronic noise in capacitive gyroscopes, following design criteria should be considered:

- The sensing capacitor area,  $A$ , should be increased.
- The sensing capacitor gap,  $d_0$ , should be decreased.
- The input referred equivalent noise of the detection circuit,  $V_n$ , should be decreased.
- The resonant frequency of the gyroscope,  $\omega_0$ , should be decreased.
- The quality factor of sensing mode,  $Q$ , should be increased.
- The amplitude of the driving mode,  $q$ , should be increased.
- The angular gain of the gyroscope,  $A_g$ , should be increased.
- The mismatch frequency between sensing and driving mode,  $|\omega - \omega_0|$ , should be decreased.
- The polarization voltage,  $V_p$ , should be increased.
- The total amount of the rest capacitances attached to the output node,  $C_{s_0} + C_{pad} + C_{inp}$ , should be decreased.

Among the important parameters that are mentioned to reduce noise,  $T$ ,  $V_n$ ,  $V_p$ ,  $C_{s_0} + C_{pad} + C_{inp}$ , are not design parameters. While,  $q$ ,  $m$ ,  $\omega_0$ ,  $Q$ ,  $A_g$ ,  $|\omega - \omega_0|$ ,  $A$ ,  $d_0$ , are design parameters which should be optimized. Figure 2.5 shows the design checklist of low-noise CVGs.

<b>Both noises:</b>	<b>Electronic noise:</b>	<b>Thermomechanical noise:</b>
Large sensing $Q$ -factor	Large capacitive area	Large effective mass
Large driving amplitude	Small sensing capacitor gap	Large resonant frequency
Large angular gain	Small resonant frequency	
Small mismatch frequency		

**Figure 2.5:** Design checklist of CVGs.

$q$ ,  $A$ , and  $d_0$ , are parameters that do not need analysis and they should be increased or decreased as much as there is no geometrical restriction. To optimize  $m$ ,  $\omega_0$ ,  $Q$ ,  $A_g$ ,  $|\omega - \omega_0|$  in gyroscopes, these parameters need to be estimated. There are some theoretical or numerical approaches for calculating some these parameters, while there is a need for developing new models or numerical approach for others. These approaches will be completely explained in chapters 4 and 5, where MEMS gyroscopes are designed for inertial navigation.

## 2.4 Conclusion

In this chapter, the operational principle of vibratory gyroscopes was explained, and their dynamical behavior was modeled. The model includes three DoF equations that express the behavior of vibratory gyroscopes very comprehensively. Then, possible errors in the vibratory gyroscopes were investigated. It was found that dynamical (inertial) errors, scale factor nonlinearity, scale factor and bias drift/instability, Earth's rotation, and thermomechanical and

electronic noises might degrade performance of gyroscopes. It was explained that among these errors, noises are the only sources of errors in gyroscopes that fundamentally limit their performance. The effects of other errors can be eliminated or reduced.

Thermomechanical and electronic noises of CVGs were comprehensively modeled. The models show that these noises depend on different parameters. A summary of effects of these parameters on the noises is shown in Table 2.3. Among these parameters  $T, V_n, V_p, C_{s_0} + C_{pad} + C_{inp}$ , are not design parameters, whereas  $q, m, \omega_0, Q, A_g, |\omega - \omega_0|, A, d_0$ , are design parameters whom should be optimized. Chapters 4 and 5 talk about shell and  $S^3$  gyroscopes and explain methods to optimize design parameters in them.



**TABLE 2.3: EFFECT OF INCREASING DIFFERENT PARAMETERS ON NOISES OF CVGS**

Parameter	Label	Effect of increasing this parameter on noises:	
		Thermomechanical (Brownian)	Electronic
effective mass	$m$	decreases	no effect
resonant frequency	$\omega_0$	decreases	increases
sensing mode quality factor	$Q$	decreases	decreases
driving amplitude	$q$	decreases	decreases
angular gain	$A_g$	decreases	decreases
mismatch frequency	$ \omega - \omega_0 $	increases	increase
operating temperature	$T$	increases	no effect
sensing capacitor area	$A$	no effect	decreases
sensing capacitor gap	$d_0$	no effect	increases
equivalent noise of the detection circuit	$V_n$	no effect	increases
polarization voltage	$V_p$	no effect	decreases
rest capacitances attached to the output node	$C_{s_0} + C_{pad} + C_{inp}$	no effect	increases

## **Chapter 3: Conceptual Designs for Measuring Angular Rotation Around Different Directions**

To perform inertial navigation there is a need for three different gyroscopes, which measure rotation in the pitch, roll and yaw directions with high performance. In this study, two different types of the gyroscopes will be analyzed, designed, and characterized to achieve this goal: 1) shell gyroscopes for the yaw direction measurement and 2) Super sensitive stacked ( $S^3$ ) gyroscopes for the pitch and roll directions.

In this chapter, the important features of these gyroscopes will be discussed. This introductory discussion provides general overview and structural shapes of these gyroscopes. Optimization of design parameters and performance characterization of these devices will be extensively analyzed in subsequent chapters.

### **3.1. Shell Gyroscopes**

Three-dimensional (3D) shell resonators operating in the wine-glass (WG) modes with high quality factors ( $Qs$ ) and axisymmetric structures are great candidates for high-performance rate and rate-integrating gyroscopes—because of their shape they have very similar sensing and driving resonant characteristics. A shell gyroscope, shown in Figure 3.1, consists of two main elements: shell resonator, and electrodes.

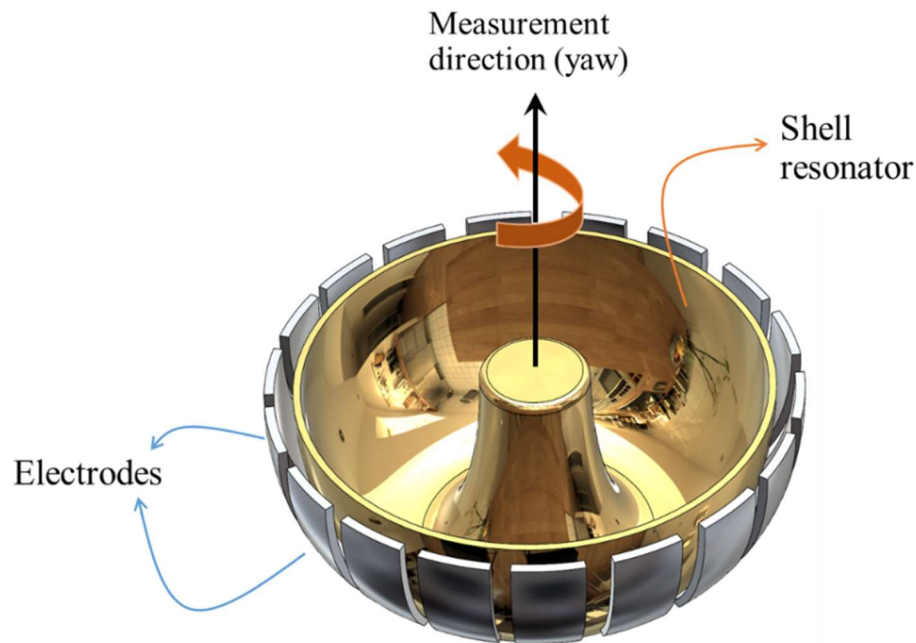


**Figure 3.1:** A schematic of a shell gyroscope including a shell resonator and electrodes.

### 3.1.1. Operating modes

In the 1960s, researchers [5] proved that hemispherical shell resonators can be used as vibratory gyroscopes when operated in the  $n = 2$  WG modes. Figure 3.2 shows these mode shapes for an axisymmetric shell structure. Contours of the deformation are also shown in this figure (they are normalized to the maximum deflection in the structure).

As shown in Figure 3.2, the highest deflection occurs at the point closest to the rim of the shell. For a perfectly symmetric structure, the resonant frequencies of these two modes are the same. In the first WG mode, two opposite points on the edge approach each other while two other points, offset by  $90^\circ$  from the first two, move apart. In the second WG mode, the same pattern occurs but the position of the points with the highest deflection (anti-nodes) shifts by  $45^\circ$ .

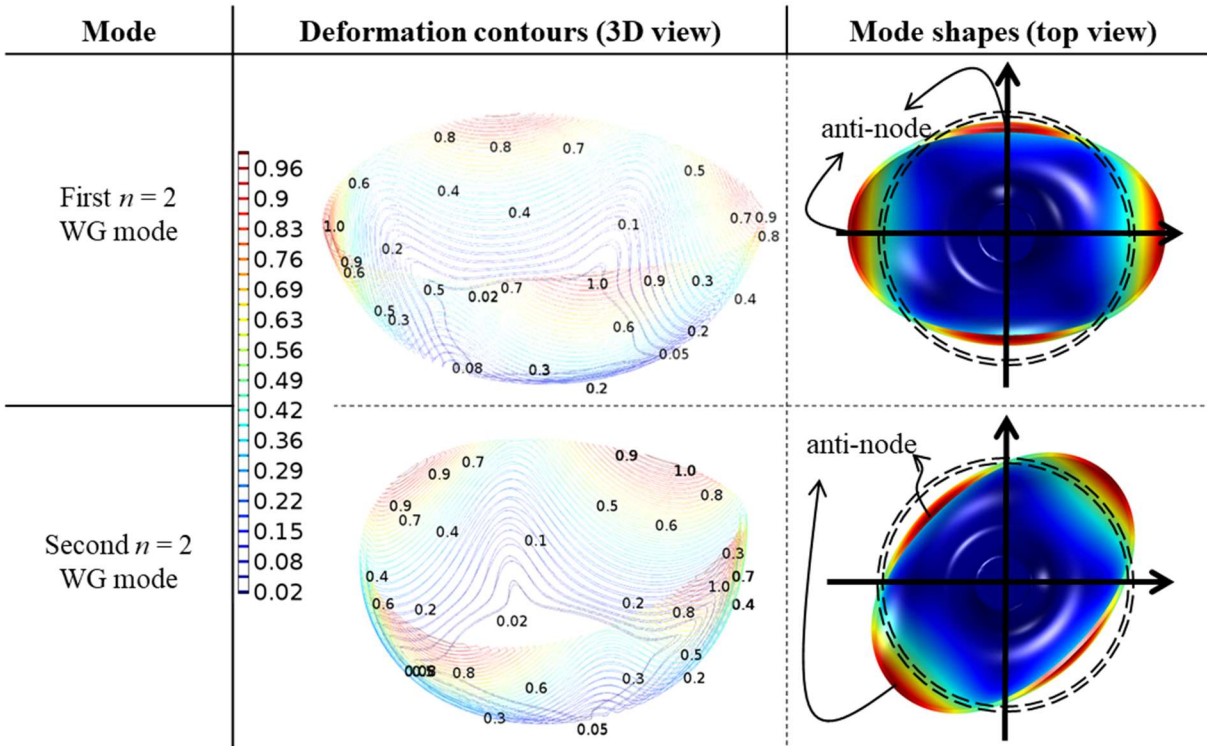


**Figure 3.2:** Deformation pattern in an axisymmetric shell structure in the  $n = 2$  WG modes. Color legend in shows normalized displacement. For a perfectly symmetric shell, resonant frequencies and vibrational behavior of the first and second  $n = 2$  WG modes have the same shape, but deformation pattern shifts by  $45^\circ$ .

### 3.1.2. Driving and sensing schemes

Electrostatic force can be used to vibrate a shell structure in driving WG mode. Figure 3.3 shows a schematic for driving a shell structure using electrostatic force.

In the case that there is rotation in the yaw direction, Coriolis acceleration causes the shell to vibrate in the other WG mode. The velocity of this vibration has direct relationship with the rotation rate; therefore, by measuring the deformation of the shell in this mode the rotation rate can be sensed. To measure this deformation, the change in capacitance between shell and sensing electrode is usually used.

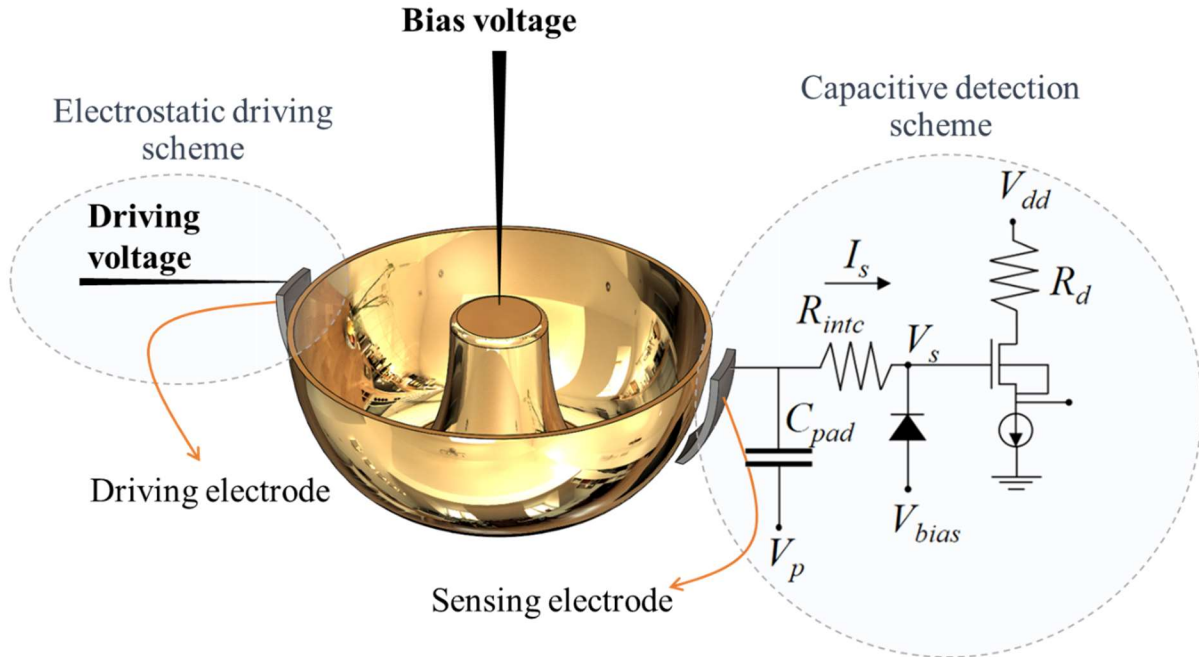


**Figure 3.3:** A schematic of driving a shell structure in one of its WG modes using electrostatic force and measuring the deflection of the shell using capacitive sensing.

Other driving and sensing schemes, such as piezoelectric driving and optical sensing, can also be used. However, they usually increase complexity and or decrease the performance of gyroscopes. Therefore, electrostatic driving and capacitive sensing are the most common approaches in MEMS gyroscopes.

### 3.1.3. Device operation

To operate a shell as a gyroscope, 16 electrodes are located around the circumference of the shell. Four of these electrodes can be used as driving electrodes. Figure 3.4 shows the schematic of their configuration and deformed shell in the driving WG mode.

When there is no rotation in the system, the sensing WG mode will not be excited, so its amplitude is zero. Rotating the gyroscope around yaw direction, excites sensing WG mode due to

the Coriolis acceleration. To measure rotation, two approaches can be used: 1) open-loop 2) force-to-rebalance.

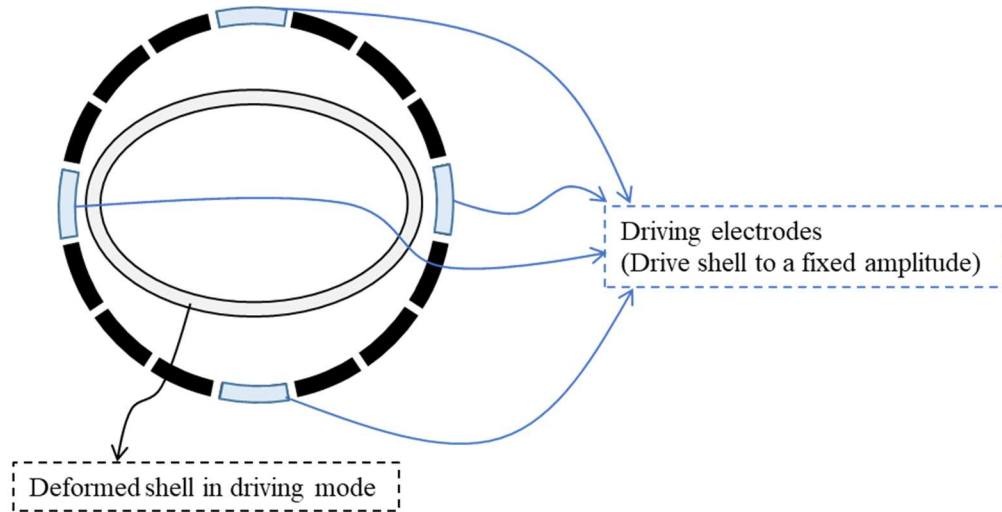


**Figure 3.4:** Configuration of driving electrodes around a shell.

In an open-loop system, the amplitude of sensing WG mode starts to buildup. Four sensing electrodes, which are shown in Figure 3.5, can be used to measure the amplitude of vibration. This amplitude has a direction relation to rotation rate. Since time is required for the sensing WG mode to build up to its steady state value, the response to the step change in rotation rate is not instantaneous. This response time is too slow for long ring-down-time ( $Q/\pi \cdot f$ ) gyroscopes; therefore, force-to-rebalance approach is usually used to improve response time.

In a force-to-rebalance system, the vibration amplitude of the sensing WG mode is monitored and driven to zero by sensing electrodes that are shown in Figure 3.6. These electrodes use electrostatic force to rebalance Coriolis acceleration induced force.

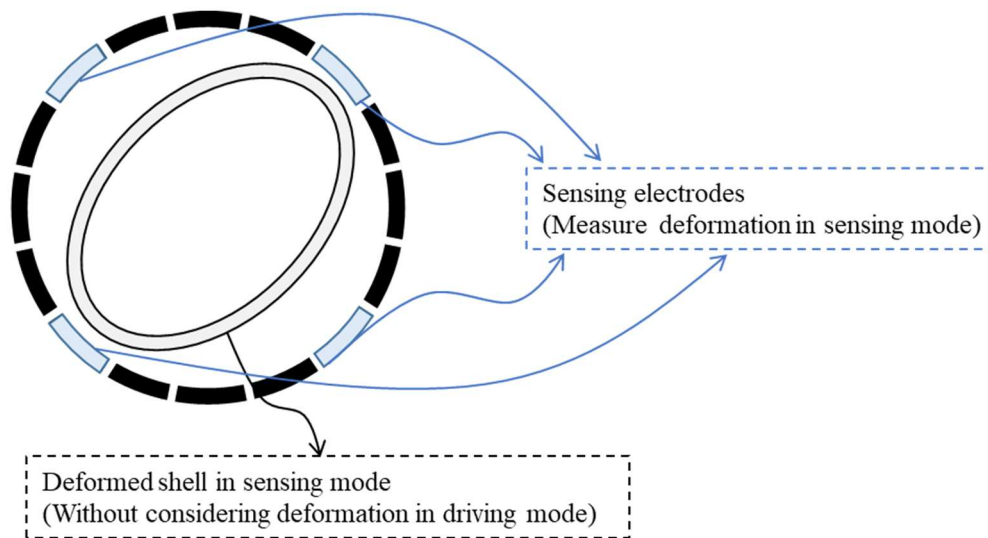


**Figure 3.5:** Configuration of sensing electrodes around a shell when operating in an open loop system.

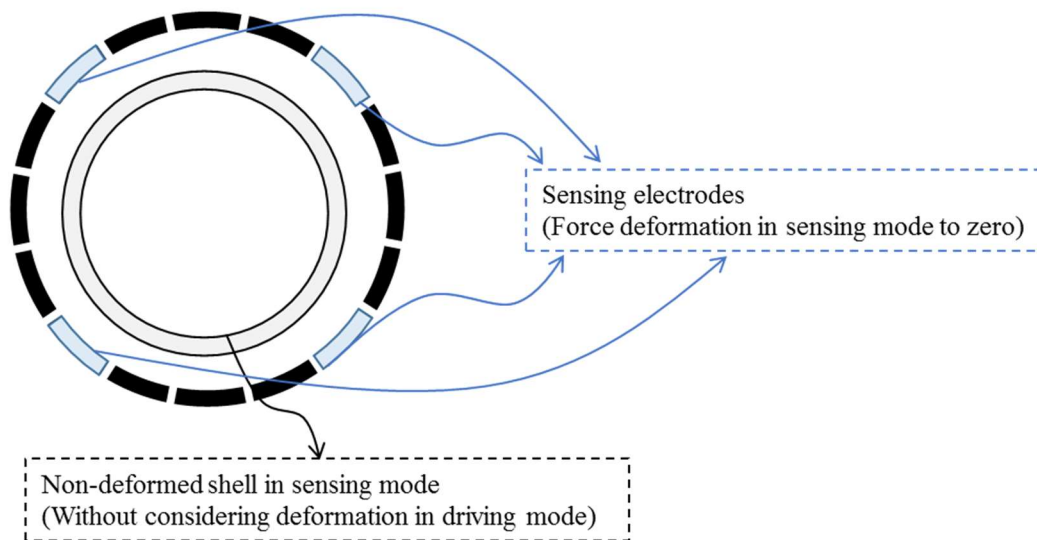


**Figure 3.6:** Configuration of sensing electrodes around a shell when operating in a force-to-rebalance system.

As explained in the previous chapter, it is extremely important to have the same driving and sensing resonant frequencies. Due to manufacturing process, actual shells have imperfections that leads to unmatched frequencies. Eight tuning electrodes that are shown in Figure 3.7 can be

used to match frequencies using the phenomenon of electrostatic softening. Electrostatic tuning of shell resonators will be explained in detail in the next chapter.

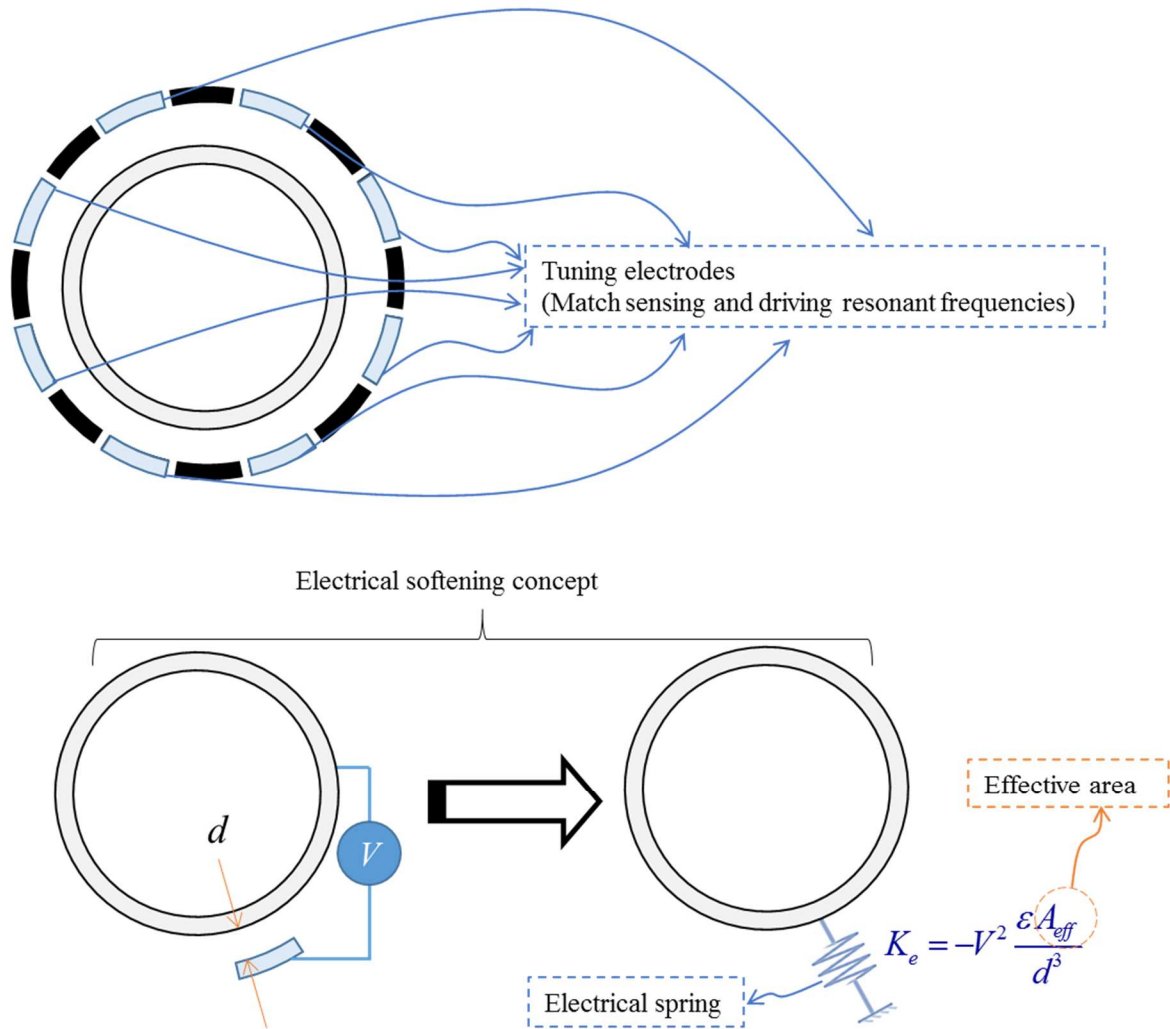


**Figure 3.7:** Configuration of tuning electrodes around a shell to match resonant frequencies of an imperfect shell.

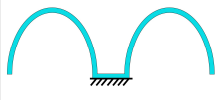
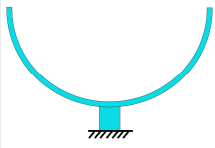
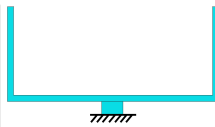


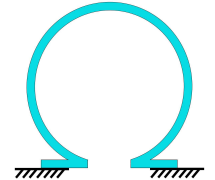
### 3.1.4. MEMS shell structure

Since 1960s, different shell resonators have been developed for CVGs. To reduce the cost, size, and power consumption, MEMS versions of shell resonators have been developed recently.



As shown in Table 3.1, these shells have been made in different shapes, such as birdbath, hemispherical, cylindrical, dome shape, bell shape, and spherical.

**TABLE 3.1: SUMMARY OF MEMS SHELL RESONATORS PERFORMANCES**

Shape	Cross section	Material	$f$ (kHz)	$\Delta f/f$ (ppm)	$Q$
<b>Birdbath or hemi-toroid</b> [33]–[39]		Fused silica, Pyrex	8.196–105	13.3–45,000	1,000–9,810,000
<b>Hemispherical</b> [40]–[49]		Polysilicon, Silicon dioxide, Aluminum oxide Fused silica, Polycrystalline diamond, Metallic glass	5.6–68	130–15,671	230–2,550,000
<b>Cylindrical</b> [50]–[53]		Metal, Fused silica, Metal-fused silica, Diamond	3.979–23	130–250	3,560–805,898
<b>Dome shape</b> [54]		Silicon nitride	126	Not reported	8,740,000
<b>Bell shape</b> [55]		Fused silica	12.9	4,898	271,000
<b>Spherical</b> [56], [57]		Pyrex	945–1,279	6,300–7,100	Not reported

Different materials, such as polysilicon, fused silica, Pyrex, silicon nitride, polycrystalline diamond, and metallic glass have been used to fabricate them. This table also shows the resonant frequency ( $f$ ), normalized mismatch frequency ( $\Delta f/f$ ), and  $Q$  for these structures (these data are the results of reported experiments until now).

All these structures can be potentially used for a yaw gyroscope when they are working in the  $n = 2$  WG modes. However, it is extremely hard to drive dome shape and spherical resonators with large amplitude. Therefore, they are not good candidates for a high performance CVG.

In the next chapter, all the important parameters for optimizing the performance of the shell gyroscopes will be analyzed to achieve navigation performance.

### 3.2. Super Sensitive Stacked (S<sup>3</sup>) Gyroscopes

As shown in the previous subsection, shell gyroscopes can be utilized for measuring rotation in the yaw direction. However, there is a need for accurately measuring rotation in the pitch and roll direction as well. One approach that was already used for inertial navigation in meso-scale is utilizing three shell gyroscopes mounted perpendicular to one another. While this can provide essential measurement signals for navigation, it occupies a large amount of space and needs very accurate assembly, which are in contrast with miniaturizing goal. Alternatively, one can mount yaw, pitch, and roll gyroscopes on the same plane. This requires that one has access to a high-performance pitch-roll gyroscopes. Existing pitch or roll gyroscopes have extremely low performance due to their small mass and or low  $Q$ . In the case of pitch or roll gyroscopes, it is particularly important that the resonator has a large  $Q$  in the out-of-plane resonant mode. To increase the mass, the thickness of a resonator should be increased; however, our simulation, which will be explained in chapter 5, shows increasing the thickness of common resonators dramatically reduces their  $Q$  in the out-of-plane mode. Therefore, a new type of gyroscopes with high performance for measuring rotation in the pitch or roll directions is invented. Figure 3.8 shows the schematic of this type of gyroscopes.

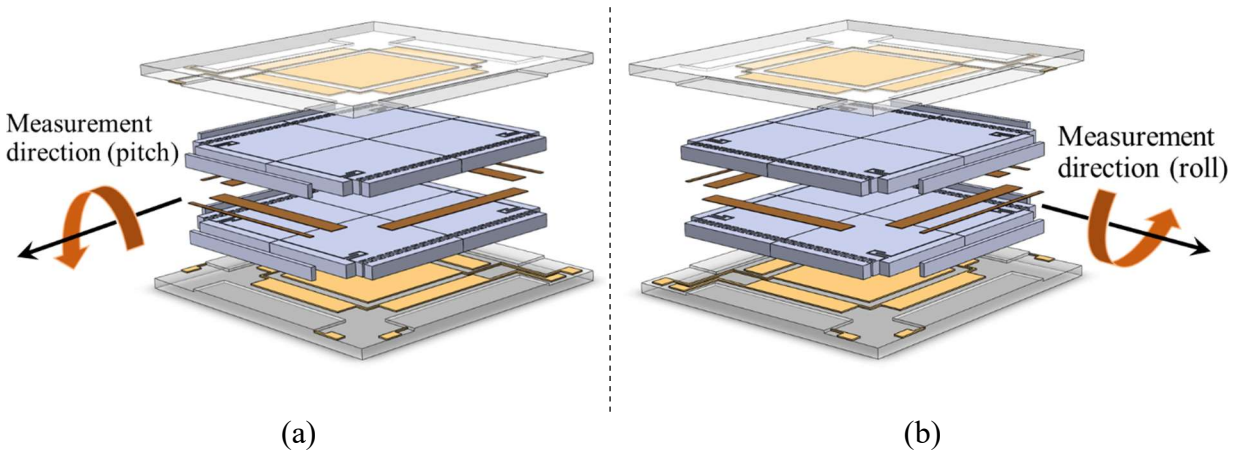


**Figure 3.8:** Schematic of  $S^3$  gyroscopes for (a) pitch and (b) roll measurements.

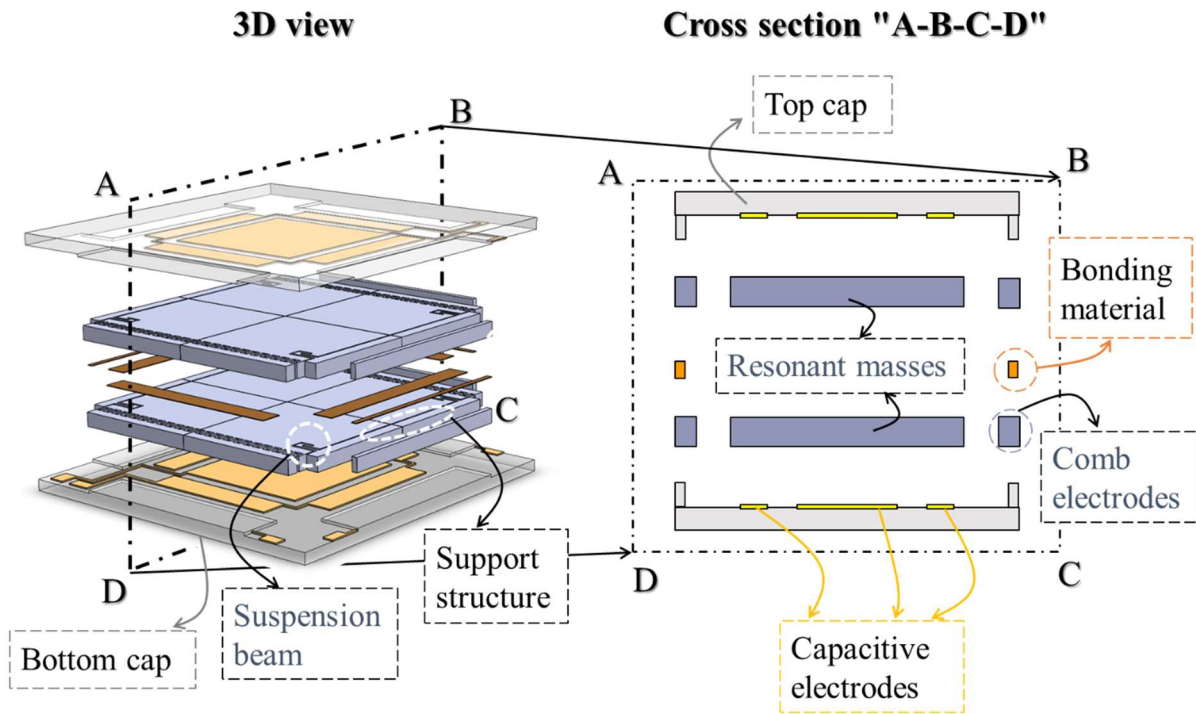
This type of gyroscope can be used for pitch or roll directions. The only difference is that during the assembly one of them should be rotated 90 degrees. In the following parts of this dissertation, only  $S^3$  gyroscope for roll direction will be analyzed.

Figure 3.9 shows different elements of this type of gyroscope. It consists of two device layers, which are coupled together and two cap layers on top and bottom of the device layers. In each device layer, there is a resonant mass that is connected to the perimeter with suspension beams. Cap layers consist of sensing and tuning electrodes. These four layers are stacked on top of each other, while there are spaces between the active part of each layer and neighbor layers (this allows the resonant masses to move without contacting other layers).

### 3.2.1. Operating modes

Figure 3.10 shows the working modes of a  $S^3$  gyroscope. In the driving mode, suspended masses are driven in plane in opposite directions. When there is a rotation in the system, Coriolis

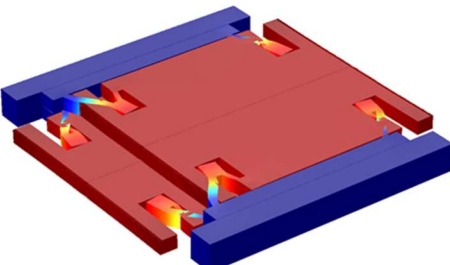
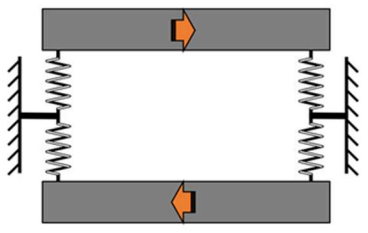
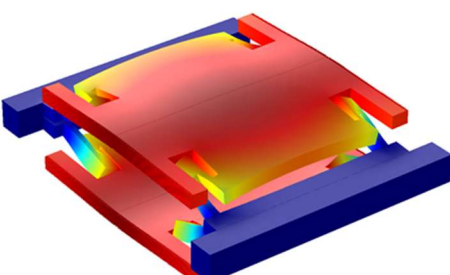
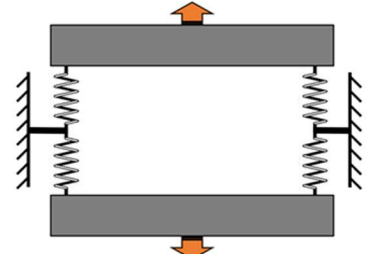
acceleration causes the masses to oscillate out-of-plane in opposite directions, this movement is the sensing mode of the device.



**Figure 3.9:** Schematic of different part of a S<sup>3</sup> gyroscope.

### 3.2.2. Driving and sensing schemes

Figure 3.11 shows the schematic of the operation of a S<sup>3</sup> gyroscope. In the driving mode, suspended masses are driven electrostatically in plane in opposite directions; this can be done using comb drives or parallel plate actuators. However, using parallel plate actuator will experience nonlinear behavior if the driving amplitude is large (larger than 10% of the gap between actuators plate); therefore, comb-drive actuators have been chosen for this design.

Mode	Mode shapes (3D view)	lumped model (cross section)
In-plane (out-of-phase) mode		
Out-of-plane (out-of-phase) mode		

**Figure 3.10:** Operating mode shapes of a  $S^3$  gyroscope.

In the case that there is rotation in the roll direction, the masses start to oscillate out-of-plane in opposite directions due to Coriolis acceleration. The sensing scheme that is shown in Figure 3.11 can be used to read the out-of-plane motion using change in capacitance between masses and sensing electrodes.

### 3.2.3. Device operation

To operate this structure as a gyroscope, resonant masses are forced to vibrate in opposite directions in driving mode using comb-drive electrodes. Figure 3.12 shows the configuration of driving electrodes and movement of resonant masses in the driving mode.

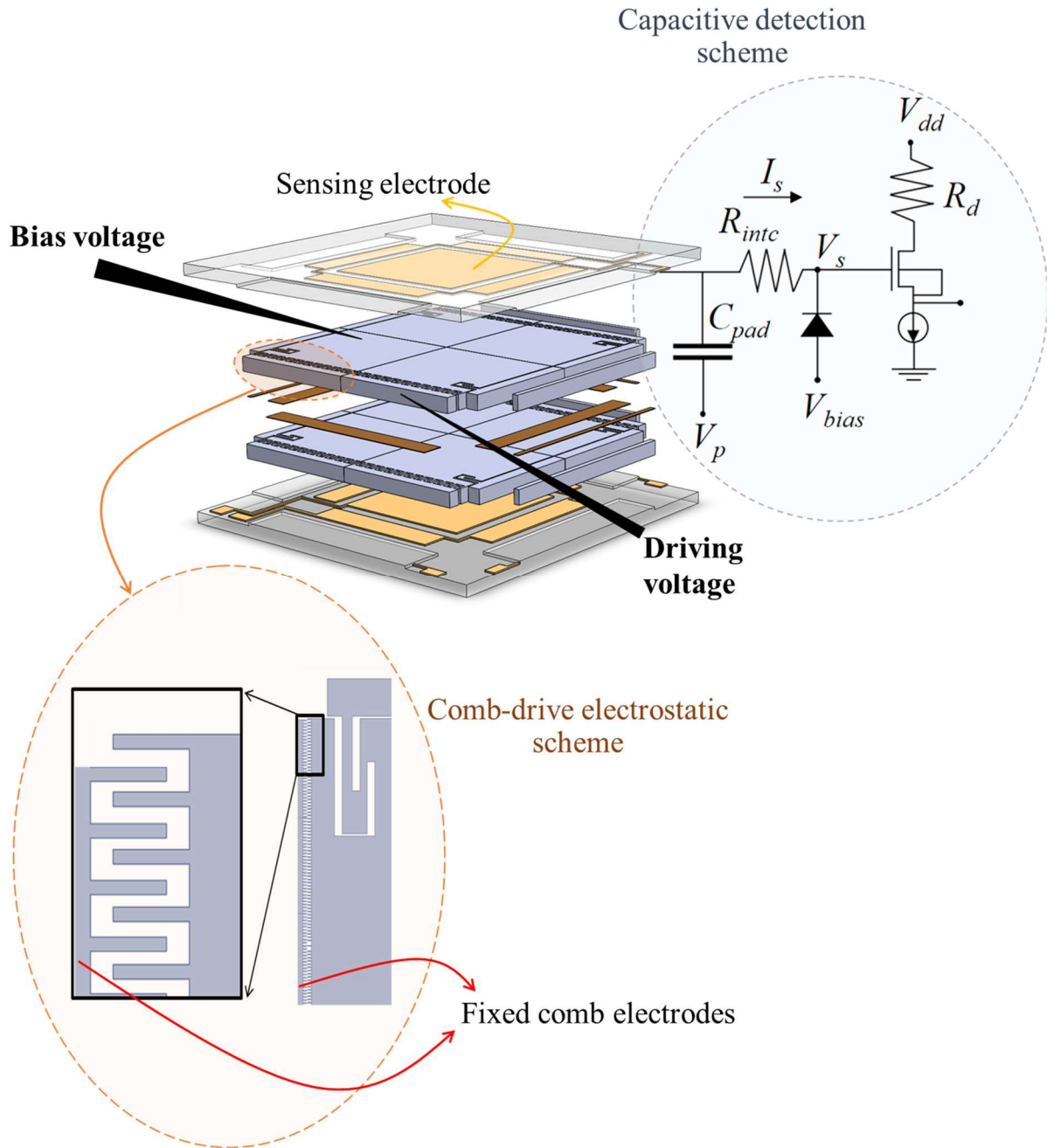


**Figure 3.11:** A schematic of driving a  $S^3$  gyroscope using comb-drive actuators and measuring the deflection of the resonant masses using capacitive sensing.

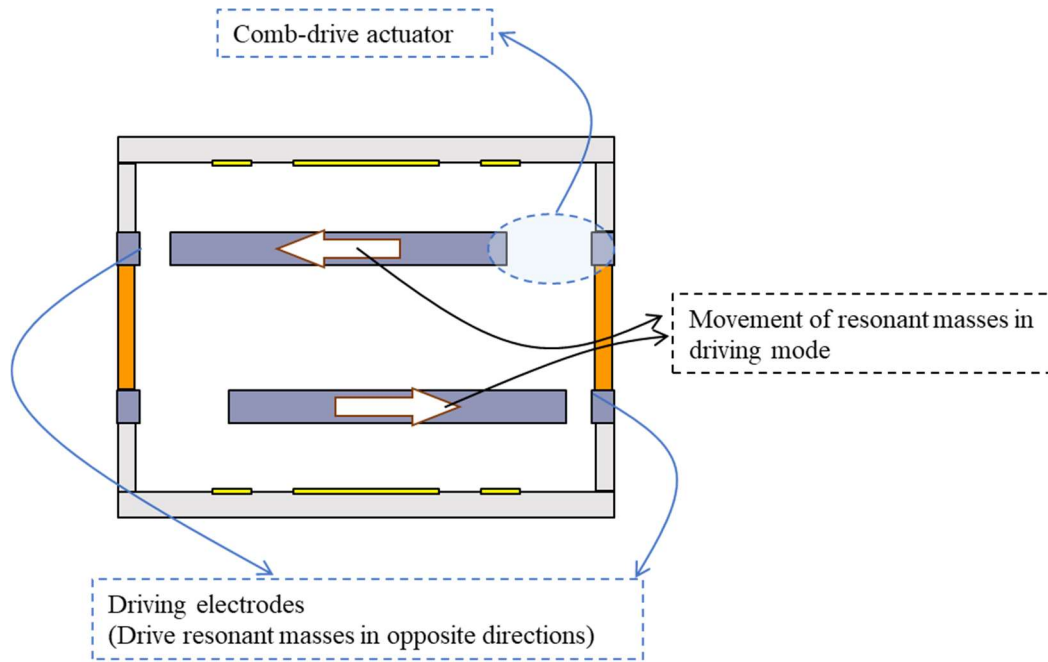


**Figure 3.12:** Configuration of driving mode operation of a S<sup>3</sup> gyroscope.

When there is no rotation in the roll direction, the sensing mode will not be excited, so its amplitude is zero. Rotating the gyroscope around roll direction, excites the sensing mode due to the Coriolis acceleration. As discussed before, two approaches can be used to measure this motion: 1) open-loop 2) force-to-rebalance.

In an open loop system, the amplitude of sensing mode starts to buildup. Sensing electrodes that are shown in Figure 3.13, can be used to measure displacement. This amplitude has a direction relation to rotation rate in roll direction. As discussed before, response time for this approach might be too long, so force-to-rebalance approach can be used to improve response time.

In a force-to-rebalance system, there is a need for an extra layer between resonant masses. In this case, the vibration amplitudes of the resonant masses are monitored and driven to zero by sensing electrodes that are shown in Figure 3.14. These electrodes use electrostatic force to rebalance Coriolis acceleration induced force.

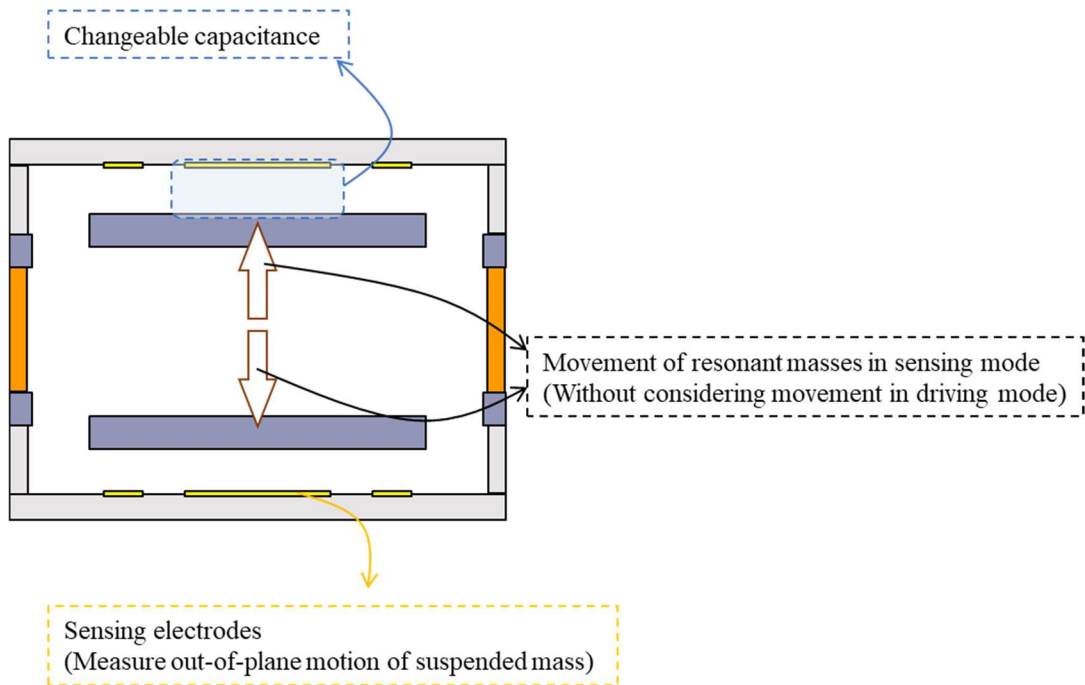


**Figure 3.13:** Configuration of sensing electrodes on top and bottom of resonant masses when system operating in an open loop readout.

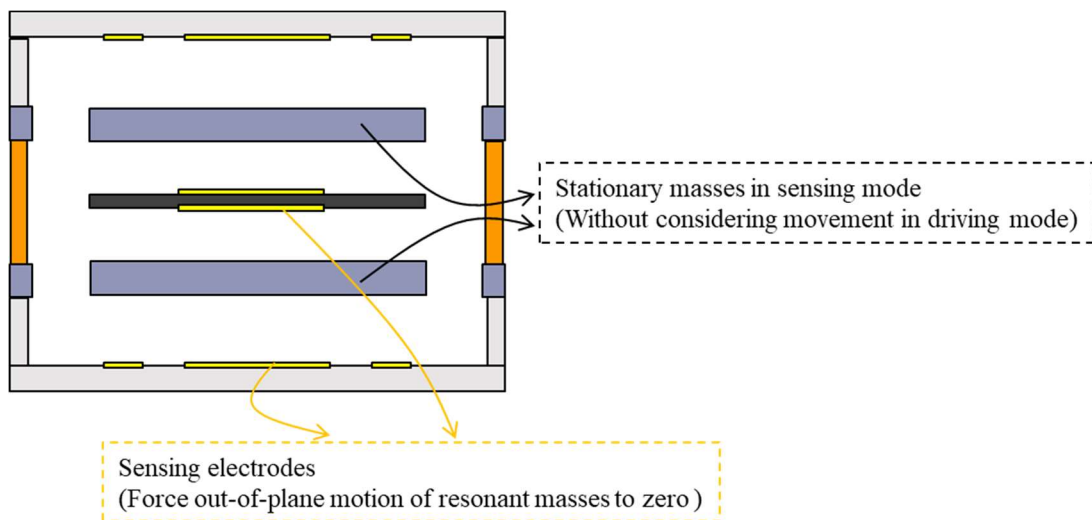


**Figure 3.14:** Configuration of sensing electrodes around a shell when operating in a force-to-rebalance system.



To match driving and sensing resonant frequencies, tuning electrodes as shown in Figure 3.15 are used. These electrodes can only reduce sensing resonant frequency. Therefore, initial  $S^3$  gyroscope design should have a little higher frequency in sensing mode comparing to driving mode. As a result, tuning can be done by reducing sensing resonant frequency to match the driving frequency.

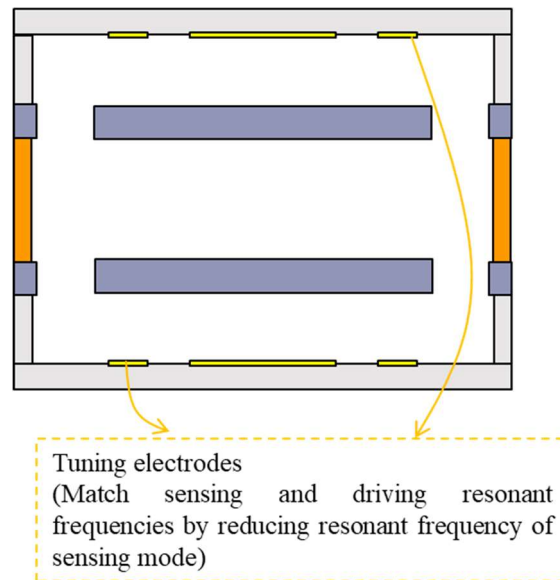


**Figure 3.15:** Configuration of tuning electrodes to match resonant frequencies of a  $S^3$  gyroscope.

### 3.3. Summary

This chapter has introduced three MEMS gyroscopes to measure rotation rate in all navigational directions. Figure 3.16 shows these gyroscopes and their measurement directions. Chapters 4 and 5 investigate and optimize design parameters for these gyroscopes to achieve navigation grade performance.

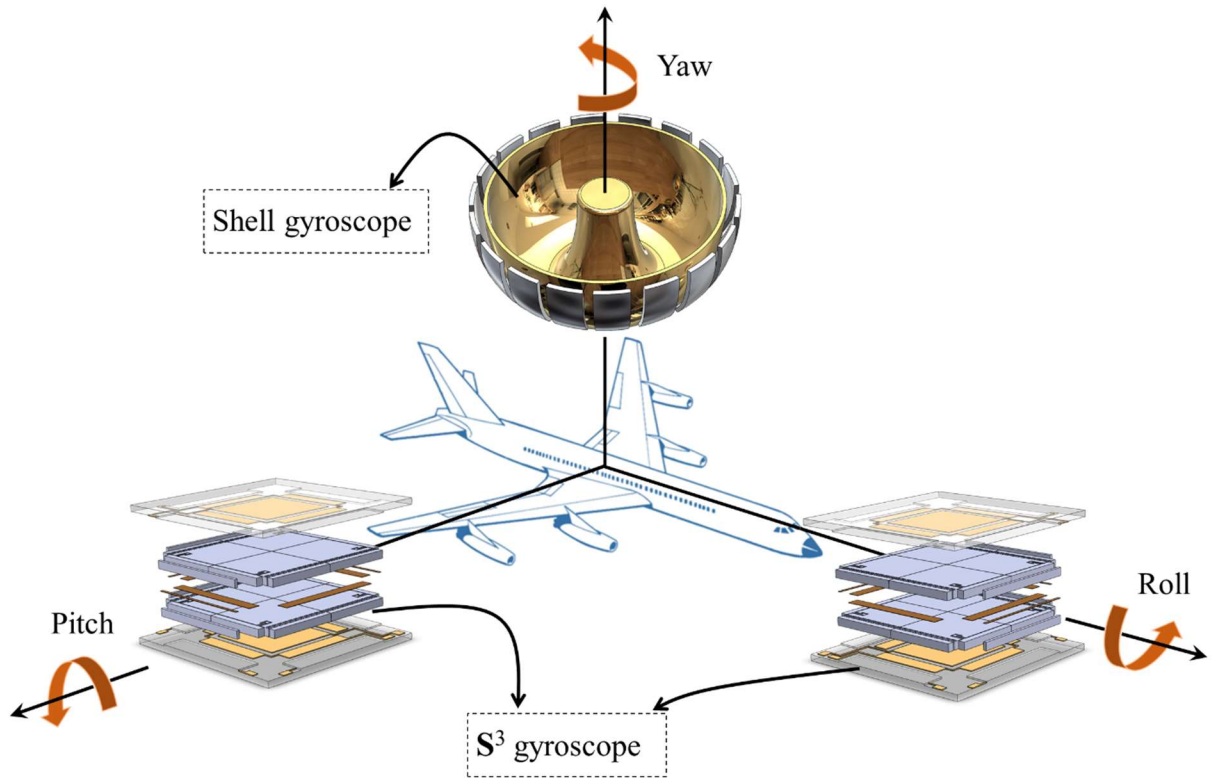


**Figure 3.16:** Shape of considered MEMS gyroscopes for inertial navigation.

## Chapter 4: Design and Analysis of Extremely High-Performance MEMS Shell Gyroscopes

As explained in chapter 2, the most important factor in performance of CVGs is noise (ARW) in the gyroscope. The conceptual design of shell gyroscopes and their operation were explained in the previous chapter. In this chapter, optimization of the design parameters shown in Figure 4.1 using theoretical, numerical and/or experimental methods will be discussed. At the end, the testing result (performed by other group members) of the fabricated shell gyroscope will be presented and compared with theoretical estimation. One can use the step-by-step design of shell gyroscopes presented in this chapter as a comprehensive guideline for designing ultra-high-performance gyroscopes.

Both noises:	Electronic noise:	Thermomechanical noise:
Large sensing $Q$ -factor	Large capacitive area	Large effective mass
Large driving amplitude	Small sensing capacitor gap	Large resonant frequency
Large angular gain	Small resonant frequency	
Small mismatch frequency		

**Figure 4.1:** Design checklist for CVGs.

To design a low-noise CVG, the checklist shown in Figure 4.1 should be satisfied. In this chapter, design parameters shown in these figure will be analyzed in different sections with the following order:

- 4.1 Quality factor
- 4.2 Effective mass
- 4.3 Angular gain
- 4.4 Resonant frequency
- 4.5 Frequency split between driving and sensing modes
- 4.6 Driving amplitude, sensing gap and area

Detail investigation of each parameter is provided in the following sections:

#### **4.1 Sensing Quality Factor**

Quality factor ( $Q$ ) is a commonly-used metric for evaluating mechanical resonator performance. Resonators with higher  $Q$  lead to lower thermomechanical and electronic noises, higher sensitivity, and lower power consumption.  $Q$  in mechanical resonators is defined as the ratio of energy stored to energy dissipated per oscillation period; therefore, high- $Q$  resonators have low energy dissipation. Understanding the energy dissipation mechanisms of shell resonators is critical for improving their  $Q$ .

Figure 4.2 illustrates the major energy dissipation mechanisms in shell structures, including dissipation due to:

- 1) Anchor loss
- 2) Thermoelastic dissipation (TED)
- 3) Interactions between the resonator structure and surrounding fluid

- 4) Phonon interactions,
- 5) Internal dissipation
- 6) Surface loss

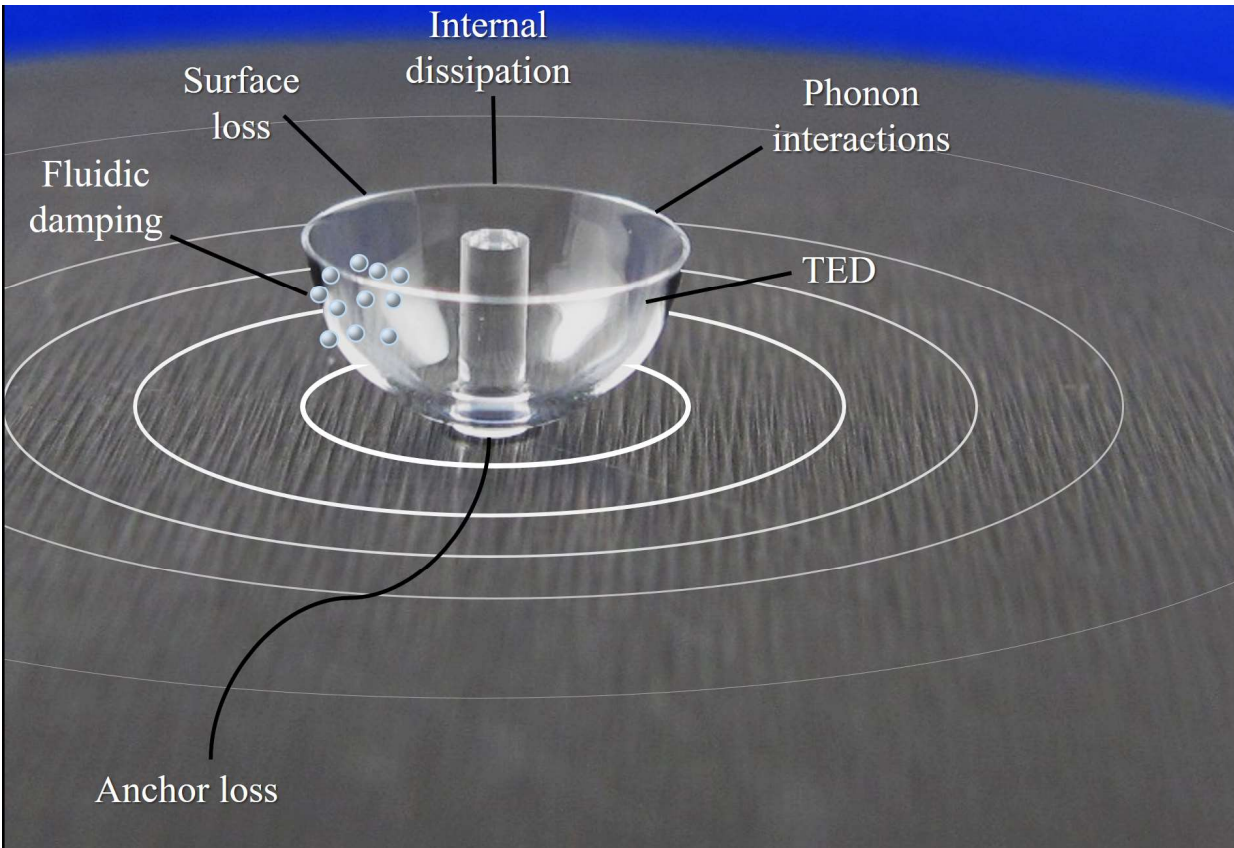


**Figure 4.2:** Illustration of the major dissipation mechanisms in shell resonators. These dissipation mechanisms are anchor loss, surface loss, fluidic damping, phonon interaction, internal dissipation, and TED.

In this section, all of these mechanisms will be investigated in shell resonators and design guidelines for reducing them will be provided.

#### **4.1.1 Anchor loss**

The anchor can be a major source of energy dissipation in resonators. This dissipation is due to mechanical wave propagation from the resonator into the substrate. The best approach to

reduce anchor loss is to design resonators with their anchors at the nodal points of the waves, where the displacement of a certain vibrational mode is zero.

Hao *et al.* [58] modeled the energy dissipation through the anchors for micro-cantilevers and micro-bridges. Their model shows that thinner and longer beams can achieve higher  $Q$ s. Judge *et al.* [59] investigated the effect of the substrate thickness on anchor loss, and showed that a resonator attached to a thick substrate can achieve several times higher  $Q$  than a resonator attached to a substrate with the same thickness as the resonator. Based on their model, the anchor loss of cantilevers has a direct relation to the following term:

$$\left(\frac{t_{resonator}}{t_{substrate}}\right)^2 + C\left(\frac{t_{resonator}}{t_{substrate}}\right)^{5/2} + C'\left(\frac{t_{resonator}}{t_{substrate}}\right)^3 \quad (4.1)$$

where  $t_{resonator}$  and  $t_{substrate}$  are thicknesses of the resonator and substrate, respectively, and  $C$  and  $C'$  are constants, which depend weakly on Poisson's ratio. Both of these studies used analytical approaches to model anchor loss. These approaches are applicable to simple beam-type resonators with known vibrational characteristics.

For complicated geometries, numerical approaches, such as finite element method (FEM), have to be used. Bindel and Govindjee [60] took a general numerical approach and constructed an FEM model of a disk resonator and a finite portion of the substrate. They showed that anchor loss can be the main source of energy dissipation in disk resonators. Pandey *et al.* [61] analyzed the effect of a trench in a resonator's substrate on anchor loss. They observed that some of the propagated mechanical waves can be reflected back to the resonator by using an appropriate trench in a desired location that was found by an FEM model, thus improving  $Q$ . Thakar and Rais-Zadeh [62] showed that by numerically optimizing the resonator tether geometry, low anchor loss can be achieved. We [63] investigated the effect of substrate thickness on anchor loss of mechanical

resonators numerically. To prevent the elastic waves from being reflected back from the boundary into the resonator and producing incorrect simulation results, a "perfectly matched layer" (PML) was added to the outer boundary of the substrate portion of our model. Their resulting anchor loss predictions show an excellent agreement with the experimental data reported in [59].

Shell resonators that rely on continuous vibration for operation may lose significant energy through their anchors to the substrate. The results of this subsection provide guidelines for choosing the shape of the shell. First, anchor loss in hemispherical structure will be analyzed.

Figure 4.3 shows simulated relative (normalized) deformation inside the substrate beneath a hemispherical shell resonator (HSR) when the shell is vibrating in one of the WG modes. This figure provides a visual representation for wave propagation inside the substrate at five different times ( $t'$ ). In this figure,  $\tau$  is the time period of vibration ( $1/f$ ). It is considered that the resonator is not moving initially (at  $t' = 0$ ). The highest deformation occurs near the anchor—located in the upper right corners of these figures—while places far from the anchor have the lowest deformation.

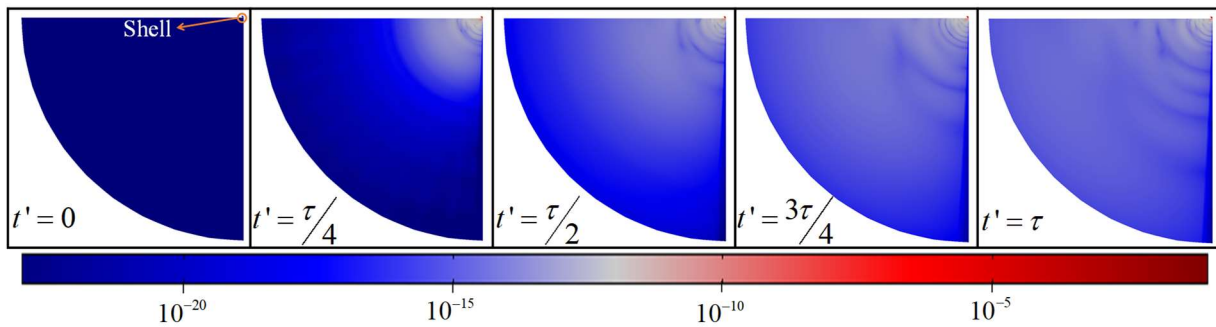


**Figure 4.3:** Normalized deformation distribution inside the substrate beneath an HSR when the shell is vibrating in one of the WG modes—the shell is located in the upper right corners of these figures.

HSRs can be fabricated with different micromachining processes. As some HSRs shown in Figure 4.4, they are made from different materials with different types and sizes of attachments

to the substrate. The reported  $Q$  of these shells spans from a few hundred up to more than two million. Usually, an HSR should be fixed on a substrate through a stem to operate as a resonator.

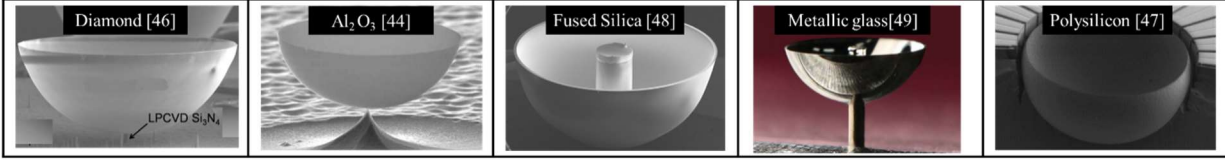


**Figure 4.4:** Micromachined HSRs fabricated from different materials. Different configurations can be used to attach the shell to the substrate. Usually, a stem is utilized to connect the shell and substrate together. As shown in this figure, the size, shape, and configuration of these stems can be different.

A cross sectional view of a shell with a stem is shown in Figure 4.5. The shell outer radius and thickness and the stem radius and height are designated as  $R$ ,  $t$ ,  $r$ , and  $h$ , respectively. This figure also shows the nominal dimensions used in this subsection. We consider the nominal dimensions of micromachined HSRs to be  $R_o = 2.5 \text{ mm}$ ,  $t_o = 100 \mu\text{m}$ ,  $r_o = 500 \mu\text{m}$ , and  $h_o = 100 \mu\text{m}$ .

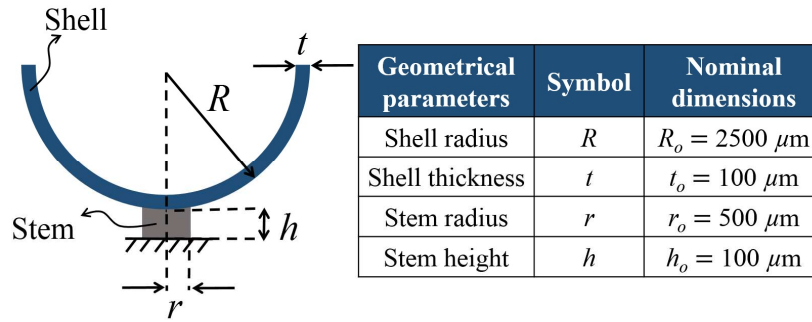


**Figure 4.5:** Cross sectional view of an HSR with a stem (left), and geometrical parameters and nominal dimensions used in this subsection (right).

#### 4.1.1.1 Numerical simulation of anchor loss in resonators

To predict the mechanical energy that is transmitted via the anchor, the substrate of an HSR can be considered as an elastic half-space. Only outgoing waves are allowed in this infinite-domain



problem [60]. Using FEM, it is not possible to model an infinite substrate. Therefore, the substrate is considered as a finite-domain structure surrounded by artificial boundaries that mimic the infinite substrate. The main property of the infinite substrate is that as waves enter the substrate, they will not reflect back from the boundaries. One method to achieve this condition is using a non-reflecting boundary for a finite substrate. However, this boundary has a significant limitation; it only works if the incident waves are exactly normal to the boundary. Therefore, a better method is required to prevent the reflection of all waves reaching the boundary.

A non-physical absorbing layer can be added along the exterior boundary of the substrate to absorb all outgoing waves before they reach the absorbing layer's finite boundary. Figure 4.6 shows a schematic of key modeling requirements for numerical simulation of anchor loss using an absorbing layer around the finite substrate boundary. The substrate and absorbing layer do not need to be modeled to reflect the geometry of the whole device's substrate, but only to ensure that waves do not reflect back from the absorbing layer's fixed boundary into the vibrating resonator.

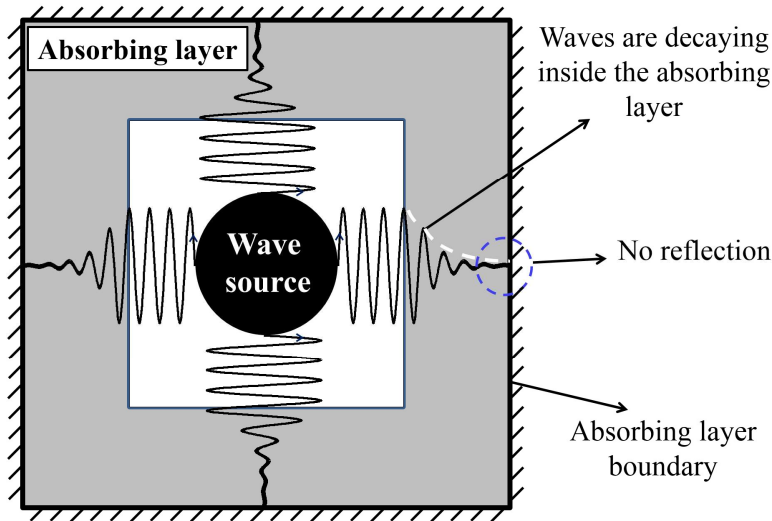


**Figure 4.6:** Schematic of wave propagation into an absorbing layer. As waves enter the absorbing layer, they start decaying. If the thickness of the absorbing layer is large enough, waves are damped before reaching the boundary of the layer; therefore, there is not any wave reflection from the absorbing layer to the wave source.

A PML can be used as an absorbing layer. As a wave enters the PML, it is attenuated exponentially and damped by this layer. In fact, a PML works as a complex material that adds damping to the waves. To be modeled mathematically, waves are transformed from a real-coordinate solution to a complex-coordinate solution inside the PML region. Therefore, the amplitude of wave solution inside the PML has an exponentially decaying coefficient. If the size of the PML region is large enough, using an exponentially decaying coefficient ensures that waves are attenuated to a very small amount. Even if these attenuated waves reflect from the PML's boundary, the returning waves reaching the resonator after one round trip through the PML are extremely small, so their effect becomes negligible. This PML coordinate transformation uses (4.2) to transform the real-coordinate to the complex-coordinate [64]:

$$x' = \left( \frac{x}{\Delta_w} \right)^n (1-i)\lambda\alpha \quad (4.2)$$

where  $x$  is the general coordinate variable.  $\Delta_w$ ,  $n$ ,  $\lambda$ , and  $\alpha$  are the width of the PML region, the PML order, the wavelength, and the PML scale factor, respectively. In this subsection, to simulate  $Q$  of HSRs, the PML order and scale factor are fixed to one. As reported in [63], we found an excellent agreement between the experimental data for anchor loss of geometries reported in [59] and the simulation results with the aforementioned PML parameters.

Depending on a resonator design and its boundaries, Cartesian, cylindrical or spherical PMLs can be used for absorbing waves. Spherical PMLs are highly effective in absorbing waves in the radial direction; therefore, they are chosen for simulation in this paper. It is assumed that the shell, stem, substrate, and PML are all made of fused silica. Fused silica's material properties are considered to be Young's modulus:  $E_{FS} = 70$  GPa, Poisson's ratio:  $\nu_{FS} = 0.17$ , and density:  $\rho_{FS} = 2200$  kg/m<sup>3</sup>.

Since anchor loss is considered the only dissipation mechanism in our simulations in this subsection,  $(Q_{Anchor})^{-1}$  and anchor loss have exactly the same behavior. Therefore, we simulate  $Q_{Anchor}$  to understand anchor loss in HSRs.

$Q_{Anchor}$  of each mode can be found from the following equation:

$$Q_{Anchor} = \left| \frac{\text{Re}(\omega)}{2\text{Im}(\omega)} \right| \quad (4.3)$$

where  $\text{Re}(\omega)$  and  $\text{Im}(\omega)$  are the real and imaginary parts of the angular resonant frequency ( $\omega$ ) of that mode, respectively [65]. COMSOL Multiphysics 5.1 [66] is utilized to solve the eigenfrequency problem numerically.

In utilizing a PML to calculate  $Q_{Anchor}$ , the element quality is critical. Generally, a poor mesh quality results in poor convergence for iterative solvers and causes the problem ill-conditioned [64]. Two different types of meshing are considered to simulate  $Q_{Anchor}$  of HSRs. The first one is shown in Figure 4.7. In order to create the first configuration, quadrilateral elements are generated in a 2D plane, then they are revolved to generate a 3D mesh distribution. In the second configuration, instead of quadrilateral elements, triangular elements are used in the 2D plane. In both mesh configurations, the shell and stem geometries are discretized using “extremely fine mesh”. However, to minimize solving time, mesh density inside the PML is variable. Mesh distribution changes from very small elements in the regions close to the substrate to larger elements in the regions close to the PML outer boundary.

Based on our simulation results, it is essential that the PML is meshed such that there are more than 12 nodes per wavelength across the PML. A lower number of mesh elements inside the PML may reduce the accuracy of the numerical calculation. For example, our simulation shows that 9 nodes across PML underestimates anchor loss about 15% and 3% for quadrilateral and

triangular elements, respectively. By increasing the number of nodes per wavelength, the anchor loss underestimation reduces and the results converge to a constant number. Albeit, it should be taken into account that increasing the number of nodes per wavelength, increases the computational cost—computational cost: number of degrees of freedom solved for each simulation. For example, using 30 nodes per wavelength instead of 12 nodes per wavelength, increases the computational cost by 24% and 20% for quadrilateral and triangular elements, respectively. In this dissertation, to achieve a high accuracy we used more than 30 nodes per wavelength in each simulation.

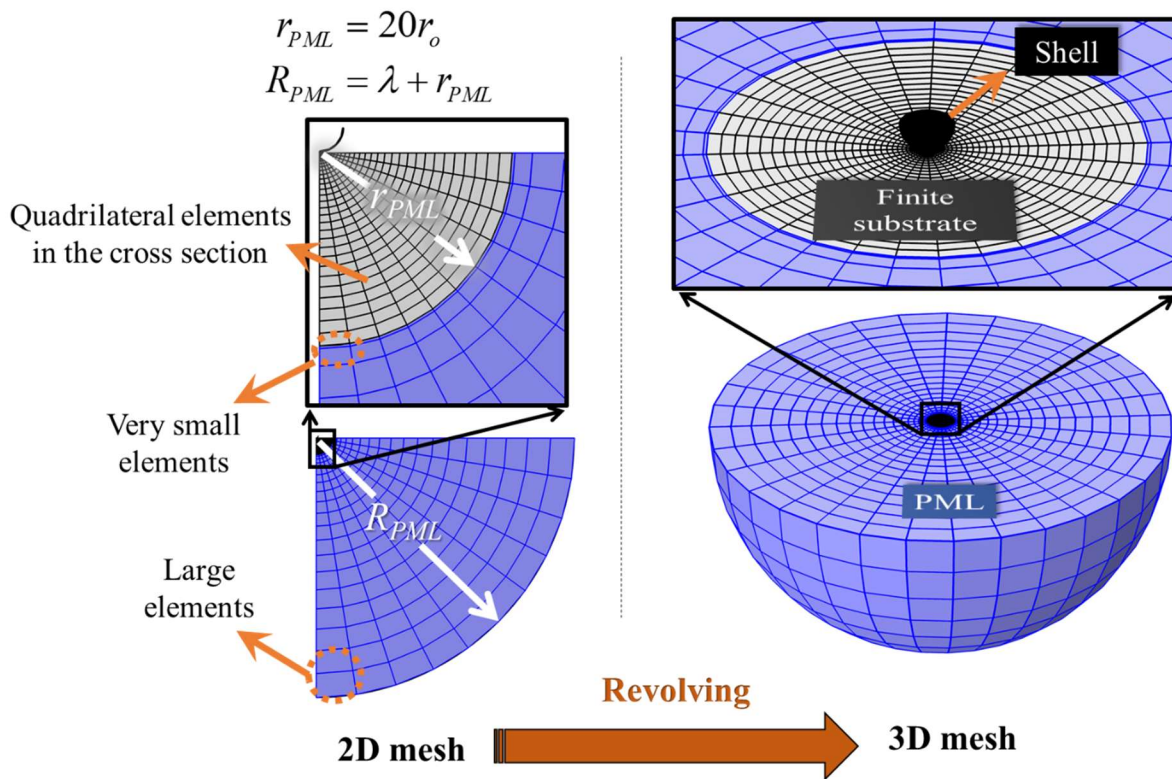


**Figure 4.7:** One of mesh configurations used to simulate  $Q_{Anchor}$  in HSRs. To create this mesh, quadrilateral elements are generated in a 2D plane and then these elements are revolved to generate a 3D mesh distribution. It is important that the PML is meshed such that there are more than 12 nodes per wavelength across the PML.

PML inner radius,  $r_{PML}$ , is also an important parameter in calculating  $Q_{Anchor}$ . In our simulation,  $r_{PML}$  is changed from very small to larger values. For the mesh with quadrilateral elements in the cross section, it is found that when the PML inner radius is small (less than  $10r_o$ ), the simulated  $Q_{Anchor}$ s fluctuate. After increasing the  $r_{PML}$  to larger values, the simulated  $Q_{Anchor}$ s converge to a constant number. It is found that the difference between the simulated  $Q_{Anchor}$ s is less than 10% when  $r_{PML} > 20r_o$ . For the mesh with triangular elements in the cross section, it is found that the simulated  $Q_{Anchor}$ s fluctuate when the PML inner radius is less than  $5r_o$ ; as  $r_{PML}$  becomes larger than  $10r_o$ , the simulated  $Q_{Anchor}$ s converge to a constant number—the difference between the simulated  $Q$ s is less than 10%. For both mesh configurations, the results converge to very similar values with a less than 2% difference. The results that are presented in this subsection are for the case with triangular elements and  $r_{PML} = 20r_o$ .

To obtain an accurate result, the thickness of the PML—the difference between the PML outer radius ( $R_{PML}$ ) and  $r_{PML}$ —is fixed to the wavelength of the propagating wave in each simulation. For a mechanical resonator, the wavelength equals

$$\lambda = \frac{C}{f} \quad (4.4)$$

where  $f$  and  $C$  are the resonant frequency and speed of sound inside the substrate material, respectively. For longitudinal waves inside a solid material,  $C$  can be calculated from (4.5):

$$C = \sqrt{\frac{E(1-\nu)}{\rho(1+\nu)(1-2\nu)}} \quad (4.5)$$

where  $E$ ,  $\nu$ , and  $\rho$  are Young's modulus, Poisson's ratio, and density of the material, respectively.

Utilizing a PML with one wavelength thickness ensures that waves are damped before reaching the PML boundary. By using a PML with thickness smaller than one wavelength, some

waves may not be completely damped; therefore, there are some waves returning into the resonator that cause an incorrectly simulated value for  $Q_{Anchor}$ . However, PMLs with thicknesses larger than one wavelength do not yield significantly higher accuracy. Based on our simulation results, if the PML thickness is larger than 20% of the wavelength, the simulated  $Q_{Anchor}$ s are almost the same for all PML thicknesses—less than 10% difference. However, if the PML thickness is 10% of the wavelength, the simulated  $Q_{Anchor}$  is about 45% different from the cases with large PML thicknesses.

In addition to the PML mesh quality, inner radius, and thickness, the PML scale factor also affects simulation results. We suggest to use a scale factor of one in simulations—based on our discussion with experts at COMSOL, changing the value of the scale factor might cause inaccuracies in the prediction of  $Q$ . In our case, the simulation results show that for a scale factor in the range of 0.2 to 2, the calculated number for  $Q_{Anchor}$  is almost the same with a scale factor of 1. However, for scale factors out of this range, the predicted  $Q_{Anchor}$ s deviate from that case. In general, changing the scale factor may cause some problems in a numerical simulation that are explained below:

1. Scale factor is used to linearly scale the coordinates [67], and the coordinate scaling yields an equivalent scaling of the mesh that may result in a poor element quality, which causes inaccuracies in the numerical simulation [64].
2. Changing the scale factor changes the exponential decay rate in the PML. Very large decay rate (a PML with high absorption) may result in numerical reflections in the boundary between the PML and the finite substrate [68]. On the other hand, using a very small decay rate may cause the outgoing waves in the PML do not experience enough

attenuation; therefore, the PML cannot absorb all of them, which may result in reflection of them back from the PML's fixed boundary into the resonator.

#### 4.1.1.2 Impact of various parameters on anchor loss of hemispherical shell resonators

Different parameters have impact on anchor loss of shell resonators. These parameters are shown in Figure 4.8.

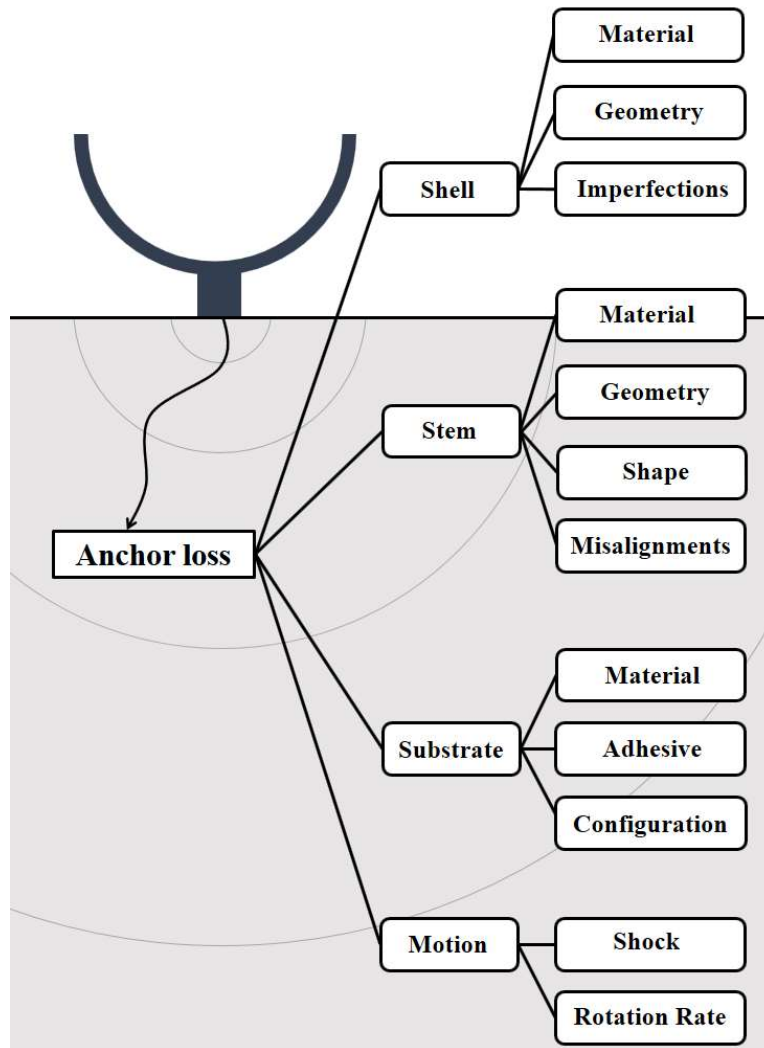


**Figure 4.8:** Classification of important parameters affecting anchor loss in HSRs. The anchor loss depends on the shell, stem, substrate properties, and the external motion of an HSR. The effects of all of these properties are investigated in this subsection.

This subsection describes the effects of the properties shown in Figure 4.8 on anchor loss of HSRs.

To calculate the anchor loss of HSRs, a series of simulations is performed using PMLs. In all simulations, the PMLs peripheral boundaries are fixed. The other boundaries are considered to be free. Simulation for modal analysis is conducted. This analysis provides mode shapes, angular resonant frequencies, and relative deformations. The angular resonant frequency values are used to calculate  $Q_{Anchor}$ . For an HSR with the nominal dimensions shown in Figure 4.5,  $Q_{Anchor}$  is calculated to be 3.4 billion, which is used to normalize values of  $Q_{Anchor}$  (normalized  $Q_{Anchor} = Q_{Anchor} / 3.4 \times 10^9$ ) in this subsection.

In the following subsections, the effects of different parameters on  $Q_{Anchor}$  are analyzed. It should be noticed that changing the shell properties changes its resonant frequencies and hence the wavelength inside the PML; therefore, to simulate  $Q_{Anchor}$  correctly in each case, the PML thickness is adjusted for the shell with the new property. However, changing the stem and substrate properties or existence of any external motion in the system do not cause a significant change in the resonant frequencies.

These parameters are categorized in four subsections that include:

- a) Shell properties
- b) Stem properties
- c) Substrate properties
- d) External motion of shell

Each of them will be discussed in detail and guidelines to reduce anchor loss in shell resonators will be provided.



### a) Effect of Shell Properties on Anchor Loss

In this subsection, the effects of the shell properties on anchor loss are investigated. These properties include shell material properties, thickness and radius, unbalanced mass, non-circularity, and imperfect cutting.

The shell material properties' effects on anchor loss are shown in Figure 4.9. In this figure, normalized  $Q_{Anchor}$  is depicted over the shell material properties—normalized  $Q_{Anchor}$  is one when the whole system (shell, stem, substrate, and PML) is made from fused silica. To simulate the effects of the shell material properties on anchor loss, the material properties of the shell is changed, while keeping the stem, substrate, and PML material properties fixed. As shown in Figure 4.9, by increasing the shell's Young's modulus, anchor loss increases because a stiffer shell can deform the substrate easier; therefore, more energy escapes from the shell to the substrate. This figure also shows that increasing the shell's density reduces anchor loss because a denser shell can keep more kinetic energy. Furthermore, this figure shows that the shell's Poisson's ratio has less of an effect than its Young's modulus and density.

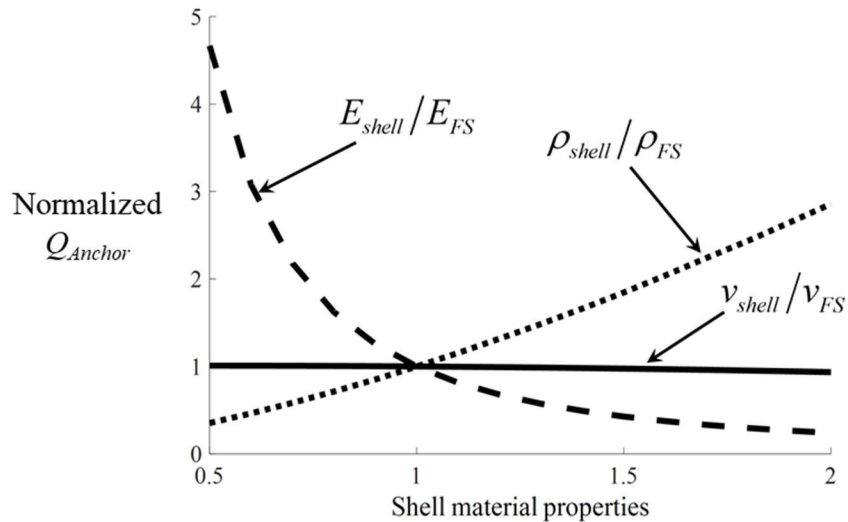


**Figure 4.9:** Effect of shell material properties on  $Q_{Anchor}$ . By increasing the shell's Young's modulus and density,  $Q_{Anchor}$  changes. However, the shell's Poisson's ratio has a negligible effect on  $Q_{Anchor}$ .

To analyze the effects of the shell radius and thickness on anchor loss, a group of shells with different radii and thicknesses are modeled. Their radii vary from 1250  $\mu\text{m}$  to 5000  $\mu\text{m}$  and their thicknesses vary from 50  $\mu\text{m}$  to 400  $\mu\text{m}$ . The results of this investigation are depicted in Figure 4.10. These results show that shells with a larger radius have lower anchor loss. In shells with a large radius, the distance from the anti-nodes (and other places with large deformation) to the anchor is further than shells with a small radius. The same phenomenon can be observed in simple cantilever resonators, where anchor loss has an inverse relation to the cube of the cantilever length [58]. Our investigation also shows that by increasing the shell thickness, anchor loss increases. Indeed, thicker shells cause larger deformation and wave propagation in the substrate. Comparing to simple cantilever resonators, the same pattern can be observed—thicker cantilevers show larger anchor loss compared to thin cantilevers [58].

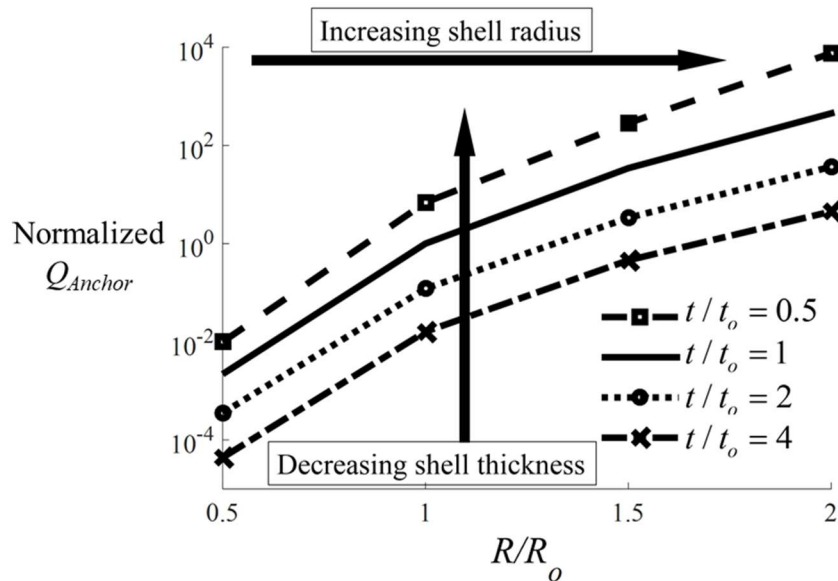


**Figure 4.10:** Effect of shell radius and thickness on  $Q_{Anchor}$ . By increasing the shell radius,  $Q_{Anchor}$  increases. However, by increasing the shell thickness,  $Q_{Anchor}$  decreases.

Figure 4.11 shows the normalized deformation contours in a portion of the substrate cross section of shells with different geometries—this portion is a semicircle with a 2 mm radius. As

shown in this figure, the deformation in the substrate of the thick shells is larger than the thin ones. This figure also shows that in a WG mode, the highly deformed rim of the shell is farther from the stem when the shell radius becomes larger, so the amount of the energy escaping to the substrate drops. Furthermore, the minimum amount of normalized deformation,  $D_m$ , in the portion of substrate for each shell is shown in this figure. As expected,  $D_m$  follows the same pattern as anchor loss—shells with a smaller  $D_m$  have lower anchor loss.

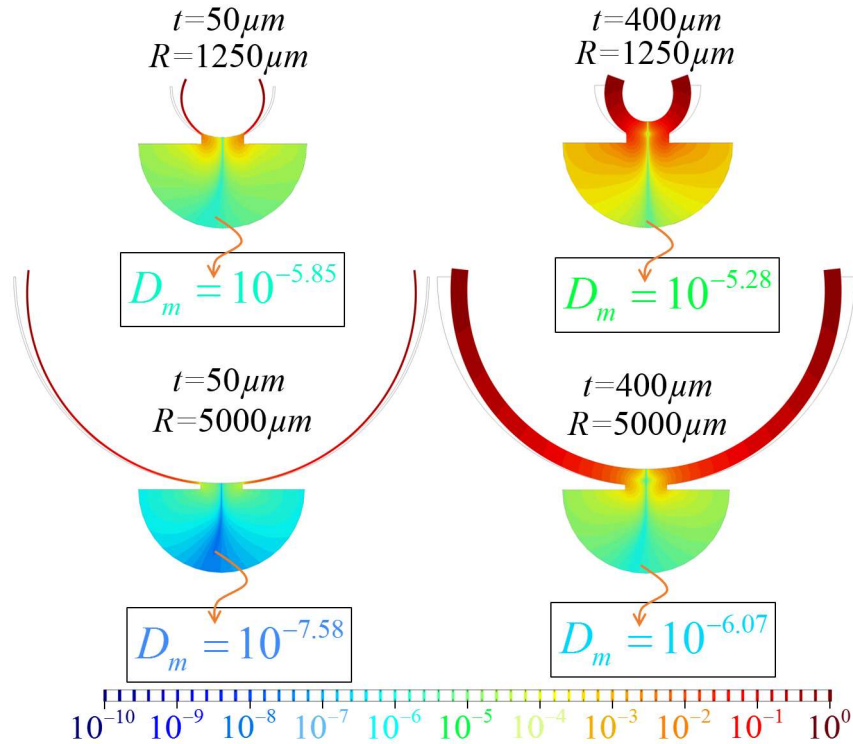


**Figure 4.11:** Contours of the normalized deformation distribution in the cross section for the thin (left) and thick (right) shells. Upper shells have a smaller radius ( $R = 1250 \mu\text{m}$ ) than lower shells ( $R = 5000 \mu\text{m}$ ). In each case, the largest normalized deformation is fixed to one. In this figure, the minimum amount of normalized deformation in the substrate,  $D_m$ , is shown for each case. The deformation in the substrate of the thicker shells is larger than the thin ones. It is also observed that the shells with smaller radii cause larger deformations in the substrate.

The fabricated shells are not perfectly symmetric. This asymmetry may affect anchor loss. To capture the effect of the mass imperfections on anchor loss, an imbalanced mass,  $\Delta m$ , is added on top of the shell rim as shown in Figure 4.12. This figure also shows the normalized  $Q_{Anchor}$

versus the normalized mass imperfection,  $\Delta m/m$ , where  $m$  is the mass of the shell. According to this figure, a mass imperfection increases anchor loss—this increase might be more than 1,000 times. Indeed, any imperfection in the rim changes the location of the nodal points of vibration in HSRs. In this case, the nodal points of vibration are no longer located along the vertical axis of the stem. This increases the deflection in the stem and therefore energy loss through the anchor. Additionally, the simulation results show that this imbalanced mass affects the first WG mode more than the second one. When there is an imbalanced mass, an HSR resonates in a way that two of its anti-nodes in the first WG mode are along the line that connects the shell center to the imbalanced mass, while in the second WG mode, the anti-nodes are located  $45^\circ$  away from this line. Therefore, the first mode is affected by the imperfection more than the second mode, so the first mode is more dissipative. This may cause damping mismatch and bias drift in HSR gyroscopes.

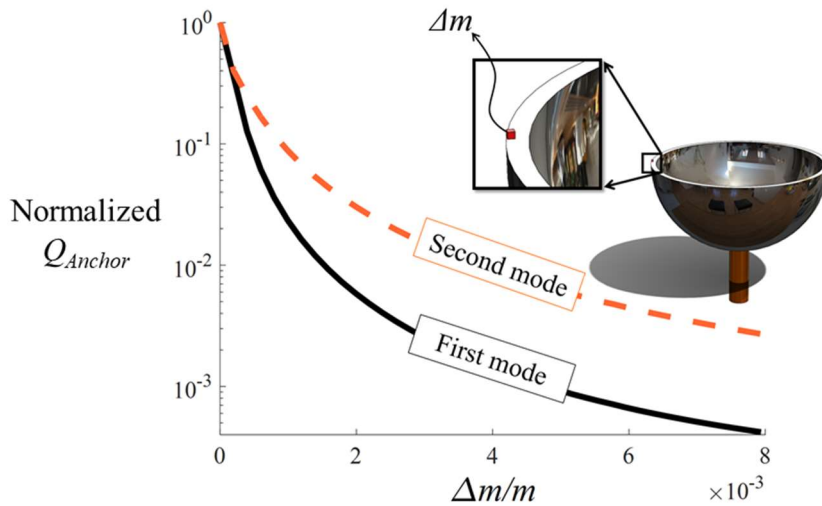


**Figure 4.12:** Effect of an imbalanced mass on  $Q_{Anchor}$ . Mass imperfection, which is modeled as an extra point mass at the rim of a shell, reduces the  $Q_{Anchor}$  of both WG modes; however, it reduces the  $Q_{Anchor}$  of the first mode more than the second one.

Fabricated shells might have out-of-roundness or non-circularity in the rim, which could affect anchor loss of HSRs. To investigate the effect of this imperfection, the radius of one side of the shell is distorted up to a maximum of ten percent of the initial radius of the shell. Figure 4.13 shows the effect of this type of imperfection on  $Q_{Anchor}$ . This graph demonstrates that  $Q_{Anchor}$  is significantly reduced due to rim non-circularity. Rim non-circularity causes imbalance in the shell and therefore changes the vibrational pattern of the  $Q_{Anchor}$  modes such that the anchor is no longer located at the nodal points of vibration. According to the FEM analysis, this imperfection has more effect on one of the WG modes than the other one. A 100  $\mu\text{m}$  imperfection in the radius reduces the second WG mode's  $Q_{Anchor}$  about 1,000 times, while it reduces the first mode's  $Q_{Anchor}$  about 50 times. This is because in a non-circular shell, just one of the anti-nodes of the first WG mode is affected by non-circularity, but for the second mode two of the anti-nodes are in the non-circular part and are affected—in a non-circular shell, an HSR resonates such that two of its anti-nodes in the first WG mode are along the line that connects the shell center to the maximum non-circularity, while in the second WG mode, the anti-nodes are located  $45^\circ$  away from this line.

In some fabrication processes, shells are cut from their host wafers using lapping and CMP. It is possible that the fabricated shell is not cut horizontally, such that one side of the shell is taller than the other—this imperfection is called imperfect cutting. The angle of this imperfection is considered to be  $\Phi$ . To capture the effect of imperfect cutting, the edge of a perfect shell is locally cut up to a maximum of  $2^\circ$ . The FEM analysis results are shown in Figure 4.14. This graph reveals that imperfect cutting changes the anchor loss significantly— $1^\circ$  of imperfection in the cutting increases the anchor loss about 10,000 times. When the cutting is imperfect, the system has a revolution axis that is not along the stem's central axis; therefore, the stem, which connects the

shell to the substrate, is not attached to the region in the shell that has the lowest deformation, so a large amount of energy propagates from the shell to the substrate.

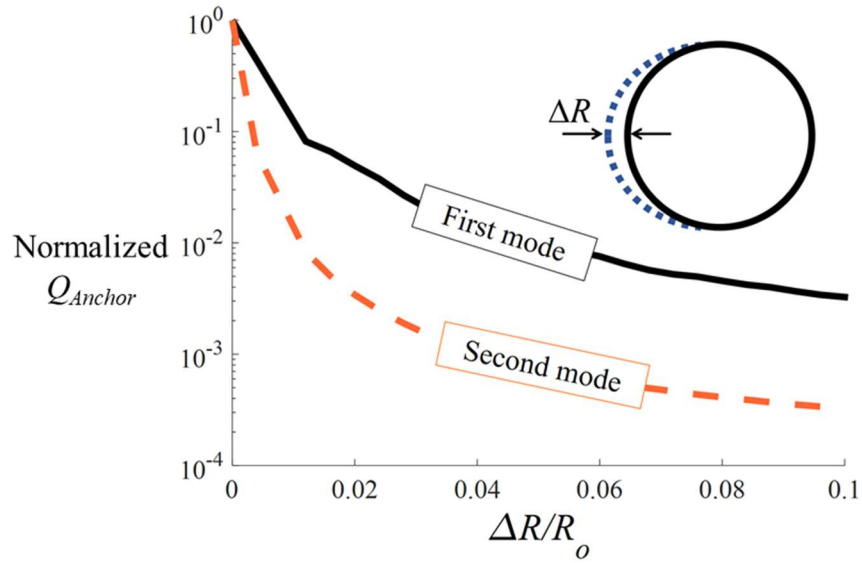


**Figure 4.13:** Effect of non-circularity imperfection on  $Q_{Anchor}$ . Non-circularity reduces  $Q_{Anchor}$  of both WG modes; however, it reduces the  $Q_{Anchor}$  of the second mode more than the first one.

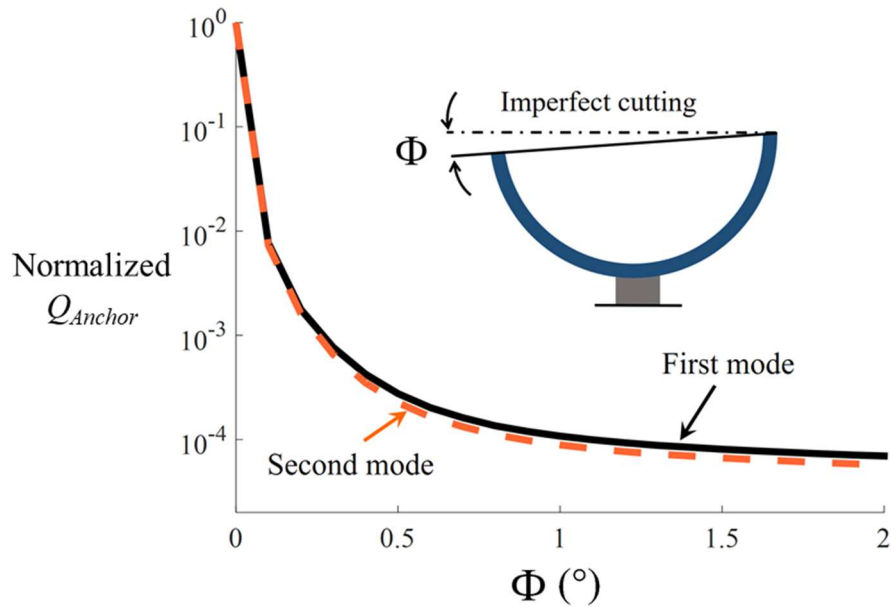


**Figure 4.14:** Effect of imperfect cutting on  $Q_{Anchor}$ . Imperfect cutting reduces the  $Q_{Anchor}$  of both WG modes similarly.

The results of imperfection simulations indicate that a controlled fabrication process is extremely important for the manufacturing of the high- $Q$  HSRs. Otherwise; these resonators suffer from a large amount of anchor loss.

### ***b) Effect of Stem Properties on Anchor Loss***

A fabricated shell needs to be bonded to a substrate before it is used as a resonator. Different materials such as glass frit or Crystalbond 509 (SPI Supplies, West Chester, PA, USA) have been tested for this process. In some cases [48], an external rod is added to the system as a stem. This section investigates the effects of the stem properties—stem material, stem radius and height, a hole inside the stem, stem shape, and stem-shell misalignments.

Figure 4.15 shows the effects of the stem material properties on anchor loss. In this figure, the normalized  $Q_{Anchor}$  is depicted over the stem material properties. This figure shows that the stem material properties do not have a large effect on anchor loss. According to the simulation results, if the stem's Young's modulus is around 1.5 times larger than fused silica's Young's modulus, anchor loss is maximized. The material properties of the system are changed from fused silica to polysilicon, metallic glass, aluminum oxide, and diamond and the simulations are repeated. In all cases, anchor loss is maximized when the stem's Young's modulus is around 1.5 times larger than the Young's modulus of other parts of the system. We are not sure about the reason for this trend—more investigation is needed to understand it. As shown in this figure, by increasing the Poisson's ratio of the stem, anchor loss increases slightly. In HSRs, as radial forces cause compression or stretching in the stem, the Poisson's effect causes some waves along the stem's vertical direction. These vertical waves increase the amount of energy that escapes from the shell's anchor to the substrate; therefore, any increase in the stem's Poisson's ratio increases

anchor loss. The simulation results show that stem density does not play a significant role in anchor loss. Indeed, the stem's density does not change the resonant characteristics of the system.

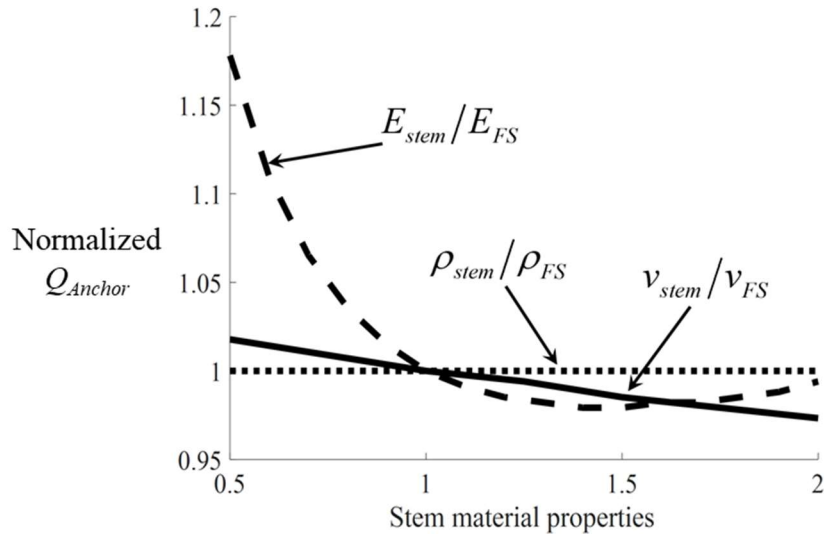


**Figure 4.15:** Effect of stem material properties on  $Q_{Anchor}$ . By increasing the stem's Young's modulus and Poisson's ratio,  $Q_{Anchor}$  changes. However, the stem's density has a negligible effect on  $Q_{Anchor}$ .

In Figure 4.16, the effects of the stem radius and height on anchor loss are depicted. This figure shows that a resonator with a thin and tall stem can have a high  $Q_{Anchor}$ . Figure 4.17 shows clearly that a thinner stem can reduce the amount of energy propagating into the substrate. The vibration of HSRs in the WG modes is symmetric with respect to the shell's central axis, so the deformation of the top center of the stem where it attaches to the shell is very small if the center line of the designed stem is exactly connected to the shell crown (the lowest point of the shell located along the shell's axis of revolution). In reality, a stem with finite dimensions attaches to areas far from this central point that undergo larger deformations; therefore, if the stem radius is too large, lots of energy propagate from the anchor to the substrate—Figure 4.18 (c) and (d) are schematics of large wave propagation from thick stems. Additionally, when the stem height increases, waves that come from both sides of the shell have more space to cancel each other out before reaching the substrate. As shown schematically in Figure 4.18 (b), the majority of the waves



cancel each other out in a tall stem. If the stem is short, some of the waves can escape from the shell into the substrate, increasing anchor loss. In the case of a thick stem, waves that are in the stem's central axis can experience the same phenomenon; therefore, they do not escape from the shell with tall stems. However, the waves that are far from the stem's central axis do not experience that much cancelation. Thus, increasing the stem height in thick stems should not be as effective as increasing it in thinner stems—the simulation results shown in Figure 4.16 confirm this hypothesis.

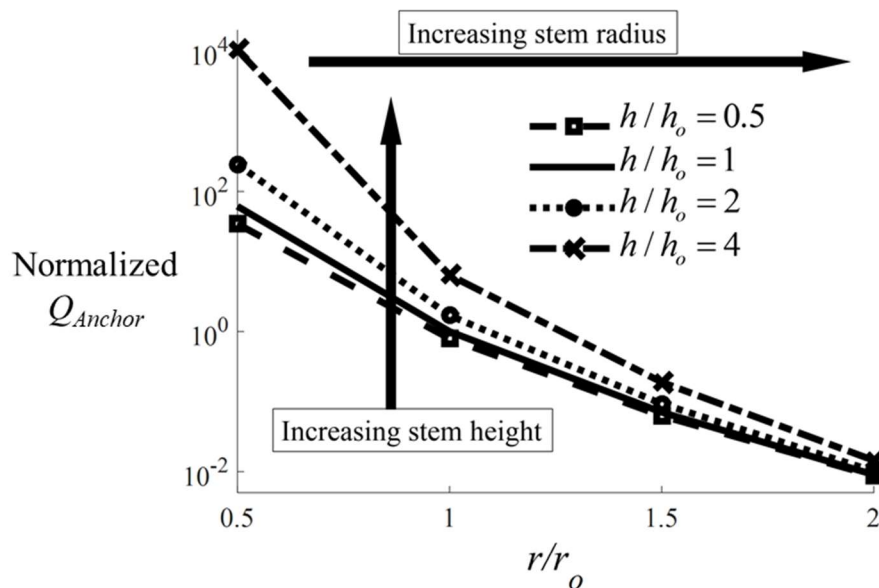


**Figure 4.16.** Effect of stem radius and height on  $Q_{Anchor}$ . By increasing the stem radius,  $Q_{Anchor}$  decreases. However, by increasing the stem height,  $Q_{Anchor}$  increases.

In [44], Gray *et al.* experimentally measured a  $Q$  of 230 for an HSR with a 14  $\mu\text{m}$  stem diameter. As shown in Figure 4.19, when they reduced the stem diameter of the same shell to 6  $\mu\text{m}$ ,  $Q$  increased to 1,270. Recently, Shao *et al.* [47] performed an experiment on the effect of the stem height on  $Q$  of HSRs. Their result showed that a shell without a long stem has a  $Q$  of 9,500. However, a shell made in the same wafer with a long stem showed a  $Q$  of 40,400. The trends in

these two studies are similar to our simulation results, thus confirming our numerical approach for modeling anchor loss.

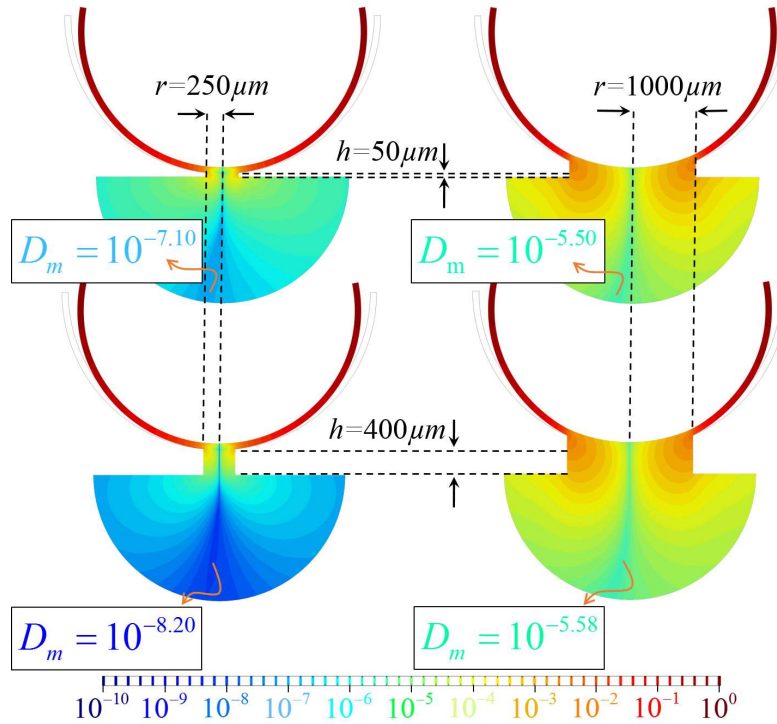


**Figure 4.17:** Contours of the normalized deformation distribution in the cross section for systems with thin stems (left) and thick stems (right). In each case, the largest normalized deformation is fixed to one. Upper shells have shorter stems ( $h = 50 \mu\text{m}$ ) than lower shells ( $h = 400 \mu\text{m}$ ). The deformation in the substrate of the thicker stems is larger than the thin ones. It is also observed that the shells with shorter stem cause larger deformations in the substrate.

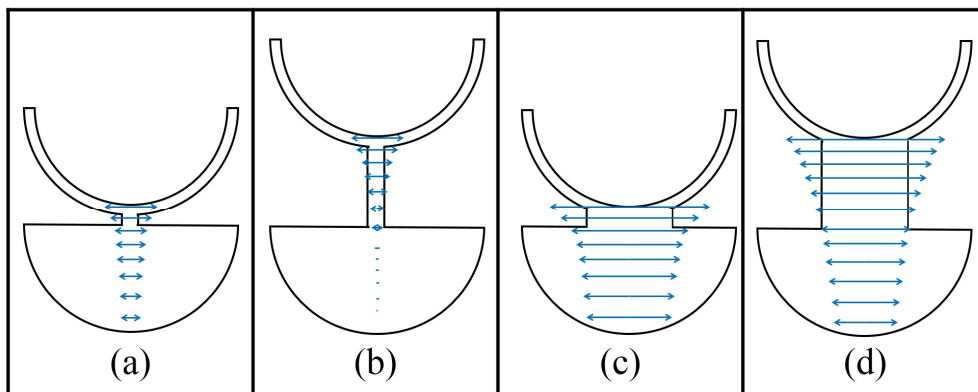


**Figure 4.18:** Schematic of the wave propagation from shells with different stem sizes: (a) thin and short, (b) thin and tall, (c) thick and short, and (d) thick and tall.

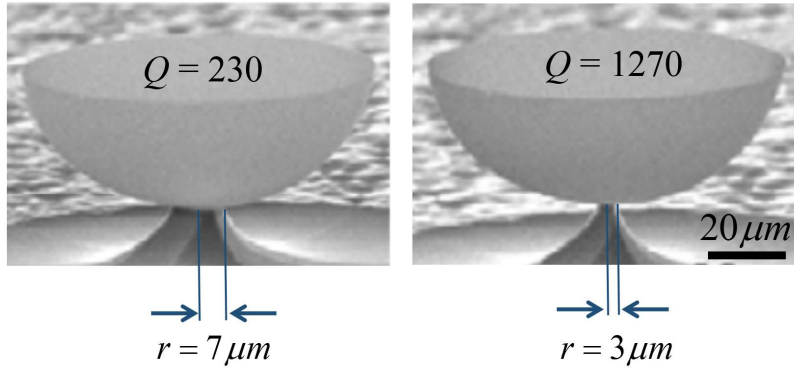
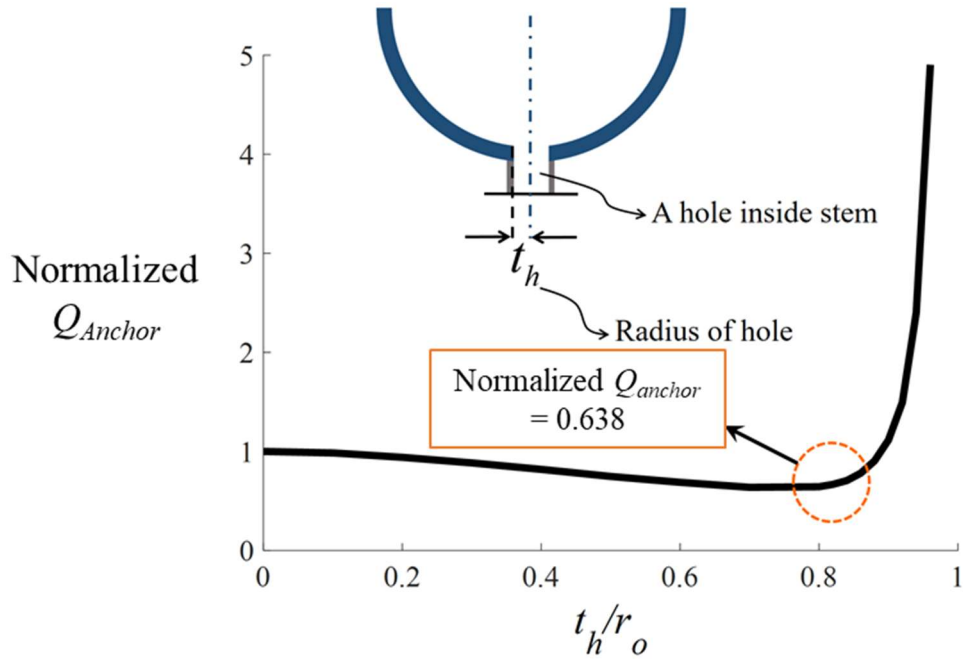


**Figure 4.19:** Experimental data reported in [44] about the effect of the stem radius on  $Q$ . In this experiment,  $Q$  of a shell is measured when it is on top of a thick stem, then again when the radius of the stem is reduced from  $7 \mu\text{m}$  to  $3 \mu\text{m}$ . The results show that  $Q$  improves more than 5 times for the case with the thinner stem.

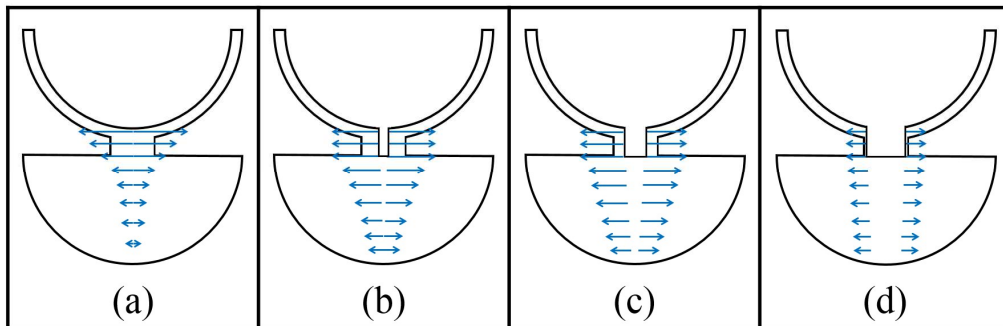
In some cases, shell resonators have been made with a hollow stem instead of a solid stem. To characterize the effect of a hollow stem on anchor loss, a cylindrical hole with radius  $t_h$  is removed from the middle of the stem and  $Q_{Anchor}$  is simulated. The results, which are shown in Figure 4.20, reveal that creating a small hole in the middle of stem increases anchor loss, and as the radius of this hole increases, anchor loss increases further. However, when the hole becomes very large, anchor loss decreases.

Figure 4.21 shows the schematics of the wave propagation for different situations. In Figure 4.21 (a), it is shown that when the stem is solid, waves from two different sides of the stem cancel each other out; therefore, anchor loss is not large. After creating a hole inside the stem, some of the waves are not canceled in the middle of the stem and they will be lost; however, some part of these waves will cancel each other out in the substrate (Figure 4.21 (b)). As the hole radius increases, the distance between the waves that come from the two different sides increases; therefore, it is harder for them to be canceled in the substrate (Figure 4.21 (c)). Thus, anchor loss increases further. When the hole radius becomes very large, the stem wall thickness reduces to a very small amount. As this amount becomes smaller than the shell thickness, the shell vibration

does not cause a large deformation in the substrate. In this case, even though the waves that come from both sides of the shell cannot cancel each other out (Figure 4.21 (d)), they are too small to cause a large amount of energy dissipation. In fact, when the stem wall thickness starts to become very small, anchor loss starts to decrease.



**Figure 4.20:** Effect of radius of a cylindrical hole in the stem on  $Q_{Anchor}$ . The results show that shells with a solid stem have higher  $Q_{Anchor}$ s than shells with a hollow stem when the stem wall thickness is not very small. If the stem wall thickness becomes very small  $Q_{Anchor}$  starts to improve.



**Figure 4.21:** Schematic of the wave propagation from shells with different stems: (a) solid stem, (b) stem with a small hole, (c) stem with a large hole, and (d) stem with a very large hole.

The shape of the stem can also be an important factor for anchor loss. Figure 4.22 shows three different shapes that can be used as a stem:

1. The stem is just considered to be a simple rod—  $Q_{Anchor}$  of this case is calculated to be  $Q_1$ .
2. Some material is removed from the middle of the stem—hourglass shape. The simulation results show that in this case  $Q_{Anchor}$  improves a large amount compared to the first case. The tapered shape guides waves that come from two different sides of the stem to its central axis where they cancel each other out, hence anchor loss decreases.
3. The middle of the stem becomes thicker—ball shape. In this case, waves have space to spread out; therefore, some of them might not cancel out. So, anchor loss increases in this case; however, this increase is not very much because the other part of the stem is still thinner and waves can be canceled there.

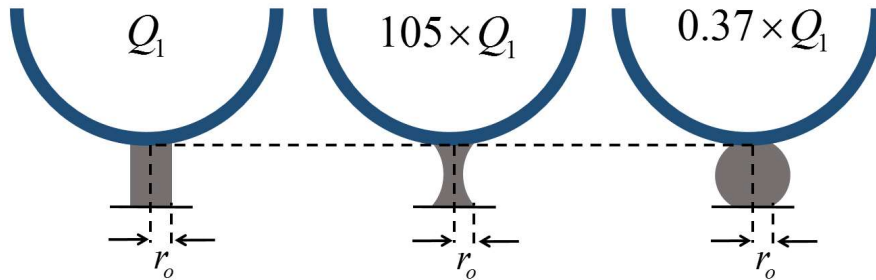


**Figure 4.22:** Effect of stem shape on  $Q_{Anchor}$ . A shell with a stem with hourglass shape shows the highest  $Q_{Anchor}$ .

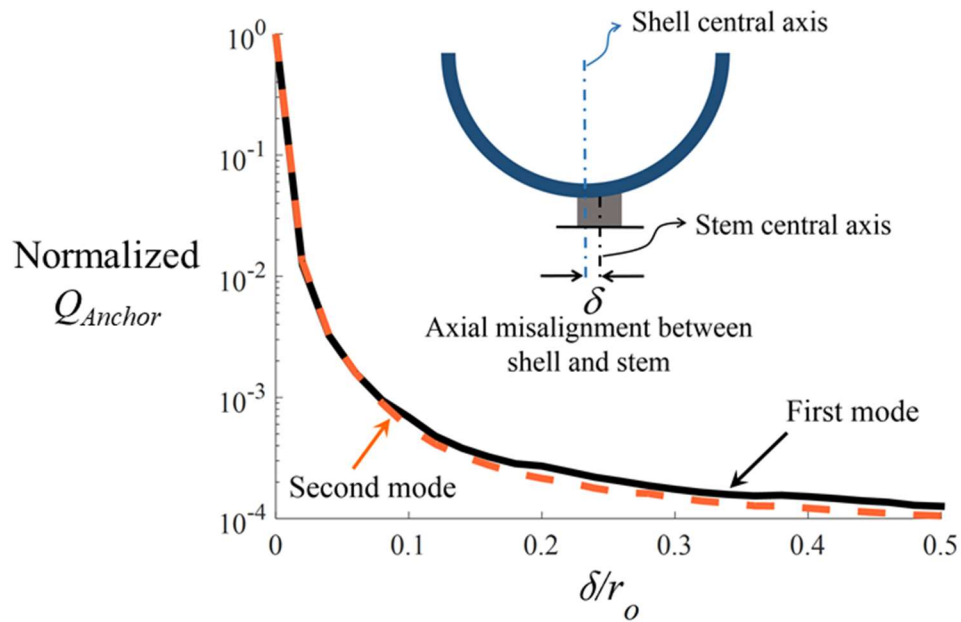
It is hard to attach a shell to the stem via a perfectly controlled bonding process. There are two different types of misalignments during the bonding: a) axial misalignment and b) angular misalignment. During the bonding process of the shell to the substrate, the stem's central axis might not have coincided with the axis of revolution of the shell (Figure 4.23 (a)). This is called

axial misalignment. It is also possible that the shell is tilted when it is attached to the substrate (angular misalignment) as shown in Figure 4.23 (b). These misalignments cause the stem's central line to be in a different position than the nodal points of vibration. The effects of these misalignments are plotted in Figure 4.23 (a) and (b). Figure 4.23 (a) shows that the axial misalignment degrades  $Q_{Anchor}$ . Indeed, a 40  $\mu\text{m}$  misalignment between the shell and stem axes increases anchor loss about 1,000 times. As Figure 4.23 (b) shows, anchor loss of an HSR is highly depended on angular misalignment. Even  $1^\circ$  tilting during the bonding between the stem and shell will increase anchor loss more than 1,000 times. The high sensitivity of  $Q_{Anchor}$  to these misalignments necessitates utilizing a very accurate bonding process.

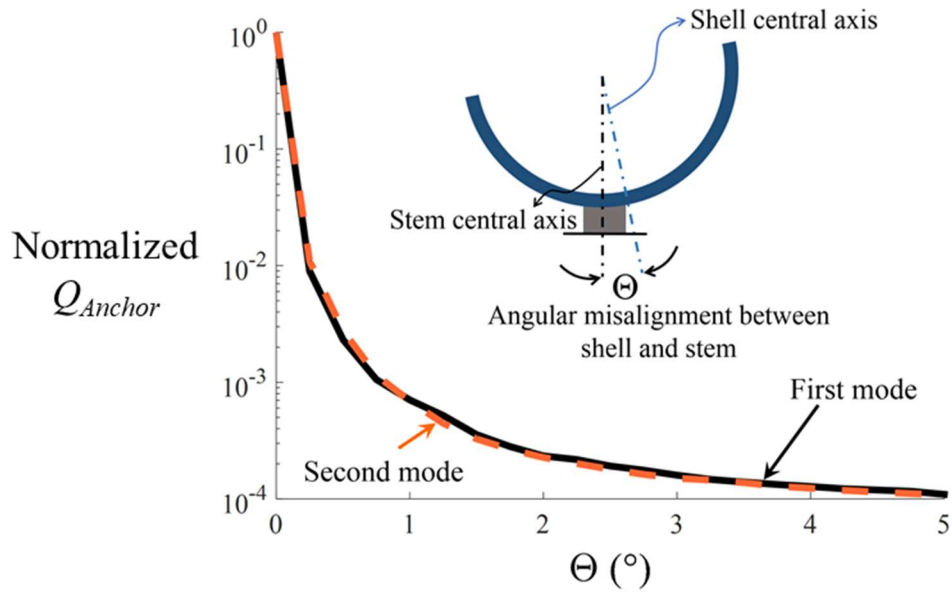
### ***c) Effect of Substrate Properties on Anchor Loss***

In this part, the effects of the substrate properties on anchor loss are studied. These include substrate material properties, using an adhesive material between the stem and substrate, and the attachment configuration between the stem and substrate.

The effects of substrate material properties on anchor loss are shown in Figure 4.24. To simulate these effects, the material properties of the substrate and PML are changed simultaneously. It is taken into account that as the material properties of these domains are changed, the wavelength is changed; therefore, the PML thickness is adjusted. Figure 4.24 shows that by increasing the substrate's Young's modulus, anchor loss decreases. In this case, the deflection in the substrate decreases due to the increase in substrate rigidity. Indeed, as the substrate becomes stiffer, shell cannot deform the substrate easily—hence, more energy stays in the resonator during the oscillation. This figure also reveals that the substrate's density is an important parameter in anchor loss. It is found that a lower density substrate shows lower anchor



(a)



(b)

**Figure 4.23:** (a) Effect of an axial misalignment on  $Q_{Anchor}$ . (b) Effect of an angular misalignment on  $Q_{Anchor}$ . These misalignments reduce  $Q_{Anchor}$  significantly.

loss because it absorbs less energy than a substrate made from a high density material. Numerical simulations show that substrate's Poisson's ratio has less of an effect than its Young's modulus and density. This is expected, because Poisson's effect creates some vertical forces from horizontal forces and vice versa and this should not have a major impact on the amount of energy that is already in the substrate.

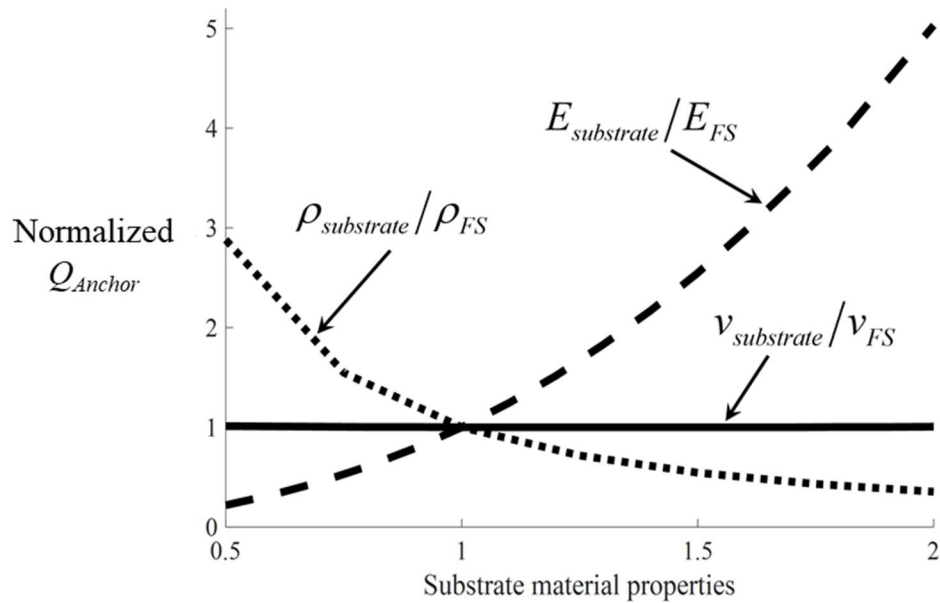


**Figure 4.24:** Effect of substrate material properties on  $Q_{Anchor}$ . By changing substrate's Young's modulus and density  $Q$  changes. However, substrate's Poisson's ratio has a negligible effect on  $Q_{Anchor}$ .

In all of the simulations, it is considered that the shell, stem and substrate are made together, so there is no need for any adhesive material. In reality, this might not be the case. For example, the stem of the HSR that is made in our group [48] is bonded to the substrate using glass frit as a glue. Figure 4.25 shows the schematic of a system with glass frit as an adhesive material. Glass frit material properties are considered to be Young's modulus: 49 GPa, Poisson's ratio: 0.25, and density: 6300 kg/m<sup>3</sup>. To investigate the effect of this attachment, the radius of the glass frit section,  $r_b$ , is changed and  $Q_{Anchor}$  is simulated. The results are shown in Figure 4.25. It is found that using



an adhesive material between the stem and substrate reduces anchor loss. In fact, this adhesive material can be considered as a part of a new and taller stem. This figure shows that as the adhesive material radius increases anchor loss increases—the same behavior was observed by increasing the stem radius. As adhesive material radius becomes larger,  $Q_{Anchor}$  starts to converge to  $Q_{Anchor}$  of the system when there is no adhesive material. This is because when adhesive material becomes very large it behaves like a part of the substrate.

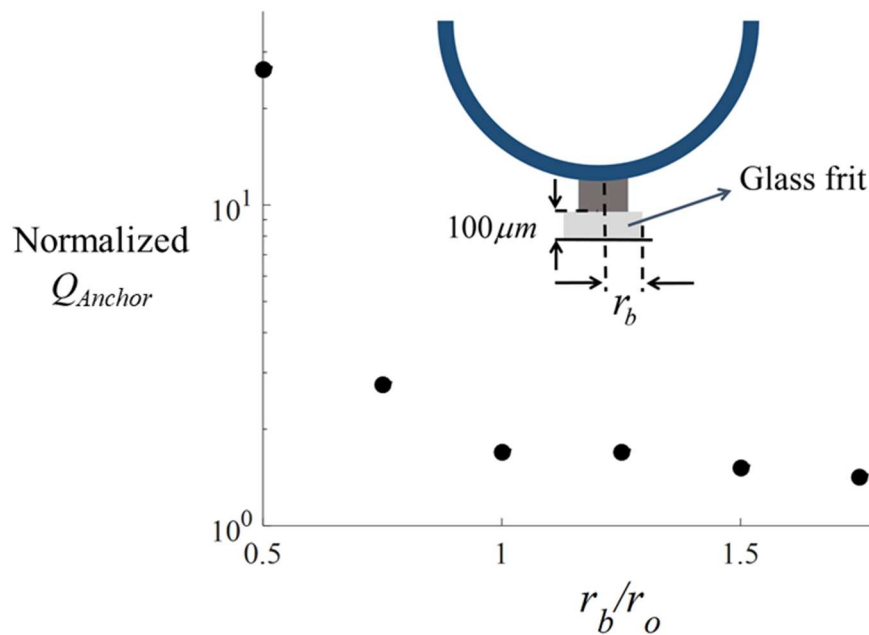


**Figure 4.25:** Effect of radius of the adhesive material on  $Q_{Anchor}$ . Utilizing an adhesive material between the stem and substrate increases  $Q_{Anchor}$ ; however, as the radius of this material increases  $Q_{Anchor}$  decreases and converges to the case that there is not any adhesive material.

As shown in Figure 4.26 (a), it is possible to use different configurations for attaching the stem to the substrate:

1. In the first configuration, a short stem outside of the shell is directly attached to the substrate. For this case,  $Q_{Anchor}$  is calculated to be  $Q_o$ .

2. In the second configuration, the stem is attached to the inside of the shell, so its length must be very large (tall stem) and therefore,  $Q_{Anchor}$  should be higher than  $Q_o$ . Simulation confirms this hypothesis—  $Q_{Anchor}$  improves about a hundred million times when the stem is used inside the shell.
3. The third configuration is a combination of the first and second ones—in this case a stem from inside and another one from outside of the shell are bonded to two substrates. It is found that  $Q_{Anchor}$  is a little higher (25%) than the first configuration. In this case, the majority of the waves are propagated from the outer stem to the substrate. Also, some of waves that go to the inner tall stem cancel each other; therefore,  $Q_{Anchor}$  is higher than the first case.
4. The fourth configuration is holding the stem from its edge.  $Q_{Anchor}$  of a group of resonators with different holding heights are simulated and results are shown in Figure 4.26 (b)— in this simulation, the distance from the shell and substrate is kept constant. This investigation shows when the stem is held from its edge,  $Q_{Anchor}$  is smaller than the case that the stem is directly attached to the substrate. As the holding height increases,  $Q_{Anchor}$  also increases. In fact, holding the stem from its edge is like the first configuration but there is a long cylindrical hole through the central axis of the substrate. As discussed before, some of the waves that come from two different sides of the shell cancel each other in the central axis of the substrate. If the holding height is very small, the hole inside the substrate is large, so a lot of the waves cannot cancel each other and anchor loss increases. By increasing the holding height, the length of the cylindrical hole decreases and waves find a space to cancel each other. As holding height becomes very large,  $Q_{Anchor}$  converges to  $Q_o$ .

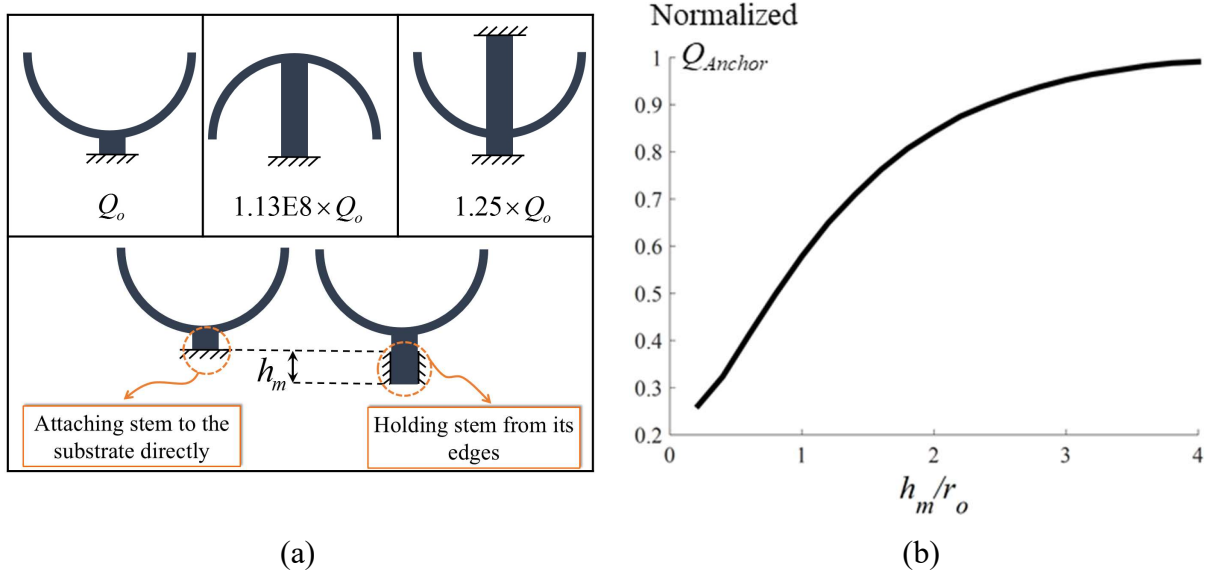


**Figure 4.26:** (a) Different configurations for attaching the stem to the substrate. The best configuration is using a stem inside the shell. (b) Effect of the holding height on  $Q_{Anchor}$  when the stem is held from its edge. By increasing the holding height,  $Q_{Anchor}$  increases; however,  $Q_{Anchor}$  is smaller than the case where the stem is directly attached to the substrate.

#### d) Effect of External Motion of Shell on Anchor Loss

The motion that an HSR experiences during operation might change its anchor loss. In this part, the effects of shocks and rotation rate on anchor loss are investigated.

The existence of shock causes stress and deformation in a solid structure—this changes its resonant pattern. To understand the effects of shock, a group of prestressed eigenfrequency simulations is conducted. In this analysis, first a stationary simulation should be conducted to find the deformation and stress in the shell under shock. To simulate shock, a body force, which is equal to the amount of the shock multiplied by the density of the structure is exerted on the system. In the second step, an eigenfrequency simulation is conducted for the system that is prestressed with the existing deformations and stresses from the first step. Two different types of shocks are exerted on the shell: vertical and horizontal. The amount of these shocks is changed from 0 to 50,000g. The results of this simulation are depicted in Figure 4.27. When there is a vertical shock,

the shell moves upward or downward—depending on the shock direction. This vertical shock has a small effect on anchor loss because the vertical movement does not change the shell’s axisymmetric shape, so anchor loss is not very sensitive to the vertical shock. However, in the case of a horizontal shock, the shell starts to move and tilt toward one side of the shell—this makes the system non-axisymmetric. Therefore, anchor loss increases as the horizontal shock increases.

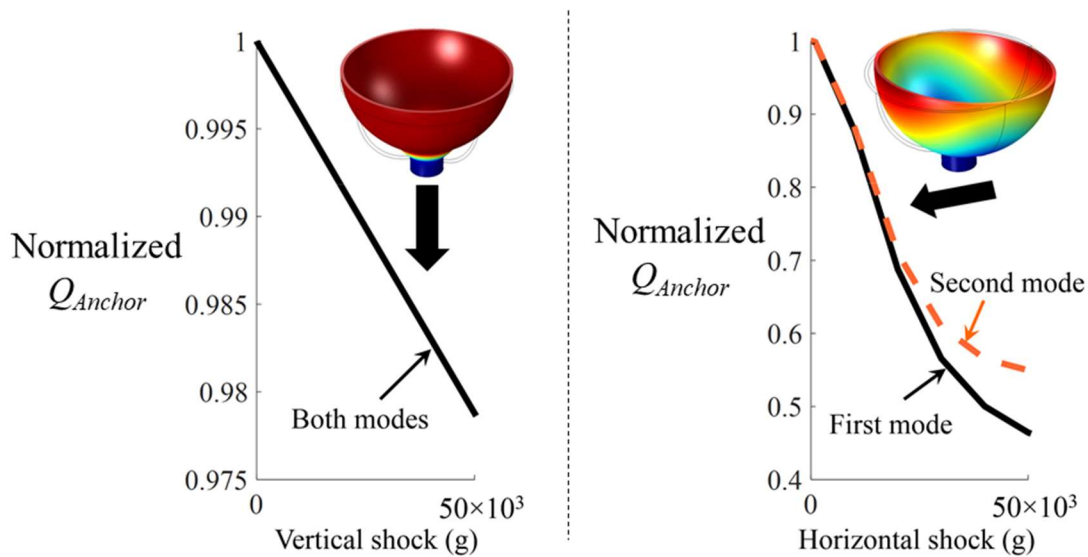


**Figure 4.27:** Effect of vertical and horizontal shocks on  $Q_{Anchor}$ . Horizontal shocks have larger impact on  $Q_{Anchor}$ .

Rotation also might change anchor loss because it causes centrifugal force in the system (this centrifugal force is proportional to the square of the rotation rate). The same method for calculating the effect of shock on  $Q_{Anchor}$  is used to simulate the effect of rotation rate on  $Q_{Anchor}$ ; however, instead of exerting body force, the condition of a rotating frame is utilized. Figure 4.28 shows the effect of the rotation rate on  $Q_{Anchor}$ . This figure shows that the rotation rate has a very small effect on anchor loss—a rotating frame with a speed of 1,000 rad/s causes less than a 1% change in anchor loss. A rotation around the shell axis revolution does not cause any non-axisymmetric behavior in the system; thus, anchor loss is not very sensitive to the rotation rate. If

anchor loss was very sensitive to the rotation rate, gyroscope would exhibit a nonlinear behavior, which is not desirable in sensors.

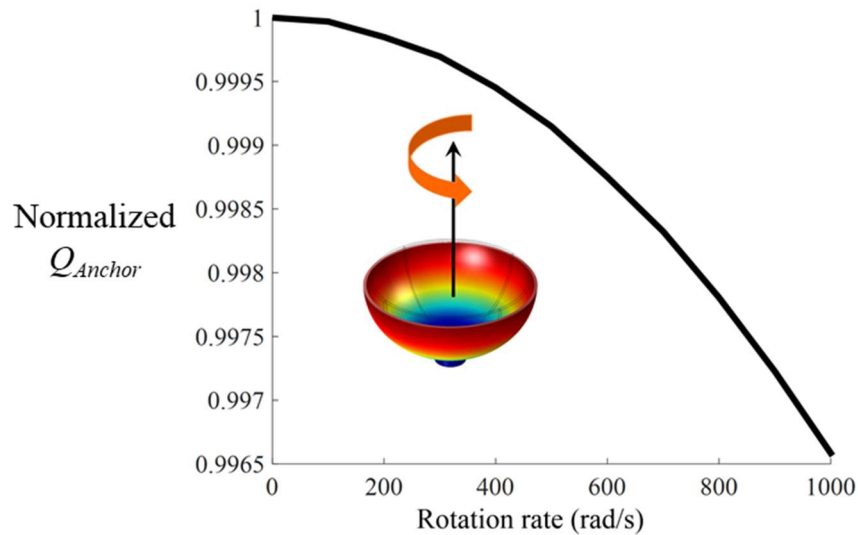


**Figure 4.28:** Effect of rotation rate on  $Q_{Anchor}$ .

Simulations have shown that anchor loss in HSRs depends on many parameters. The effective parameters are classified into four categories and a summary of the impact of them on anchor loss presented in Table 4.1. More detail can be found in [69]. These results showed that to decrease the anchor loss, the shell resonator structure should satisfy following design criteria:

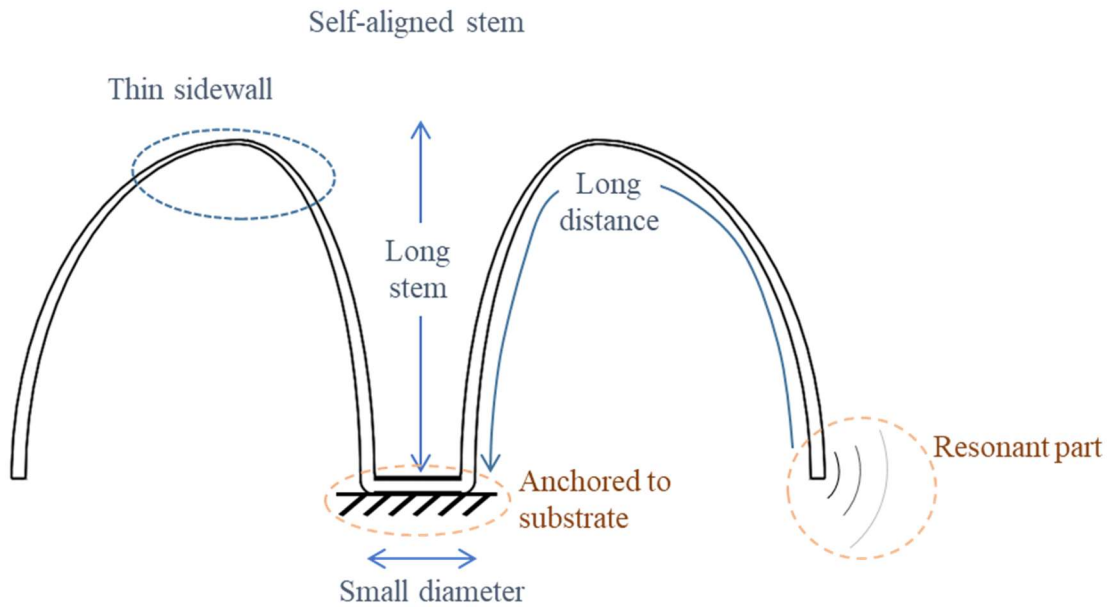
- The distance between the shell resonant part and substrate should be large
- Shell should be thin
- Stem should be tall
- Stem radius should be small
- In the case of a hollow stem, the stem wall thickness should be thin

**TABLE 4.1:** SUMMARY OF THE EFFECTS OF DIFFERENT PARAMETERS ON ANCHOR LOSS OF HSRs.

Category	Effective parameters	Amount of impact	Comments
<b>Shell</b>	Material	Moderate	<ul style="list-style-type: none"> <li>Increasing the shell's Young's modulus increases anchor loss.</li> <li>Increasing the shell's density decreases anchor loss.</li> <li>Shell's Poisson's ratio does not have a significant effect on anchor loss.</li> </ul>
	Geometry	High	<ul style="list-style-type: none"> <li>Increasing the shell radius decreases anchor loss significantly.</li> <li>Increasing the shell thickness increases anchor loss significantly.</li> </ul>
	Imperfections	High	<ul style="list-style-type: none"> <li>Mass imperfection increases anchor loss significantly. Anchor loss increases in the first WG mode more than the second mode.</li> <li>Non-circularity increases anchor loss significantly. Anchor loss increases in the second WG mode more than the first mode.</li> <li>Imperfect cutting increases anchor loss significantly. Anchor loss increases in both WG modes equally.</li> </ul>
<b>Stem</b>	Material	Low	<ul style="list-style-type: none"> <li>Anchor loss is a nonlinear function of the stem's Young's modulus.</li> <li>Stem's density does not have a significant effect on anchor loss.</li> <li>Increasing the stem's Poisson's ratio increases anchor loss slightly.</li> </ul>
	Geometry	High	<ul style="list-style-type: none"> <li>Increasing the stem radius increases anchor loss significantly.</li> <li>Increasing the stem height decreases anchor loss significantly.</li> </ul>
	Shape	High	<ul style="list-style-type: none"> <li>HSRs with narrower stem shapes have lower anchor loss.</li> </ul>
	Misalignments	High	<ul style="list-style-type: none"> <li>Axial and angular misalignments increase anchor loss significantly. The effects of these misalignments is the same for both WG modes.</li> </ul>
<b>Substrate</b>	Material	Moderate	<ul style="list-style-type: none"> <li>Increasing the substrate's Young's modulus decreases anchor loss.</li> <li>Increasing the substrate's density increases anchor loss.</li> <li>Substrate's Poisson's ratio does not have a significant effect on anchor loss.</li> </ul>
	Adhesive	High	<ul style="list-style-type: none"> <li>Using an adhesive material for attaching the stem to the substrate decreases anchor loss. As radius of this adhesive material increases anchor loss increases.</li> </ul>
	Configuration	High	<ul style="list-style-type: none"> <li>Using a stem inside the shell instead of outside decreases anchor loss significantly.</li> <li>Using a stem inside and another stem outside of the shell decreases anchor loss slightly compared to case with only a stem outside the shell.</li> <li>Holding the stem from its edges (clamping the stem from its peripheral boundary) instead of attaching it directly to the substrate increases anchor loss. As height of the holding area increases anchor loss decreases.</li> </ul>
<b>Motion</b>	Shock	Moderate	<ul style="list-style-type: none"> <li>Vertical shocks increase anchor loss slightly.</li> <li>Horizontal shocks increase anchor loss moderately.</li> </ul>
	Rotation rate	Low	<ul style="list-style-type: none"> <li>If the shell rotates very fast, its anchor loss increases slightly.</li> </ul>

In addition, the results indicated that the design parameters are not the only critical factors in controlling the anchor loss of shell resonators. Because any imperfection in the shell or attachment increases anchor loss by orders of magnitude, a precise fabrication process is also extremely crucial. It is very hard to achieve the desired level of fabrication precision using current microfabrication and assembly techniques. Therefore, there is a need for a new design and fabrication process that could produce shells with very small **geometrical imperfections** and **misalignments between the shell and stem**.

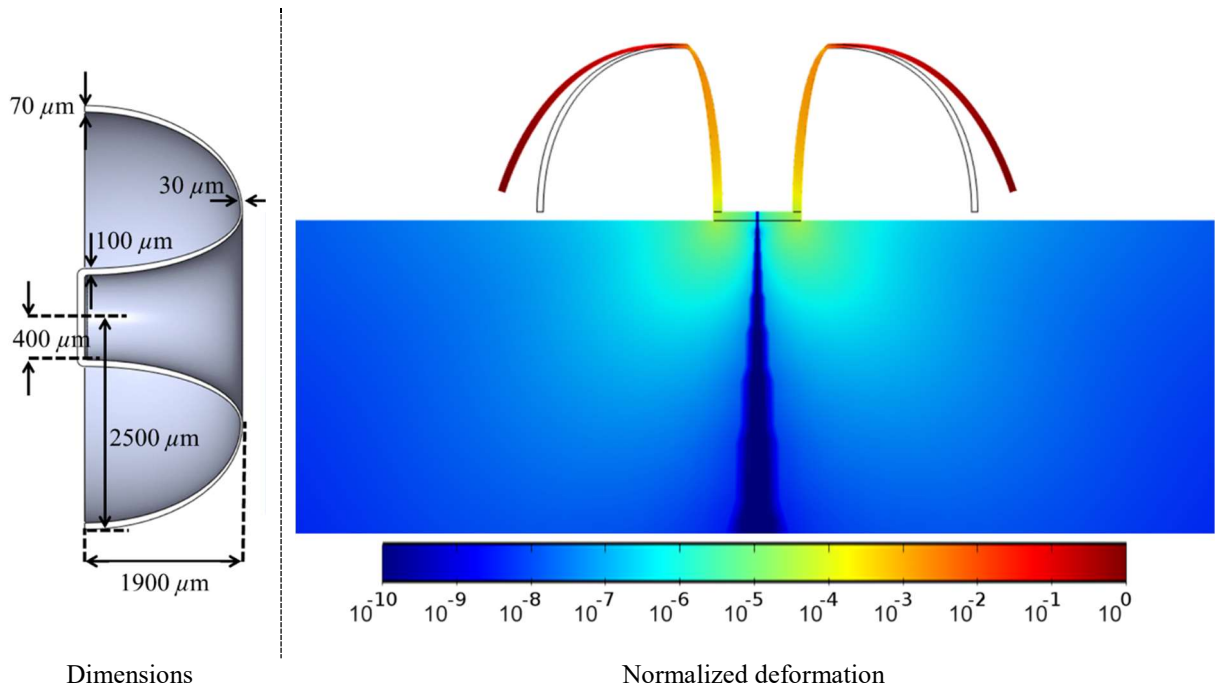
#### 4.1.1.3 Optimized design for reducing anchor loss in shell resonators



**Figure 4.29:** Schematic of a low anchor loss shell. This shell has the shape of a birdbath with thickness varying along its curvature.

To achieve this goal a shell structure shown in Figure 4.29 is designed. This shell has the shape of a birdbath (hemi-toroid) with thickness varying along its curvature, being thinnest at the top. It is attached to a supporting substrate at the anchor. The hollow column in the middle of the

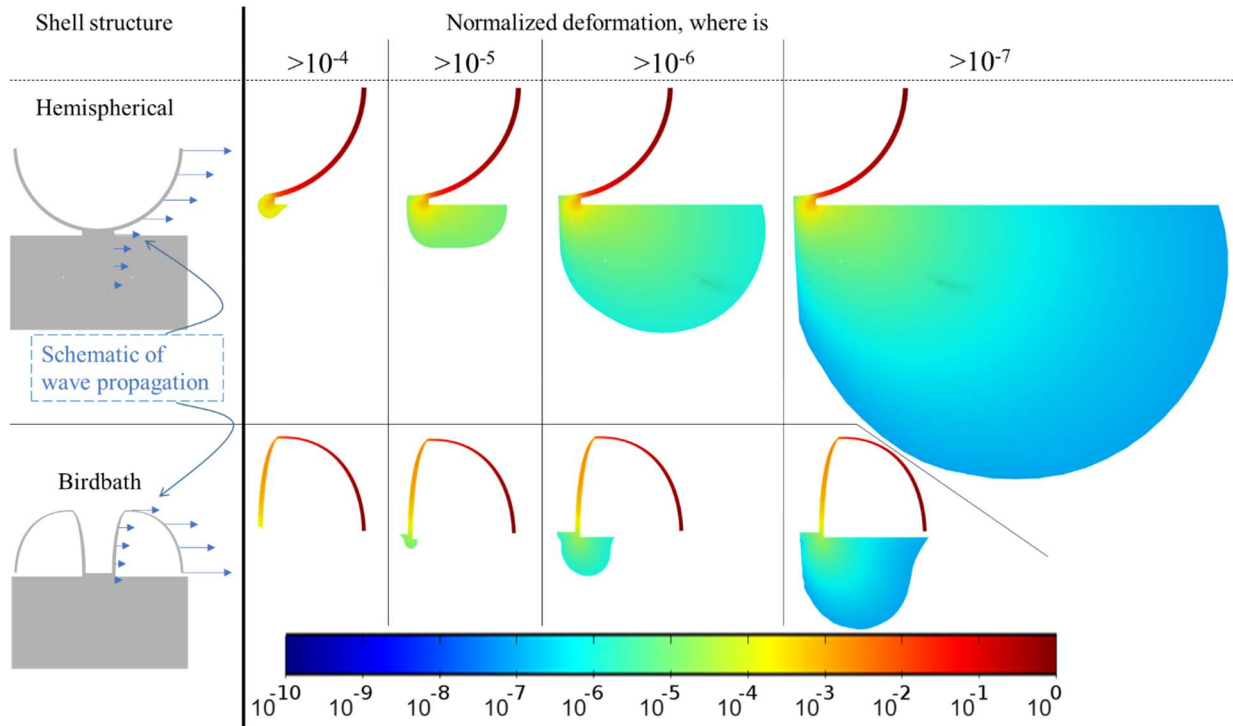
structure, stem, is long with a small diameter. The distance between the resonant part to the substrate is longer than a HSR with the same dimensions. This shell has a transient area with thin sidewalls that reduces energy transformation to the substrate. Furthermore, the shell and stem can be fabricated together; therefore, they are self-aligned.



**Figure 4.30:** Left: dimensions used for anchor loss simulation in BSR. Right: normalized deformation in BSR and the substrate beneath it.

As a result, this shell provides all the important criteria of a low anchor loss shell resonator. To calculate the anchor loss of a birdbath shell resonator (BSR), numerical simulation is used to conduct modal analysis with an appropriate PML around the substrate. Figure 4.30 shows the dimensions used for this simulation and the relative deformations in the shell and its substrate.  $Q_{Anchor}$  in this BSR calculated to be larger than  $10^{14}$ , which is about five orders of magnitude better than the initial HSR.





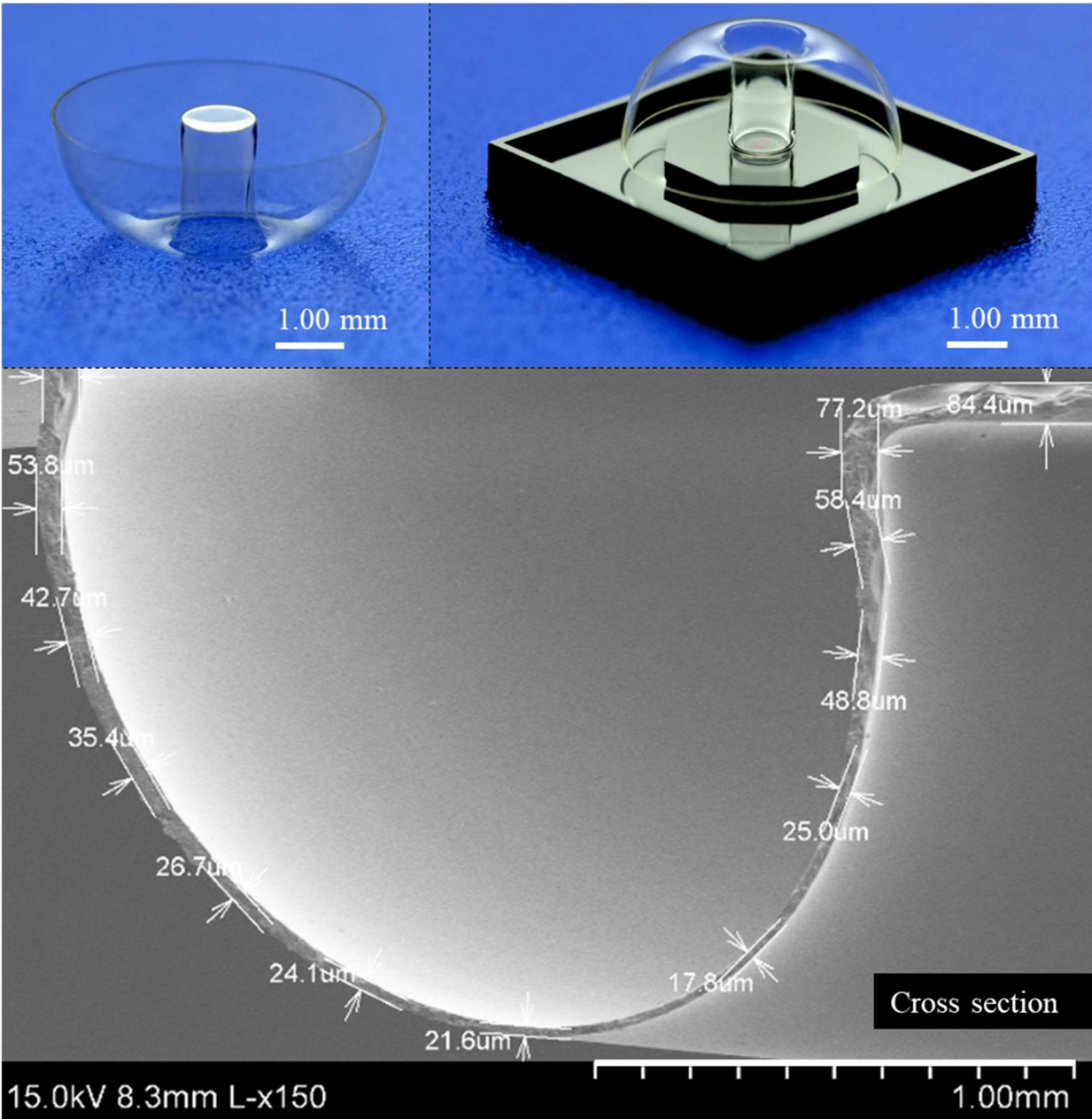
**Figure 4.31:** Left: schematic of wave propagation in the HSR and BSR. Right: normalized deformation in the substrate of these shells for different amount of deformation.

Figure 4.31 clearly shows that deformation in the substrate of a BSR is much smaller than an HSR. In this figure, deformations are shown for different amount in the substrate. When just deformations larger than  $10^{-4}$  are sketched, there is no deformation in the BSR substrate. As deformations are larger than  $10^{-5}$ , just a small portion of BSR substrate experiences it. Comparing deformation in the substrates of BSR and HSR shows an order of magnitude larger deformation in the HSR substrate, which causes larger anchor loss. This figure also includes schematic of wave propagations, in the case of BSR since wave should travel longer distance and thinner areas smaller amount of energy will reach to substrate, causing lower anchor loss in BSRs compared to HSRs.

#### 4.1.1.4 Fabricated shell structures with small anchor loss

During the past years, birdbath shell structures have been made in the university of

Michigan utilizing blowtorch molding process (fabrication process is briefly discussed in Appendix A) in different sizes. Figure 4.32 shows photograph and scanning electron microscope (SEM) image of this type of shells.



**Figure 4.32:** Top: an axisymmetric birdbath shell that is made out of fused silica using blowtorch reflow process. Bottom: cross section of a fabricated shell is shown in right-hand side of this figure.

Changing blowtorching parameters and the mold design allowed us to fabricate shells with different radii and aspect ratios. In this process, since the shell is fabricated monolithically, the stem is self-aligned. Furthermore, the high temperature flame smooths the shell surface with average roughness of the fabricated shell being less than 2 Å, which could reduce surface loss (this will be discussed in subsection 4.1.6). This process initially started by Dr. Jae Young Cho and later has been improved by Dr. Tal Nagourney and Mr. Sajal Singh.

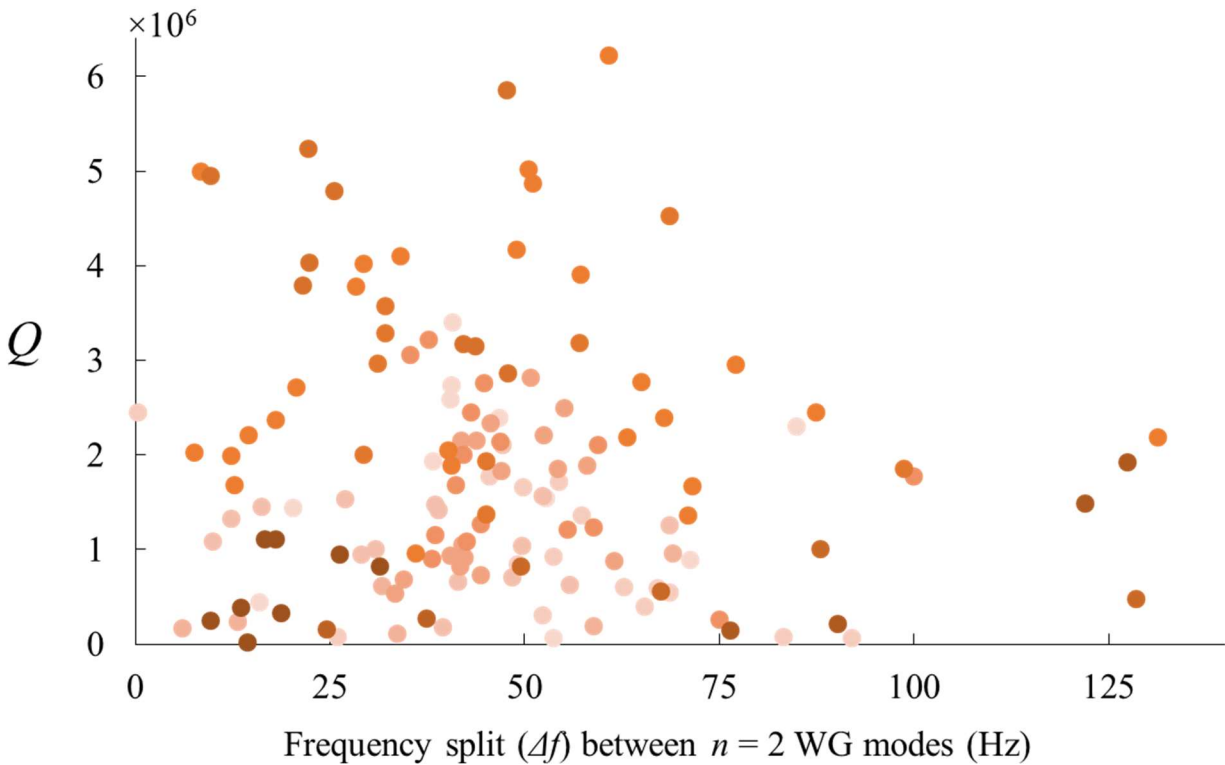


**Figure 4.33:** Effect of frequency split on  $Q$  of BSRs with 5 mm diameter. Different colors indicate different fabrication batches. No correlation between frequency split and  $Q$ s, suggests that anchor loss is not a major dissipation mechanism in the designed shell structure.

$Q$  of fabricated shells varies from less than 10,000 to more than 10 million. Figure 4.33 shows the  $Q$  of shells with 5 mm diameter versus frequency split between WG modes (data are provided by Dr. Jae Young Cho, Dr. Tal Nagourney, and Mr. Sajal Singh). These results show that

there is no clear correlation between  $Q$  and frequency split. Frequency split is a result of imperfection in shells. Therefore, devices with more imperfections tend to produce larger frequency split. Hence, these results show that there is no correlation between imperfections in BSRs and  $Q$ s. As a result, we believe that  $Q$  due to anchor loss in shells with the proposed geometry and dimension is not a dominant dissipation mechanism, showing successful low anchor loss design for MEMS shell resonators.

As a summary to this subsection, anchor loss in shell resonators investigated extensively and BSRs with an extremely small anchor loss are successfully designed, and tested. TED in MEMS resonators will be explained in the next part.

#### **4.1.2 Thermoelastic dissipation (TED)**

TED is one of the main causes of energy dissipation in MEMS resonators. In a deformed structure, some regions experience tension and some compression. Tensile and compressive stresses produce cold and hot regions in the structure, respectively. As a result of this coupling between the strain and temperature fields, periodic local temperature gradients are formed in an oscillating structure. In order to relax back to thermal equilibrium, heat flows irreversibly from the hot to cold regions. This dissipation mechanism is called TED [70–85] and it becomes significant when the resonator thermal transport time constant is close to the period of its elastic deformation [79].

Understanding TED in resonators has been the subject of numerous studies. In the 1930s, Zener [70, 71] presented a general model for calculating thermoelastic  $Q$  ( $Q_{TED}$ ) of wires and reeds by considering one-dimensional heat transfer across their bending direction. Nayfeh and Younis [75] analytically modeled  $Q_{TED}$  of micro-plates with general shapes and boundary conditions. They

showed that the geometric properties of a micro-plate could have a significant effect on  $Q_{TED}$ . Chandler *et al.* [76] studied the effect of slots placed between the hot and cold regions of micro-beam resonators on  $Q_{TED}$ , both numerically and experimentally. Ghaffari and Kenny [80] analyzed the effect of a silicon dioxide thin film on TED in silicon micro-resonators. They showed that this thin film affects thermal relaxation of the resonator and changes its  $Q$ .

#### 4.1.2.1 Fully coupled thermo-mechanical formulation

To find the TED in shell resonators, fully coupled thermo-mechanical formulation of solid materials is developed in the following paragraphs.

Stress-strain relations in linear solids when there is a temperature difference of  $\Delta T$  from the equilibrium temperature can be expressed as (4.6):

$$\begin{bmatrix} \sigma_{11} \\ \sigma_{22} \\ \sigma_{33} \\ \sigma_{23} \\ \sigma_{13} \\ \sigma_{12} \end{bmatrix} = \begin{bmatrix} c_{11} & c_{12} & c_{13} & c_{14} & c_{15} & c_{16} \\ c_{12} & c_{22} & c_{23} & c_{24} & c_{25} & c_{26} \\ c_{13} & c_{23} & c_{33} & c_{34} & c_{35} & c_{36} \\ c_{14} & c_{24} & c_{34} & c_{44} & c_{45} & c_{46} \\ c_{15} & c_{25} & c_{35} & c_{45} & c_{55} & c_{56} \\ c_{16} & c_{26} & c_{36} & c_{46} & c_{56} & c_{66} \end{bmatrix} \times \begin{pmatrix} \begin{bmatrix} \varepsilon_{11} \\ \varepsilon_{22} \\ \varepsilon_{33} \\ 2\varepsilon_{23} \\ 2\varepsilon_{13} \\ 2\varepsilon_{12} \end{bmatrix} - \Delta T \begin{bmatrix} \alpha_{11} \\ \alpha_{22} \\ \alpha_{33} \\ 2\alpha_{23} \\ 2\alpha_{13} \\ 2\alpha_{12} \end{bmatrix} \end{pmatrix} \quad (4.6)$$

where  $\sigma_{ij}$ ,  $\varepsilon_{ij}$ ,  $c_{ij}$ , and  $\alpha_{ij}$  are stresses, strains, elastic stiffnesses, and thermal expansion coefficients of the material, respectively.

For isotropic materials, the stress-strain equations can be simplified to (4.7), where  $E$ ,  $\nu$ , and  $\alpha$  are Young's modulus, Poisson's ratio, and coefficient of thermal expansion of material, respectively.

Furthermore, the equations of motion in the  $x$ ,  $y$ , and  $z$  directions are represented in (4.8)–(4.10).

$$\begin{bmatrix} \sigma_{11} \\ \sigma_{22} \\ \sigma_{33} \\ \sigma_{23} \\ \sigma_{13} \\ \sigma_{12} \end{bmatrix} = \frac{E}{(1+\nu)(1-2\nu)} \times \begin{bmatrix} 1-\nu & \nu & \nu & 0 & 0 & 0 \\ \nu & 1-\nu & \nu & 0 & 0 & 0 \\ \nu & \nu & 1-\nu & 0 & 0 & 0 \\ 0 & 0 & 0 & \frac{(1-2\nu)}{2} & 0 & 0 \\ 0 & 0 & 0 & 0 & \frac{(1-2\nu)}{2} & 0 \\ 0 & 0 & 0 & 0 & 0 & \frac{(1-2\nu)}{2} \end{bmatrix} \times \begin{bmatrix} \varepsilon_{11} \\ \varepsilon_{22} \\ \varepsilon_{33} \\ 2\varepsilon_{23} \\ 2\varepsilon_{13} \\ 2\varepsilon_{12} \end{bmatrix} - \frac{E\alpha\Delta T}{1-2\nu} \begin{bmatrix} 1 \\ 1 \\ 1 \\ 0 \\ 0 \\ 0 \end{bmatrix} \quad (4.7)$$

$$\rho \frac{\partial^2 u}{\partial t^2} = \left( \frac{\partial \sigma_{11}}{\partial x} + \frac{\partial \sigma_{12}}{\partial y} + \frac{\partial \sigma_{13}}{\partial z} \right) \quad (4.8)$$

$$\rho \frac{\partial^2 v}{\partial t^2} = \left( \frac{\partial \sigma_{12}}{\partial x} + \frac{\partial \sigma_{22}}{\partial y} + \frac{\partial \sigma_{23}}{\partial z} \right) \quad (4.9)$$

$$\rho \frac{\partial^2 w}{\partial t^2} = \left( \frac{\partial \sigma_{13}}{\partial x} + \frac{\partial \sigma_{23}}{\partial y} + \frac{\partial \sigma_{33}}{\partial z} \right) \quad (4.10)$$

where  $u$ ,  $v$  and  $w$  are displacements in the  $x$ ,  $y$ , and  $z$  directions, respectively, and  $\rho$  is the density of the material. Thermal dynamics are governed by the heat conduction equation:

$$k\nabla^2 T - \rho C_{SP} \frac{\partial T}{\partial t} = \frac{E\alpha T}{1-2\nu} \frac{\partial e}{\partial t} \quad (4.11)$$

where  $k$  is the thermal conductivity,  $C_{SP}$  is the specific heat capacity and  $e$  is the dilatation strain, which is defined as (4.12):

$$e = \varepsilon_{11} + \varepsilon_{22} + \varepsilon_{33} \quad (4.12)$$

In most cases,  $T$  in the right hand side of (4.11) can be replaced by the nominal average temperature  $T_0$  to obtain a linear equation for the temperature [75]. Using (4.7)–(4.12) and strains to displacements relations, coupled thermoelastic equations can be written as (4.13)–(4.16):

$$\rho \frac{\partial^2 u}{\partial t^2} = \frac{E}{2(1+\nu)} \left( \frac{\partial^2 u}{\partial x^2} + \frac{\partial^2 u}{\partial y^2} + \frac{\partial^2 u}{\partial z^2} \right) + \frac{E}{2(1+\nu)(1-2\nu)} \times \left( \frac{\partial^2 u}{\partial x^2} + \frac{\partial^2 v}{\partial x \partial y} + \frac{\partial^2 w}{\partial x \partial z} \right) - \frac{E\alpha}{1-2\nu} \frac{\partial T}{\partial x} \quad (4.13)$$

$$\rho \frac{\partial^2 v}{\partial t^2} = \frac{E}{2(1+\nu)} \left( \frac{\partial^2 v}{\partial x^2} + \frac{\partial^2 v}{\partial y^2} + \frac{\partial^2 v}{\partial z^2} \right) + \frac{E}{2(1+\nu)(1-2\nu)} \times \left( \frac{\partial^2 u}{\partial y \partial x} + \frac{\partial^2 v}{\partial y^2} + \frac{\partial^2 w}{\partial y \partial z} \right) - \frac{E\alpha}{1-2\nu} \frac{\partial T}{\partial y} \quad (4.14)$$

$$\rho \frac{\partial^2 w}{\partial t^2} = \frac{E}{2(1+\nu)} \left( \frac{\partial^2 w}{\partial x^2} + \frac{\partial^2 w}{\partial y^2} + \frac{\partial^2 w}{\partial z^2} \right) + \frac{E}{2(1+\nu)(1-2\nu)} \times \left( \frac{\partial^2 u}{\partial z \partial x} + \frac{\partial^2 v}{\partial z \partial y} + \frac{\partial^2 w}{\partial z^2} \right) - \frac{E\alpha}{1-2\nu} \frac{\partial T}{\partial z} \quad (4.15)$$

$$k\nabla^2 T = \rho C_{sp} \frac{\partial T}{\partial t} + \frac{E\alpha T_0}{1-2\nu} \left( \frac{\partial \dot{u}}{\partial x} + \frac{\partial \dot{v}}{\partial y} + \frac{\partial \dot{w}}{\partial z} \right) \quad (4.16)$$

These four equations represent the thermoelastic behavior of an isotropic solid material. In these equations,  $u$ ,  $v$ ,  $w$ , and  $T$  are unknowns. To find TED, these coupled equations should be solved simultaneously.

For simple beam resonator, Zener [70, 71] suggested that the  $Q_{TED}$  can be estimated from (4.17):

$$Q_{TED} = \frac{\rho C_{sp}}{E\alpha^2 T_0} \frac{1 + (\omega_{mech} \cdot \tau_{th})^2}{\omega_{mech} \cdot \tau_{th}} \quad (4.17)$$

where  $\omega_{mech}$  is the angular resonant frequency and equals  $2\pi f$ — $f$  is the mechanical resonant frequency.  $\tau_{th}$  is the thermal transport time constant of the resonator and can be found from (4.18):

$$\tau_{th} = \frac{b^2}{\pi^2 D} \quad (4.18)$$

where  $b$  is the thickness of the beam in the bending direction, and  $D$  is the thermal diffusivity of the beam material and equals  $k/(\rho \cdot C_{SP})$ . Based on Zener's equation,  $Q_{TED}$  is equal to the product of  $Q_{mat}$  and  $Q_{freq}$ :

$$Q_{mat} = \frac{\rho C_{SP}}{E \alpha^2 T_0} \quad (4.19)$$

$$Q_{freq} = \frac{1 + (\omega_{mech} \cdot \tau_{th})^2}{\omega_{mech} \cdot \tau_{th}} \quad (4.20)$$

$Q_{mat}$  depends only on the temperature and the material properties of the resonator, and is independent from the resonator geometry. It can be used to choose the best materials; materials with small  $E$  and  $\alpha$  and large  $\rho$  and  $C_{SP}$  are good candidates for high- $Q$  resonators.

$Q_{freq}$  is a function of  $\omega_{mech} \cdot \tau_{th}$  and has a minimum value of 2 at  $\omega_{mech} \cdot \tau_{th} = 1$ .  $Q_{freq}$  can be increased by increasing  $\omega_{mech} \cdot \tau_{th}$  when it is larger than 1 or by decreasing it when it is smaller than 1. When  $\omega_{mech} \cdot \tau_{th} \ll 1$ , the deformation time of the resonator is much larger than the thermal transport time (isothermal regime); thus, the resonator remains in thermal equilibrium and a very small amount of energy is dissipated through TED. When  $\omega_{mech} \cdot \tau_{th} \gg 1$ , the resonator deforms so fast that thermal relaxation cannot occur (adiabatic regime); therefore, a small amount of energy is dissipated due to TED.

Figure 4.34 shows the results of calculating  $Q_{TED}$  using (4.17) for fused silica beams with three different thicknesses. The temperature for this calculation is 293.15 K, and fused silica material properties are: Young's modulus  $E_{FS} = 70$  GPa, Poisson's ratio  $\nu_{FS} = 0.17$ , density  $\rho_{FS} = 2200$  kg/m<sup>3</sup>, thermal conductivity  $k_{FS} = 1.4$  W/(m·K), specific heat capacity  $C_{SPFS} = 730$  J/(kg·K), and coefficient of thermal expansion  $\alpha_{FS} = 5 \times 10^{-7}$  1/K. All three cases have a minimum  $Q_{TED}$  of



626,000 that is twice that of  $Q_{mat}$ . This minimum occurs at lower resonant frequencies for thicker beams because the thermal transport time constant increases with thickness.

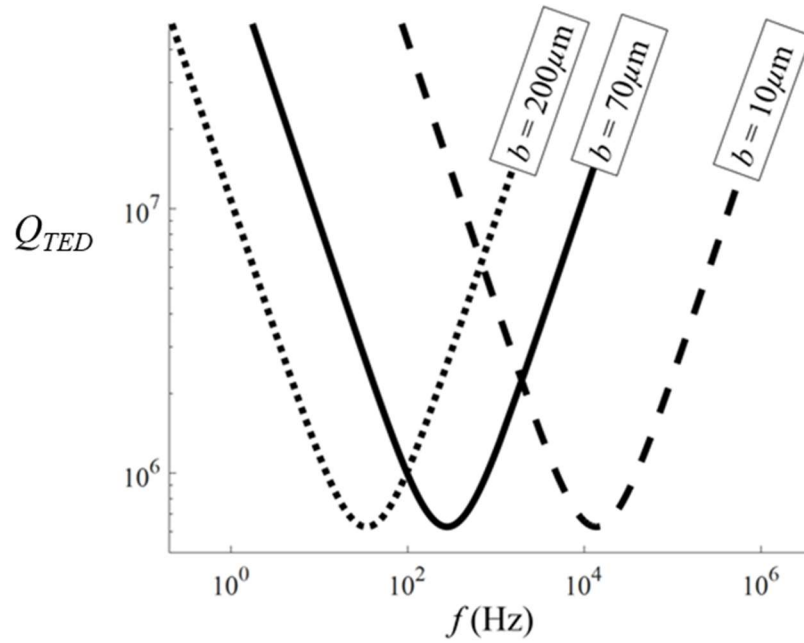


**Figure 4.34:**  $Q_{TED}$  versus resonant frequency of beam resonators with different thicknesses. All beams have a same minimum  $Q_{TED}$ . This minimum occurs in lower resonant frequencies for thicker beams.

#### 4.1.2.2 Numerical simulation of thermoelastic dissipation in birdbath shell structures

While (4.17) helps to understand and estimate  $Q_{TED}$  in beam-type resonators, it is not sufficient for more complicated structures. For a 3D structure, the  $Q$  can be estimated using (4.21) below:

$$Q_i = \frac{1}{2} \frac{|\operatorname{Re}(\omega_i)|}{|\operatorname{Im}(\omega_i)|} \quad (4.21)$$

where  $Q_i$  and  $\omega_i$  are  $Q$  and the eigenvalue (angular resonant frequency) of the  $i^{\text{th}}$  mode, respectively. Finding the eigenvalues of (4.13)–(4.16) for a birdbath structure analytically is not possible; therefore, a numerical based approach such as FEM should be used. COMSOL

Multiphysics is used to numerically solve the fully coupled thermo-mechanical FEM eigenvalue problem.

A shell with birdbath shape is considered for this investigation. For this subsection, the most important geometrical parameters of the shell are illustrated in Figure 4.35. They include the outer shell radius ( $R$ ), the top wall thickness ( $t_t$ ), the rim thickness ( $t_r$ ), the stem wall thickness ( $t_a$ ), the anchor radius ( $r$ ), and the shell height ( $h$ ). The nominal dimensions for a typical shell used throughout this section are  $R_o = 2500 \mu\text{m}$ ,  $t_{to} = 30 \mu\text{m}$ ,  $t_{ro} = 70 \mu\text{m}$ ,  $t_{ao} = 100 \mu\text{m}$ ,  $r_o = 400 \mu\text{m}$ , and  $h_o = 1900 \mu\text{m}$ .

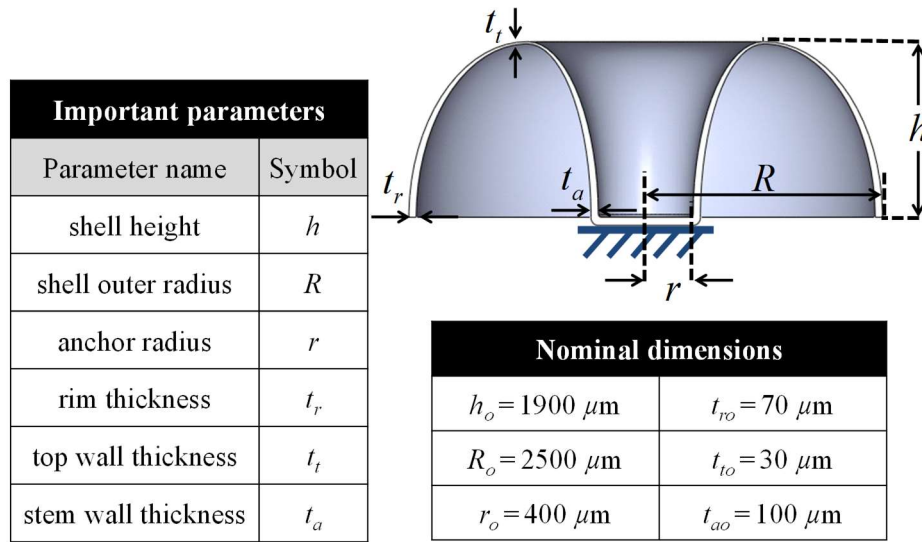


**Figure 4.35:** Cross sectional view of a micro-birdbath shell. Important geometrical parameters for this shell are designated as shown. Nominal dimensions are used as the reference geometry in this subsection.

The mesh configuration shown in Figure 4.36 is considered for numerical simulation. To produce this mesh, quadrilateral elements are created in the cross section of the shell in a 2D plane, and then the 2D mesh is revolved. Only when a shell has a chipped edge or its rim is trimmed, free tetrahedral elements are utilized for meshing. By using very small elements for meshing, both of

these mesh generation techniques result in the same value of  $Q_{TED}$ . In fact, our simulations show that the  $Q_{TED}$  simulation is not very sensitive to mesh quality for uncoated shells.

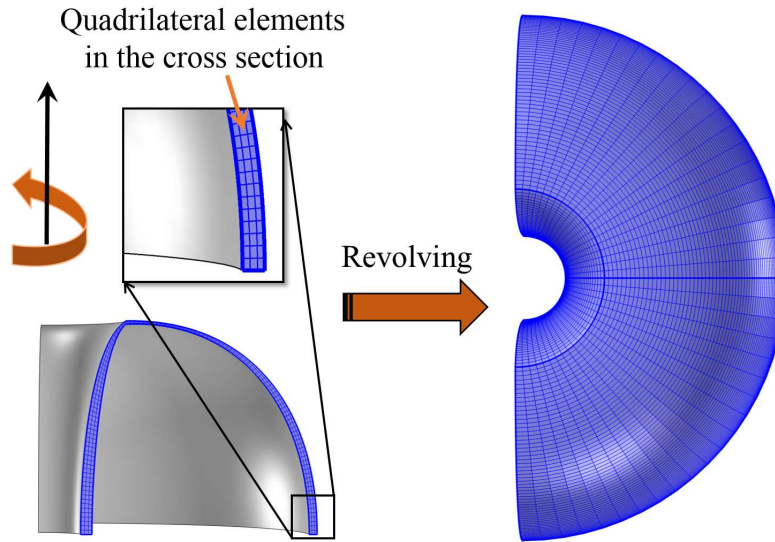


**Figure 4.36:** Mesh configuration of a birdbath shell structure. To produce this mesh, quadrilateral elements have been created in the cross section of the shell, and then these 2D elements are revolved.

In this subsection, the  $Q$  of micro-birdbath shell resonators is simulated under the assumption that TED is the only dominant dissipation mechanism. Fused silica is chosen as the reference material. By solving (4.13)–(4.16) numerically at  $T_0 = 293.15$  K for the mesh configuration shown in Figure 4.36, the eigenvector that includes deformations and temperature in each node, and the corresponding eigenvalue are calculated. The simulated temperature distribution and mode shape of a shell in an  $n = 2$  WG mode is shown in Figure 4.37 (a). The largest temperature gradients are found at the rim and the top part of the shell. These are the regions with a large stress concentration and a large shell curvature. Figure 4.37 (b) shows that heat can transfer between the hot and cold regions mainly in five different directions:

1. Across the rim.
2. Across the top wall.

3. In the polar direction between the rim and the top part.
4. In the azimuthal direction between the hot and cold regions in the rim.
5. In the azimuthal direction between the hot and cold regions in the top wall.

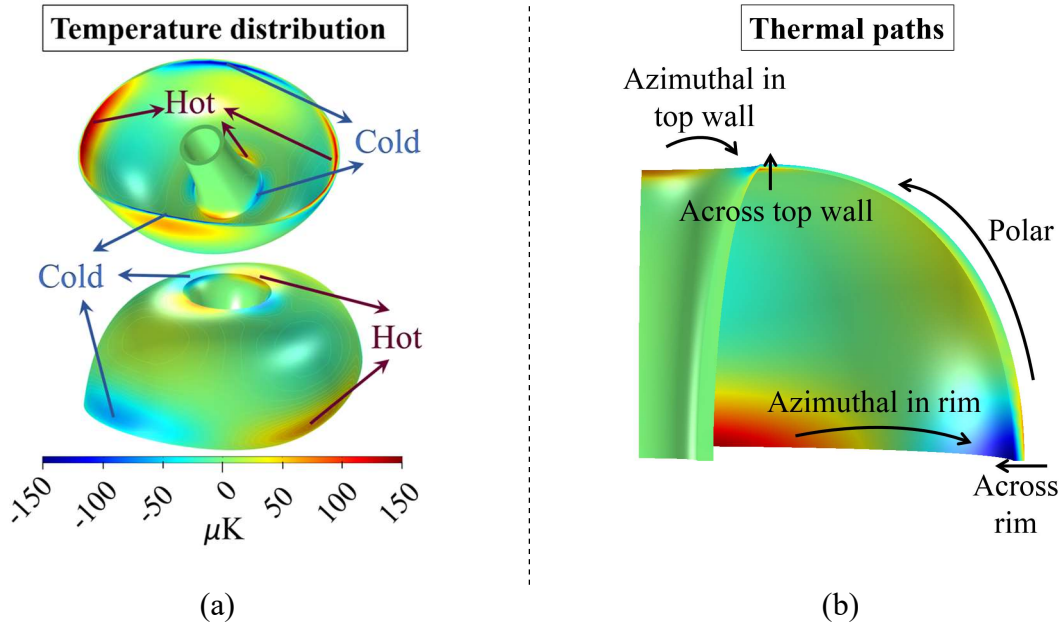


**Figure 4.37:** (a) Temperature distribution of a shell resonator in a WG mode. Large temperature gradients are found at the rim and top part of the shell. (b) Thermal paths in a shell when it is vibrating in a WG mode. These paths are across the rim, across the top of the shell, in the polar direction between the rim and top part, in the azimuthal direction between the hot and cold regions in the rim, and in the azimuthal direction between the hot and cold regions in the top part.

By using the results of the eigenvalue simulation and (4.21),  $Q_{TED}$  of the fused silica shell with nominal dimensions is found to be 75 million—this value is used as the reference value in order to normalize  $Q_{TED}$  in this subsection. This high value is promising for micro-scale resonators. We have not seen any higher value reported in the literature for MEMS resonators (the  $Q$ s of the majority of MEMS resonators are less than 1 million). The simulation results also show that the resonant frequencies are 14,670 Hz for the  $n = 2$  WG modes of the reference geometry. Using a beam approximation with a thickness of 70  $\mu\text{m}$ , Zener’s model suggests that the minimum  $Q_{TED}$

occurs when the resonant frequency of a fused silica resonator is around 279 Hz, which is much smaller than the resonant frequency of the simulated shell. Therefore, the shell experiences a quasi-adiabatic process and dissipates a low amount of energy through TED.

#### 4.1.2.3 Analytical model for thermoelastic dissipation in birdbath shell resonators

Although it is impossible to solve (4.13)–(4.16) analytically for a complicated structure, in this subsection we develop a formula to approximate  $Q_{TED}$  of resonators as they vibrate in the WG modes.

To model  $Q_{TED}$ , the shell is considered to consist of three different parts: (a) hollow central part referred to as the stem, (b) middle structure, and (c) rim. The elastic strain energy in each part is calculated when the shell is vibrating in a WG mode. As shown in Figure 4.38, the majority of the elastic energy is stored in the middle structure and rim.

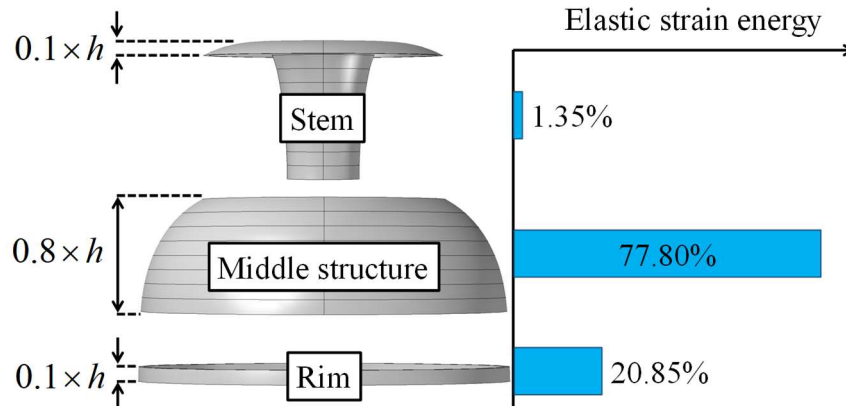


**Figure 4.38:** Amount of elastic strain energy in different parts of the shell. Strain energy in the stem is very small compared to the other parts.

The total dissipation in the system equals the sum of dissipations in the stem, middle structure, and rim. Because a low amount of energy is stored in the stem, the dissipation in this region is neglected. Therefore,

$$\frac{E_{tot}}{Q_{tot}} = \frac{E_m}{Q_m} + \frac{E_r}{Q_r} \quad (4.22)$$

where  $E_{tot}$ ,  $E_m$ ,  $E_r$  are elastic strain energies and  $Q_{tot}$ ,  $Q_m$ ,  $Q_r$  are  $Q$ s in the whole structure, middle structure, and rim, respectively. Since the thermal path in the polar direction in the middle structure is very long, the thermal transport time constant in this direction is also very long, hence there is not enough time for heat to transfer (adiabatic process). Therefore,  $Q_m$  is considered to be very large, and  $Q_{tot}$  can be estimated from (4.23):

$$Q_{tot} \approx \left( \frac{E_{tot}}{E_r} \right) \cdot Q_r \quad (4.23)$$

So,  $Q_{tot}$  simplifies to  $Q_r$  times a constant.

To find  $Q_r$ , we consider the rim as a ring resonator. Since there are two thermal paths in a ring resonator, across the ring and the azimuthal directions along the ring,  $Q_r$  can be found from (4.24):

$$\frac{1}{Q_r} = \frac{1}{Q_{across-r}} + \frac{1}{Q_{azimuthal-r}} \quad (4.24)$$

where  $Q_{across-r}$  and  $Q_{azimuthal-r}$  are  $Q$ s in the across and azimuthal directions, respectively. For more information about calculating  $Q_{TED}$  when there are two thermal paths in beam resonators, we refer to [74]. Equation (4.17) can be used to calculate  $Q_{across-r}$  and  $Q_{azimuthal-r}$ . Therefore, (4.17) and (4.24) lead to:

$$\frac{1}{Q_r} = \frac{1}{Q_{mat}} \cdot \left( \left( \frac{\omega_{mech} \cdot \tau_{across-r}}{1 + (\omega_{mech} \cdot \tau_{across-r})^2} \right) + \left( \frac{\omega_{mech} \cdot \tau_{azimuthal-r}}{1 + (\omega_{mech} \cdot \tau_{azimuthal-r})^2} \right) \right) \quad (4.25)$$

and  $\tau_{across-r}$  and  $\tau_{azimuthal-r}$  can be found from (4.26) and (4.27):

$$\tau_{across-r} = \frac{t_{ring}^2}{\pi^2 D} \quad (4.26)$$

$$\tau_{azimuthal-r} = \frac{R_{ring}^2}{4D} \quad (4.27)$$

where  $t_{ring}$  and  $R_{ring}$  are the ring thickness and radius, respectively.

To confirm the accuracy of (4.25), the  $Q_{TED}$  of a ring resonator made from single-crystal silicon with a  $47 \mu\text{m}$  thickness and  $1,350 \mu\text{m}$  radius is calculated both analytically and numerically (using the aforementioned FEM). These theoretical results are compared with experimental results [6]. The analytical model and FEM simulation predict  $Q_{TED}$  of 11,660 and 10,300, respectively. Our theoretical approximations for fluidic damping, surface loss, internal dissipation, phonon interactions, and anchor loss predict a  $Q$  higher than 1,000,000 for a single-crystal silicon ring resonator with aforementioned dimensions. Therefore, it can be assumed that TED is the main source of dissipation in this resonator. The experimental value of  $Q$  for this same exact structure was measured to be 12,000, showing excellent agreement with, and validating, analytical and FEM results.

By using (4.23) and (4.25), the  $Q_{TED}$  of micro-birdbath shell resonators can be approximated from (4.28):

$$Q_{tot} \approx \left( \frac{E_{tot}}{E_r} \right) \cdot \frac{\rho C_{SP}}{E \alpha^2 T_0} \cdot \left( \frac{\omega_{mech} \cdot \left( \frac{t_r^2}{\pi^2 D} \right)}{1 + \left( \omega_{mech} \cdot \left( \frac{t_r^2}{\pi^2 D} \right) \right)^2} + \frac{\omega_{mech} \cdot \left( \frac{R^2}{4D} \right)}{1 + \left( \omega_{mech} \cdot \left( \frac{R^2}{4D} \right) \right)^2} \right)^{-1} \quad (4.28)$$

Equation (4.28) for a fused silica shell with the dimensions shown in Figure 4.35 predicts a  $Q_{TED}$  of 79 million, which is very close to the numerical simulation value of 75 million. This approach can be used to approximate  $Q_{TED}$  in other types of WG shell resonators as well.

#### 4.1.2.4 Impact of various parameters on TED of birdbath shell resonators

In the following subsections, the effect of the parameters listed in Figure 4.39 on the  $Q_{TED}$  of BSRs are discussed with the following order:

- a) Shell material
- b) Shell geometry
- c) Rim chipping and trimming
- d) Operating temperature
- e) Metal coating

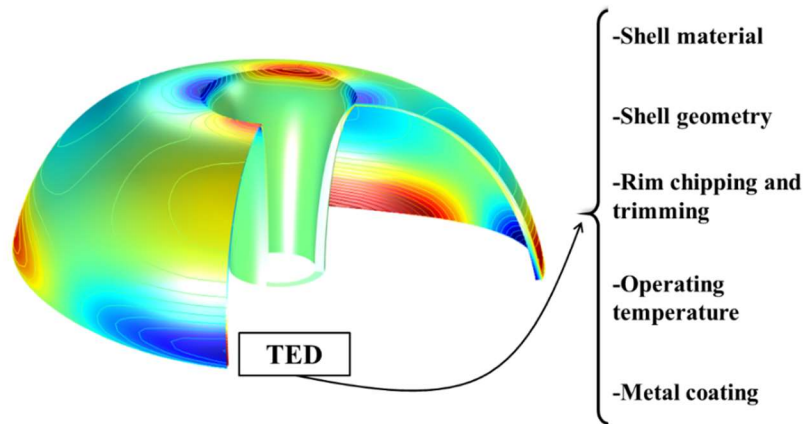


**Figure 4.39:** Important parameters in TED of shell resonators. TED depends on material properties, geometry, rim conditions, operating temperature, and metal coating.



### a) Effect of Shell Material on TED

As shown in (4.13)–(4.16), the thermo-mechanical behavior of resonators depends on their material's  $E$ ,  $C_{SP}$ ,  $\rho$ ,  $\nu$ ,  $\alpha$ , and  $k$ . In order to compare the effect of different material properties, we consider the effect of varying each one while the others remain fixed at their intrinsic values for fused silica. Figure 4.40 shows the change in the normalized  $Q_{TED}$ , defined as  $Q/(7.5 \times 10^7)$ , versus change in normalized material properties.

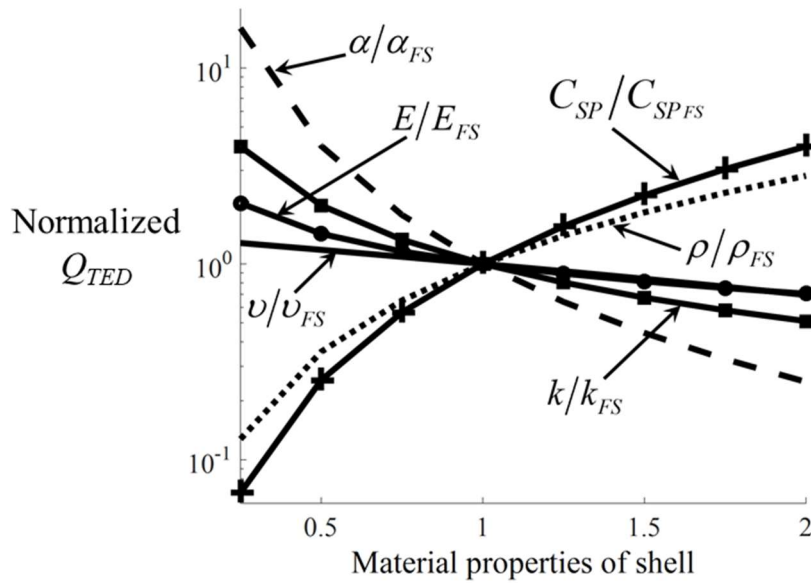


**Figure 4.40:** Effect of shell's material properties on its  $Q_{TED}$ . Increasing  $\alpha$ ,  $k$ ,  $E$ , or  $\nu$  decreases  $Q_{TED}$ , while increasing  $C_{SP}$  or  $\rho$  increases  $Q_{TED}$  of a shell that operates in the quasi-adiabatic regime.

The results show that  $Q_{TED}$  of BSRs strongly depends on the material properties of the structure. As shown,  $Q_{TED}$  decreases significantly as  $\alpha$  increases. While increasing  $\alpha$  results in a greater effect of the mechanical domain on the thermal domain according to (4.16), it also results in a greater effect of the thermal domain on the mechanical domain according to (4.13)–(4.15). Therefore,  $\alpha$  is the parameter that couples the thermal and mechanical domains. Thus, to achieve a very high  $Q_{TED}$  in resonators, it is essential to use a material with a low  $\alpha$ . Figure 4.40 shows that

reducing  $k$  enhances  $Q_{TED}$ . This is because the reduction in  $k$  results in decreased thermal diffusivity and therefore a longer thermal transport time constant, thereby reducing irreversible heat transfer and increasing  $Q_{TED}$ . It should be noted that this resonator works in the quasi-adiabatic regime as opposed to the quasi-isothermal regime where increasing the thermal transport time constant would reduce  $Q_{TED}$ . In (4.13)–(4.16), all the terms that have  $\alpha$  as a coefficient also include  $E$ , so increasing  $E$  will amplify the coupling between the mechanical and thermal domains and must lead to a lower  $Q_{TED}$ . The simulation results shown in Figure 4.40 confirm this hypothesis; however,  $E$  and  $\alpha$  do not have the exact same effect. In fact, increasing  $E$  increases the resonator's resonant frequency, while the thermal transport time constant is invariant. Indeed, increasing  $E$  does increase the effect of  $\alpha$ , which should lead to a lower  $Q_{TED}$ , but also causes the resonator to operate in a more adiabatic regime, which should lead to a higher  $Q_{TED}$ . The combination of these two effects results in a net decrease in  $Q_{TED}$ , with  $\alpha$  having a stronger influence than  $E$ . By increasing  $\rho$  and  $C_{SP}$ , the heat capacity of the material  $C = \rho C_{SP}$  increases, which helps to reduce irreversible heat transfer and thereby improves  $Q_{TED}$ , as shown in Figure 4.40. However, since increasing  $\rho$  reduces the resonant frequency and causes the resonator to operate in a less adiabatic regime,  $C_{SP}$  has a greater influence than  $\rho$ . Looking at (4.13)–(4.16), the thermo-mechanical behavior of a material depends on its  $\nu$ , and this dependency is very complicated. A change in  $\nu$  alters the resonant frequency as well as the coupling between the thermal and mechanical domains. Based on the simulation results, increasing  $\nu$  decreases  $Q_{TED}$  slightly.

Eleven different materials (whose material properties are extracted from [64], [86], and [87]) are considered for the shell structure and their  $Q_{TED}$  values are calculated numerically; the results are summarized in Table 4.2.

TABLE 4.2:  $Q_{TED}$  OF BSRs WITH DIFFERENT MATERIALS

Material	$E$ (GPa)	$\nu$	$\rho$ (kg/m <sup>3</sup> )	$k$ (W/(m·K))	$\alpha$ (10 <sup>-6</sup> ×1/K)	$C_{SP}$ (J/(kg·K))	$Q_{TED}$ (FEM)	$Q_{TED}$ (Analytical model)
SiO <sub>2</sub>	70	0.17	2200	1.4	0.5	730	7.5×10 <sup>7</sup>	7.9×10 <sup>7</sup>
Zerodur	90.3	0.24	2530	1.46	0.02	820	4.6×10 <sup>10</sup>	5.9×10 <sup>10</sup>
Al <sub>2</sub> O <sub>3</sub>	400	0.22	3965	35	6.5	730	1.7×10 <sup>4</sup>	1.8×10 <sup>4</sup>
SiC(6H)	748	0.45	3216	490	4.3	690	8.2×10 <sup>3</sup>	6.5×10 <sup>3</sup>
Si <sub>3</sub> N <sub>4</sub>	250	0.23	3100	20	2.3	700	1.8×10 <sup>5</sup>	2.0×10 <sup>5</sup>
Borosilicate	63	0.2	2230	1.13	3.3	754	2.0×10 <sup>6</sup>	2.5×10 <sup>6</sup>
GaAs	85.9	0.31	5316	33	5.7	550	5.2×10 <sup>4</sup>	5.2×10 <sup>4</sup>
Ge	103	0.26	5323	58	5.9	310	2.1×10 <sup>4</sup>	1.5×10 <sup>4</sup>
InSb	409	0.35	5770	18	5.4	200	5.7×10 <sup>3</sup>	6.8×10 <sup>3</sup>
C[100]	1050	0.1	3515	990	0.8	520	3.3×10 <sup>5</sup>	1.8×10 <sup>5</sup>
Si(c)	170	0.28	2329	130	2.6	700	6.7×10 <sup>4</sup>	4.7×10 <sup>4</sup>

According to these results, Zerodur (Class 0) and fused silica are the best choices for the shell material due to their low  $\alpha$ . After them, borosilicate glass shows the highest value for  $Q_{TED}$ ; however, the  $Q_{TED}$  of a shell made from borosilicate glass is 37.5 times smaller than that of a shell made from fused silica. It should be taken into account that TED is just one of the important parameters for choosing shell material—compatibility with the fabrication process and other intrinsic dissipation mechanisms are also important factors. This table also shows the  $Q_{TED}$  calculated from (4.28) for shells with different materials. The results are very similar to the results calculated with FEM, thus validating the analytical model.

### b) Effect of Shell Geometry on TED

The effect of changes in the geometry of the shell structure on its  $Q_{TED}$  is shown in Figure 4.41. The most important geometrical properties are the shell height, shell radius, anchor radius, rim thickness, top wall thickness, and stem wall thickness.

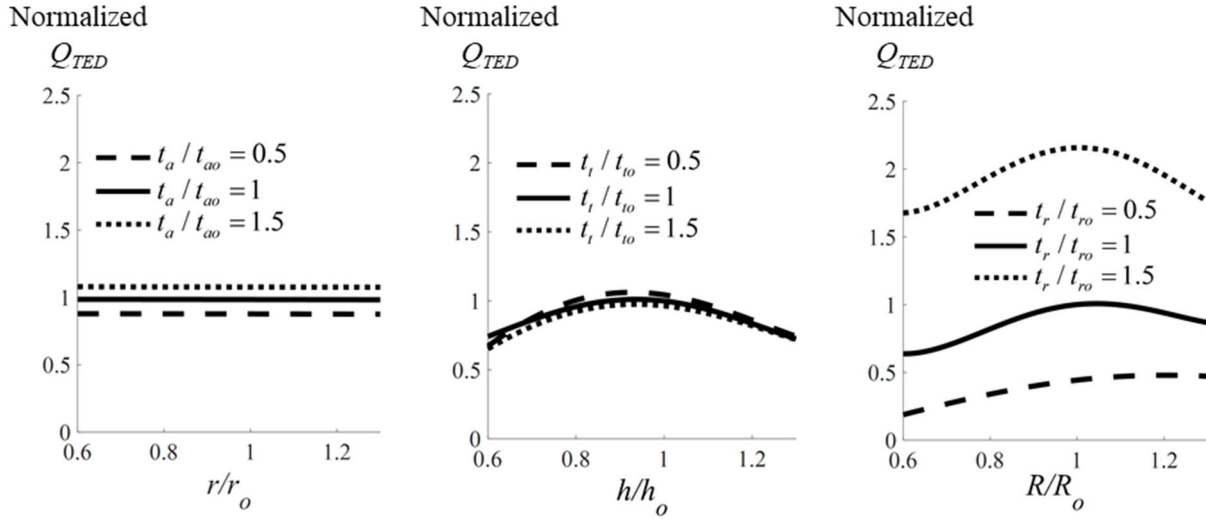


**Figure 4.41:** Effect of geometrical parameters on  $Q_{TED}$ . Simulation results show that by increasing the rim thickness,  $Q_{TED}$  increases. The results also reveal that other geometrical parameters do not have a significant effect on  $Q_{TED}$ .

Increasing the rim thickness increases  $Q_{TED}$ . Since the shell resonates in a quasi-adiabatic regime, its  $Q_{TED}$  increases if either its resonant frequency or its thermal transport time constant increases. Increasing the rim thickness increases the distance and thermal resistance between the hot and cold regions across the rim, thus the thermal transport time constant increases. Furthermore, our simulation shows that the resonant frequency increases significantly as the rim becomes thicker. Both of these effects increase  $Q_{TED}$ . Therefore, to achieve a high- $Q$  shell, its rim thickness should be increased (however, it should be taken into account that if a shell resonator operates in a quasi-isothermal regime, increasing the rim thickness might decrease  $Q_{TED}$ ).

The results shown in Figure 4.41 indicate that other geometrical parameters do not have a significant effect on  $Q_{TED}$ . Changing the shell radius or height only moderately affects  $Q_{TED}$ , but there is no clear trend; increasing the shell radius or height initially increases  $Q_{TED}$ , but then begins to reduce it. Our simulation results show that increasing the shell radius reduces the resonant frequency and since this resonator operates in a quasi-adiabatic regime, this should reduce  $Q_{TED}$ .

However, as the shell radius increases, the thermal path between the hot and cold regions in the azimuthal direction around the rim increases—this should increase the thermal transport time constant and therefore the  $Q_{TED}$ . The same thing happens when the shell height increases—the resonant frequency decreases and the thermal path along the polar direction between the rim and the top part of the shell increases. When the shell radius or height is small, heat transfer from the rim in the azimuthal or polar directions are important and increasing these parameters improves  $Q_{TED}$ . This effect diminishes as the radius or height become very large, and thus only the reduction in the resonant frequency plays a role in  $Q_{TED}$ . Increasing the stem wall thickness moderately improves  $Q_{TED}$  due to the resulting increase in resonant frequency. Additionally, anchor radius and top wall thickness have either a very small or negligible impact on  $Q_{TED}$ . They do not affect the critical thermal path along the rim, and even a 100% change in these parameters only shifts the resonant frequency by less than 1%.

### ***c) Effect of Rim Chipping and Trimming on TED***

As discussed before, the shell rim is responsible for the majority of TED. Therefore, its properties can have a significant effect on  $Q_{TED}$ . In this subsection, first the effect of imperfections in the rim on  $Q_{TED}$  is investigated, then several trimming approaches in the rim are discussed.

In the case of the blowtorch microfabrication process, the shell is released from its fused silica host substrate using lapping and CMP. These steps may create small chipped areas around the rim. Figure 4.42 (a) shows a SEM image of the rim of one shell. To investigate the effect of these imperfections on  $Q_{TED}$ , shells with different numbers of chips around the rim edges are modeled. Figure 4.42 (b) shows the structure of one of the modeled shells. The chips are considered

to be triangular prisms where the length of the base triangle's sides and the prism height are  $10 \mu\text{m}$ .

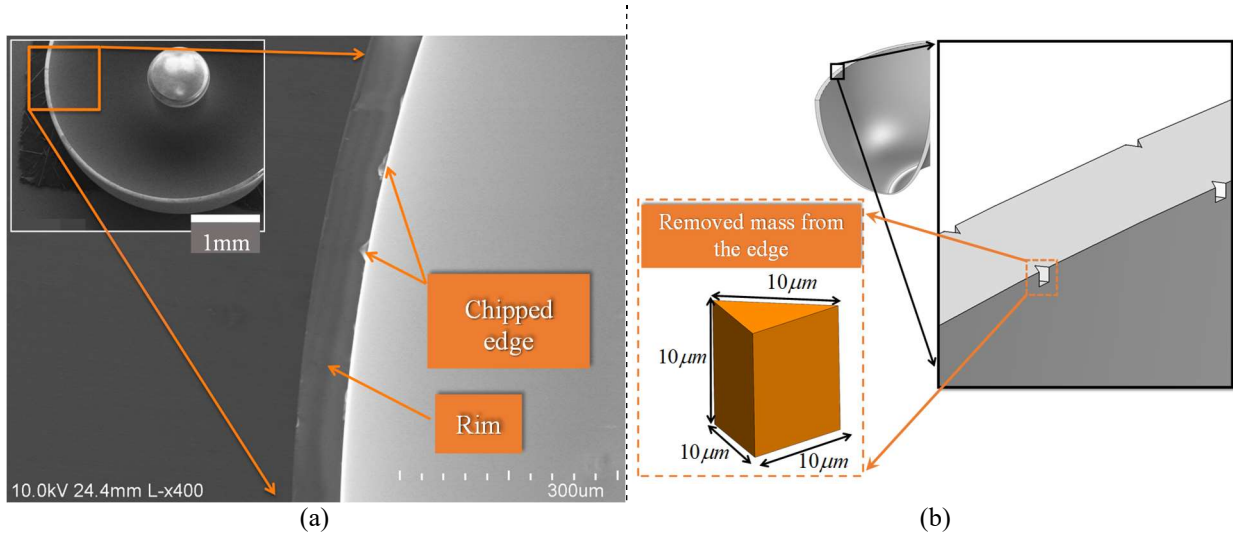


**Figure 4.42:** (a) SEM image of the birdbath resonator rim. As shown in this figure, polishing may cause some chips around the rim edges. (b) A model for a chipped rim. In this model, the chips are considered to be triangular prisms. The length of base triangle's sides and the prism height are assumed to be  $10 \mu\text{m}$ .

Table 4.3 summarizes our simulations results, which indicate that chips around the rim only slightly reduce  $Q_{TED}$ . This reduction is due to stress concentrations around the chipped areas that cause larger heat generation in those areas, resulting in higher TED. However, since these imperfections affect very small areas, the change in  $Q_{TED}$  is very small, such that 200 chips decrease  $Q_{TED}$  by only 0.74%. Still, these chips might have a larger effect on the overall  $Q$ , as they imbalance the shell and could increase wave propagation through the anchor.

**TABLE 4.3:** NORMALIZED  $Q_{TED}$  OF CHIPPED EDGE SHELLS

Number of chips	Normalized $Q_{TED}$
40	0.9983
80	0.9972
120	0.9950
160	0.9939
200	0.9926

As discussed in [76] and [78],  $Q_{TED}$  can be improved by strategically removing some part of a beam resonator. In the next few paragraphs, three trimming approaches for improving the  $Q_{TED}$  of BSRs are discussed.

The first trimming approach involves rounding the edges of the shell outer rim to reduce the stress around the rim edges, as shown in Figure 4.43. FEM results show that rounding the rim edges improves  $Q_{TED}$  by only about 0.45%. The improvement is not significant because only a small region of the shell is affected by this trimming.

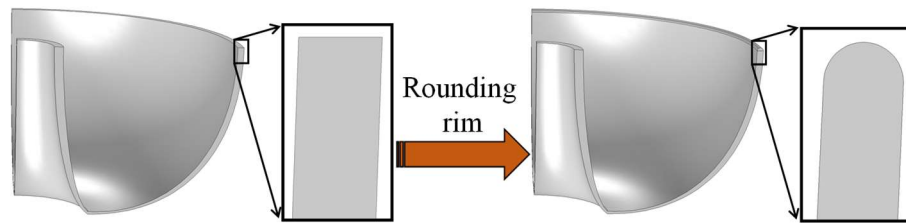


**Figure 4.43:** Schematic view of a shell with rounded rim edges.

The second trimming approach involves cutting out some areas from the rim, which might be useful for elimination of heat transfer in the azimuthal direction. This kind of mass removal from the rim was already utilized in [5] to balance imperfect shells.

The  $Q_{TED}$  of shells with rectangles of various dimensions periodically cut out around their rims, where the rectangles are defined as if projected outward from the center, is calculated. Figure 4.44 (a) shows the resulting structure and relevant dimensions. The cutouts have a height of 200  $\mu\text{m}$  and arc lengths calculated from the central angle  $\theta$ . The simulation results are shown in Figure 4.45. These results show that this type of trimming actually causes a drop in the  $Q_{TED}$ , such that the creation of sixteen rectangular cutouts around the rim with arc lengths corresponding to  $\theta = 1^\circ$  decreases the  $Q_{TED}$  by about 33%.

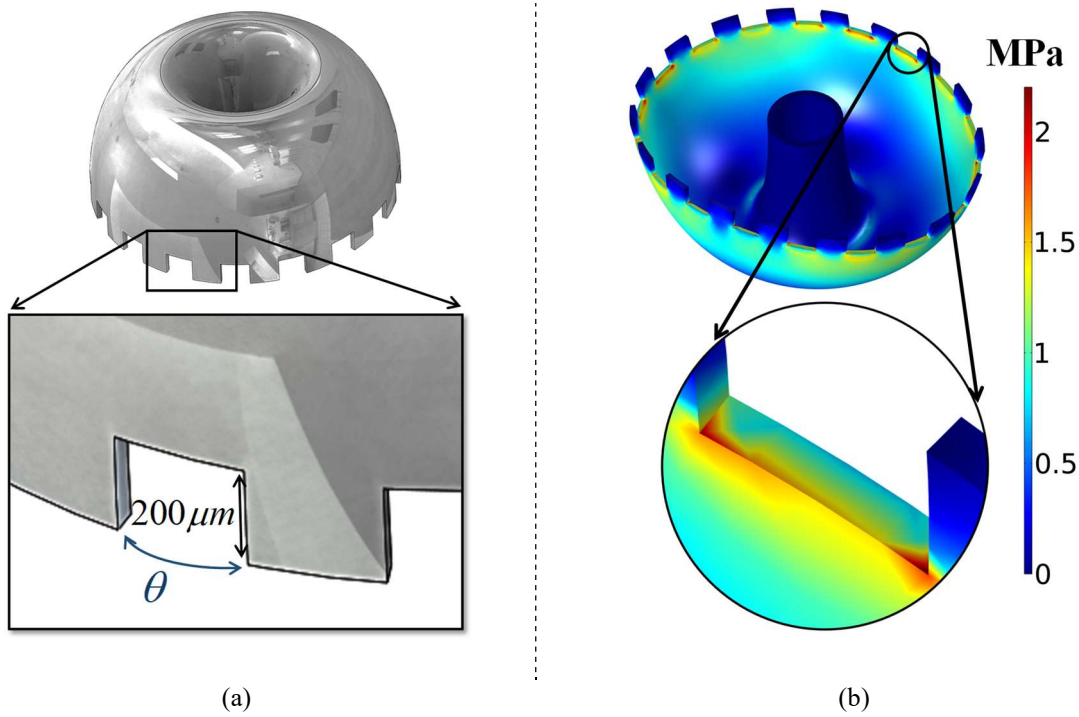


**Figure 4.44:** (a) Schematic view of a shell with cutouts from its rim. This method was used to rebalance imperfect shell resonators in [5]. Here, it is considered that the removed masses have a height of  $200 \mu\text{m}$  and arc length calculated from the central angle  $\theta$ . (b) von Mises stress in a shell with rectangular cutouts from its rim. It is found that cutting out some areas from the rim creates concentration of stress at the trimmed corners, which reduces  $Q_{TED}$ .

In order to understand these results, the von Mises stresses in the trimmed shell are calculated numerically. It is found that cutting out some areas from the rim creates stress concentrations at the trimmed corners as shown in Figure 4.44 (b). This overcomes the gains from preventing azimuthal heat transfer along the rim, thus reducing the overall  $Q_{TED}$ .

Figure 4.45 also shows that if there are four cutouts, the first and second  $n = 2$  WG modes have different values of  $Q_{TED}$ . This is because the cutouts are located at the antinodes of the second WG mode, but at the nodes of the first mode. Therefore, the deformations and resulting stress concentrations at the cutouts are much greater for the second mode. However, if the number of cutouts is 8, 12, or 16, the change in  $Q_{TED}$  is almost the same for both modes because the locations



of the cutouts relative to the nodes and antinodes of the first and second WG modes are almost the same.

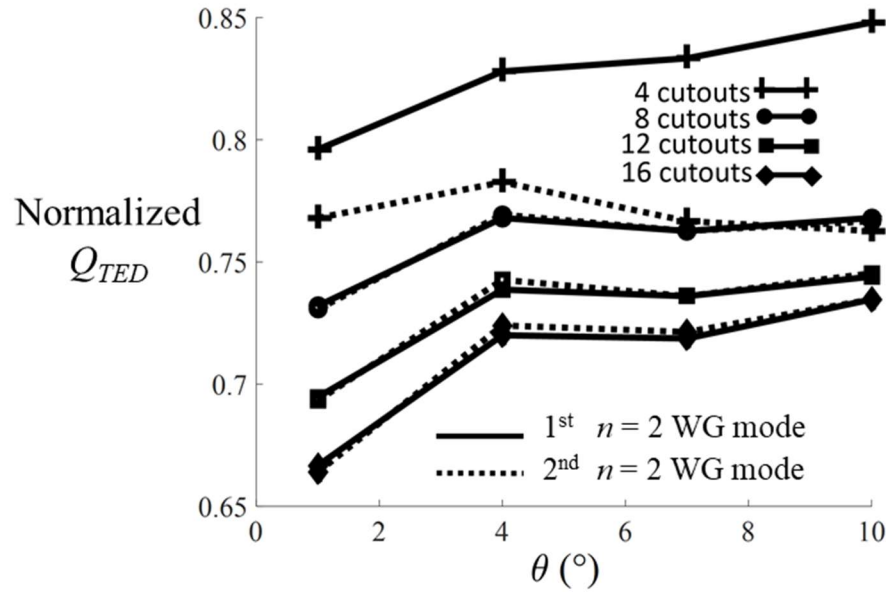


**Figure 4.45:** Normalized  $Q_{TED}$  as a function of arc length for different number of rectangular cutouts around the rim. In this figure,  $Q_{FS}$  is  $Q_{TED}$  of a shell without any rectangular cutouts. As the number of cutouts increases,  $Q_{TED}$  decreases.

The results also show that  $Q_{TED}$  decreases as the number of cutouts increases due to the greater number of regions with elevated stress concentrations and therefore greater heat generation and dissipation.

Additionally, Figure 4.45 shows that shells with cutouts with arc lengths corresponding to  $\theta = 1^\circ$  have the lowest  $Q_{TED}$ . Our investigation of stress generation in shells shows that when  $\theta$  is  $1^\circ$ , stress is more than twice of the stress when  $\theta$  is  $4^\circ$ ,  $7^\circ$ , or  $10^\circ$ . Therefore, cutouts with a narrow opening should be avoided.

The third trimming approach involves creating a lengthwise groove along the rim to reduce heat transfer across the rim thickness, which is the main source of TED in WG resonators, as

shown in Figure 4.46 (a). The width and height of the groove are  $a_d$  and  $h_d$ , respectively. Figure 4.46 (b) clearly shows that grooving the rim changes the heat transfer pattern across the rim, which can change  $Q_{TED}$ .

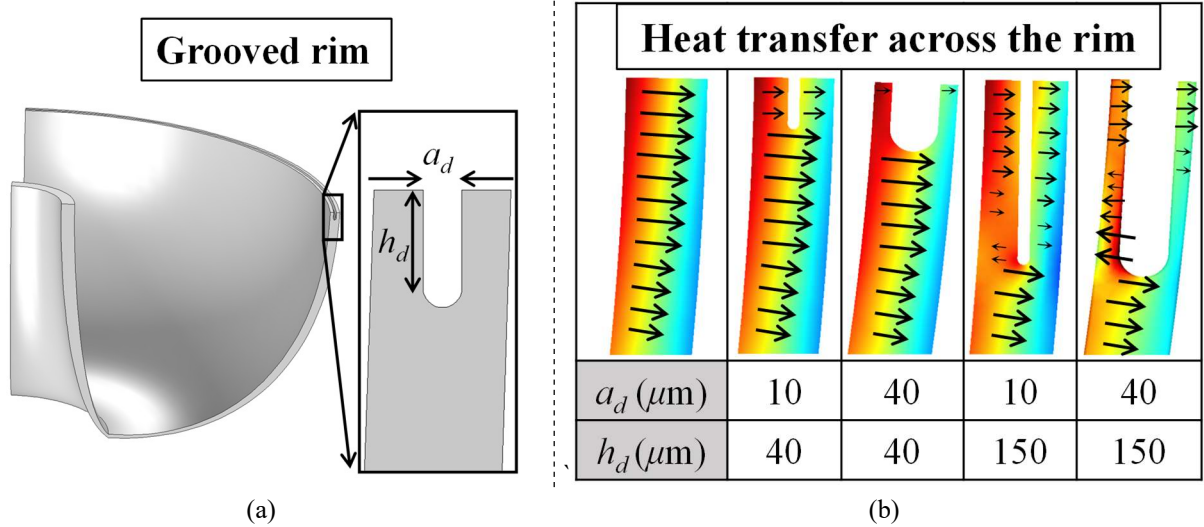


**Figure 4.46:** (a) Schematic view of a grooved rim. (b) Heat transfer across the rim with different groove dimensions.

The effect of grooving on  $Q_{TED}$  is shown in Figure 4.47. This figure shows that if the dimensions of the groove are chosen appropriately,  $Q_{TED}$  can be improved due to a reduction in heat transfer across the rim. When the groove is not very deep, increasing the groove width improves  $Q_{TED}$  because it reduces the amount of heat transfer across the grooved section (Figure 4.46 (b):  $a_d = 40 \mu\text{m}$  and  $h_d = 40 \mu\text{m}$ ). When the groove is very deep, increasing its width causes the remaining part of the rim to become very flexible and to deflect around a hinging point. This deflection creates a large thermal gradient, so a large amount of energy is dissipated through heat transfer around the hinge (Figure 4.46 (b):  $a_d = 40 \mu\text{m}$  and  $h_d = 150 \mu\text{m}$ ). Therefore, the groove geometry should be designed to leave rigid sidewall.

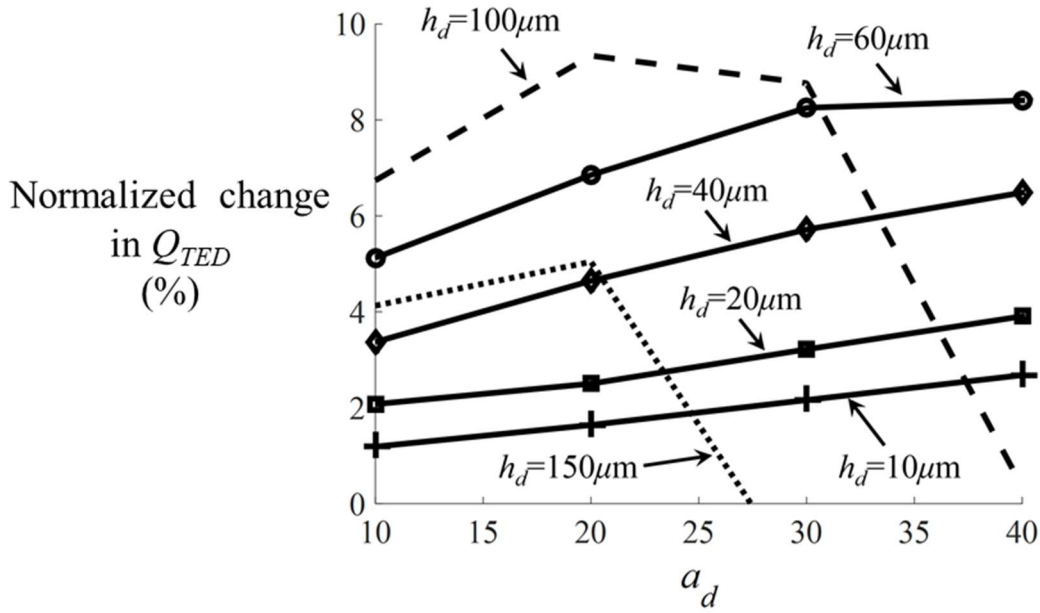


**Figure 4.47:** Effect of dimension of a groove in the rim on  $Q_{TED}$ .

#### **d) Effect of Operating Temperature on TED**

Equation (4.17) shows that the term that couples the mechanical deformation to the thermal domain is a function of temperature such that the coupling increases as temperature increases. The material properties of the shell are also a function of temperature. Therefore, any change in temperature might change  $Q_{TED}$ . To investigate these effects, the operating temperature of the resonator is changed and  $Q_{TED}$  is calculated for two different cases. In the first case, the material properties of fused silica are kept constant while the operating temperature is changed. Figure 4.48 (dashed line) shows that as the temperature increases,  $Q_{TED}$  decreases by about  $0.34 \text{ } \%/^{\circ}\text{C}$  even if the material properties of fused silica remain constant. In the second case, the effect of change in the material properties is also taken into account. For this simulation, it is considered that fused silica material properties change linearly with temperature. The changes in  $E_{FS}$ ,  $\rho_{FS}$ ,  $\nu_{FS}$ ,  $\alpha_{FS}$ ,  $C_{SPFS}$ , and  $k_{FS}$  are calculated from [88] and [89] to be  $141.4 \text{ ppm}/^{\circ}\text{C}$ ,  $0 \text{ ppm}/^{\circ}\text{C}$ ,  $588.1 \text{ ppm}/^{\circ}\text{C}$ ,  $8.8 \times 10^3$

ppm/°C,  $2.13 \times 10^3$  ppm/°C, and  $1.57 \times 10^3$  ppm/°C, respectively. As shown in Figure 4.48 (solid line), as temperature increases,  $Q_{TED}$  decreases by 2.07 %/°C. This huge change in  $Q_{TED}$  is mostly due to the strong dependence of  $\alpha_{FS}$  on temperature.

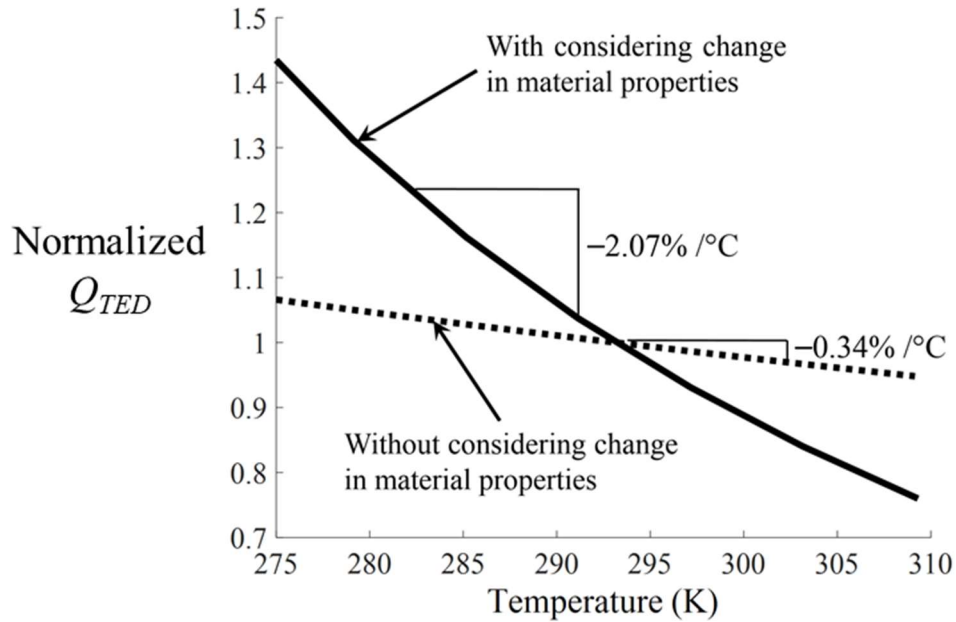


**Figure 4.48:** Normalized  $Q_{TED}$  versus temperature. By increasing the temperature, coupling between the thermal and mechanical domains, also  $\alpha_{FS}$  increases; therefore,  $Q_{TED}$  decreases.

### e) Effect of Thin Conductive Coatings on TED

Fused silica, Zerodur, and borosilicate are good candidates for high- $Q_{TED}$  resonators but they have very low electrical conductivities. To electrostatically actuate a resonator made from one of these materials, it is necessary to coat it with a conductive metal layer. Unfortunately, most metals have a large  $\alpha$ , which increases TED. The effects of a thin metal coating on TED is presented in this part.

Mesh quality is extremely important in simulating the  $Q_{TED}$  of resonators with a thin coating. Since the coating is much thinner than the resonator, there is a need for a huge number of

mesh elements. To reduce the complexity of numerical calculations, a combination of the analytical model developed previously and the numerical simulation for a coated ring having the same rim thickness and resonant frequency as the BSR is used. Gold (Au), with Young's modulus  $E_{Au} = 70$  GPa, Poisson's ratio  $\nu_{Au} = 0.44$ , density  $\rho_{Au} = 19300$  kg/m<sup>3</sup>, thermal conductivity  $k_{Au} = 317$  W/(m.K), specific heat capacity  $C_{SPAU} = 129$  J/(kg.K), and coefficient of thermal expansion  $\alpha_{Au} = 14.2 \times 10^{-6}$  1/K [66] is used as the coating layer. We change the number of mesh elements in the azimuthal and thickness directions in the coating layer and simulate  $Q_{TED}$ . Our results show that it is extremely important to use enough mesh elements in the coating layer, especially in the azimuthal direction. Therefore, to eliminate numerical errors, the results presented below are for a mesh configuration with 15,000 mesh elements in the azimuthal and 15 mesh elements in the thickness directions.

Figure 4.49 shows the effect of coating thickness ( $t_{Au}$ ) on  $Q_{TED}$ . As shown, a gold layer with a thickness equal to 1% of the rim reduces  $Q_{TED}$  more than 100 times compared to an uncoated resonator. A metal layer on the surface increases energy dissipation due to its high TED, which increases heat and entropy generation in the coating. As the thickness of the coating increases, the amount of entropy generation also increases; therefore,  $Q_{TED}$  decreases. Thus, to achieve a high- $Q$  resonator, the coating layer should be as thin as possible.

The effect of the coating material properties on TED is shown in Figure 4.50. In this figure the normalized  $Q_{TED}$  for coated resonators,  $Q/Q_{Au}$ , is shown as different material properties are changed.  $Q_{Au}$  is the  $Q_{TED}$  of a resonator coated with gold, where the thickness of gold is 0.1% of the rim thickness. Figure 4.50 reveals that in order to improve  $Q_{TED}$ , the coating material should have a very low  $E$ ,  $\alpha$ , and  $\nu$ . However,  $k$ ,  $\rho$ , and  $C_{SP}$  are not critical parameters. The low dependency of  $Q_{TED}$  on the  $k$  of the coating material shows that  $Q_{TED}$  decreases in the coated resonators because

of heat generation inside the coating, not because of a reduction of thermal resistivity between the hot and cold regions of the resonator. According to Figure 4.50,  $E$  and  $\alpha$  have the same impact on  $Q_{TED}$ . Equations (4.13)–(4.16) shows that the coupling terms between the thermal and mechanical domains have a direct relation to  $E \cdot \alpha$ , so increasing  $E \cdot \alpha$  should reduce  $Q_{TED}$ . However, in the case of an uncoated resonator, changing  $E$  of the resonator changes the resonant frequency, hence  $E$  and  $\alpha$  of the resonator do not have the same impact on  $Q_{TED}$ . In the case of a coated resonator, the  $E$  of the coating does not have any significant impact on resonant frequency; therefore, it is expected to have the same effect on  $Q_{TED}$  as  $\alpha$ .

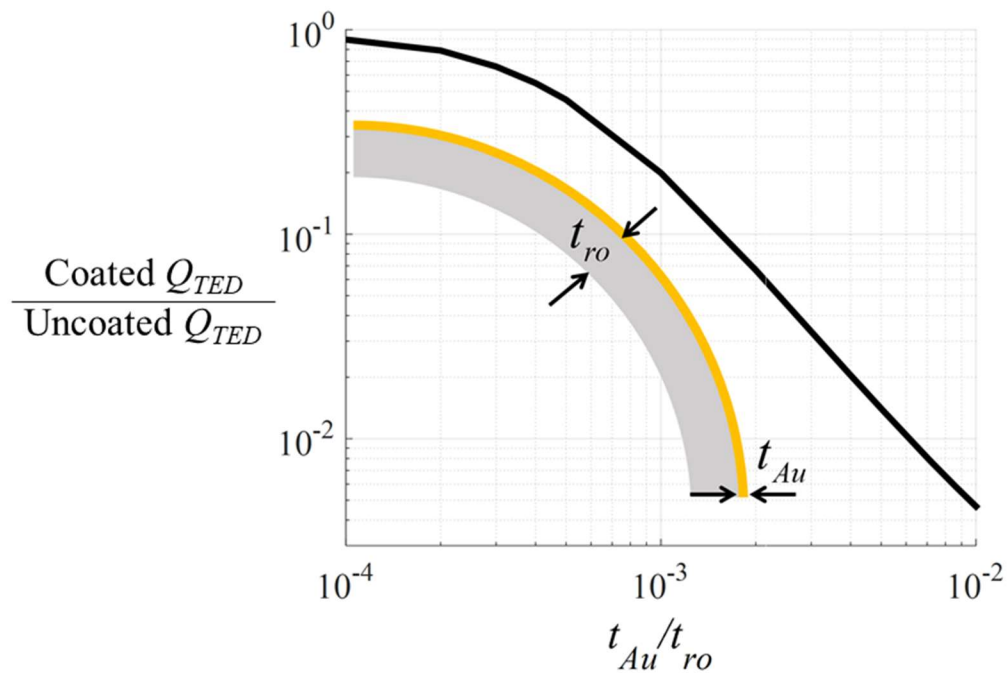


**Figure 4.49:**  $Q_{TED}$  versus thickness of metal coating, normalized to an uncoated resonator. Metal coating has a huge effect on  $Q_{TED}$ . However, as coating thickness becomes very small, the  $Q_{TED}$  of a coated resonator approaches that of an uncoated resonator.

To compare common conductive materials that are candidates for coating resonators, different metals are considered and  $Q_{TED}$  is simulated. The results show that indium (In), chromium

(Cr), lead (Pb), titanium (Ti), and antimony (Sb) could improve  $Q_{TED}$  compared to gold; while, aluminum (Al), copper (Cu), silver (Ag), and nickel (Ni) would decrease  $Q_{TED}$ . Platinum (Pt) shows almost the same  $Q_{TED}$  as gold.

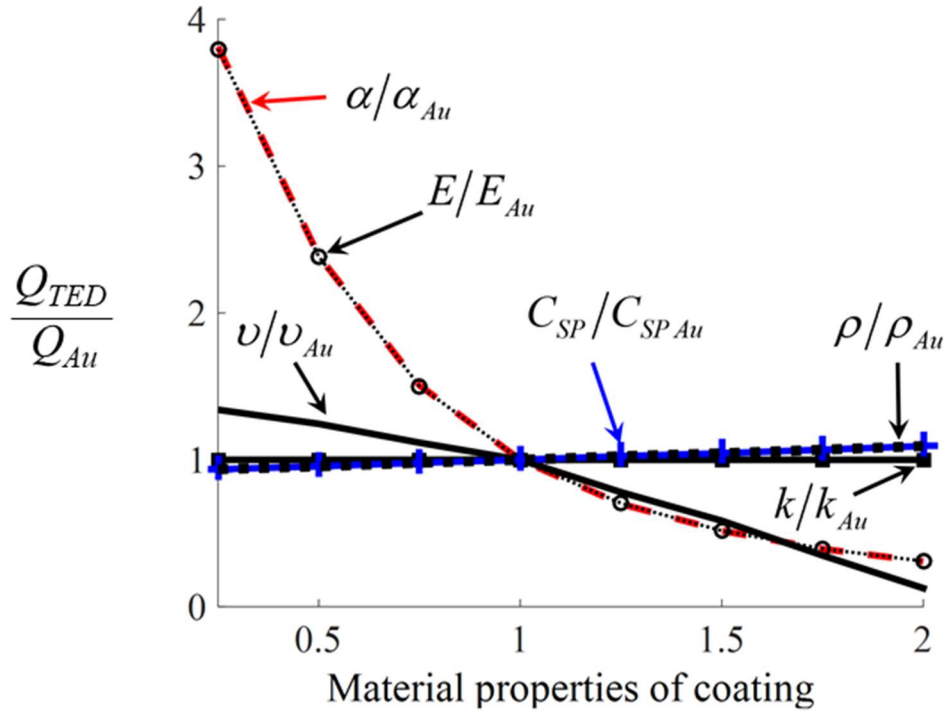


**Figure 4.50:** Effect of coating material properties on  $Q_{TED}$ . Increasing  $E$ ,  $\alpha$ , or  $\nu$  decreases  $Q_{TED}$ , while  $k$ ,  $\rho$ , and  $C_{SP}$  do not have a remarkable effect.

Different parameters affect TED in BSRs. The effective parameters are classified into five categories and a summary of the impact of them is presented in Table 4.4.

As a conclusion, a fused silica BSR with a thin metal coating can provide very large  $Q_{TED}$  and  $Q_{Anchor}$ .

Other dissipation mechanisms will be explained in the subsequent parts.

TABLE 4.4: SUMMARY OF THE EFFECTS OF DIFFERENT PARAMETERS ON TED OF BSRs.

Effective parameters	Amount of impact	Comments
Material	High	<ul style="list-style-type: none"> <li>Increasing <math>\alpha</math>, <math>k</math>, <math>E</math>, or <math>\nu</math> decreases <math>Q_{TED}</math>, while increasing <math>C_{SP}</math> or <math>\rho</math> increases <math>Q_{TED}</math> of a shell that operates in the quasi-adiabatic regime.</li> <li>It has been observed that fused silica and Zerodur are excellent materials for high-<math>Q</math> resonators due to their low <math>\alpha</math>.</li> </ul>
Geometry	Moderate	<ul style="list-style-type: none"> <li>The rim thickness plays a significant role in determining <math>Q_{TED}</math>; however, other geometries do not have a major impact.</li> </ul>
Rim condition	Moderate	<ul style="list-style-type: none"> <li>Chips around the rim only slightly reduce <math>Q_{TED}</math>.</li> <li>Cutting out some areas from the rim reduces <math>Q_{TED}</math> due to increased stress concentration when the shell is deformed in the WG mode.</li> <li>Grooving can reduce heat transfer across the rim thickness. Deeper and wider grooves are more effective as long as they do not make the remaining sidewalls too flexible.</li> </ul>
Temperature	Moderate	<ul style="list-style-type: none"> <li>Increasing the operating temperature reduces <math>Q_{TED}</math>.</li> </ul>
Coating	High	<ul style="list-style-type: none"> <li>TED in a metal coating layer is very large, so the thickness of the coating needs to be minimized in order to reduce energy dissipation.</li> <li><math>Q_{TED}</math> depends strongly on the <math>E</math>, <math>\alpha</math>, and <math>\nu</math> of the coating material; however <math>k</math>, <math>\rho</math>, and <math>C_{SP}</math> are not very effective parameters.</li> </ul>

### 4.1.3 Fluidic damping

Fluidic damping is one of the major dissipation mechanisms in mechanical resonators. As a resonator vibrates, its surface collides with its surrounding fluid molecules and moves them, during the collision some amount of momentum is transferred from the resonator to the fluid. Furthermore, the movement of a resonator inside a viscous fluid causes energy dissipation due to friction. To reduce fluidic damping, many resonators are operated in very low-pressure environments.

Our investigation shows that when a shell vibrates in atmosphere, its  $Q$  is as low as a few thousands, but by decreasing the pressure, fluidic damping is reduced. Figure 4.51 shows the effect of pressure on  $Q$  of a shell when it is vibrating in a low-pressure environment. As shown, even when pressure is very low,  $100 \mu\text{Torr}$  ( $1.316 \times 10^{-7}$  Atm), fluidic damping is the main source of



dissipation. As pressure is reduced below 10  $\mu\text{Torr}$ ,  $Q$  becomes independent from pressure; therefore, fluidic damping is no longer the  $Q$ -limiting mechanism in a shell resonator.

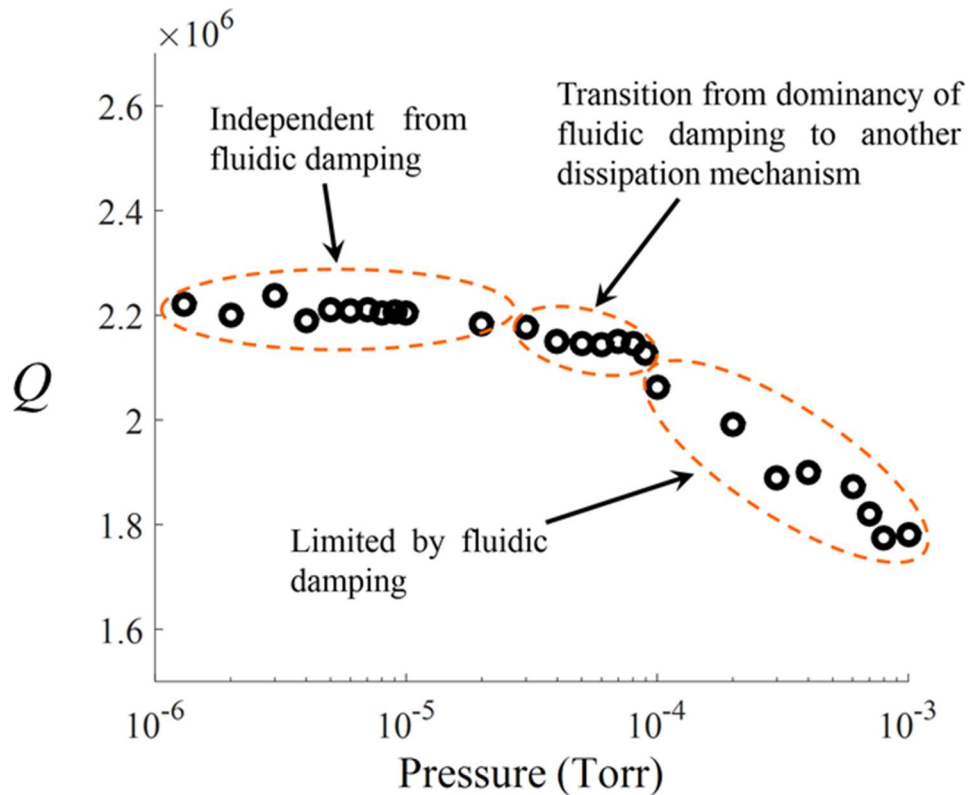


**Figure 4.51:** Effect of operating pressure on the  $Q$  of a fused silica BSR. When the pressure is larger than 100  $\mu\text{Torr}$ , fluidic damping is the  $Q$ -limiting mechanism. As pressure goes below 10  $\mu\text{Torr}$ , other dissipation mechanisms limit  $Q$ .

Dependency of the  $Q$  to pressure necessities vacuum packaging for high performance shell gyroscopes.

#### 4.1.4 Phonon interactions

Phonon-phonon interactions are formulated for two different regimes [90]:

**Akheiser regime:** in the case that the acoustic wavelength ( $\lambda$ ) is considerably larger than the mean free path of phonons ( $\omega < 1/\tau$ ),  $Q_{Phonon}$  can be estimated from (4.29):

$$Q_{Phonon} = \frac{\rho V_a^2 (1 + (\omega\tau)^2)}{C_v T \gamma^2 \tau f} \quad (4.29)$$

**Landau-Rumer regime:** When  $\lambda$  is less than the phonon mean free path ( $\omega > 1/\tau$ ),  $Q_{Phonon}$  can be calculated from (4.30):

$$Q_{Phonon} = \frac{15 \rho V_a^5 h^3}{\pi^5 K^4 \gamma^2 T^4 f} \omega \quad (4.30)$$

where, symbols are  $\omega$ : acoustic angular frequency,  $f$ : resonant frequency,  $\rho$ : density,  $V_a$ : acoustic velocity,  $C_v$ : volumetric heat capacity,  $T$ : absolute temperature,  $\gamma$ : Grüneisen parameter,  $h$ : Planck constant,  $\tau$ : phonon relaxation time, and  $K$ : Boltzmann constant.

Majority of shell resonators are low frequency devices (<100 kHz). In these devices,  $\omega < 1/\tau$ , which means they are working in Akheiser regime (Equation (4.29)). With the assumption the frequency of vibration is low enough to allow the phonons to interact and reach a new equilibrium ( $\omega \ll 1/\tau$ ), (4.29) reduces to (4.31)[91]:

$$Q_{Phonon} = \frac{\rho V_a^4}{2\pi k T \gamma^2 f} \quad (4.31)$$

where  $k$  is thermal conductivity.

For a resonator with resonant frequency of 10,000 Hz, this equation suggests  $Q_{Phonon}$  presented in Table 4.5 for different material (the data for calculation are extracted from [91]). It can be concluded that  $Q_{Phonon}$  is larger than 1 billion for these devices and phonon-phonon interactions is not an important factor in total  $Q$  of shell resonators.

**TABLE 4.5:** AKHIEZER  $Q$  FOR SHELL RESONATORS WITH RESONANT FREQUENCY OF 10,000HZ

<b>Material</b>	<b><math>Q_{Phonon}</math></b>
Si	$2.3 \times 10^9$
Quartz	$3.2 \times 10^9$
AlN	$2.5 \times 10^9$
Diamond	$3.7 \times 10^9$
Sapphire	$1.13 \times 10^{10}$
SiC	$6.4 \times 10^{10}$

#### 4.1.5 Internal dissipation

Internal dissipation or intrinsic loss in a resonator is usually due to internal friction that might be caused by the motion of defects within a resonator [92]. Defects can arise from different sources: contamination, resulting mainly in water, hydrocarbon and oxide molecules; intrinsic impurity atoms in the bond structure; and dangling or broken bonds on the surface due to the termination of the crystal structure on the surface [93]. Energy dissipations from defects in bulk part of the material is usually referred to internal dissipation and losses that arises from defects on the surface referred to surface loss that will be studied in the next subsection.

If a high-quality material without any defects is used for the resonator, this dissipation is negligible. In [94], it is shown that fused silica resonators can achieve a  $Q$  higher than 200 million. However, they investigation showed that  $Q$  is highly dependent on the fused silica quality, they obtained about a factor of 3 different results with different brands of fused silica. Therefore, it is important to use high quality fused silica material. Nevertheless, we expect to achieve a  $Q_{Internal}$  higher than 50 million in shells using high-quality fused silica.

#### 4.1.6 Surface loss

When the size of a resonator is small, its surface-to-volume ratio is large; therefore, any defect, impurity, roughness or other imperfections on the resonator surface could dissipate energy [95, 96]. This dissipation mechanism is called surface loss and is not well understood; however, some experimental data have shown that surface treatments such as annealing could reduce it [58, 97].

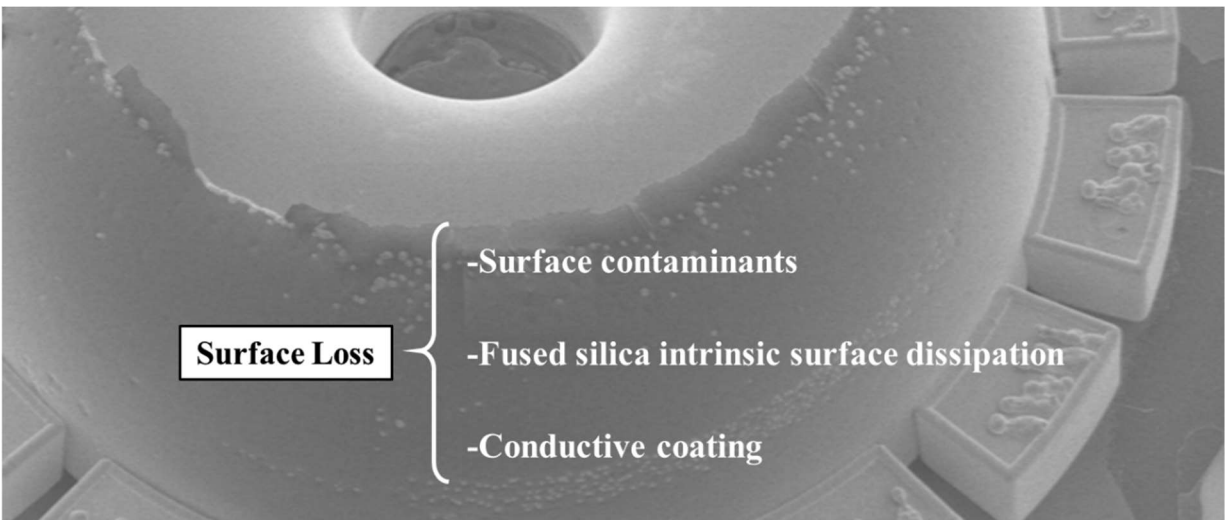


**Figure 4.52:** Different sources of surface loss in fused silica shell resonators. Energy might dissipate in surface of fused silica resonators due to the contaminants, intrinsic fused silica dissipation and conductive coating.

Due to the large surface-to-volume ratio ( $S/V$ ) in shells ( $S/V$  is about  $50,000 \text{ m}^{-1}$  for a 5mm diameter shell), they are sensitive to surface effects; therefore, surface loss could limit  $Q$  of shell resonators. Using experimental data and the analytical models presented in [58] for single-crystal silicon cantilevers,  $Q_{Surface}$  of a cantilever with the same surface-to-volume ratio is approximated to be around 2 million. However, this approximation might not be valid for fused silica shells made with the blowtorch fabrication process. Therefore, there is a need for further investigation.

As shown in Figure 4.52, surface loss in fused silica resonators can originate from several sources. These sources will be discussed in the following subsections.

#### 4.1.6.1 Surface contaminants

To find the effect of contaminants on  $Q$ , several tests are run. For these tests, a shell is operated in a pressure below  $10 \mu\text{Torr}$  to eliminate the effect of fluidic damping.

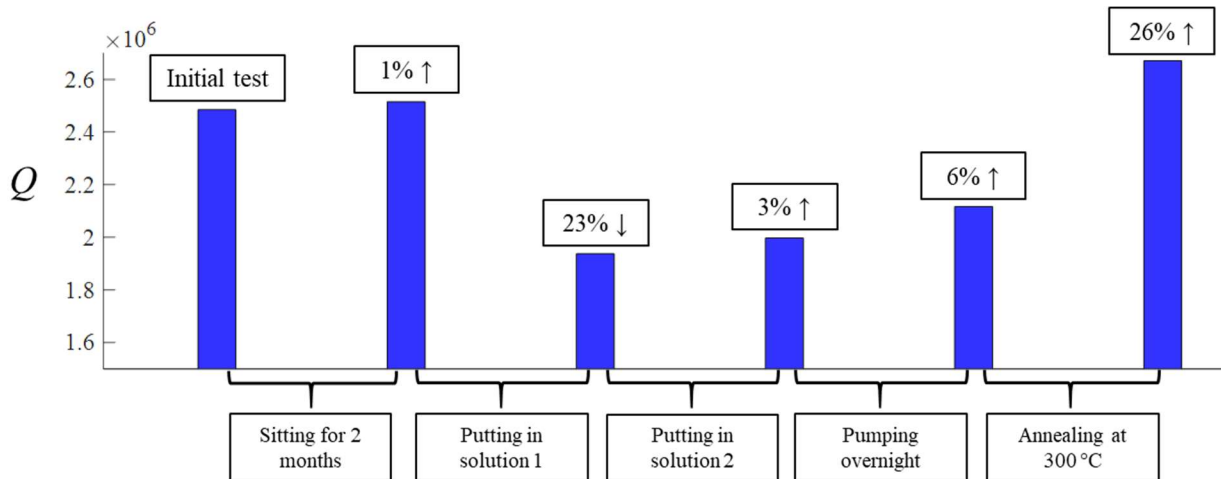


**Figure 4.53:** A summary of several testing steps regarding the effect of surface rinsing on  $Q$  of a fused silica BSR. The results show that surface rinsing has an impact on  $Q$ . Data is provided by Dr. Tal Nagourney.

In the first experiment, the effect of rinsing on  $Q$  is investigated. A summary of the results of this is represented in Figure 4.53. In the first step,  $Q$  of a shell is measured after two months, but the change in  $Q$  found to be negligible. After this step, the shell is put in a solution. Measurement after this step shows about a 23% drop in  $Q$ . This suggests that probably some residue remains on the surface of the shell after rinsing and this residue has an impact on  $Q$ . In the next step, the shell is put in another solution. This step improved  $Q$  by about 3%. Putting the shell in a vacuum chamber for a day while it is pumped down improves  $Q$ ; however,  $Q$  is still less than the initial value. So, there is likely still some residue remaining on surface of the shell from the

solvent cleaning steps. In the last test, the shell annealed at 300 °C for 1 *hr*. This step brought  $Q$  above the initial value tested several months prior.

In another experiment, the effect of annealing on  $Q$  is investigated. Several shell resonators have been annealed at 450 °C for eight hours.  $Q$  in these resonators typically improved by  $\sim 2\times$  as a result of annealing.

From these test results, the following conclusions could be derived:

- Careful cleaning of the shell to remove particulates, organic contaminants, and debris of various kind significantly improves the  $Q$ ;
- Annealing of the shell to repair damage in the resonator, and to remove water molecules, provided significant improvement in  $Q$ .

In addition, it is found that the removal of contaminants from the surface of BRS using annealing might be temporary. It is observed that  $Q$  also tends to drop over time about 40 % in three months for a shell stored in a  $\sim 200$  Torr chamber in air. These performance reductions suggesting that the water hydration might be a major cause of energy loss in fused silica shells and it is extremely important that the shells stored in a dry environment.

#### **4.1.6.2 Fused silica intrinsic surface dissipation**

It has been found that even for the extremely clean fused silica resonators  $Q$  has some dependency to  $V/S$ . Figure 4.54 shows this trend for some of the highest performance fused silica resonators [98]. This means there is a dissipation mechanism associated with the fused silica surface.

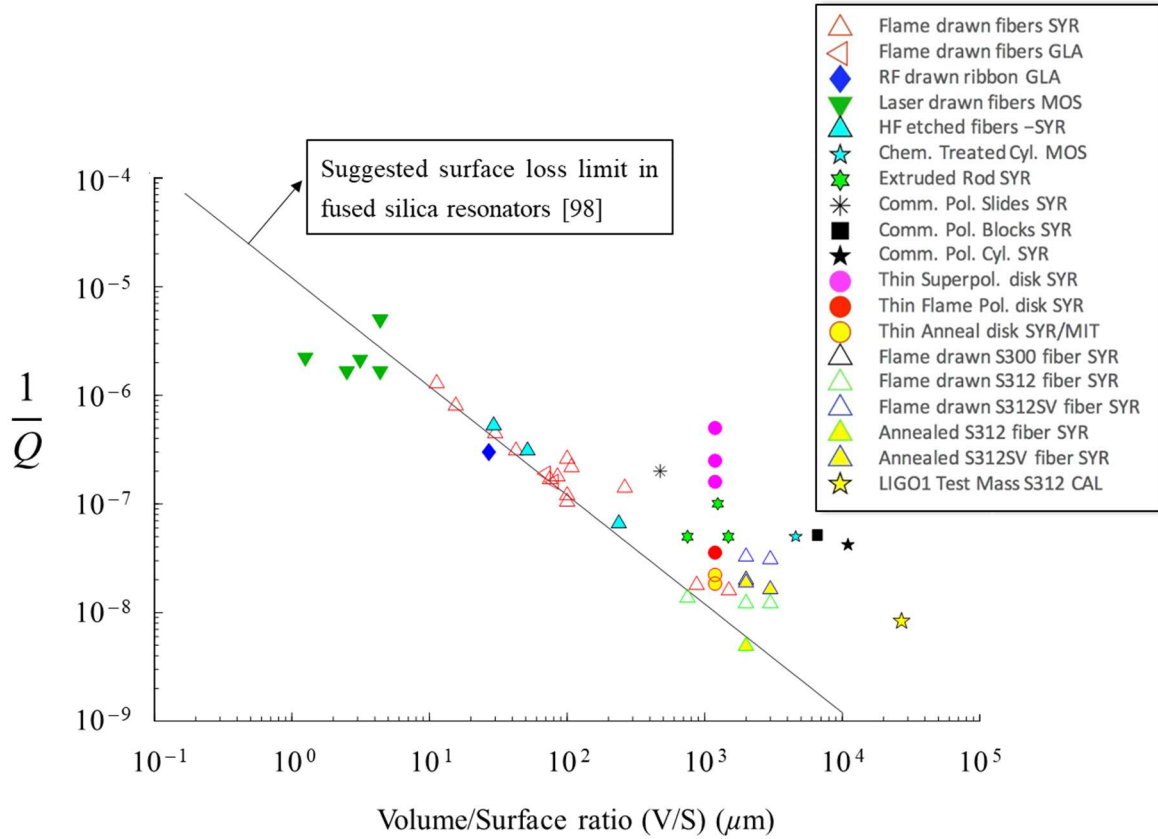


**Figure 4.54:** Dependency of fused silica resonators  $Q$  on their  $V/S$  (original plot is from [98]). As  $V/S$  increases in fused silica resonators  $Q$  improves.

It is not clear what mechanism causes dissipation in the surface of fused silica resonators. One possible scenario is that strained Si-O-Si (siloxane) surface groups with larger bond angle distributions near the surface than the bulk are responsible for energy dissipation due to applied strain [98]. Nevertheless, this suggests that even if other dissipation mechanisms in fused silica are removed there would be some intrinsic loss at the surface. Using the surface loss limit suggested in [98], it is estimated that upper-limit of  $Q$  in fused silica resonators is:

$$Q_{limit} \approx 10^5 \times V/S \quad (\mu\text{m}) \quad (4.32)$$

During past few years, several fused silica shell resonators with different dimensions and different fabrication process steps have been fabricated in the University of Michigan. Relationship

between their  $Q$  and  $V/S$  ratio is shown in Figure 4.55. These results confirm the suggested trend (by increasing  $V/S$ ,  $Q$  increases). However, there are devices that achieved better  $Q$  comparing to the suggested upper limit. This could be due to the blowtorch fabrication process that produces an extremely smooth fused silica, which has a surface roughness less than  $2 \text{ \AA}$ . Data sketched in Figure 4.54 also shows that laser drawn fibers also tend to provide better performance comparing to suggested limit. This means the suggested fused silica surface loss limit is not an absolute value and fabrication process plays a role.

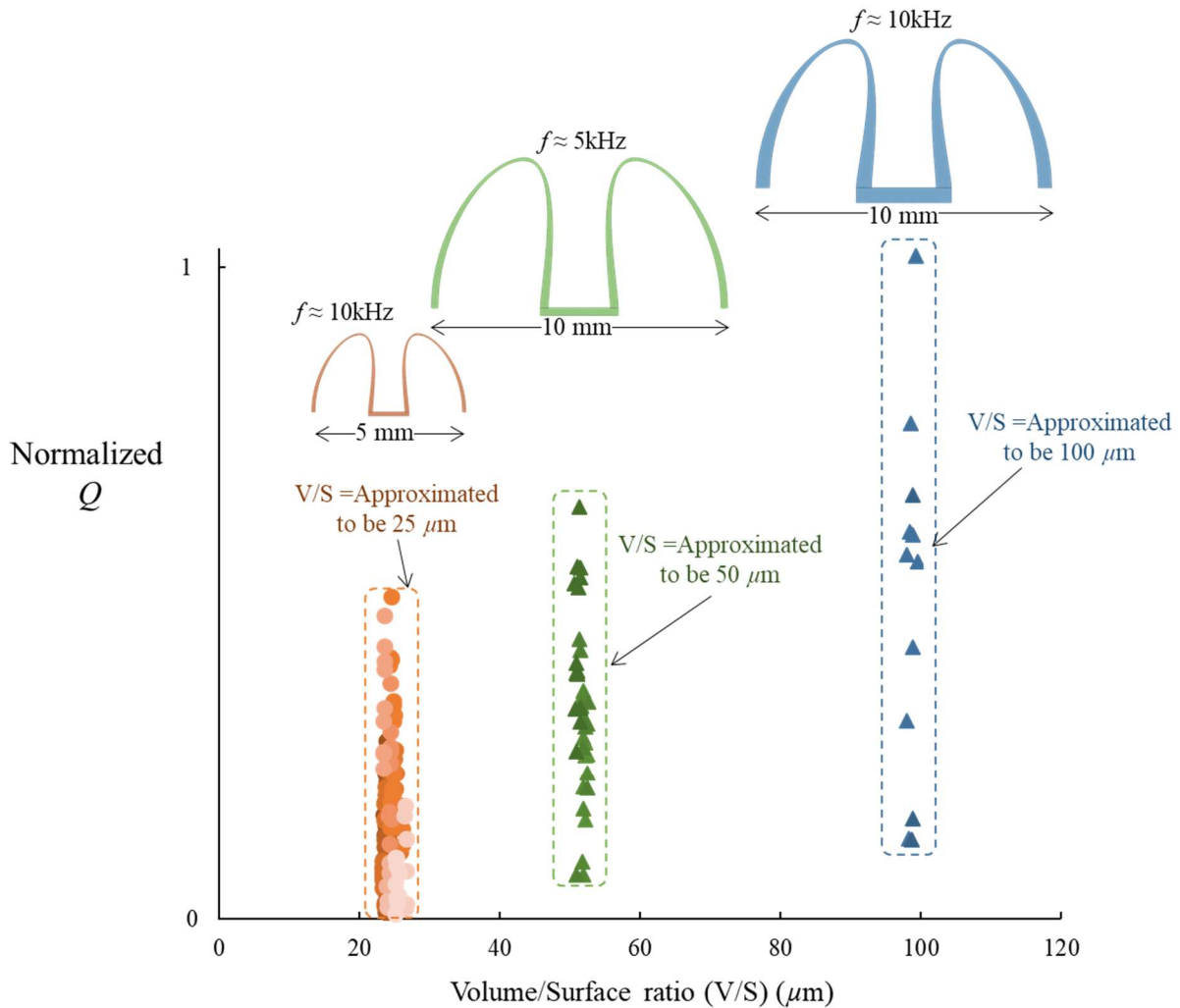


**Figure 4.55:** Normalized  $Q$  versus  $V/S$  of fabricated fused silica BSRs. It appears that increasing  $V/S$  increases  $Q$  limit in BSRs.  $Q$  values are provided by Dr. Jae Young Cho, Dr. Tal Nagourney, and Mr. Sajal Singh.



### 4.1.6.3 Conductive coating

The above discussion relates only to shells that are not coated with a conductive layer. In gyroscope application, the shells need to be coated with a thin conductive layer to allow electrostatic actuation and sensing. Our experiments have shown that the conducting layer is the most dominant factor influencing the  $Q$  of fused silica shells. One of our experimental results described below demonstrates this effect.

Coated and uncoated shell resonators have been fabricated and their  $Q$ s have been measured. The effect of the coating thickness on  $Q$  is measured for two different fused silica samples operating at  $<10 \mu\text{Torr}$  as shown in Figure 4.56. Both samples were made in the same fabrication process. The two uncoated samples had WG resonant frequencies of 9663.8/9667.3 Hz and 10299.4/10303.0 Hz. These samples were then coated with different metal thickness. The coating changes the resonant frequencies only by  $<3$  Hz. Both uncoated samples had average surface roughness of 0.18 nm. Before depositing any metal, the  $Q$ s of both shells were higher than 1.2 million. After coating these samples with sputtered films of 15/20 Å Cr/Au, the  $Q$ s of both samples dropped. Adding three consecutive 40-Å-thick layers of Au to the two resonators continues to reduce their  $Q$ s by more than  $2\times$ . These results show that the metal coating is the limiting factor for the  $Q$  of coated fused silica shell resonators.

At first glance, one might consider that TED is the reason for this significant drop in  $Q$ . Our simulation results in Figure 4.49 showed that as the relative thickness of a coating of gold on the fused silica shell increases, the  $Q$  drops significantly. The tested shells have a rim thickness ( $t_{ro}$ ) of  $70\mu\text{m}$ . According to our simulations, a coating of gold with a thickness ( $t_{Au}$ ) of  $70\text{Å}$  (ratio of  $t_{Au}/t_{ro} = 10^{-4}$ ) should not affect the  $Q$  due to TED. However, the measurement results shown

above clearly show that the  $Q$  drops by more than a factor of  $2\times$ . Therefore, there must be another dissipation mechanism that affects the  $Q$  when the shell is covered by thin-film coatings.

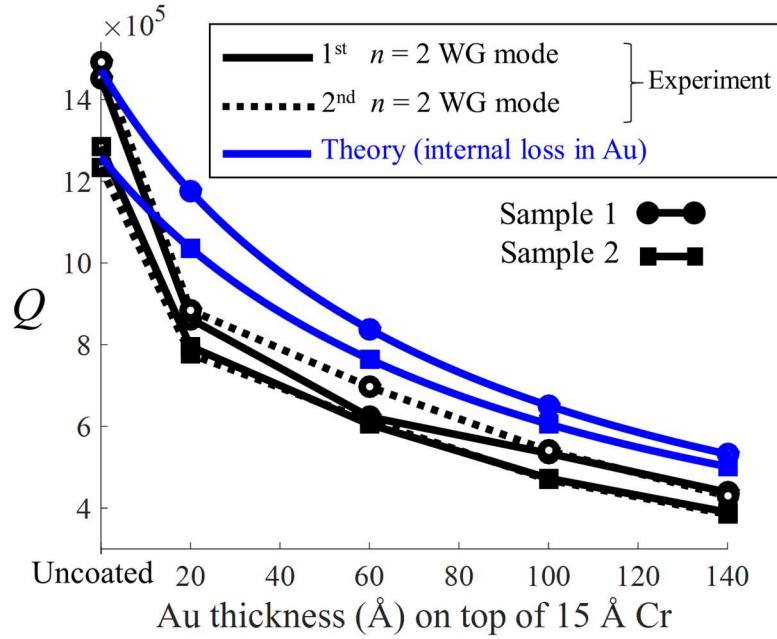


**Figure 4.56:** Effect of coating thickness on  $Q$  of shell resonators. For both samples,  $Q$  decreases significantly with the first metal deposition of Cr/Au 15/20 Å, then approximately linearly for each additional 40 Å of Au deposited. The results show a good agreement with theoretical value for internal dissipation in metal films.

One reason for  $Q$  reduction in metal-coated shells might be internal dissipation in metal films [99]. To confirm whether internal dissipation in the metal film is the source of  $Q$  drop, the theoretical model for internal dissipation in coatings developed for beams [100] is used. Based on this model, the  $Q$  of the metal coating is estimated using:

$$Q_{coating} = \frac{1}{3} \frac{E_s}{E_f} \frac{t_s}{t_f} \frac{1}{\delta_f} \quad (4.33)$$

where,  $E_s$ ,  $E_f$ ,  $t_s$ , and  $t_f$  are substrate and film Young's modulus and thickness, respectively [100]. In this equation,  $\delta_f$  is a coefficient that represents intrinsic viscoelasticity in the film. For resonators operating at 10kHz,  $\delta_f$  is estimated to be 0.002 for gold coatings [100]. A corresponding value for chromium has not been found. However, since the thickness of the chromium layer is not large,

we ignore internal dissipation in the chromium layer. By using the rim thickness for the shell as the substrate thickness in (4.33) and knowing the value of  $Q$  of uncoated shells from the experiment, one can estimate the total  $Q$  of the coated shells. Figure 4.56 shows the results of this estimation for these two samples. As evident, estimated values for  $Q$ s of coated shells match the measured  $Q$ s of resonators reasonably well, except when the gold thickness is small and close to chromium thickness, and internal dissipation in the chromium layer cannot be neglected. It should be noticed that (4.33) is valid for beam resonators and utilizing it for shell resonators is just an approximation. Furthermore, intrinsic viscoelasticity that is used for gold in our case might be different than the value extracted from [100].

In [101], intrinsic damping in metals have been extensively investigated. The results showed that damping in metals depends on material property, temperature, grain size, internal stress, defects, etc. In our case, coating the shell might change surface roughness or residual stress on the resonator surface—both of these parameters might have impact on  $Q$ . Coating might also add some defects to the resonator surface, so dissipation due to surface loss might increase by adding metal layers. To investigate the effect of these phenomena on  $Q$ , coated shells are annealed and  $Q$  is tested.

Furthermore, it is found that annealing metal-coated shells, changes  $Q$  dramatically. The results of experiment reported in [102] show that annealing could change roughness, residual stress, and material composition of the coating. All of these properties could have an impact on  $Q$ . However, mentioned results show this annealing approach is not a reliable method to recover  $Q$  of coated shells.

Another method that can be used to reduce coating dissipation is utilizing other materials instead of Cr/Au. Dr. Tal Nagourney [30] tested titanium/platinum (Ti/Pt), titanium nitride (TiN),

and indium tin oxide (ITO) and all of them reduces  $Q$  of uncoated shell. Further investigation is need to find proper conductive layer to recover  $Q$  of fused silica shells. Nonetheless, these results suggest that the dissipation in the thin film metal coating cannot be ignored. To reduce this dissipation, it is strongly recommended to use a very thin conductive layer.

#### **4.1.7 Conclusion on $Q$ investigation of MEMS shell resonators**

In this section, all the loss mechanisms including anchor loss, surface loss, fluid damping, phonon interactions, internal dissipation, and TED have been extremely investigated and design guidelines to eliminate or reduce them provided. As a result, a shell resonator fabricated in our group provided  $Q$  larger than 10 million that is the highest  $Q$  reported in any MEMS resonator.

Therefore, sensing  $Q$  is successfully optimized in shell gyroscopes. Other important parameters in performance of shell gyroscopes will be discussed in the following sections.

## **4.2 Effective Mass**

As discussed in chapter 2, to reduce the thermomechanical noise it is important that resonators have large effective mass. This section investigates the effect of the shape characteristics of the birdbath structure on its effective mass. To find the effective mass of the shell resonator, reduced order model for dynamics of the shell resonators should be provided.

### **4.2.1 Reduced order model of shells in $n = 2$ WG modes**

In order to obtain such a model, the deformation of point  $p$  in the structure (this point is shown in Figure 4.57 is considered to be:

$$\begin{bmatrix} u(p) \\ v(p) \\ w(p) \end{bmatrix} = \begin{bmatrix} \phi_{1x}(p) \\ \phi_{1y}(p) \\ \phi_{1z}(p) \end{bmatrix} q_1(t) + \begin{bmatrix} \phi_{2x}(p) \\ \phi_{2y}(p) \\ \phi_{2z}(p) \end{bmatrix} q_2(t) \quad (4.34)$$

where  $u$ ,  $v$ , and  $w$  are deformations in the  $x$ ,  $y$ , and  $z$  directions respectively,  $\phi_i = [\phi_{ix} \ \phi_{iy} \ \phi_{iz}]^T$  ( $i = 1, 2$ ) are mode shapes in first and second WG modes, and  $q_1(t)$  and  $q_2(t)$  are amplitudes of motion in generalized coordinates. Potential energy ( $PE$ ) of the shell when it is vibrating in the WG modes can be written as:

$$PE = \frac{1}{2} \iiint (\sigma_{xx}\epsilon_{xx} + \sigma_{yy}\epsilon_{yy} + \sigma_{zz}\epsilon_{zz} + \tau_{xy}\gamma_{xy} + \tau_{yz}\gamma_{yz} + \tau_{xz}\gamma_{xz}) dx dy dz \quad (4.35)$$

where  $\epsilon$  and  $\sigma$  are the strain and stress at point  $p$ , respectively.

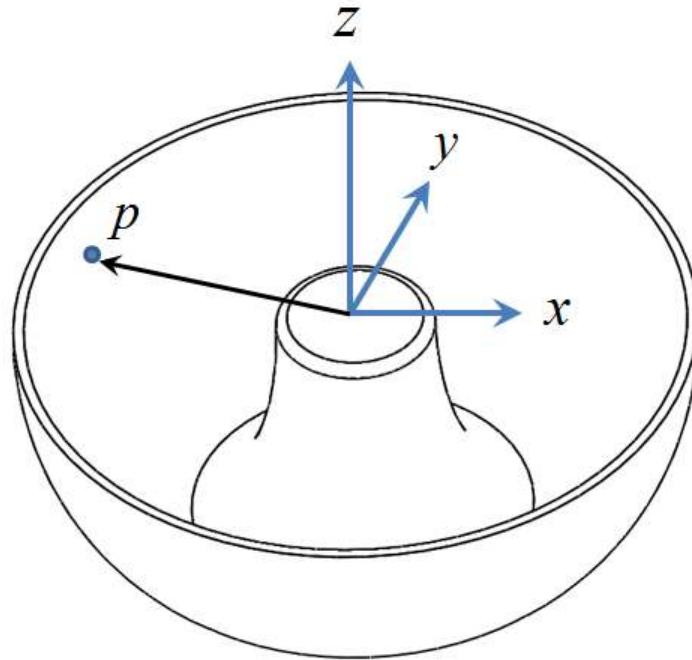


**Figure 4.57:** An arbitrary point  $p$  in a shell structure.

Strains at  $p$  are equal to (4.36):

$$\begin{bmatrix} \varepsilon_{xx}(p) \\ \varepsilon_{yy}(p) \\ \varepsilon_{zz}(p) \\ \gamma_{yz}(p) \\ \gamma_{xz}(p) \\ \gamma_{xy}(p) \end{bmatrix} = \begin{bmatrix} \frac{\partial \phi_{1x}(p)}{\partial x} \\ \frac{\partial \phi_{1y}(p)}{\partial y} \\ \frac{\partial \phi_{1z}(p)}{\partial z} \\ \frac{\partial \phi_{1y}(p)}{\partial z} + \frac{\partial \phi_{1z}(p)}{\partial y} \\ \frac{\partial \phi_{1x}(p)}{\partial z} + \frac{\partial \phi_{1z}(p)}{\partial x} \\ \frac{\partial \phi_{1y}(p)}{\partial x} + \frac{\partial \phi_{1x}(p)}{\partial y} \end{bmatrix} q_1 + \begin{bmatrix} \frac{\partial \phi_{2x}(p)}{\partial x} \\ \frac{\partial \phi_{2y}(p)}{\partial y} \\ \frac{\partial \phi_{2z}(p)}{\partial z} \\ \frac{\partial \phi_{2y}(p)}{\partial z} + \frac{\partial \phi_{2z}(p)}{\partial y} \\ \frac{\partial \phi_{2x}(p)}{\partial z} + \frac{\partial \phi_{2z}(p)}{\partial x} \\ \frac{\partial \phi_{2y}(p)}{\partial x} + \frac{\partial \phi_{2x}(p)}{\partial y} \end{bmatrix} q_2 \quad (4.36)$$

Using stress–strain relations for an isotropic material, the potential energy of the structure can be written as:

$$PE = \frac{1}{2} K_1 q_1^2 + \frac{1}{2} K_2 q_2^2 + \frac{1}{2} K_{12} q_1 q_2 \quad (4.37)$$

where:

$$\begin{aligned} K_1 = \frac{E}{1+\nu} \iiint & \left( \frac{1-\nu}{1-2\nu} \left( \left( \frac{\partial \phi_{1x}}{\partial x} \right)^2 + \left( \frac{\partial \phi_{1y}}{\partial y} \right)^2 + \left( \frac{\partial \phi_{1z}}{\partial z} \right)^2 \right) + \frac{2\nu}{1-2\nu} \left( \frac{\partial \phi_{1y}}{\partial y} \frac{\partial \phi_{1x}}{\partial x} + \frac{\partial \phi_{1z}}{\partial z} \frac{\partial \phi_{1x}}{\partial x} \right. \right. \\ & \left. \left. + \frac{\partial \phi_{1y}}{\partial y} \frac{\partial \phi_{1z}}{\partial z} \right) \right) + \frac{1}{2} \left( \left( \frac{\partial \phi_{1y}}{\partial x} + \frac{\partial \phi_{1x}}{\partial y} \right)^2 + \left( \frac{\partial \phi_{1y}}{\partial z} + \frac{\partial \phi_{1z}}{\partial y} \right)^2 + \left( \frac{\partial \phi_{1x}}{\partial z} + \frac{\partial \phi_{1z}}{\partial x} \right)^2 \right) dx dy dz \end{aligned} \quad (4.38)$$

$$\begin{aligned} K_2 = \frac{E}{1+\nu} \iiint & \left( \frac{1-\nu}{1-2\nu} \left( \left( \frac{\partial \phi_{2x}}{\partial x} \right)^2 + \left( \frac{\partial \phi_{2y}}{\partial y} \right)^2 + \left( \frac{\partial \phi_{2z}}{\partial z} \right)^2 \right) + \frac{2\nu}{1-2\nu} \left( \frac{\partial \phi_{2y}}{\partial y} \frac{\partial \phi_{2x}}{\partial x} + \frac{\partial \phi_{2z}}{\partial z} \frac{\partial \phi_{2x}}{\partial x} \right. \right. \\ & \left. \left. + \frac{\partial \phi_{2y}}{\partial y} \frac{\partial \phi_{2z}}{\partial z} \right) \right) + \frac{1}{2} \left( \left( \frac{\partial \phi_{2y}}{\partial x} + \frac{\partial \phi_{2x}}{\partial y} \right)^2 + \left( \frac{\partial \phi_{2y}}{\partial z} + \frac{\partial \phi_{2z}}{\partial y} \right)^2 + \left( \frac{\partial \phi_{2x}}{\partial z} + \frac{\partial \phi_{2z}}{\partial x} \right)^2 \right) dx dy dz \end{aligned} \quad (4.39)$$

$$\begin{aligned}
K_{12} = & \frac{E}{(1+\nu)} \iiint \left( \frac{2(1-\nu)}{(1-2\nu)} \left( \frac{\partial \phi_{1x}}{\partial x} \frac{\partial \phi_{2x}}{\partial x} + \frac{\partial \phi_{1y}}{\partial y} \frac{\partial \phi_{2y}}{\partial y} + \frac{\partial \phi_{1z}}{\partial z} \frac{\partial \phi_{2z}}{\partial z} \right) + \frac{2\nu}{(1-2\nu)} \left( \frac{\partial \phi_{1y}}{\partial y} \frac{\partial \phi_{2x}}{\partial x} \right. \right. \\
& + \frac{\partial \phi_{2y}}{\partial y} \frac{\partial \phi_{1x}}{\partial x} + \frac{\partial \phi_{1z}}{\partial z} \frac{\partial \phi_{2x}}{\partial x} + \frac{\partial \phi_{2z}}{\partial z} \frac{\partial \phi_{1x}}{\partial x} + \frac{\partial \phi_{1y}}{\partial y} \frac{\partial \phi_{2z}}{\partial z} + \frac{\partial \phi_{2y}}{\partial y} \frac{\partial \phi_{1z}}{\partial z} \left. \right) + \left( \frac{\partial \phi_{1y}}{\partial x} + \frac{\partial \phi_{1x}}{\partial y} \right) \left( \frac{\partial \phi_{2y}}{\partial x} \right. \\
& \left. \left. + \frac{\partial \phi_{2x}}{\partial y} \right) + \left( \frac{\partial \phi_{1y}}{\partial z} + \frac{\partial \phi_{1z}}{\partial y} \right) \left( \frac{\partial \phi_{2y}}{\partial z} + \frac{\partial \phi_{2z}}{\partial y} \right) + \left( \frac{\partial \phi_{1x}}{\partial z} + \frac{\partial \phi_{1z}}{\partial x} \right) \left( \frac{\partial \phi_{2x}}{\partial z} + \frac{\partial \phi_{2z}}{\partial x} \right) \right) dx dy dz \quad (4.40)
\end{aligned}$$

In these equations,  $E$  is Young's modulus and  $\nu$  is Poisson's ratio of the resonator material.

Velocity of point  $p$  equals to:

$$\vec{v} = \begin{bmatrix} \phi_{1x}(p) \\ \phi_{1y}(p) \\ \phi_{1z}(p) \end{bmatrix} \dot{q}_1(t) + \begin{bmatrix} \phi_{2x}(p) \\ \phi_{2y}(p) \\ \phi_{2z}(p) \end{bmatrix} \dot{q}_2(t) \quad (4.41)$$

Therefore, the kinetic energy of the system,  $KE$ , can be calculated from (4.42):

$$KE = \frac{1}{2} \iiint \rho \cdot |\vec{v}|^2 dx dy dz \quad (4.42)$$

Putting (4.41) into (4.42), and simplifying the result, the kinetic energy is calculated to be:

$$\begin{aligned}
KE = & \frac{1}{2} \rho \left( \left( \iiint \left( (\phi_{1x}(p))^2 + (\phi_{1y}(p))^2 + (\phi_{1z}(p))^2 \right) dx dy dz \right) (\dot{q}_1(t))^2 \right. \\
& + \left( \iiint \left( (\phi_{2x}(p))^2 + (\phi_{2y}(p))^2 + (\phi_{2z}(p))^2 \right) dx dy dz \right) (\dot{q}_2(t))^2 \\
& \left. + 2 \left( \iiint \left( \phi_{1x}(p)\phi_{2x}(p) + \phi_{1y}(p)\phi_{2y}(p) + \phi_{1z}(p)\phi_{2z}(p) \right) dx dy dz \right) (\dot{q}_1(t))(\dot{q}_2(t)) \right) \quad (4.43)
\end{aligned}$$

Orthogonality of normal modes causes that the last term in (4.43) be zero; therefore, the kinetic energy of this system can be represented by:

$$KE = \frac{1}{2} M_1 \dot{q}_1^2 + \frac{1}{2} M_2 \dot{q}_2^2 \quad (4.44)$$

where  $M_1$  and  $M_2$  are effective masses equal to:

$$M_1 = \iiint \rho \left( (\phi_{1x}(p))^2 + (\phi_{1y}(p))^2 + (\phi_{1z}(p))^2 \right) dx dy dz \quad (4.45)$$

$$M_2 = \iiint \rho \left( (\phi_{2x}(p))^2 + (\phi_{2y}(p))^2 + (\phi_{2z}(p))^2 \right) dx dy dz \quad (4.46)$$

Equations of motion can be obtained in terms of generalized coordinates by using Lagrange's formula of motion:

$$\frac{d}{dt} \left( \frac{\partial L}{\partial \dot{q}_1} \right) - \frac{\partial L}{\partial q_1} = 0 \quad (4.47)$$

$$\frac{d}{dt} \left( \frac{\partial L}{\partial \dot{q}_2} \right) - \frac{\partial L}{\partial q_2} = 0 \quad (4.48)$$

where  $L=KE-PE$ . Substituting the potential and kinetic energies in (4.47) and (4.48) and taking the derivatives, the model of free vibration of a shell resonator is derived as:

$$M_1 \ddot{q}_1 + K_1 q_1 + \frac{1}{2} K_{12} q_2 = 0 \quad (4.49)$$

$$M_2 \ddot{q}_2 + K_2 q_2 + \frac{1}{2} K_{12} q_1 = 0 \quad (4.50)$$

As a result, the dynamical behavior of this resonator can be simplified to the vibration of two coupled masses as shown in Figure 4.58, where  $\tilde{K}_1 = (K_1 - K_{12}/2)/2$ ,  $\tilde{K}_2 = (K_2 - K_{12}/2)/2$ , and  $\tilde{K}_{12} = K_{12}$ .

This model describes the vibrational behavior of 3D shells as vibrating in  $n = 2$  WG modes. According to this, the effective mass of a shell gyroscope can be calculated using (4.45) and (4.46). In addition to calculating effective mass. This simple model can be used for computationally



inexpensive real time analysis of WG shell structures, which is useful for predicting the dynamical response of the shell and designing a control system for WG vibratory gyroscopes.

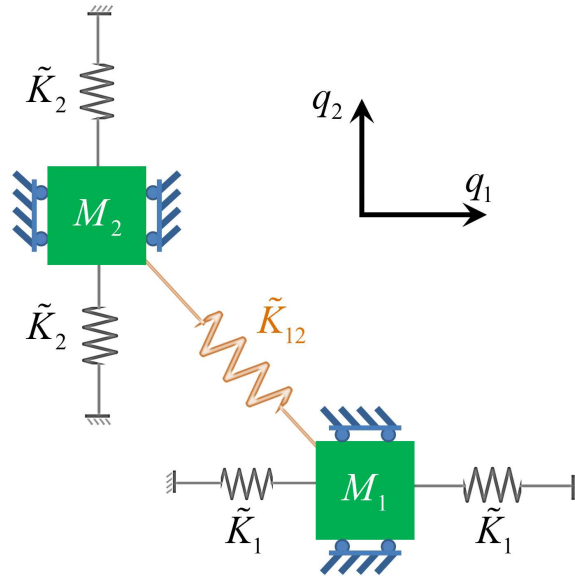


**Figure 4.58:** Reduced order model of vibration of a resonator in the WG modes. The dynamical behavior of a resonator when it is oscillating in the WG modes can be simplified to the vibration of two coupled masses.

#### 4.2.2 Numerical calculation of effective mass

Equation (4.45) and (4.46) should be used to find the effective mass of the shell resonator.

To calculate the mode shapes and integrate the data over shell geometry COMSOL Multiphysics is used for solving an eigenvalue problem numerically.

For the shell that is made from the fused silica with the dimension shown in Figure 4.35, effective masses are calculated to be:

$$M_1 = M_2 = 872 \mu\text{g} \quad (4.51)$$

where  $M_1$  and  $M_2$  are effective masses of the first and second WG modes, respectively.

To find the effect of the shell geometry on its effective mass, the geometric properties of the shell are changed and effective masses are calculated. The results of these analyses are shown in Figure 4.59.

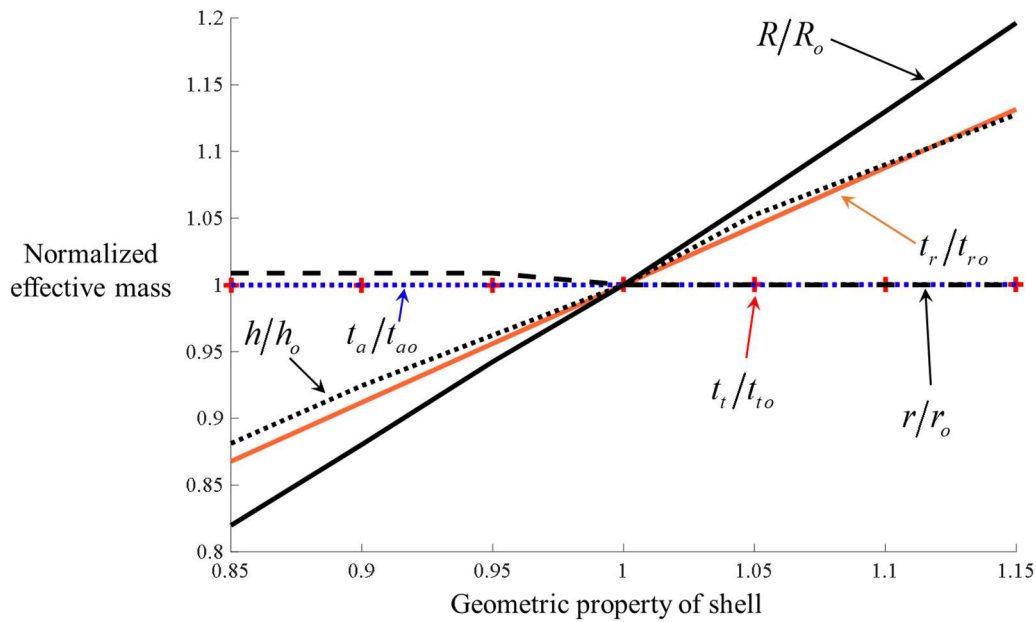


**Figure 4.59:** Effect of geometric properties of the resonator on effective mass. Increasing the rim thickness, shell radius, or height increases the effective mass, while the top and stem wall thicknesses and anchor radius have very small effect.

Numerical simulation shows that increasing the rim thickness increases the effective mass of the resonator. This was obvious since thicker rim means that larger amount of mass is located in the resonant part of the structure. It is also found that increasing shell radius or height increases the effective mass. This was expected because increasing these properties make the resonant part of the structure larger and hence heavier. Additionally, the results show that the thickness of the top part and stem as well as anchor radius have a very small effect on the effective mass since these properties affect the parts of the structure that are far from the resonant part. Figure 4.60 shows the summary of the optimization of the shell effective mass.

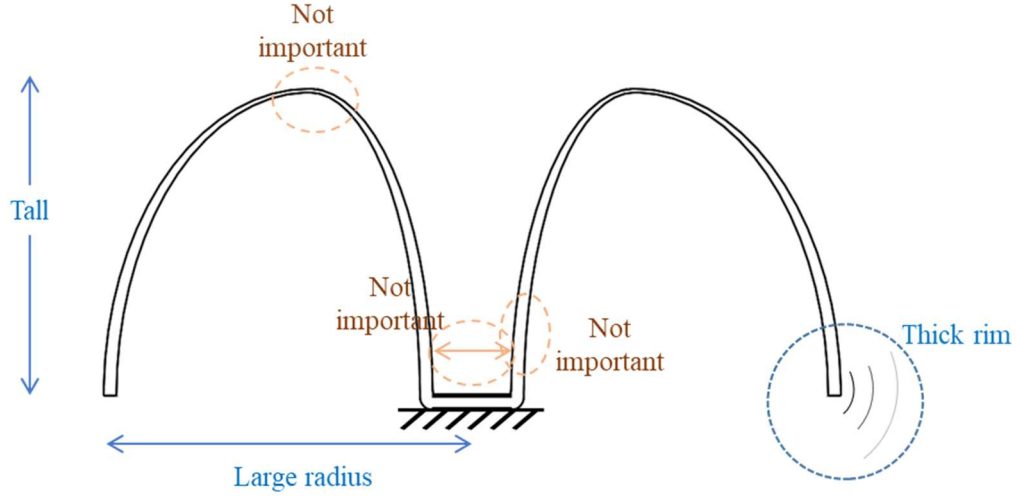


**Figure 4.60:** Schematic of a large effective mass shell. This shell is tall and has a large radius and thick rim.

### 4.3 Angular Gain

Chapter 2 showed that angular gain is a very important factor in thermomechanical and electronic noises. In this section, a theoretical model for calculating angular gain will be developed and then the effect of the shape characteristics of the birdbath structure on its angular gain investigated.

#### 4.3.1 Reduced order model of shells considering rotation in the system

To obtain the angular gain, the effect of rotation rate on the shell resonators dynamics should be considered. If the shell is rotating around z-axis with rotation rate of  $\Omega_z$ , the velocity of point  $p$  (in Figure 4.57) is:

$$\vec{v} = \begin{bmatrix} \phi_{1x}(p) \\ \phi_{1y}(p) \\ \phi_{1z}(p) \end{bmatrix} \dot{q}_1(t) + \begin{bmatrix} \phi_{2x}(p) \\ \phi_{2y}(p) \\ \phi_{2z}(p) \end{bmatrix} \dot{q}_2(t) + \Omega_z \begin{bmatrix} -y(p) - \phi_{1y}(p)q_1(t) - \phi_{2y}(p)q_2(t) \\ x(p) + \phi_{1x}(p)q_1(t) + \phi_{2x}(p)q_2(t) \\ 0 \end{bmatrix} \quad (4.52)$$

where  $x(p)$  and  $y(p)$  are positions of point  $p$  in the  $x, y$  directions, respectively. Using (4.42), the kinetic energy of the system,  $KE$ , can be recalculated as:

$$KE = \frac{1}{2}M_1\dot{q}_1^2 + \frac{1}{2}M_2\dot{q}_2^2 + \frac{1}{2}(c_1\dot{q}_1q_2 + c_2q_1\dot{q}_2 + c_3q_1\dot{q}_1 + c_4q_2\dot{q}_2 + c_5\dot{q}_1 + c_6\dot{q}_2)\Omega_z + \frac{1}{2}(c_7q_1^2 + c_8q_2^2 + c_9q_1q_2 + c_{10})\Omega_z^2 \quad (4.53)$$

where  $c_i$  ( $i=1,2,\dots,10$ ) are constants depending on the shell mode shapes and structure that can be calculated from (4.52) and (4.53). For example:

$$c_1 = 2 \iiint \rho (\phi_{1y}(p)\phi_{2x}(p) - \phi_{1x}(p)\phi_{2y}(p)) dx dy dz \quad (4.54)$$

$$c_2 = 2 \iiint \rho (\phi_{1x}(p)\phi_{2y}(p) - \phi_{1y}(p)\phi_{2x}(p)) dx dy dz$$

Substituting the new kinetic energy in (4.47) and (4.48) and taking the derivatives, the model of free vibration of a shell resonator in existence of rotation becomes:

$$M_1\ddot{q}_1 + K_1q_1 + \frac{1}{2}K_{12}q_2 + \frac{1}{2}((c_1 - c_2)\dot{q}_2)\Omega_z + \frac{1}{2}(c_1q_2 + c_3q_1 + c_5)\dot{\Omega}_z - \frac{1}{2}(2c_7q_1 + c_9q_2)\Omega_z^2 = 0 \quad (4.55)$$

$$M_2\ddot{q}_2 + K_2q_2 + \frac{1}{2}K_{12}q_1 + \frac{1}{2}((c_2 - c_1)\dot{q}_1)\Omega_z + \frac{1}{2}(c_2q_1 + c_4q_2 + c_6)\dot{\Omega}_z - \frac{1}{2}(2c_8q_2 + c_9q_1)\Omega_z^2 = 0 \quad (4.56)$$

Comparing these equations with (2.43) and (2.44), and assuming the effective masses are the same for both modes, result in:

$$A_g = \frac{c_2 - c_1}{4M} \quad (4.57)$$

Therefore, angular gain is:

$$A_g = \frac{\iiint \rho (\phi_{1x}(p)\phi_{2y}(p) - \phi_{1y}(p)\phi_{2x}(p)) dx dy dz}{\iiint \rho ((\phi_{1x}(p))^2 + (\phi_{1y}(p))^2 + (\phi_{1z}(p))^2) dx dy dz} \quad (4.58)$$

### 4.3.2 Numerical calculation of angular gain

COMSOL Multiphysics can be used to find mode shapes. Then, a numerical calculation software, such as Matlab, can be used to calculate angular gain, using (4.58). For the shell that is shown in Figure 4.34, angular gain is:

$$A_g = 0.5136 \quad (4.59)$$

The highest possible angular gain in one, so angular gain of the fabricated shell is relatively large. However, it is possible to increase this value by changing the geometry of the shell. Figure 4.61 shows the effect of geometric property of the shell on its angular gain.

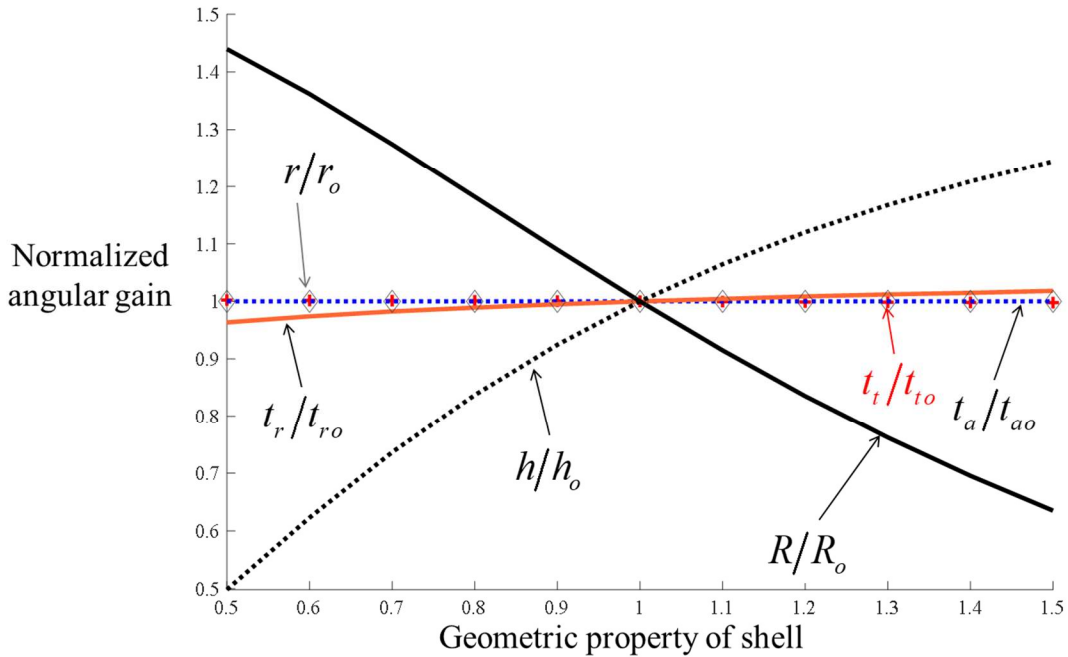


**Figure 4.61:** Effect of geometric properties of the resonator on angular gain. Increasing the aspect ratio ( $h/R$ ) of shell increases angular gain.

It is found that increasing the shell height and/or decreasing the shell radius increases angular gain. Therefore, shells with larger aspect ratios potentially could provide better performance. Figure 4.62 shows that as the aspect ratio of a shell decreases, the ratio of its deformation in horizontal direction to vertical direction increases. This means smaller amount of energy can be transferred from one of the WG mode to another one due to the Coriolis acceleration, resulting in smaller angular gain.

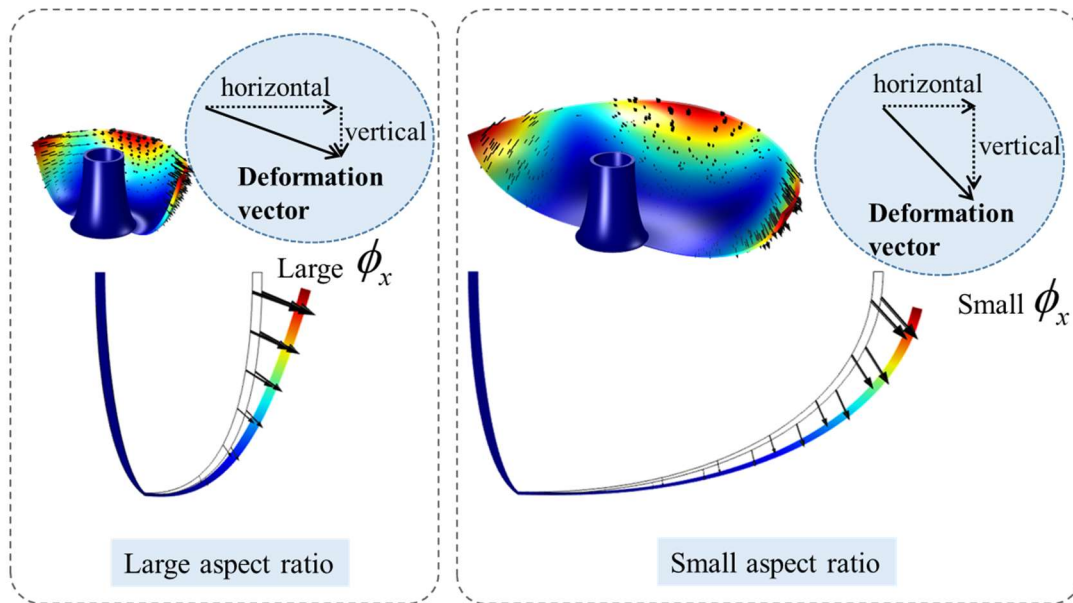


**Figure 4.62:** Deformation vectors in large and small aspect ratio shells. Majority of movement in small aspect ratio shells is in vertical direction that does not play a role for rotation around vertical axis.

#### 4.4 Resonant Frequency

Resonant frequency of a shell gyroscope affects both thermomechanical and electronic noises. This section includes an analytical model for determining the approximate resonant frequency of shell structures, and a comprehensive investigation on the effect of different

parameters on their resonant frequencies. These parameters include shell geometry, operating temperature, and shock.

#### 4.4.1 Analytical model for resonant frequency of birdbath shell resonators

In this subsection, a simple model is developed for approximating resonant frequency of the BSRs analytically.

As shown in Figure 3.2, the majority of deflection in the birdbath resonator occurs in places close to the rim of the shell; places near the stem have almost no deflection. Therefore, the shell can be considered as a structure consisting of a resonant part and a non-resonant part. Figure 4.63 shows this structure. For simplification, it is considered that the non-resonant part does not have any effect on the resonant frequency.

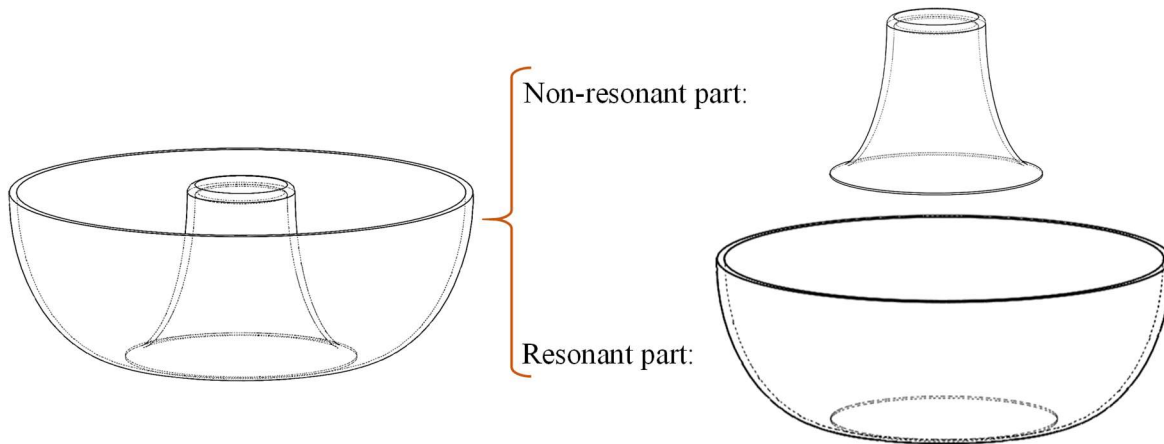


**Figure 4.63:** Birdbath structure is divided to the resonant and non-resonant parts for  $n = 2$  WG modes.

To find the resonant frequency of the resonant part, the deflection of the resonant part is assumed to come from degenerate extension of the rim part and bending of several curved beams with clamped-free ends. Figure 4.64 shows the ring and a curved beam.

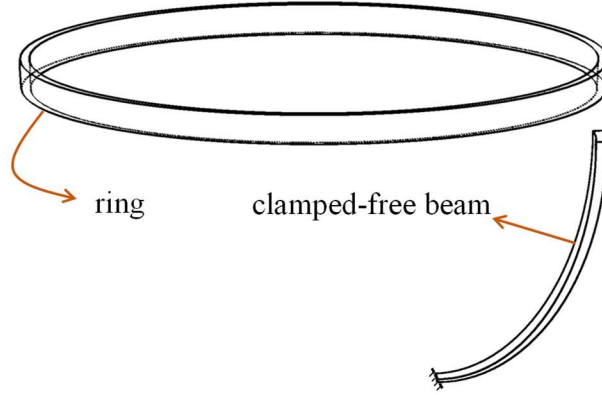


**Figure 4.64:** A ring and a curved beam that cause the deformation of resonant part of the birdbath shell.

Resonant frequency of this ring in degenerate extensional (WG) modes ( $n = 2$ ) can be calculated from (4.60):

$$f_r = \frac{1}{2\pi} \cdot \sqrt{\frac{3}{5}} \cdot \sqrt{\frac{E}{\rho}} \cdot \frac{t_r}{R^2} \quad (4.60)$$

Resonant frequency of a clamped-free beam with length  $L$  and thickness  $t_r$  can be calculated from (4.61):

$$f_b = \frac{1}{2\pi} \cdot \frac{1.875^2}{\sqrt{12}} \cdot \sqrt{\frac{E}{\rho}} \cdot \frac{t_r}{L^2} \quad (4.61)$$

By approximating the curved beam as a straight beam with thickness of  $t_r$ , and approximating the length with (4.62):

$$L = \frac{\pi}{\sqrt{8}} \cdot \sqrt{h^2 + \left(\frac{R}{2}\right)^2} \quad (4.62)$$

the resonant frequency of the beam part can be approximated by (4.63):



$$f_b = \frac{1}{2\pi^3} \cdot \frac{14.06}{\sqrt{3}} \cdot \sqrt{\frac{E}{\rho}} \cdot \frac{t_r}{h^2 + \left(\frac{R}{2}\right)^2} \quad (4.63)$$

Considering that the structure consists of several beams, which totally have the same effective mass as the ring ( $M_{eff}$ ), the total stiffness of the system is:

$$K = M_{eff} \cdot \frac{E}{\rho} \cdot t_r^2 \left( \frac{14.06^2}{3\pi^4 \left( h^2 + \left(\frac{R}{2}\right)^2 \right)^2} + \frac{3}{5R^4} \right) \quad (4.64)$$

As a result, the resonant frequency of the whole structure is approximated by (4.65):

$$f_{app} = \frac{1}{2\pi} \cdot \left( \frac{14.06^2}{3\pi^4 \left( h^2 + \left(\frac{R}{2}\right)^2 \right)^2} + \frac{3}{5R^4} \right)^{1/2} \cdot \sqrt{\frac{E}{\rho}} \cdot t_r \quad (4.65)$$

For a fused silica shell with dimensions shown in Figure 4.35, and material properties that are considered to be Young's modulus  $E_{fs} = 70$  GPa, Poisson's ratio  $\nu_{fs} = 0.17$ , and density  $\rho_{fs} = 2200$  kg/m<sup>3</sup>,  $f_{app}$  calculated to be 14,651 Hz ( $f_{app}$  should be the same for both modes).

#### 4.4.2 Numerical calculation of resonant frequency of birdbath shell resonators

To obtain resonant frequencies numerically, COMSOL Multiphysics is used to solve the finite element eigenfrequency problem. Fused silica is chosen as the material for the structure, with dimensions shown in Figure 4.35, the results of finite element simulations show that:

$$f_1 = f_2 = 15.1 \text{ kHz} \quad (4.66)$$

where  $f_1$  and  $f_2$  are resonant frequencies of the first and second WG modes, respectively. The numerical prediction is close to the analytical one, which confirms the accuracy of the analytical model.

In this part, the effect of the shape characteristics of the birdbath structure on its resonant frequency is analyzed by changing the geometric properties of the resonator. The results of this analysis are shown in Figure 4.65.

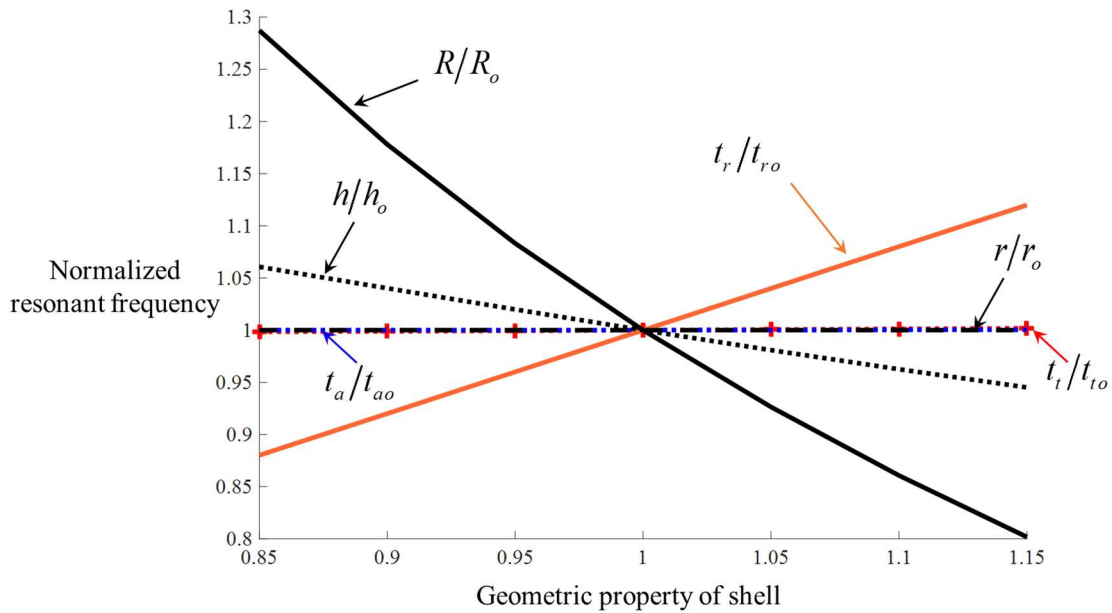


**Figure 4.65:** Effect of geometric properties of the resonator on resonant frequency. Increasing the shell radius and height decreases the resonant frequency, while increasing the rim thickness increases the resonant frequency. The top and stem wall thicknesses and anchor radius have very small effect on resonant frequency.

Numerical simulation shows that increasing the rim thickness increases the resonant frequency of the resonator. In fact, increasing the rim thickness increases both stiffness and mass of the resonant part, while it has a smaller impact on the mass; therefore, resonant frequency

increases. The analytical model that was derived in subsection 4.4.1 also shows that the resonant frequency has a direct relation with the rim thickness.

The numerical simulation also reveals that birdbath structures with the smaller outer radius and height have a higher resonant frequency. This was expected because increasing the shell height or radius decreases the stiffness of the shell for WG modes. This investigation also shows that shell radius is more effective than its height because the radius decreases the stiffness of the ring as well as the curved beams, while height only affects the curved beams.

Additionally, the results show that the thickness of the top part and stem as well as anchor radius have a very small effect on the resonant frequency since these properties affect the parts of the structure that are far from the resonant part.

#### **4.4.3 Experimental verification of modeled and simulated resonant frequencies**

To confirm the accuracy of the analytical model and numerical simulation, resonant frequencies of birdbath resonators are tested experimentally.

Figure 4.66 represents frequency sweeps of  $n = 2$  WG modes for a BSR taken with an HP4194A Gain-Phase Analyzer. There are two different resonant frequencies with about an 85 Hz frequency split, indicating imperfections in the resonator. During the fabrication process, different kinds of imperfections might occur in the birdbath structure that can cause a frequency split. This phenomenon will be analyzed extensively in subsection 4.5.

During past six years, different shells with different dimensions have been made in our group. These shells produce different resonant frequencies from less than 5 kHz to more than 35 kHz, depending on the shell dimensions. Table 4.6 compares the experimental data, analytical

model and numerical simulation. The experimental data show very good agreement with analytical and numerical results, which validates the analytical model as well as numerical simulation.

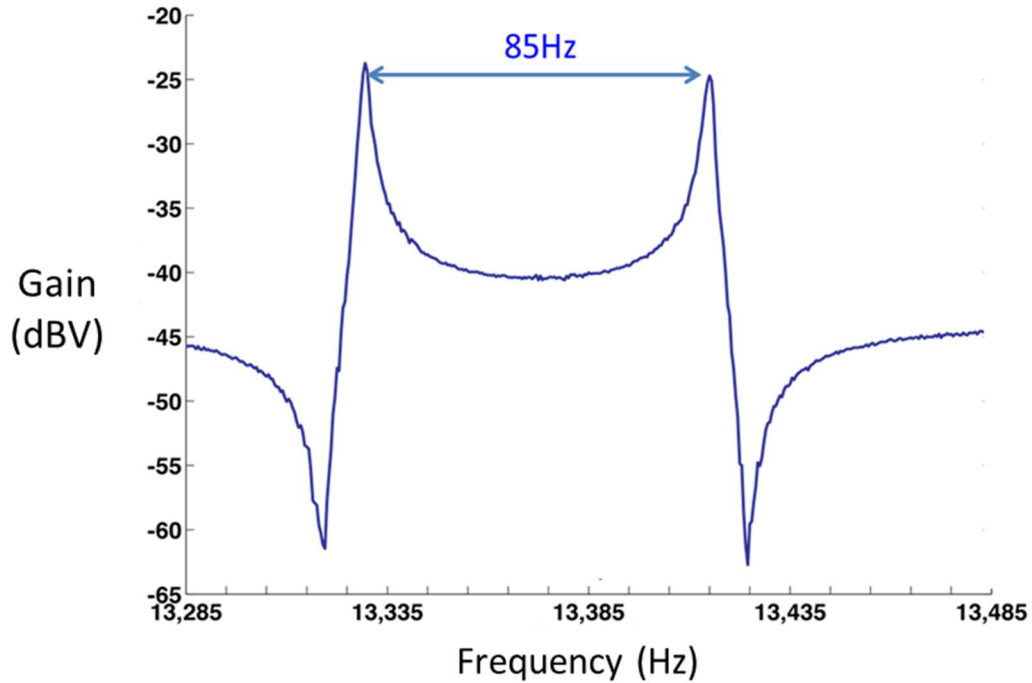


**Figure 4.66:** Frequency sweeps of  $n = 2$  WG modes for a BSR. Because of imperfections in the shell, the two modes have an 85 Hz frequency difference.

**TABLE 4.6:** COMPARING ANALYTICAL MODEL, NUMERICAL SIMULATION AND EXPERIMENTAL DATA VALUES FOR RESONANT FREQUENCY

Sample	Geometrical parameters					$f$ (KHz)		
	$R$ (mm)	$h$ (mm)	$r$ (mm)	$t_t$ ( $\mu\text{m}$ )	$t_r$ ( $\mu\text{m}$ )	Analytical model	Numerical simulation	Experiment
1	1.5	0.8	0.25	23.5	60	41.2	38.8	36.4
2	2.5	2.1	0.8	21	80	13.3	14.5	9.7
3	2.5	1.8	0.8	21.6	77.2	14.6	15.1	14.8
4	5	4.6	0.75	30	150	5.8	6.2	5.1
5	5	4.6	0.75	60	300	11.6	11.7	10.9

#### 4.4.4 Effect of temperature on resonant frequency

The material properties of fused silica are dependent on temperature. The working temperature of the system may change during operation, so the resonant frequency of the structure may vary. The effects of temperature on Young's modulus and Poisson's ratio of fused silica are depicted in Figure 4.67 (these data are extracted from [89]). It is assumed that the density of fused silica does not change with temperature. The resonant frequencies of the structure for different operating temperatures are simulated using these data. The results are normalized with respect to the resonant frequency at 296 K and shown in Figure 4.68. To verify the simulation results, a group of tests are performed at different temperatures and normalized to the resonant frequencies of the structure at 300 K—it should be taken into account that  $f$  has different values for each case.

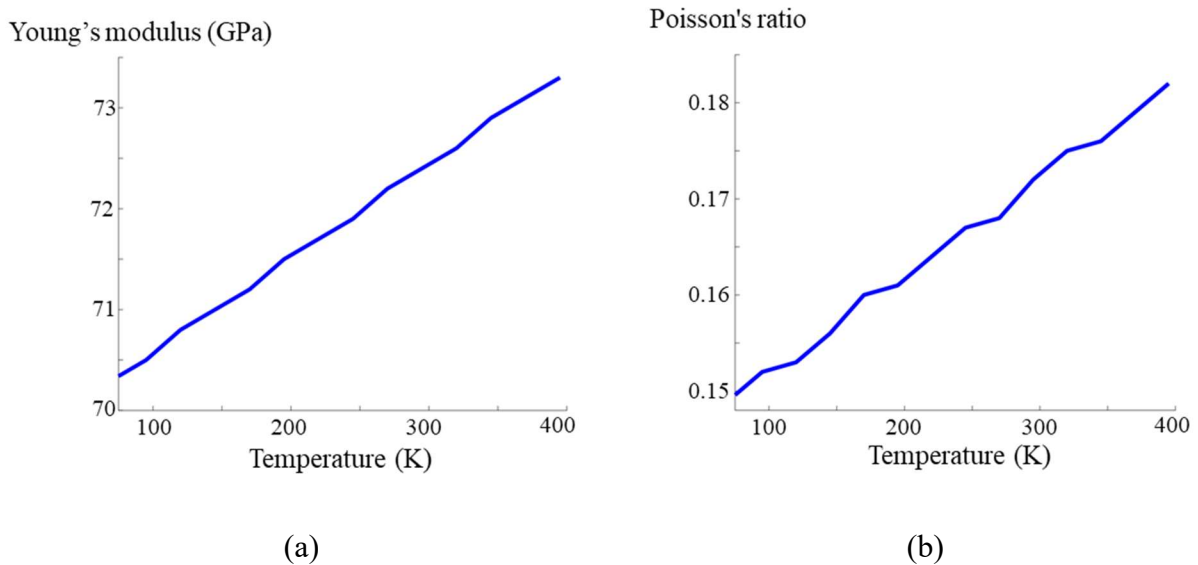


**Figure 4.67:** Effect of temperature on material properties of fused silica, which is reported in [89]. (a) Effect of temperature on Young's modulus. (b) Effect of temperature on Poisson's ratio.

Both numerical and experimental results show that the resonant frequency changes almost linearly with respect to temperature. This change can limit the performance of vibratory gyroscopes. To reduce this effect, two approaches could be used. First, utilizing a thermal

insulation platform that prevents the temperature change in the resonator. Second, utilizing an active temperature control system, which keeps the temperature of the resonator constant.

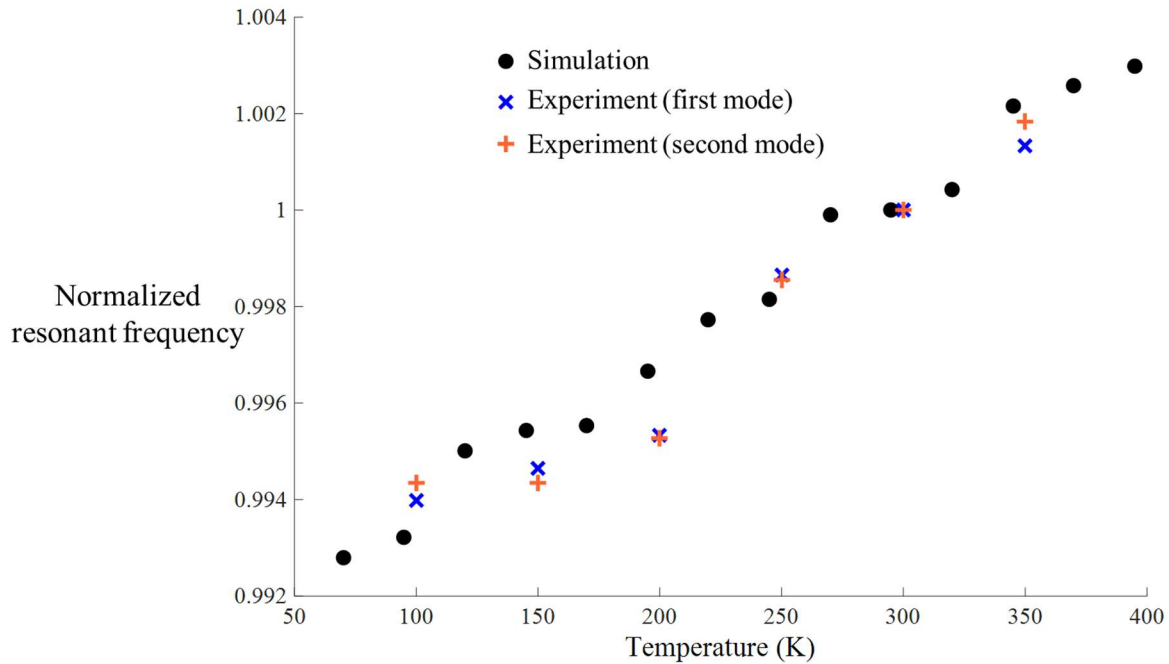


**Figure 4.68:** Effect of operating temperature of the fused silica shell resonator on its resonant frequency. Experimental data and simulation results matched together very well.

#### 4.4.5 Effect of shock on resonant frequency

The existence of shock causes stress and deformation in a shell structure, which can change its resonant pattern. A group of prestressed eigenfrequency simulations is conducted to understand the effects of shock on resonant frequency. To perform this analysis, there is need for two steps:

1) A stationary simulation is conducted to find the deformation and stress in the shell under shock. To simulate shock, a body force that is equal to the amount of shock multiplied by the density of the shell is exerted on the shell. Figure 4.69 shows von Mises stress distribution in the

shell structure under 1,000g horizontal and vertical shocks. This figure shows that both of these shocks create a large stress in the bottom part of the shell.

2) An eigenfrequency simulation is conducted for the system that is prestressed with the existing deformations and stresses from the previous step.

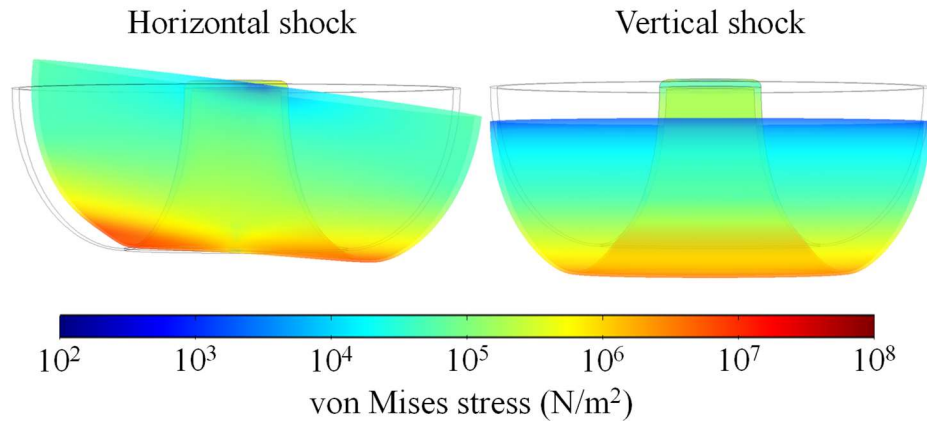


**Figure 4.69:** von Mises stress in birdbath structure under 1,000g shock. Horizontal and vertical shocks cause a large stress in the bottom part of the shell. Horizontal shock creates larger stress in resonant parts of the structure comparing to the vertical shock.

The effects of exerting vertical and horizontal shocks on resonant frequencies are depicted in Figures 4.70 and 4.71. The amounts of these shocks are changed from 0 to 50,000g. Due to the vertical shock, the shell moves upward or downward. Numerical simulation shows that the vertical shock has a small effect on resonant frequency because it does not cause a large stress in the resonating part—stress is mainly created in the bottom part. Additionally, the effects of vertical shock are the same for both modes because the vertical movement does not change the shell axisymmetric shape. In the case of a horizontal shock, the shell moves and tilts toward one side. During the large amount of horizontal shock, a relatively large stress is created in the resonant part of the shell, which changes the resonant frequency. It is also found that a horizontal shock can

cause a frequency split in the shell because it makes the shell structure non-axisymmetric. This reduces the performance of the shell vibratory gyroscopes under shock.

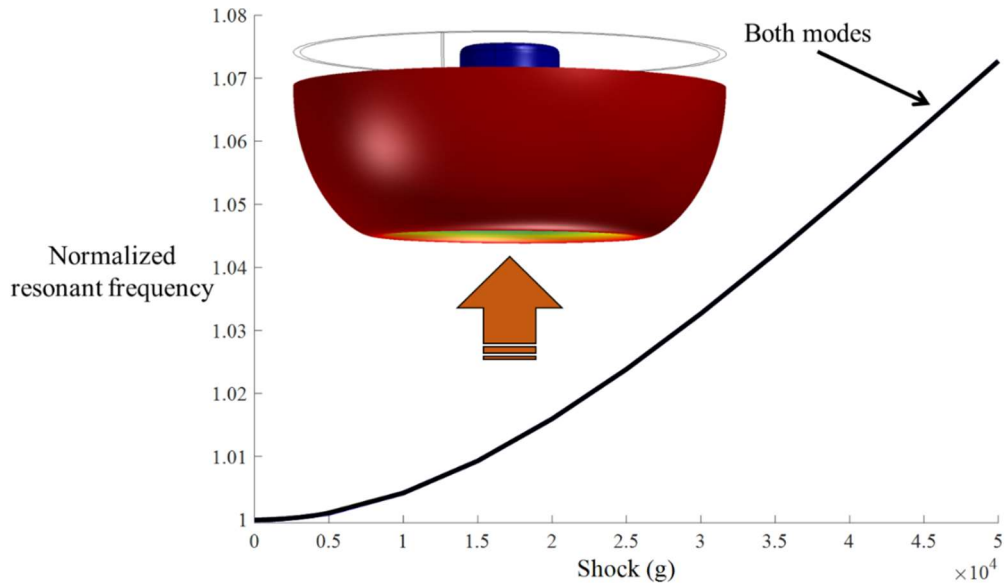


**Figure 4.70:** Effect of vertical shock on resonant frequencies. This shock has a small effect on the resonant frequencies. Additionally, it does not cause any frequency split.

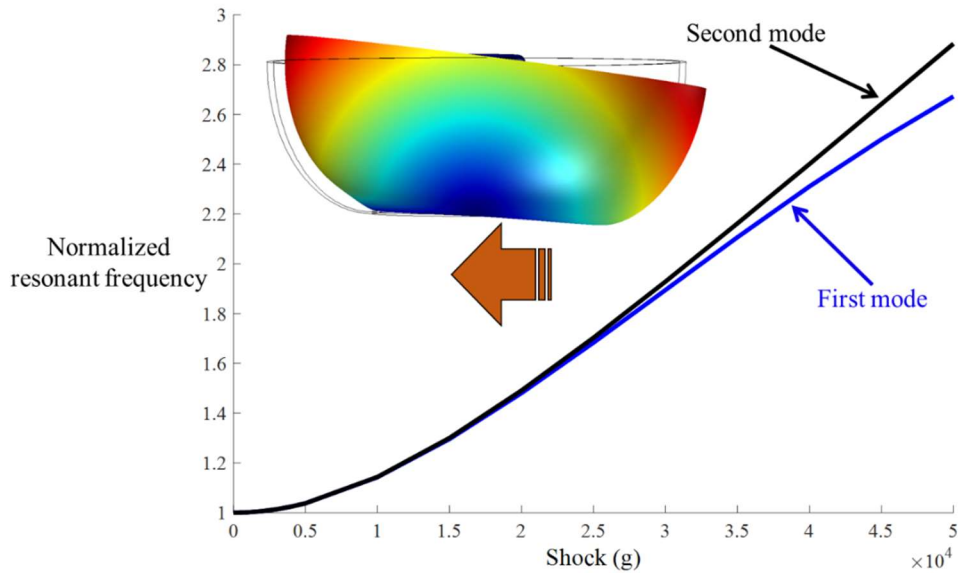


**Figure 4.71:** Effect of horizontal shock on resonant frequencies. This shock has a large effect on the resonant frequencies. Furthermore, it can create frequency split because it makes the system non-axisymmetric.



## 4.5 Frequency Split

Frequency split ( $\Delta f$ ) between sensing and driving modes causes a large performance drop in CVGs. This section talks about the effect of mass and geometric imperfections on the  $\Delta f$  of BSRs, and then an electrostatic tuning approach will be explained to remove small amount of  $\Delta f$ .

### 4.5.1 Effect of imperfection on resonant frequency

As shown in Figure 4.66, preliminary test results of a resonator show a difference between the resonant frequencies corresponding to the two WG modes. As mentioned before, it is critical for a gyroscope that the driving frequency and desired resonant frequencies of its resonator be the same. Existence of a small  $\Delta f$  can be removed by electrostatically tuning the larger resonant frequency (this will be explained in 4.5.5). However, in the case of a large  $\Delta f$ , this is not possible because this need a very large bias voltage. Therefore, imperfections that cause this behavior should be recognized and removed from the structure. This subsection talks about these imperfections.

#### 4.5.1.1 Effect of imbalanced mass at the rim on frequency split

During the fabrication process, it is possible that some extra mass remains on the rim of the resonator. In order to analyze the effect of this extra mass on  $\Delta f$ , a point mass,  $m$ , is added on top of the rim of the shell and the resonant frequencies are calculated.

Figure 4.72 shows the normalized  $\Delta f$  (normalized with respect to the initial resonant frequency of the structure) versus normalized extra mass at the rim of resonator:  $m/M$ , where  $M$  is the mass of the structure. Simulation shows that  $\Delta f$  increases linearly with the increase of the imbalanced mass. The reason is that by placing a point mass on the rim of the shell, the effective

mass of one of the modes increases (first mode), while effective mass of the other mode remains almost constant. In fact, when there is an imbalanced mass in the rim, the shell vibrates in a way that imbalanced mass is located in one of the anti-nodes of the first WG mode and in one of the nodes of second one. The results of this analysis necessitates a precise fabrication process that prevents mass imbalance at the rim.

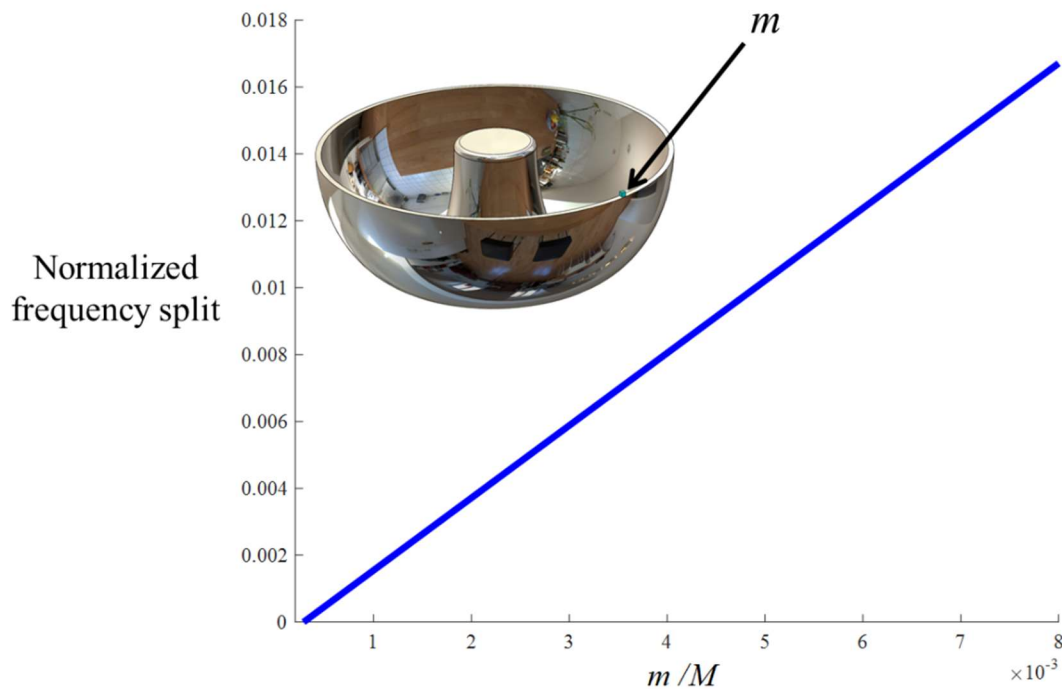


**Figure 4.72:** Normalized  $\Delta f_i$  versus normalized extra mass.  $\Delta f$  increases linearly with respect to increasing amount of point mass at the rim of the shell.

#### 4.5.1.2 Effect of geometric imperfections on frequency split

A close inspection of the fabricated shells reveals two major types of geometric imperfections that may cause the observed  $\Delta f$ : a) out-of-roundness or edge imperfection and b) height imperfection. FEM is used to identify which geometric parameter is the most critical for achieving the  $\Delta f$  tolerance required for high-performance vibratory gyroscopes.

To perform FEM on an imperfect shell, a solid model of the shell without any imperfection is created and then edge and height imperfections are created by distorting the perfect structure using scaled local loads. After creating each imperfection, all displacements from the deformation analysis are added and the geometry is updated to the new deformed configuration.

ANSYS is used to determine the mode shapes and natural frequencies of the resonator models. To capture the effect of an edge imperfection, the roundness of the edge of the perfect structure is locally distorted up to a maximum of 2.4 % of the shell radius. Figure 4.73 represents the sensitivity of the  $\Delta f$  to the edge imperfection. For the shell shown in figure 4.35, a 10  $\mu\text{m}$  edge imperfection creates a large  $\Delta f$  of about 90 Hz. To achieve  $\Delta f \leq 5$  Hz, less than 1  $\mu\text{m}$  edge imperfection is needed. Large sensitivity of the  $\Delta f$  to out-of-roundness in shell radius was expected because as discussed in subsections 4.4.1 and 4.4.2 the shell radius has a large impact on the resonant frequency of the shell. Therefore, using a fabrication process that leads to a very circular rim is essential. In the case of blowtorch molding, since the rim mimics the mold shape utilizing a perfectly circular mold is critical.

To investigate the effect of height imperfection, the height of one side of the structure is distorted by up to a maximum of 3.3 % of the initial height of the shell. Figure 4.74 represents the sensitivity of the  $\Delta f$  to the height imperfection. For the shell shown in Figure 4.35,  $\Delta f$  is not very sensitive to height imperfections less than 40  $\mu\text{m}$ , but for larger height imperfections,  $\Delta f$  can increase rapidly. For example, a 60  $\mu\text{m}$  height offset can cause about 100 Hz of  $\Delta f$ .

Our initial fabricated shells show  $\Delta f$  about 100 Hz. However, using more precise fabrication process (better mold and using a closed-loop controlled stage for blowtorch process) the majority of our shells have  $\Delta f$  less than 20 Hz (several shells achieved frequency split less than 1 Hz), which could be easily removed using electrostatic force.

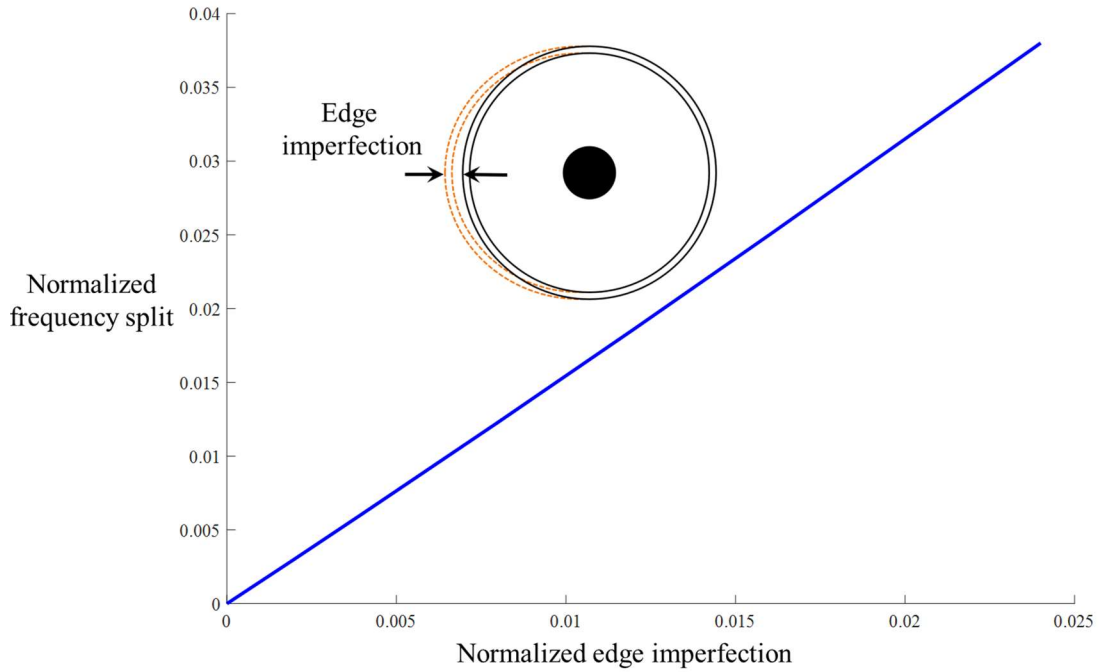


**Figure 4.73:** Effect of edge imperfection on  $\Delta f$ . The results show that the edge imperfection play a key role in  $\Delta f$  between the WG modes.

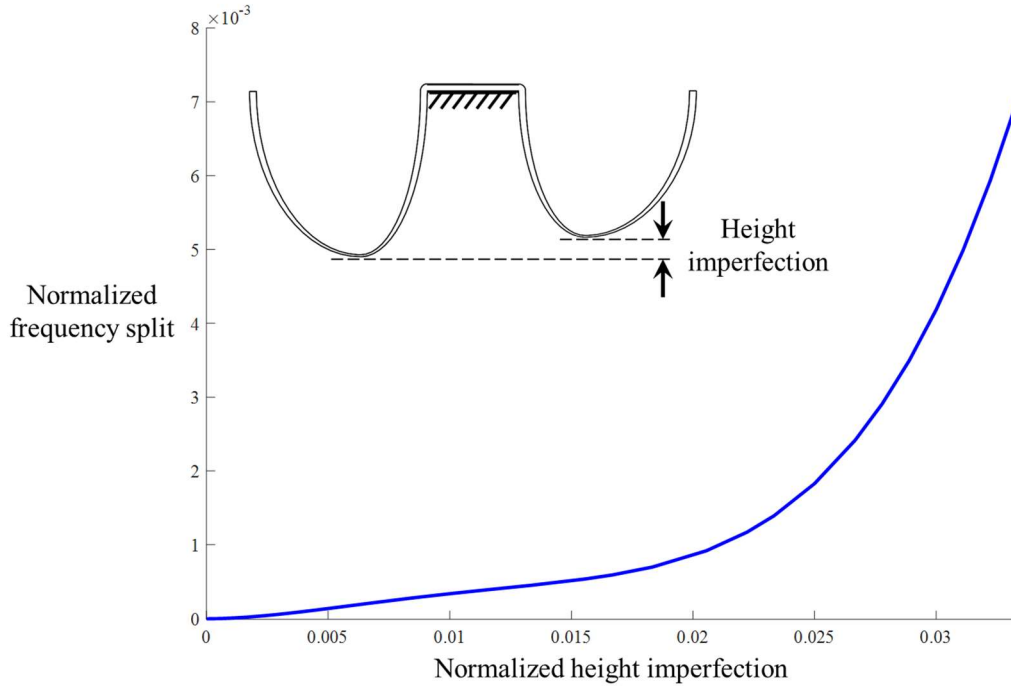


**Figure 4.74:** Effect of height imperfection on  $\Delta f$ . The frequency split is not very sensitive to height imperfections less than  $40 \mu\text{m}$ , but for larger height imperfections, it can increase rapidly.

### 4.5.1.3 Effect of electrostatic tuning on resonant frequency

In order to tune the resonant frequency of a structure, a DC bias voltage can be applied to the electrodes around the structure. This voltage adds the following term to the energy of the system:

$$U_e = -\frac{1}{2}CV^2 \quad (4.67)$$

where  $V$  is voltage and  $C$  is capacitance, given by:

$$C = \frac{\varepsilon A_{eff}}{g_{eff} - q_i} = \frac{\varepsilon A_{eff}}{g_{eff}} \left( 1 + \frac{q_i}{g_{eff}} + \left( \frac{q_i}{g_{eff}} \right)^2 + \dots \right) \quad (4.68)$$

In this equation,  $A_{eff}$ ,  $g_{eff}$ , and  $\varepsilon$  are the effective area, gap, and permittivity between the electrodes and resonator, respectively. The derivative of  $U_e$  with respect to  $q_i$  is shown in (4.69):

$$\frac{dU_e}{dq_i} = -V^2 \frac{\varepsilon A_{eff}}{2g_{eff}} \left( \frac{1}{g_{eff}} + 2 \frac{q_i}{(g_{eff})^2} + \dots \right) \quad (4.69)$$

Ignoring higher order terms, this equation shows that by applying bias voltage, an electrical stiffness is added to the system, which is equal to:

$$K_e = -V^2 \frac{\varepsilon A_{eff}}{(g_{eff})^3} \quad (4.70)$$

This stiffness has a negative value, which reduces the actual stiffness of the structure (this usually referred as electrostatic spring softening effect). This causes the resonant frequency to change as:

$$f - f_{ref} = -V^2 \frac{\varepsilon A_{eff}}{2(g_{eff})^3} \frac{f_{ref}}{K} \quad (4.71)$$

Therefore, normalized change in frequency due to electrostatic tuning is:

$$\frac{f - f_{ref}}{f_{ref}} = -\frac{\epsilon A_{eff}}{2g_{eff}^3 K} V^2 \quad (4.72)$$

Electromechanics module in COMSOL is used to numerically simulate the impact of electrostatic force on the resonant frequency of the BSRs. Figure 4.75 shows experimental data and simulation results. As shown in this figure, the resonant frequency changes linearly with respect to the tuning signal,  $V^2$ .

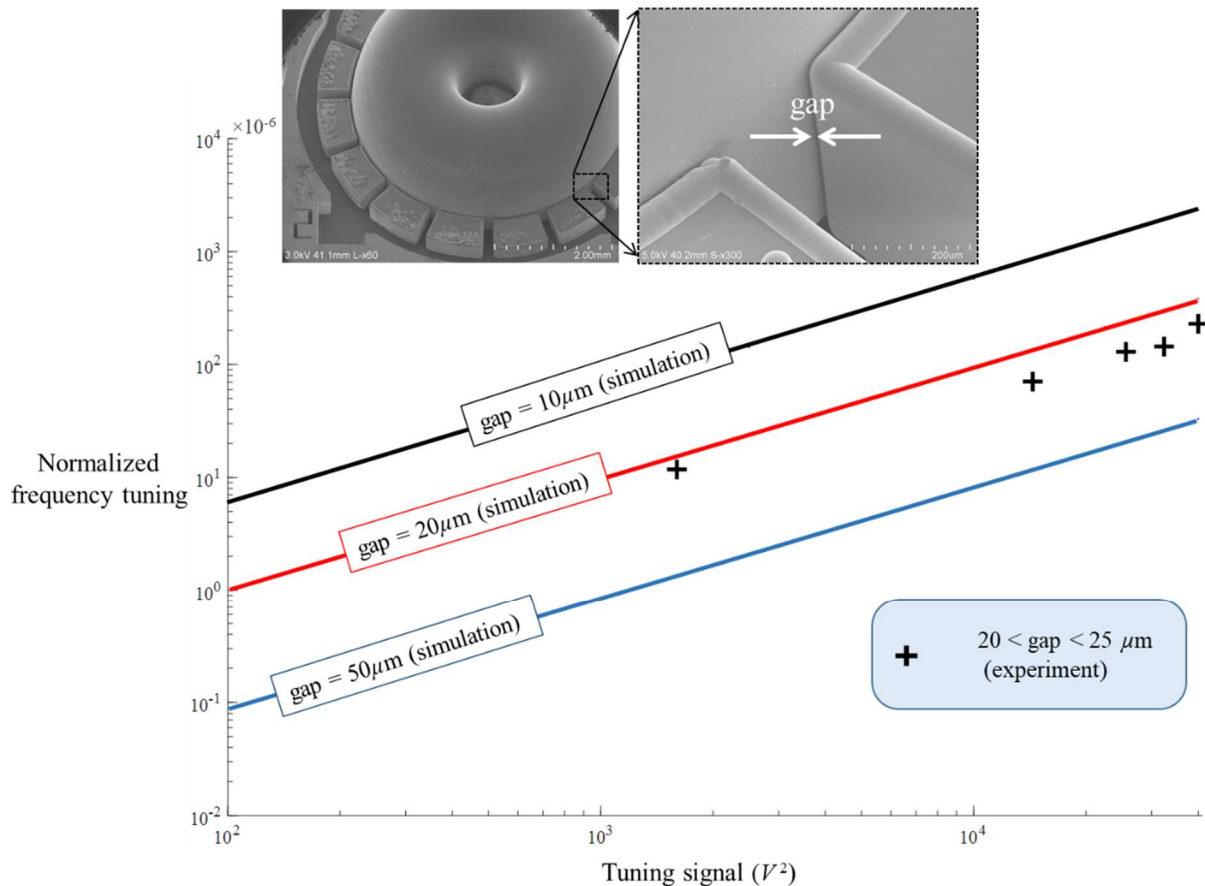


**Figure 4.75:** Effect of electrostatic tuning on normalized change in resonant frequency. The resonant frequency decreases linearly with respect to the tuning signal,  $V^2$ . Here, absolute value of change in resonant frequency is depicted.

Recently we fabricated a shell with gap smaller than  $8 \mu\text{m}$ , using electrostatic tuning we could reduce resonant frequency of this shell (with  $16.5 \text{ kHz}$  resonant frequency) about  $10 \text{ Hz}$  by

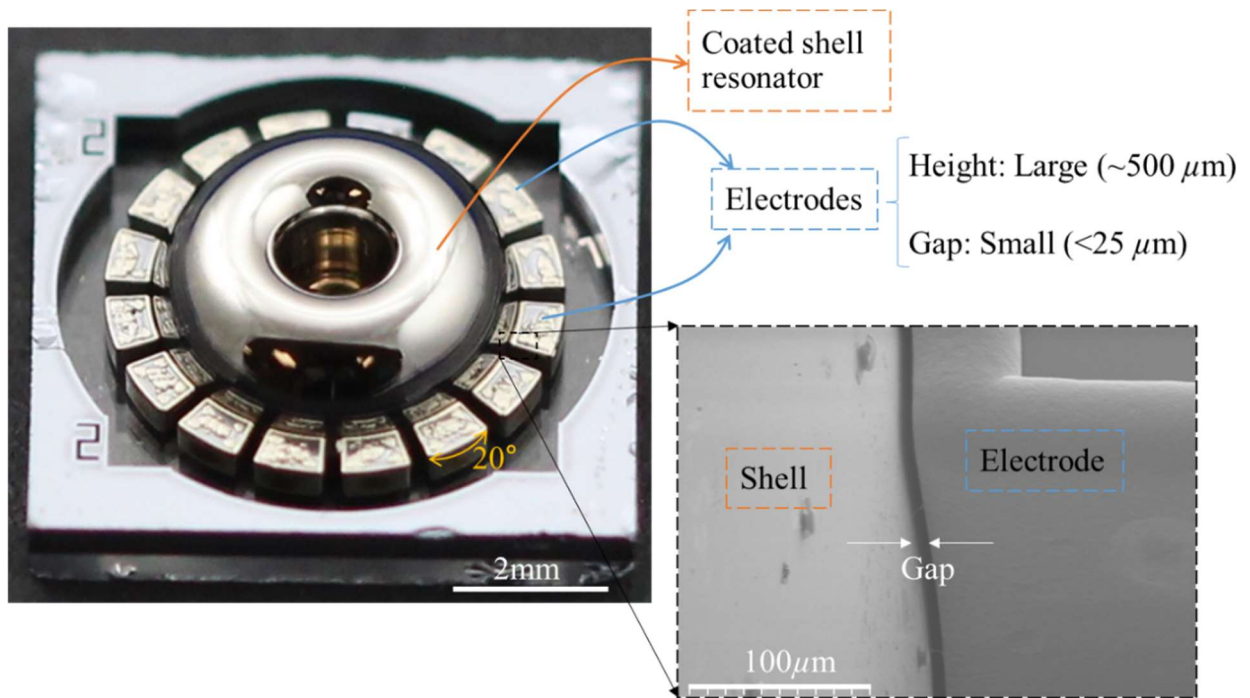
just  $10V$  tuning voltage ( $6.25 \text{ ppm}/V^2$ ). Therefore, we are able to tune a shell with about 20 Hz frequency split by less than 50  $V$  easily.

Using electrostatic tuning, resonant frequencies of one device tuned and measured for a day. The results confirmed that frequency split for this device is always less than the resonator  $BW$  ( $BW = f/Q$ ).

## 4.6 Gyroscope Operation

Shell resonators with high  $Q$ , large angular gain, and small  $\Delta f$  are successfully designed, fabricated and tested. In order to work as gyroscopes, there is a need for electrodes around the shell. Figure 4.76 shows one of these shells integrated with electrodes. These electrodes are made from silicon with  $500\mu\text{m}$  height in a silicon-on-glass process. Four of them used for testing, four for driving and eight for tuning. The gap between electrodes and shell is less than  $25 \mu\text{m}$  and the electrode area is larger than  $1\text{mm}^2$ .

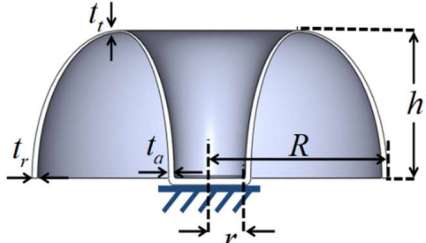
These devices are then operated in force-rebalance mode without active temperature control or scale factor compensation. Figure 4.77 shows the Allan deviation plot for a 5 mm diameter device with about  $2.2 \mu\text{m}$  driving amplitude (gyroscopic tests are done by Mr. Christopher Boyd and Dr. Jong Kwan Woo, the detail can be found in [103]). This device achieved ARW much better than  $0.005^\circ/\sqrt{hr}$ , which is one the best noise performance in any MEMS gyroscope. Furthermore, this gyroscope achieved bias instability about  $0.0391^\circ/hr$ . The gyroscope parameters for this device are shown in Table 4.7.



**Figure 4.76:** A shell integrated with silicon electrodes. Photos used in this figure are courtesy of Dr. Jae Yoong Cho.



**TABLE 4.7: TESTED BSR GYROSCOPE PARAMETERS**

Parameter	Value	Dimensions						
Effective mass, $M_{eff}$ (mg)	0.98	 <table border="1" data-bbox="1019 646 1399 793"> <tr> <td><math>R = 2.5 \text{ mm}</math></td> <td><math>t_r = 80 \mu\text{m}</math></td> </tr> <tr> <td><math>h = 2 \text{ mm}</math></td> <td><math>t_a = 20 \mu\text{m}</math></td> </tr> <tr> <td><math>r = 0.4 \text{ mm}</math></td> <td><math>t_a = 80 \mu\text{m}</math></td> </tr> </table>	$R = 2.5 \text{ mm}$	$t_r = 80 \mu\text{m}$	$h = 2 \text{ mm}$	$t_a = 20 \mu\text{m}$	$r = 0.4 \text{ mm}$	$t_a = 80 \mu\text{m}$
$R = 2.5 \text{ mm}$	$t_r = 80 \mu\text{m}$							
$h = 2 \text{ mm}$	$t_a = 20 \mu\text{m}$							
$r = 0.4 \text{ mm}$	$t_a = 80 \mu\text{m}$							
Angular gain, $A_g$	0.56							
Quality factor, $Q$ (1 <sup>st</sup> $n = 2$ WG mode)	401,176							
Quality factor, $Q$ (2 <sup>nd</sup> $n = 2$ WG mode)	419,047							
Resonant frequencies, $f$ (kHz)	9.030							
Driving amplitude, $q$ ( $\mu\text{m}$ )	2.2							
Gap (electrodes and shell), $d_0$ ( $\mu\text{m}$ )	23							

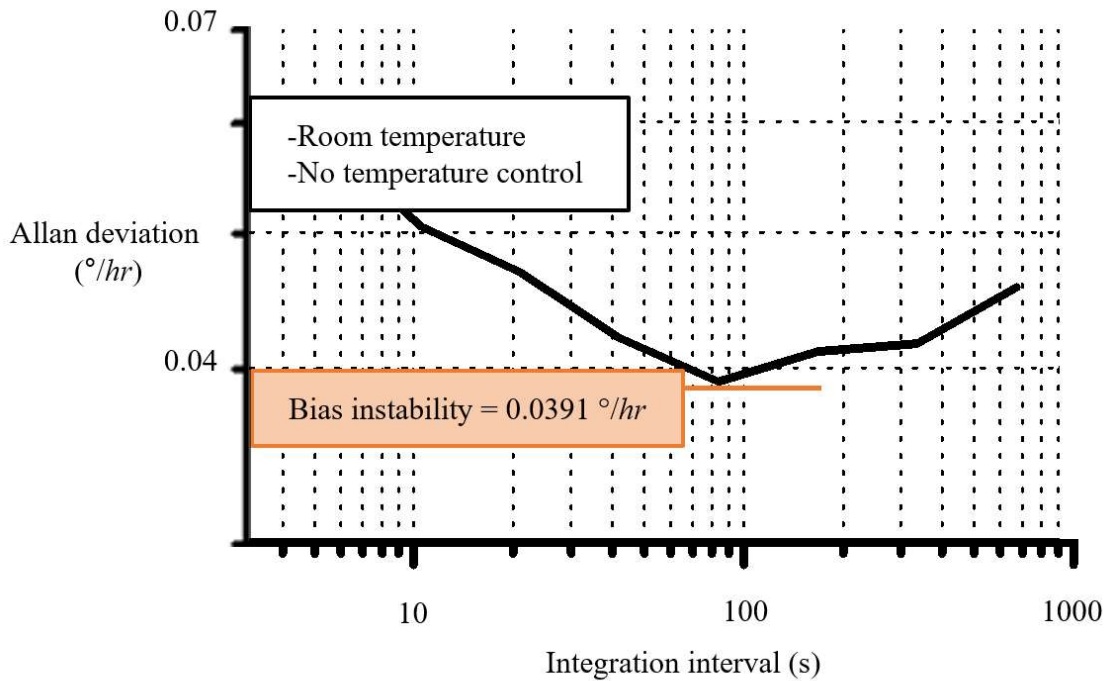


**Figure 4.77:** Allan deviation plot for a BSR gyroscope. This device achieved one of the best ARW and bias instability in MEMS gyroscopes. Test is done by Mr. Christopher Boyd and Dr. Jong Kwan Woo (the detail can be found in [103]).

Figure 4.78 shows the effect of driving amplitude on ARW of the device with parameters reported in Table 4.7. As analytically modeled in chapter 2, increasing driving amplitude should improve ARW. Figure 4.78 shows that when the driving amplitude is in the range of 10% of the gap between the shell and electrodes, increasing driving amplitude reduces ARW, as expected. However, when the driving amplitude becomes larger than  $2.2 \mu\text{m}$  (about 10% of the gap), ARW increases. We believe this is due to the non-linearity caused by electrostatic force. To remove this non-linearity, gap should be larger, which reduces tuning capability of the device. If we could make shells with smaller  $\Delta f$ , then we do not need a large tuning capability; therefore, increasing the gap size will benefit us. Figure 4.78 also confirmed the validity of analytical model developed for ARW calculation.

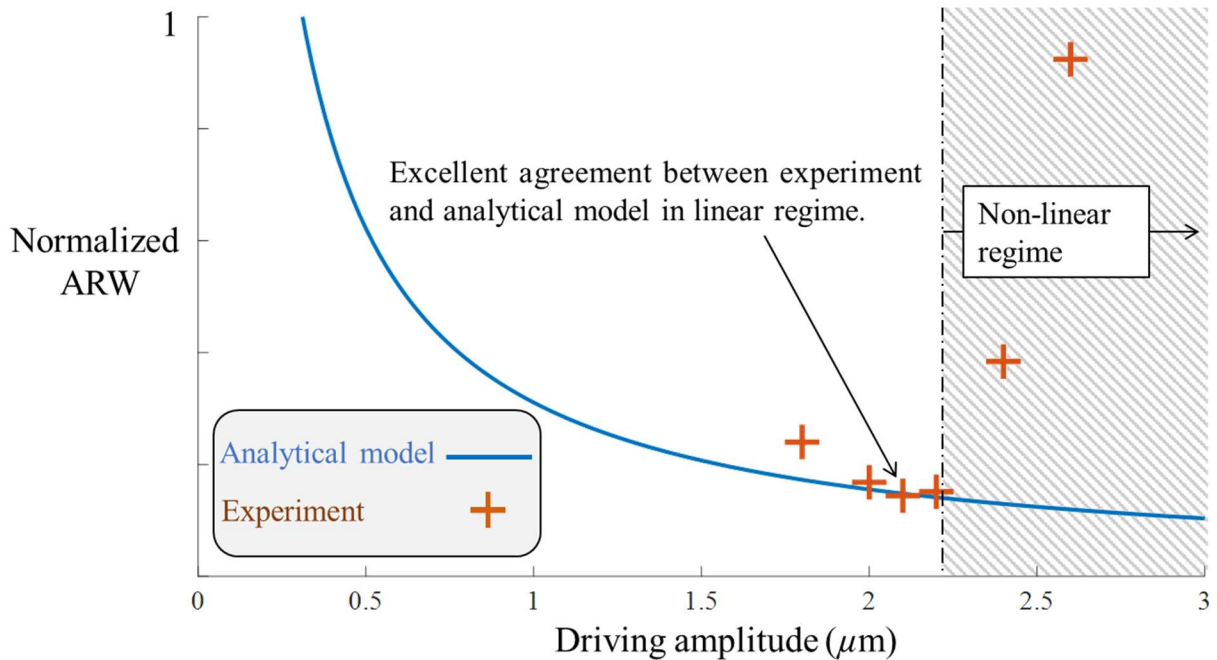


**Figure 4.78:** Effect of driving amplitude on ARW in a BSR gyroscope. Experiment is done by Mr. Christopher Boyd and Dr. Jong Kwan Woo.

## 4.7 Conclusion

A shell gyroscope has been designed, fabricated, and tested using the CVGs design-guideline that was provided in chapter 2. Theoretical, numerical and/or experimental methods have been used to optimize the shell gyroscopes parameters. As a results, BSRs have been made with  $Q$  in range of several million (one shell achieved  $Q$  higher than 10 million). Furthermore, large angular gain, small frequency split, large driving amplitude, small sensing gap, and large capacitive area have been achieved. A comprehensive investigation on resonant frequency of shell resonators has been conducted. It is found that resonant frequency is easily designable using methods provided in this chapter. However, resonant frequency should be in particular range since it has a contradictory impact on thermomechanical and electronic noises. For the design provided in this chapter as long as resonant frequency is between 2 kHz to 100 kHz, both noises should be very small.

The biggest challenge in shell gyroscopes is their small effective mass as only a small portion of rim moves in  $n = 2$  WG modes. To overcome this challenge, simulation results have suggested increasing the shell height, radius, and rim thickness. Another challenge is non-linear behavior of the gyroscope as driving amplitude becomes larger than 10 % of the gap between the shell and electrodes. This was expected since parallel plate electrostatic actuation has been used for driving BSR gyroscopes. It has been observed that when the driving amplitude in a BSR gyroscope increases in a non-linear regime, the performance of the gyroscope degraded. Nevertheless, as shown in Figure 4.79 the majority of the design parameters for low-noise CVGs are satisfied in the BSRs.

As a result, a MEMS shell resonator gyroscope with matched WG frequencies and high  $Q$  has been tested in the force-to-rebalance mode. This gyroscope provided one of the best performance in MEMS gyroscope, which satisfies requirement for inertial navigation.

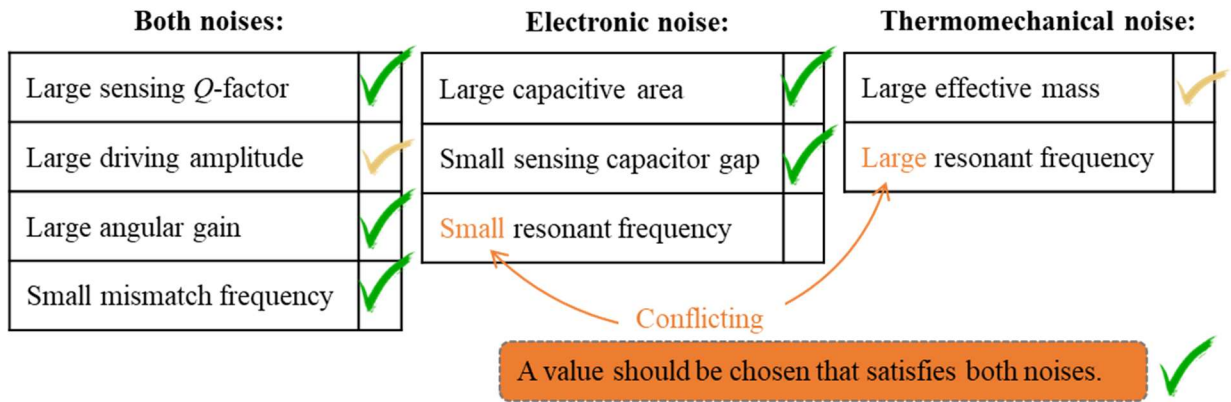


**Figure 4.79:** Checking BSR gyroscopes design parameters. BSR gyroscopes satisfy majority of the design parameters.

## Chapter 5: Design and Analysis of Extremely High-Performance Pitch or Roll Gyroscopes

As discussed in chapter 3, the  $S^3$  structure can be used as either a pitch or roll gyroscope. In this chapter, only the  $S^3$  gyroscope for roll direction will be analyzed. The CVGs checklist shown in Figure 5.1 should be satisfied for the  $S^3$  gyroscope.

In this chapter, the main problem of current roll gyroscopes will be discussed first. Then, it will be shown why the  $S^3$  gyroscope can overcome this problem. Finally, the design parameters for  $S^3$  gyroscopes will be optimized and it will be shown that these gyroscopes can achieve an extraordinary performance. Similar to previous chapter, one can use the step-by-step design of  $S^3$  gyroscopes presented here as a comprehensive guideline for designing extremely high-performance gyroscopes.

Both noises:	Electronic noise:	Thermomechanical noise:
Large sensing $Q$ -factor	Large capacitive area	Large effective mass
Large driving amplitude	Small sensing capacitor gap	Large resonant frequency
Large angular gain	Small resonant frequency	
Small mismatch frequency		

**Figure 5.1:** Design checklist for CVGs that should be satisfied for  $S^3$  gyroscopes.

In this chapter, design parameters shown in Figure 5.1 will be analyzed in different sections with the following order:

- 5.1 Sensing quality factor
- 5.2 Effective mass
- 5.3 Angular gain
- 5.4 Resonant frequency
- 5.5 Frequency split between driving and sensing modes
- 5.6 Driving amplitude, sensing gap and area

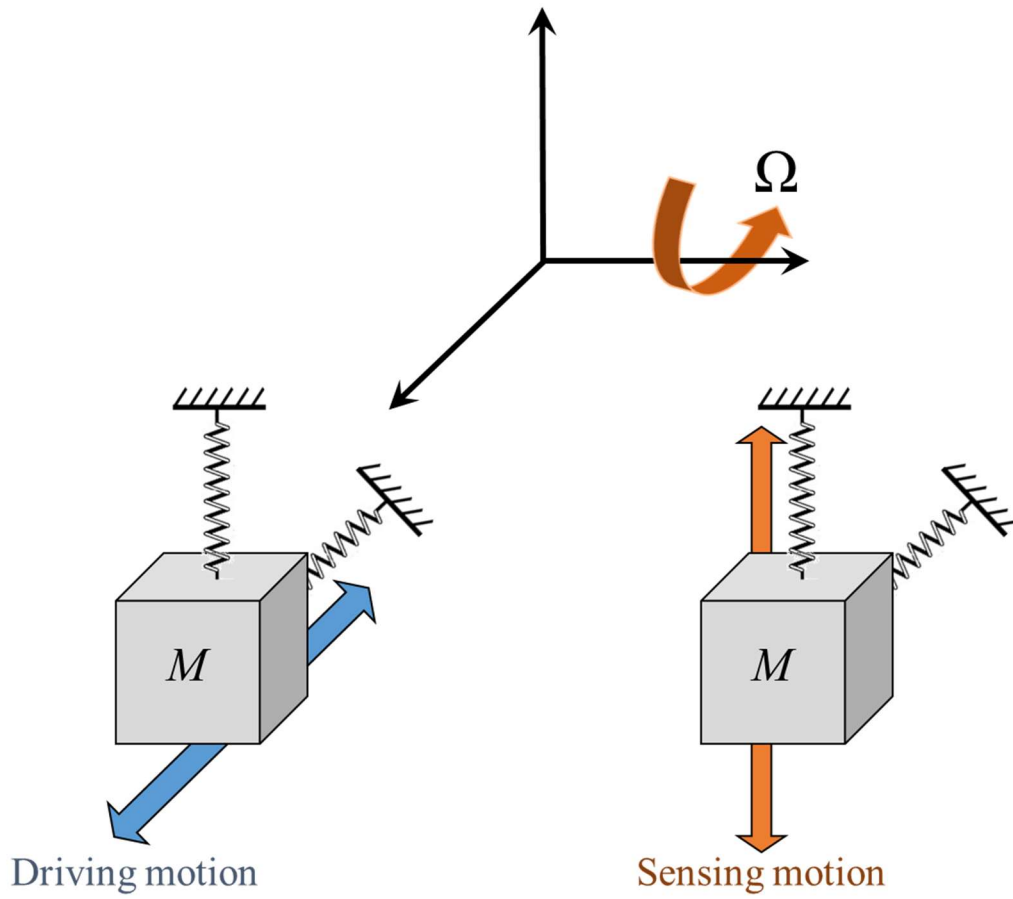
Detail investigation of each parameter is provided in the following sections:

## 5.1 Sensing Quality Factor

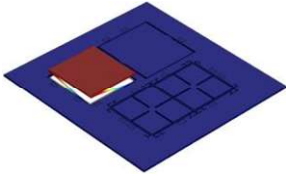
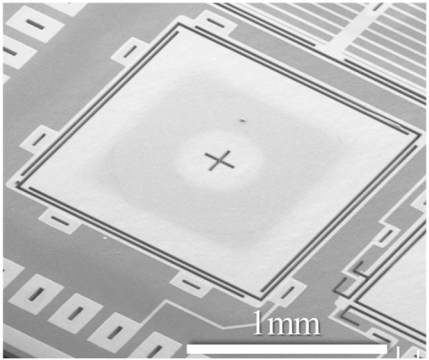
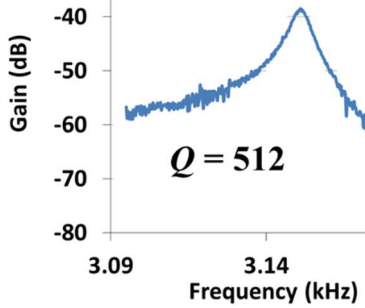
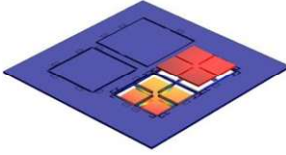
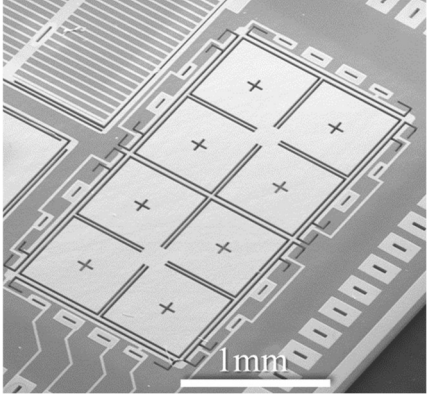
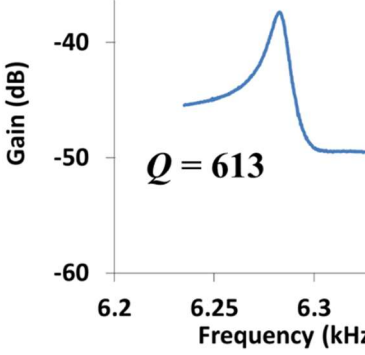
As a simple model for a roll gyroscope, the gyroscope mass should be driven in in-plane mode. When there is a rotation around the roll axis, the mass starts to vibrate in the out-of-plane mode due to Coriolis acceleration. Figure 5.2 shows this concept.

Therefore, it is very important that the vibrating mass has a very high- $Q$  in out-of-plane mode. However, existing out-of-plane mode resonators provide very small  $Q$ . Two generations of fused silica resonators vibrating in the out-of-plane mode were fabricated.

Figure 5.3 shows the first generation of resonators. In this generation, the fused silica thickness is about  $50\ \mu\text{m}$ . As seen, the  $Q$ s in the out-of-plane mode are extremely small ( $<1000$ ). However, the WG mode of a ring resonator with outside anchors made in this generation produced  $Q$  of 33,260.



**Figure 5.2:** Operation principle of a roll gyroscope. A mass is driven in the in-plane mode and it will be moved in out-of-plane mode due to Coriolis acceleration.

Device	Mode shape	SEM	Frequency response
1			
2			

**Figure 5.3:** First generation of fused silica resonators in out-of-plane mode and their frequency responses. These resonators show extremely low  $Q$  in the out-of-plane mode (the fabrication was done by Dr. Zongliang Cao and Mr. Yi Yuan and testing was done by Dr. Gouhohng He).



In the second generation of out-of-plane resonators, a supporting frame, shaped as a cross, is placed between the fused silica layers. Figure 5.4 shows SEM of the second-generation devices and their frequency responses. These figures show that  $Q$ s in out-of-plane mode are still very small, with only  $\times 4$  improvements in performance.

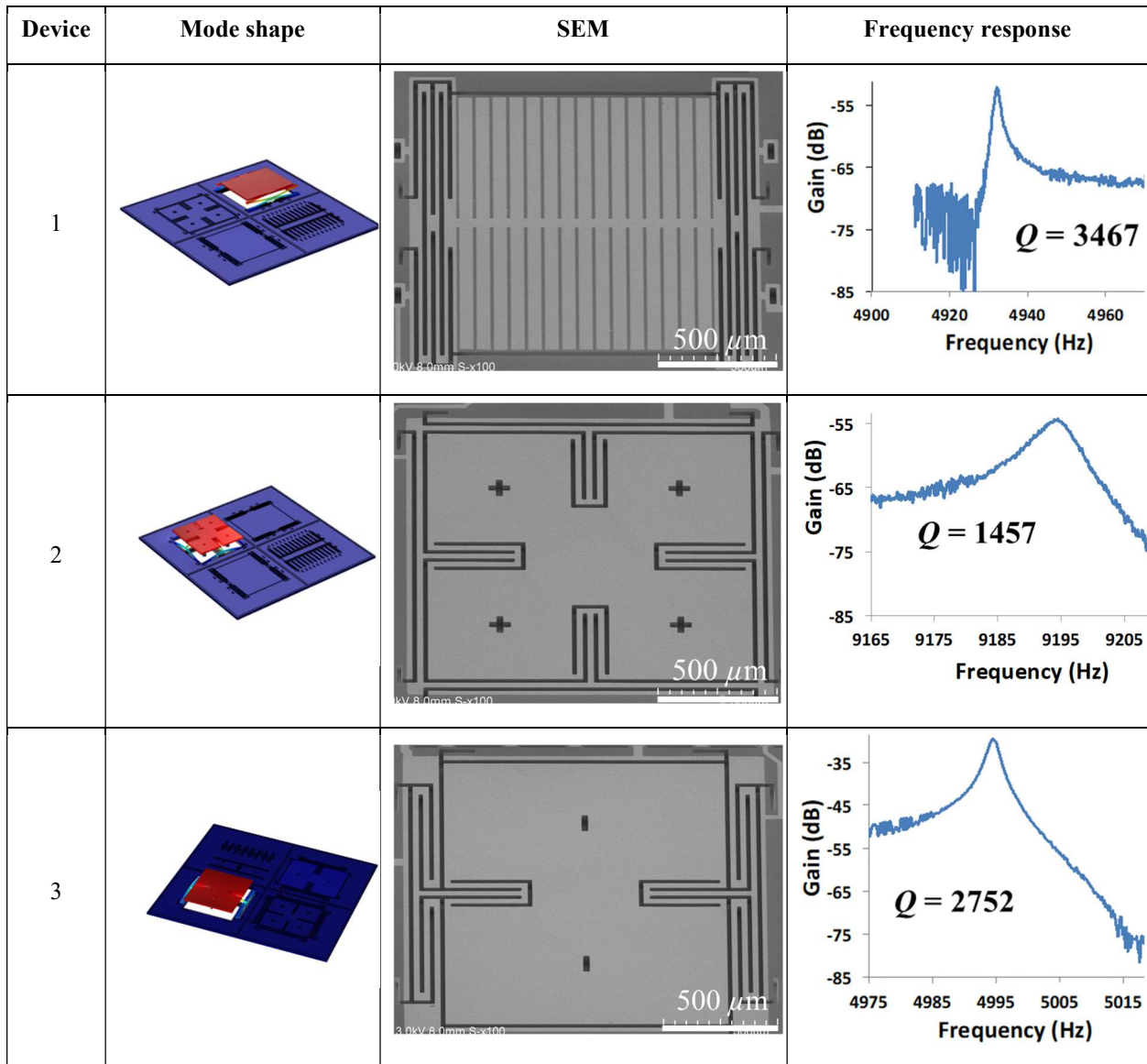


**Figure 5.4:** Second generation of fused silica resonators in out-of-plane mode and their frequency responses. These resonators show low  $Q$  in the out-of-plane mode.

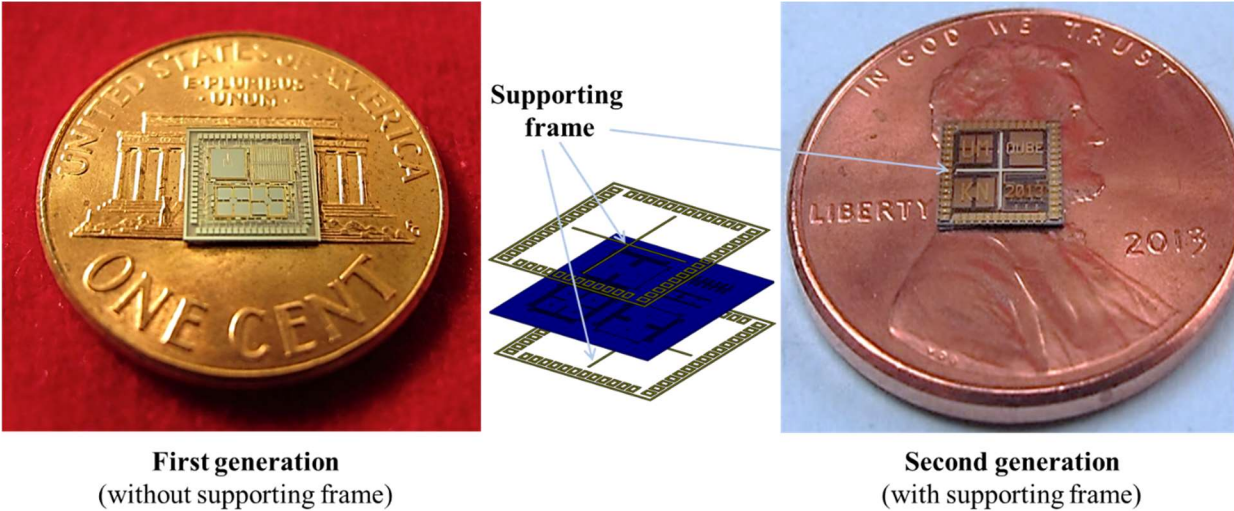


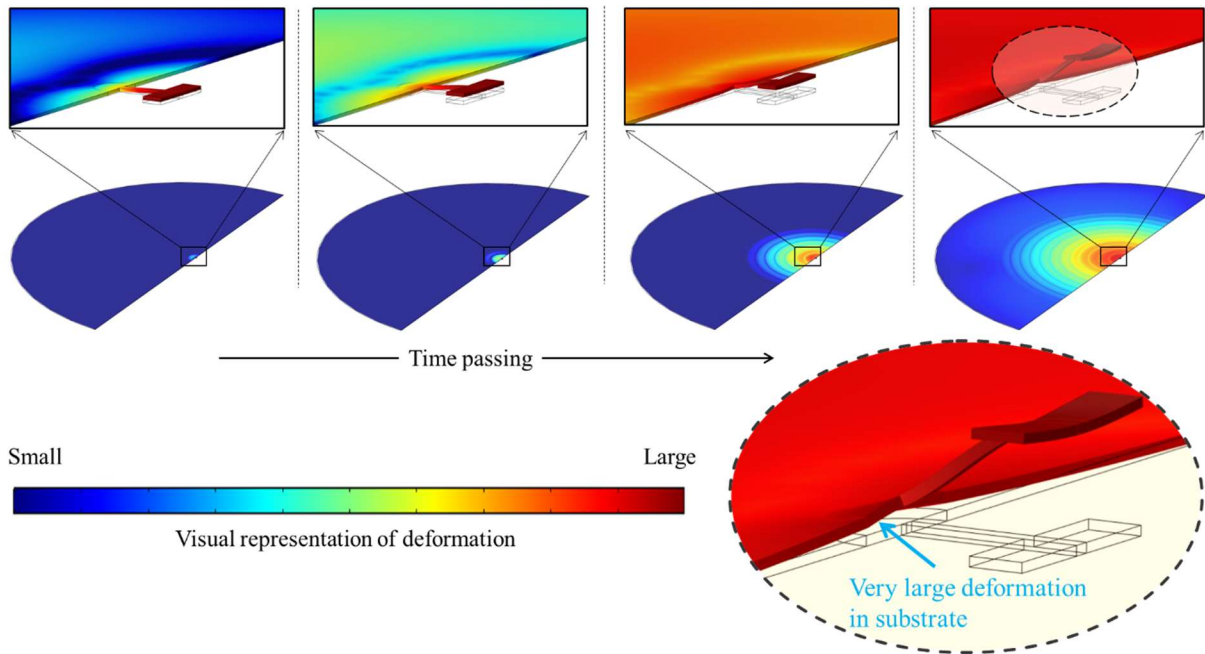
**Figure 5.5:** Difference between the first and second generations of fused silica out-of-plane resonators. In general, the second-generation devices tend to produce larger  $Q$ s in the out-of-plane mode.

In the second generation, the design was different, but the fused silica thicknesses was the same. Figure 5.5 shows the main difference between the first and second generations, which uses a supporting frame between devices. Using this supporting frame reduces motion in the anchored area that might reduce anchor loss. Nevertheless, these resonators still have orders of magnitude smaller  $Q$ s comparing to expected values from a fused silica resonator. All these devices have been tested in vacuum chamber, they are made from fused silica, and their  $V/S$  is larger than  $20 \mu\text{m}$ ; therefore, fluidic damping, TED, phonon-phonon interactions, intrinsic loss and surface loss should not cause these small values for  $Q$ s. As a result, anchor loss seems to be the main problem in dissipation of energy from these resonators when they are resonating in the out-of-plane mode. The differences between the  $Q$ s of WG mode and out-of-plane modes and the differences between the  $Q$ s of the resonators with and without supporting frame show more evidence for this hypothesis.

In the next subsection, it will be shown why micromachined devices produce low  $Q$  in out-of-plane mode. Furthermore, a novel design that will remove this problem from out-of-plane resonators will be discussed in detail.

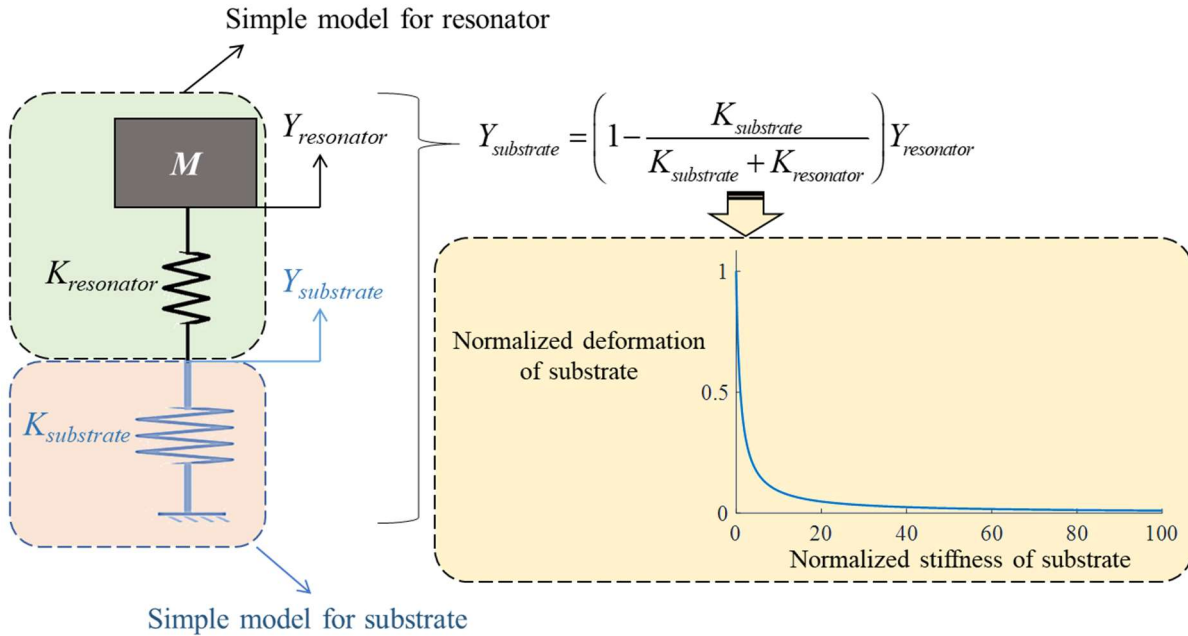
### 5.1.1 Anchor loss in out-of-plane mode

Figure 5.6 shows the substrate deformation for an out-of-plane resonator. In this case, the resonator and substrate have the same thickness as the low  $Q$  resonators presented above. Because of the substrate thickness, the deformation of the resonator in out-of-plane mode causes a large deformation in the substrate. Therefore, mechanical waves easily propagate from the resonator into the substrate, causing a large anchor loss.



**Figure 5.6:** Visual representation of deformation in substrate of a single mass resonator as vibrating in out-of-plane mode. When the substrate and resonator have the same thickness, resonator movement causes a large deformation in the substrate.

Figure 5.7 shows a simple model for the resonator and substrate vibration. In this figure, the resonator consists of a mass and spring and the substrate is just assumed to be a spring.  $Y_{resonator}$  shows the movement of the resonator and  $Y_{substrate}$  shows the effective deformation of the substrate. Based on this simplified model, as the stiffness of the substrate decreases, the deformation in the substrate increases leading to a large anchor loss.



**Figure 5.7:** A simple model for the interaction of the resonator and substrate. Decreasing ratio of the substrate to resonator stiffness, increases the deformation in the substrate, leading to a large anchor loss.

Decreasing the substrate thickness reduces its stiffness in the out-of-plane direction largely. Therefore, when the substrate and resonator have the same thickness, anchor loss is large, resulting to a low  $Q$  system. Judge *et al.* [59] investigation of the effect of the substrate thickness on  $Q$  of beam resonators has proven that decreasing the substrate thickness reduces  $Q$ . Numerical simulation using PML around the substrate, with the same thickness as the substrate, shows that  $Q$  reduction is due to anchor loss. Table 5.1 shows the experimental and numerical simulation results of the effect of substrate thickness on  $Q$ . According to these results, increasing substrate

thickness can improve  $Q_{Anchor}$  in out-of-plane mode more than 100 times. Furthermore, the agreements between the experimental data and FEM results validates accuracy of utilizing a PML around the substrate to simulate the anchor loss in resonators.

**TABLE 5.1:** EFFECT OF SUBSTRATE THICKNESS ON  $Q$  (EXPERIMENTAL DATA AND FEM SIMULATION SHOW AN EXCELLENT AGREEMENT)

Geometry				$Q$	
Beam length (mm)	Beam width (mm)	Beam thickness (mm)	Substrate thickness (mm)	Experiments [59]	$Q_{Anchor}$ (numerical simulation)
19.05	2.54	1.37	1.644	2.9	4.1
19.05	2.54	1.27	4.826	52	54.7
19.05	2.54	1.19	9.52	306	289.3
19.05	2.54	1.09	12.644	360	652.3

Resonators made using MEMS bulk micromachining usually have the same thickness as the substrate. Therefore, it is expected that they show low  $Q$  in the out-of-plane mode. Micromachined resonators usually show higher  $Q_{Anchor}$  in the in-plane mode because the substrate thickness has less effect on the stiffness of the substrate in the horizontal direction compared to the vertical direction. To confirm this hypothesis, the effects of substrate thickness on the  $Q_{Anchor}$  of a single mass resonator are simulated for in-plane and out-of-plane modes. According to Figure 5.8, the substrate thickness has 36 times more impact on the out-of-plane mode than in-plane mode.

Increasing the substrate thickness or reducing the resonator thickness increases cost, size, and complexity of the system. Therefore, another approach should be used to reduce anchor loss in out-of-plane mode of MEMS resonators.

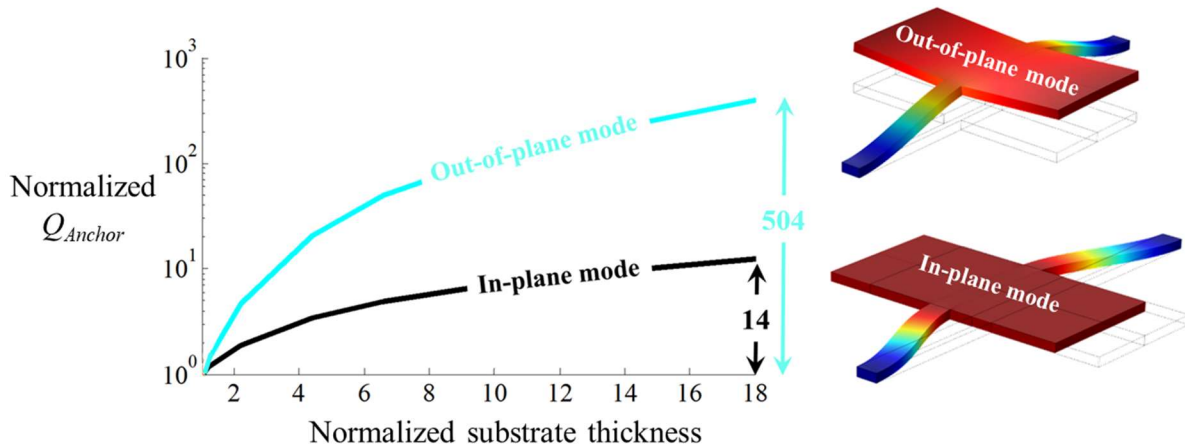


**Figure 5.8:** Effect of substrate thickness on  $Q_{Anchor}$  of in-plane and out-of-plane modes of a single mass resonator. Substrate thickness affects  $Q_{Anchor}$  of out-of-plane mode largely.

### 5.1.1.1 A novel idea to reduce anchor loss in out-of-plain mode

One approach to remove anchor loss is creating a virtual nodal point at the contact of the resonator and substrate. To understand this approach, one can consider rope-pulling game, where large values of force stretch the rope from both sides but there is no movement in the rope. This is due to the balance of the forces. Figure 5.9 shows the concept of force balancing.

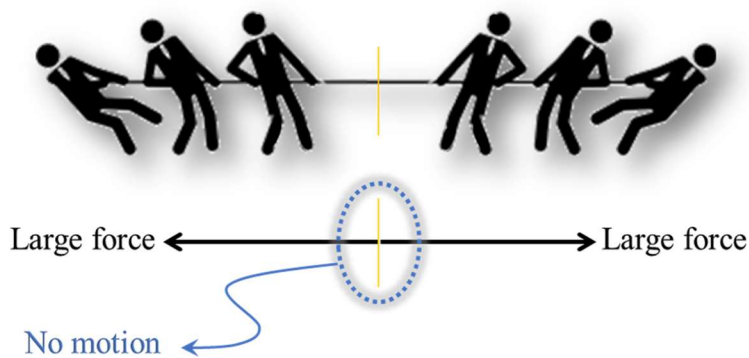


**Figure 5.9:** Schematic of force balancing in rope-pulling. Since equal forces pull the rope in opposite direction, there is no movement.

To create this force-balancing concept for out-of-plane motion, one can consider the simple model shown in Figure 5.10. In this figure, the resonator consists of two similar springs and masses, which move equally in opposite directions. Based on this simplified model, there is no motion in the substrate.

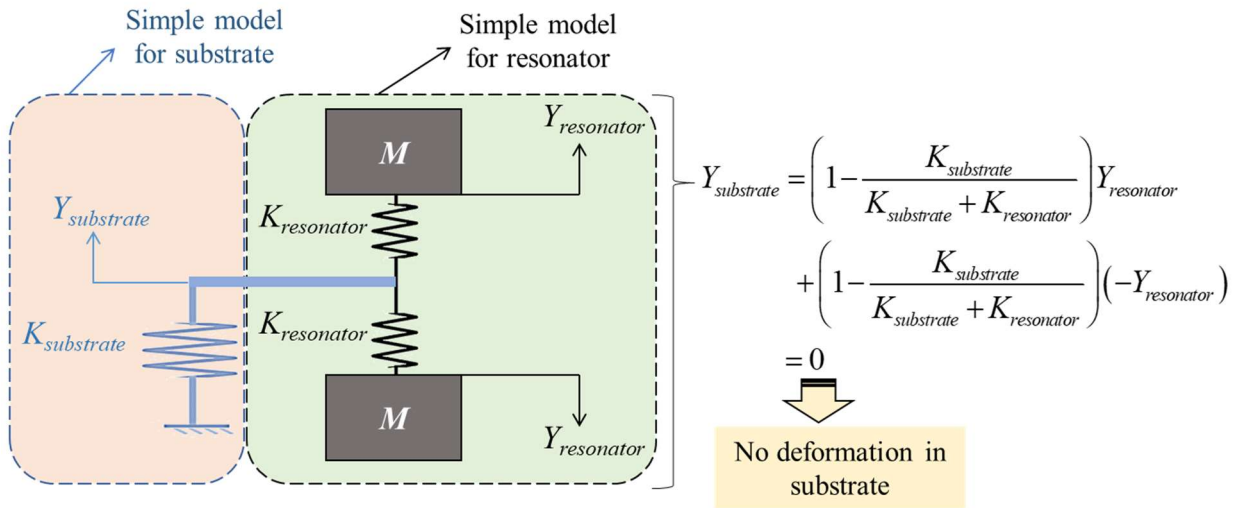


**Figure 5.10:** A simple model for the force balanced out-of-plane resonator. Based on this model, there should not be any motion in the substrate of this resonator.

This force-balanced idea should provide a very high  $Q_{Anchor}$ . To create example geometry for this idea, a resonator with two device layers stacked on top of each other can be constructed. These layers are coupled together using an intermediate bonding layer. In each device layer, there is a resonant mass that is connected to the perimeter with suspended beams. To calculate  $Q_{Anchor}$  of this type of resonators, numerical simulation is used to conduct modal analysis with an appropriate PML around the substrate. Figure 5.11 shows the dimensions used for this simulation and the relative deformations in the resonator and its substrate.

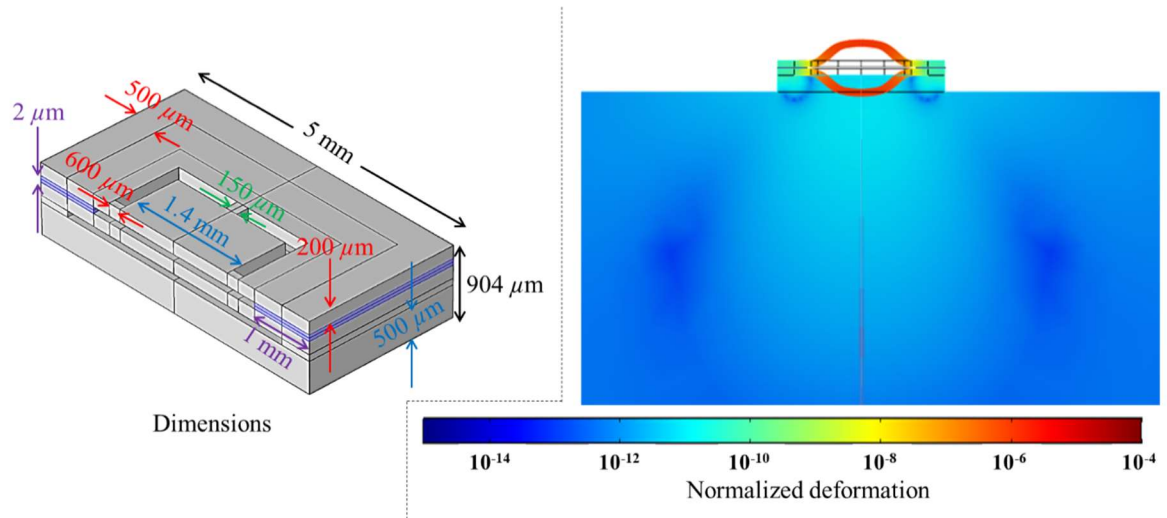


**Figure 5.11:** Left: dimensions used for anchor loss simulation in stacked force-balanced resonator. Right: normalized deformation in cross section of this resonator and the substrate beneath it.

$Q_{Anchor}$  in this stacked resonator calculated to be larger than  $1.6 \times 10^8$ , while  $Q_{Anchor}$  for non-stacked device with the same dimension is only 860. Therefore, stacking improves  $Q_{Anchor}$  by about five orders of magnitude compared to the initial resonator. Figure 5.12 clearly shows that deformation in the substrate of a stacked resonator is much smaller than a non-stacked one. In this figure, deformations are shown for different amount in the substrate. When just deformations larger than  $10^{-10}$  m are sketched, there is no deformation in the stacked resonator substrate. Comparing the deformation in the substrates of stacked and non-stacked resonators shows more than a hundred times larger deformation in the non-stacked substrate, which causes larger anchor loss. This figure also includes the schematic of wave propagations in stacked and non-stacked resonators. In the stacked resonator, forces from the top and bottom layers cancel each other out in the bond area between these layers.



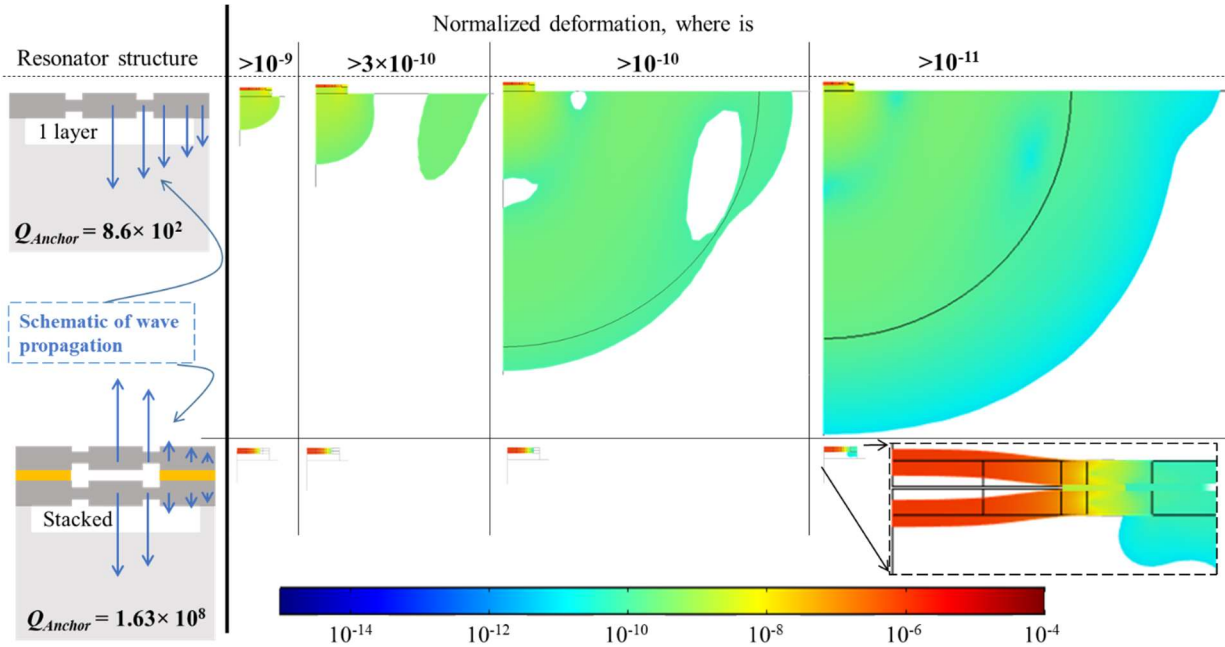


**Figure 5.12:** Left: schematic of wave propagation in the 1 layer and stacked force-balanced resonators. Right: normalized deformation in the substrate of these resonators for different amount of deformation.

**5.1.1.2 Impact of various parameters on anchor loss of stacked resonators**

Figure 5.13 shows parameters that have impact on anchor loss of the stacked resonators.

This subsection describes the effects of them on anchor loss of stacked resonators. These properties are classified in three categories:

- a) Device layer properties
- b) Bonding properties
- c) Cap layer properties

They will be discussed in detail in the following subsections.

A group of simulations is performed using PMLs to calculate the effect of these properties.

For a non-stacked resonator with the dimensions shown in Figure 5.11,  $Q_{Anchor}$  is calculated to be 860, which is used to normalize  $Q_{Anchor}$  (normalized  $Q_{Anchor} = Q_{Anchor} / 860$ ) in this subsection.

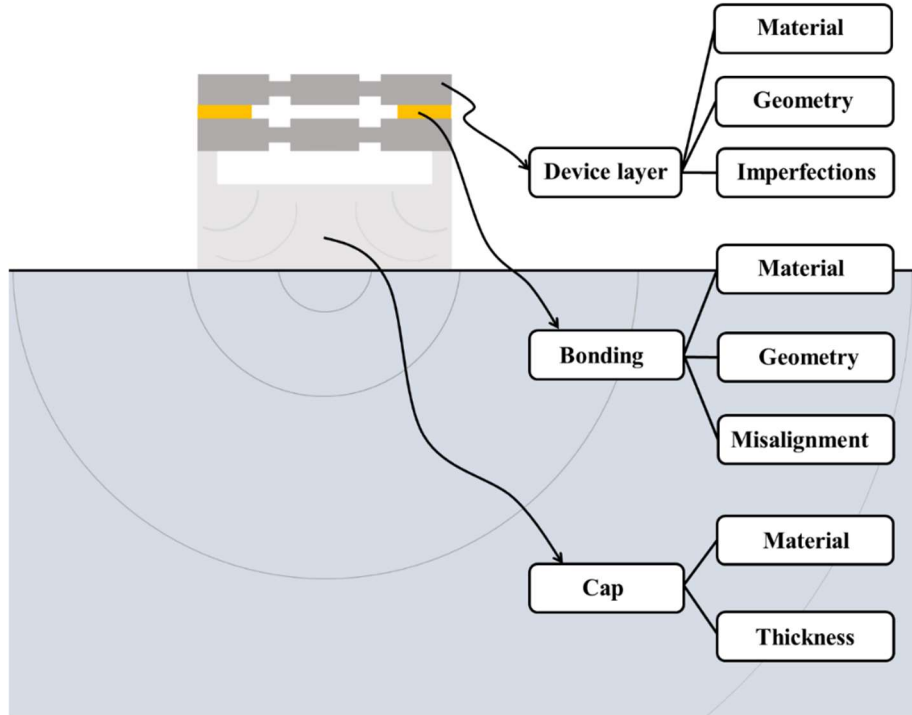


**Figure 5.13:** Classification of important parameters affecting anchor loss in stacked resonators. The anchor loss depends on the device, bonding, and cap layers properties.

**a) Effect of Device Layer Properties on Anchor Loss of Stacked Resonators**

Figure 5.14 shows the effect of device layer material properties on  $Q_{Anchor}$ . The material properties of the device layer is changed from silicon, while material properties of other parts are fixed. Figure 5.14 shows that by increasing the Young’s modulus, anchor loss increases because a stiffer device can deform the cap easier; therefore, more energy escapes from the cap to the substrate. Increasing the density reduces anchor loss because a denser resonator can keep more kinetic energy. Furthermore, this figure shows that increasing the Poisson’s ratio increases anchor loss. In fact, in-plane forces cause compression or stretching in the device layer and the Poisson’s effect converts them to out-of-plane forces. Since these out-of-plane forces are in the same

direction for both layers, they do not cancel each other out. Therefore, increasing the device layer Poisson's ratio increases anchor loss.

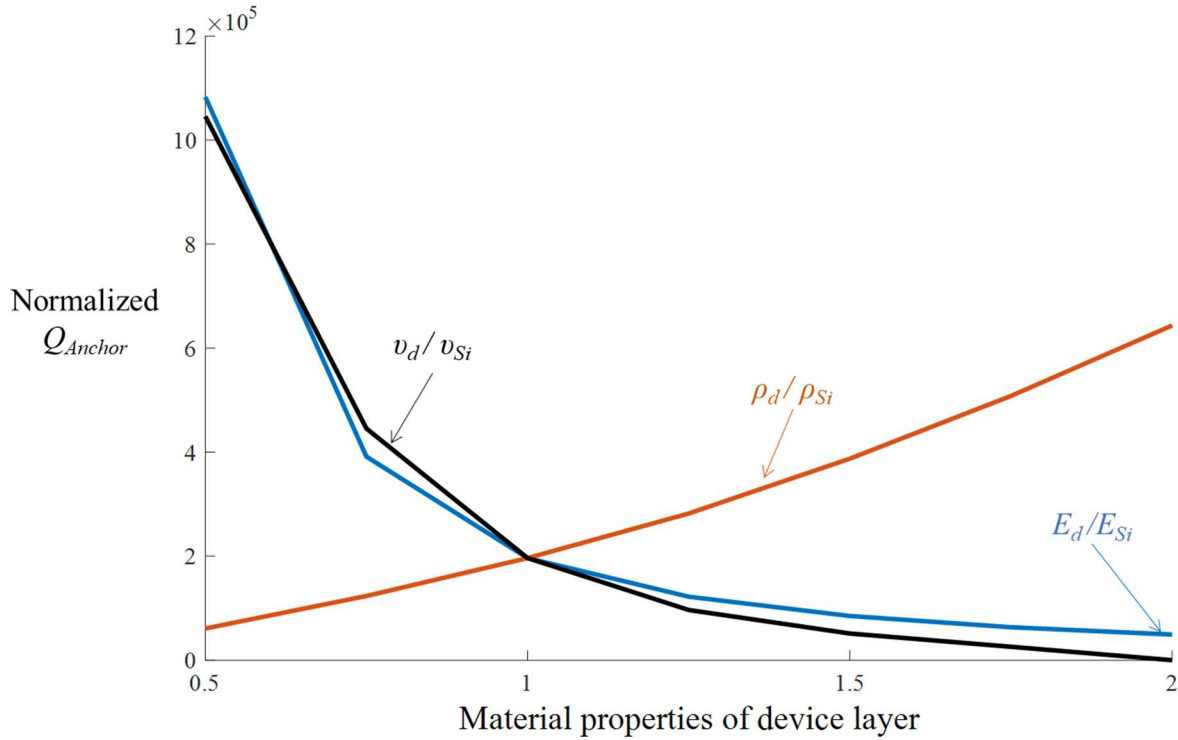


**Figure 5.14:** Effect of device layer material properties on  $Q_{Anchor}$ . By increasing the Young's modulus and Poisson's ratio,  $Q_{Anchor}$  decreases. However, increasing the density increases  $Q_{Anchor}$ .

Figure 5.15 shows the effect of device geometric properties on  $Q_{Anchor}$ . These results show that devices with longer suspensions produce lower anchor loss. Indeed, the distance from the places with large deformation in the device layer to the cap is further in long suspensions. Comparing to beam resonators, the same pattern can be observed—longer beams show smaller anchor loss [58]. Increasing the device thickness increases anchor loss because thicker devices cause larger deformation and wave propagation in the cap and substrate. The same trend was observed in simple beam resonators, where anchor loss has an inverse relation to the cube of the

beam thickness [58]. Increasing suspension width increases anchor loss because suspension has a larger connection area to the support part; therefore, larger energy goes to substrate.

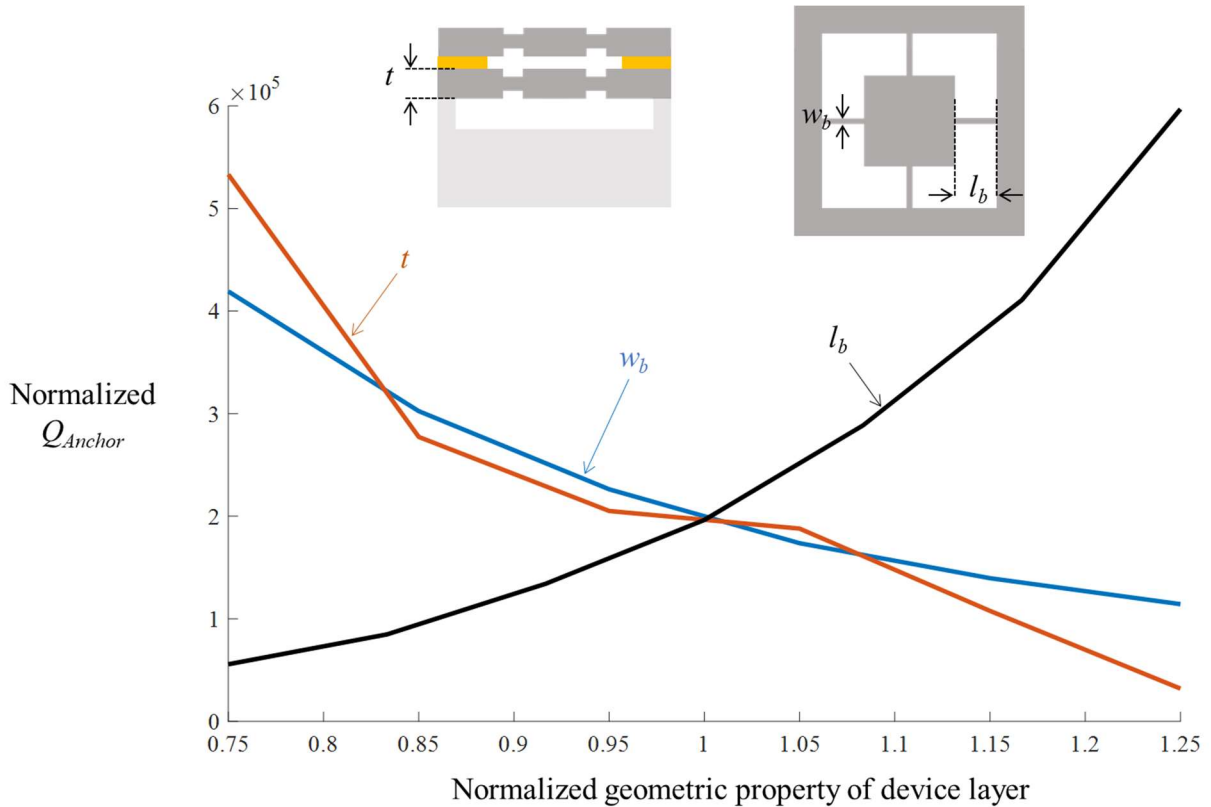


**Figure 5.15:** Effect of device layer geometric properties on  $Q_{Anchor}$ . Increasing device thickness and suspension width reduces  $Q_{Anchor}$ . While, increasing suspension beam length increases  $Q_{Anchor}$ .

Since the device layers will be fabricated separately, there might be some mismatch between their geometric parameters. This may affect anchor loss. Figure 5.16 shows the effect of mismatch between the geometric parameters of the two layers on  $Q_{Anchor}$ . It is observed that even a small mismatch between geometry of layers degrade the performance significantly. In fact, stacked resonators work according to force balancing from two layer; if these forces are not equal, then forces are not completely balanced. As a result, anchor loss increases. Therefore, it is important to fabricate this device very similarly.

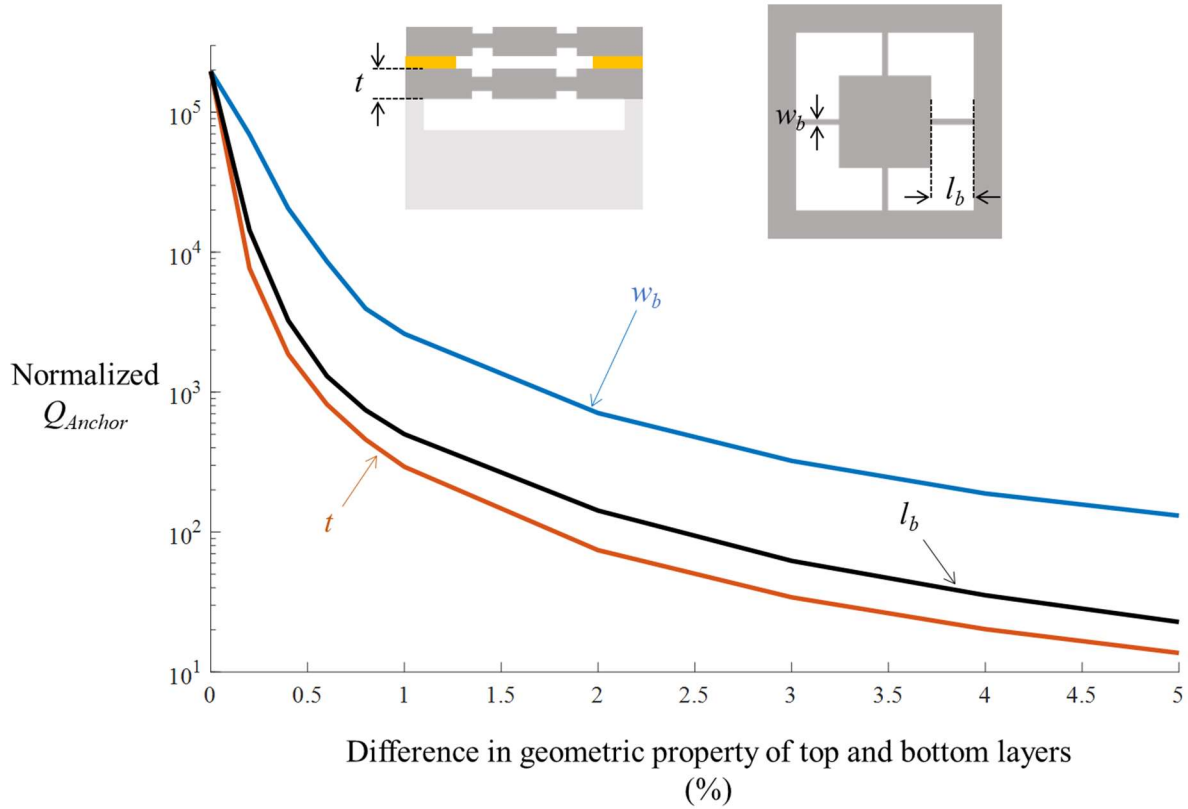


**Figure 5.16:** Effect of imperfections in geometry of device layers on  $Q_{Anchor}$ . Difference between the geometry of two layers reduces  $Q_{Anchor}$  significantly.

### **b) Effect of Bonded Layer Properties on Anchor Loss of Stacked Resonators**

Two device layers should be bonded together. Properties of the bonded layer might affect anchor loss.

Figure 5.17 shows the effects of the bonding material properties on  $Q_{Anchor}$ . It is observed that bonding material properties do not have a large effect on anchor loss. Due to the fact that Poisson's effect converts the in-plane forces to out-of-plane non-balanced forces, increasing Poisson's ratio of the bonding decreases  $Q_{Anchor}$ .

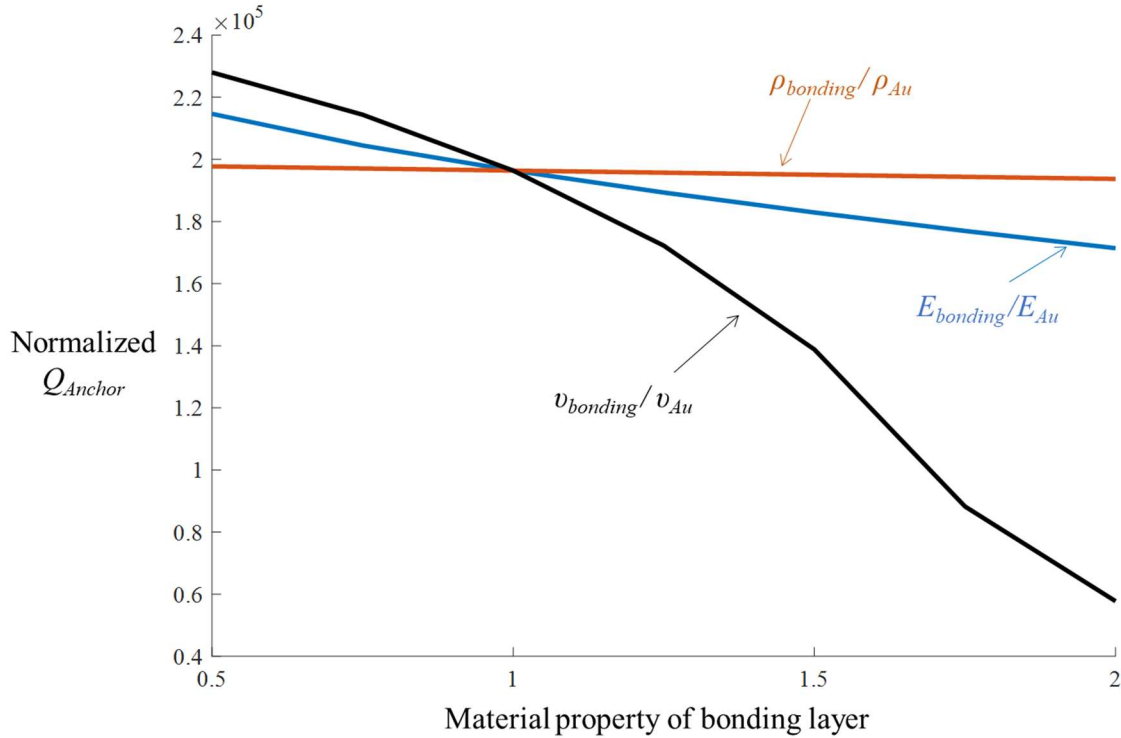


**Figure 5.17:** Effect of bonding material properties on  $Q_{Anchor}$ . Increasing the bonding Poisson's ratio decreases  $Q_{Anchor}$  changes. However, the bonding Young's modulus and density have negligible effects on  $Q_{Anchor}$ .

In Figure 5.18, the effect of the bonding area geometry on  $Q_{Anchor}$  is depicted. This figure shows that increasing length or reducing thickness of the bonding area increases  $Q_{Anchor}$ . In fact, by increasing length and reducing the thickness, coupling between two device layers increases, providing better balancing. It should be noticed that when the bonding length is the same as the length of the contact area between the cap and the device layer,  $Q_{Anchor}$  of a stacked resonator degrades and approaches to the  $Q_{Anchor}$  of non-stacked device. In fact, majority of forces deform the cap and create mechanical waves in substrate before they could be balanced in the bonding.

During bonding two layers together, there might be misalignments between layers. This misalignment affects  $Q_{Anchor}$ . Figure 5.19 shows the effect of misalignments between layers on  $Q_{Anchor}$ . Misalignment decreases  $Q_{Anchor}$  because it reduces balancing between layers. However, it seems that for misalignment less than  $20 \mu\text{m}$ ,  $Q_{Anchor}$  reduction is not a big challenge.

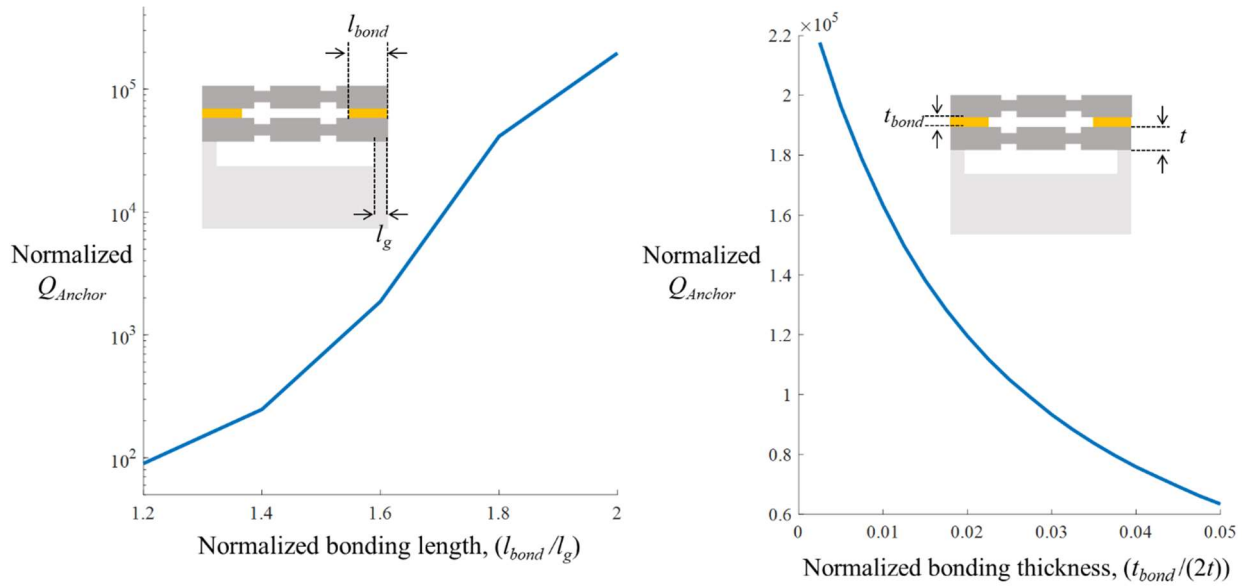


**Figure 5.18.** Effect of bonding layer length and thickness on  $Q_{Anchor}$ . By increasing the bonding length,  $Q_{Anchor}$  increases. However, by increasing the bonding thickness,  $Q_{Anchor}$  decreases.

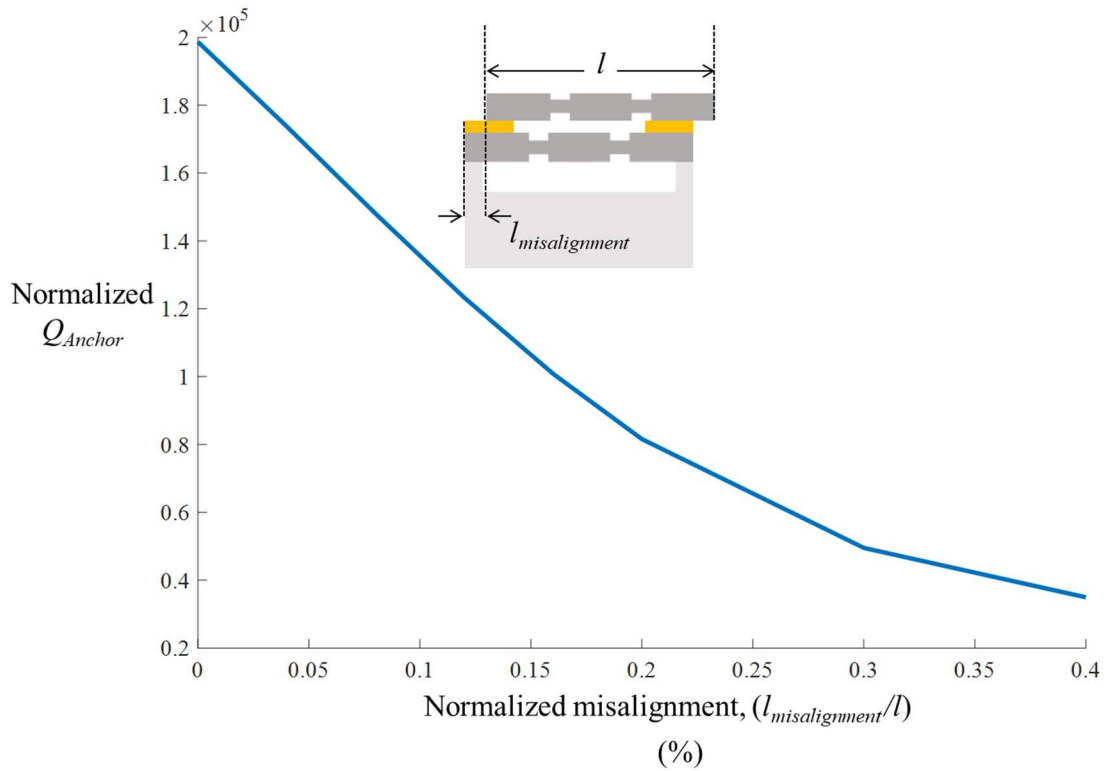


**Figure 5.19:** Effect of misalignment on  $Q_{Anchor}$ . Misalignments decreases  $Q_{Anchor}$  moderately.

**c) Effect of Cap Layer Properties on Anchor Loss of Stacked Resonators**

Different material can be used as the cap layer. The effects of cap material properties on anchor loss are shown in Figure 5.20. To simulate these effects, the material properties of the cap are changed, while material properties of substrate and PML are fixed. Figure 5.20 shows that increasing the cap's Young's modulus decreases anchor loss. In this case, the deflections in the cap and therefore substrate decrease due to the increase in cap rigidity. As the cap becomes stiffer, device layer cannot deform the cap easily, causing more energy stays in the resonator during the oscillation. It is found that cap's density and Poisson's ratio have less of effects than its Young's modulus.

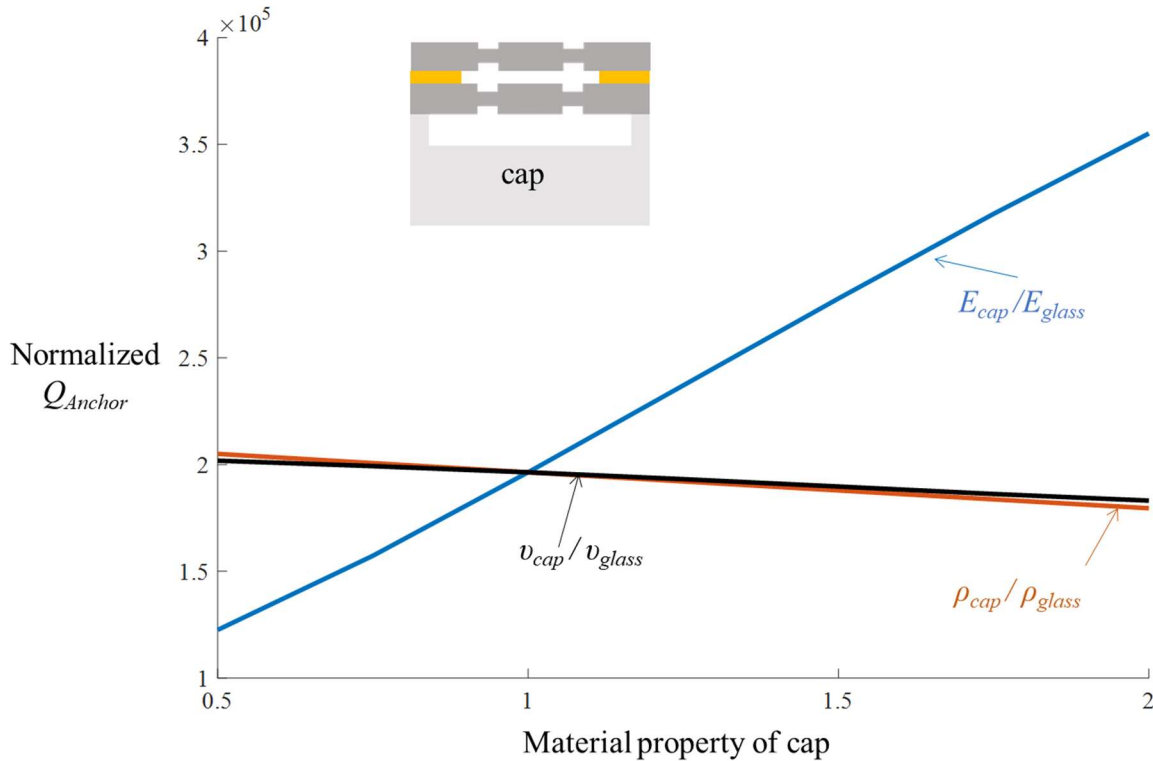


**Figure 5.20:** Effect of cap material properties on  $Q_{Anchor}$ . By changing cap's Young's modulus  $Q_{Anchor}$  changes. However, cap's density and Poisson's ratio have negligible effects on  $Q_{Anchor}$ .



Thickness of the cap layer can be determined during the design process and it might have some impact on  $Q_{Anchor}$ . Figure 5.21 shows the effect of cap thickness on  $Q_{Anchor}$ . Increasing the cap thickness increases  $Q_{Anchor}$ , because the distance between the resonator and substrate increases.

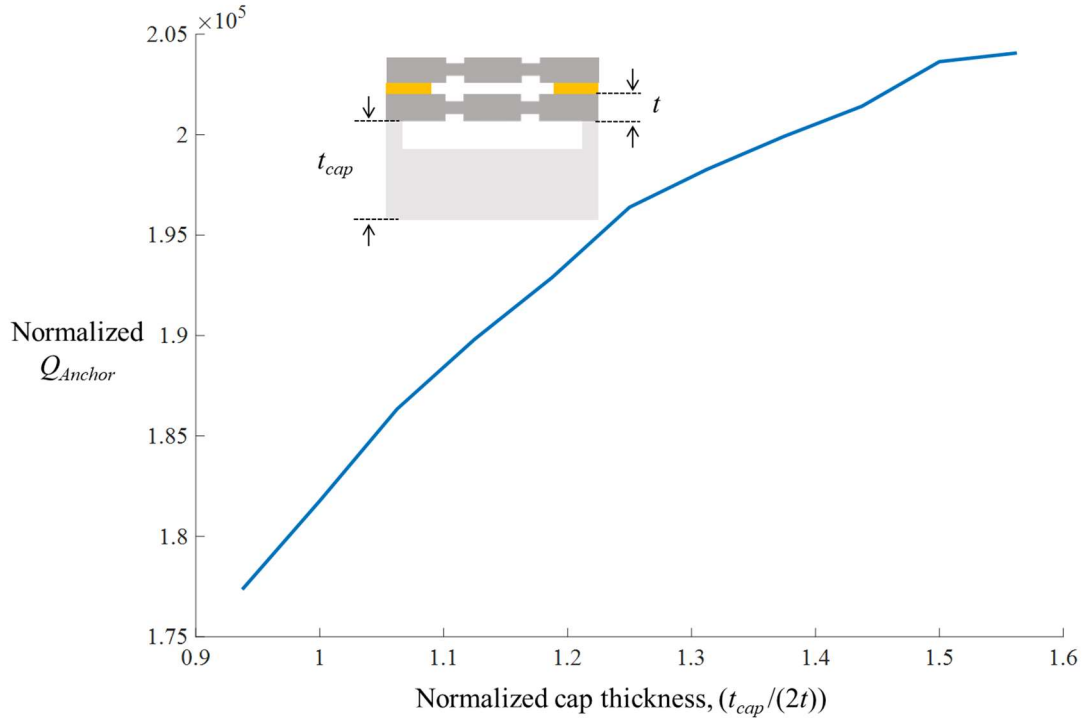
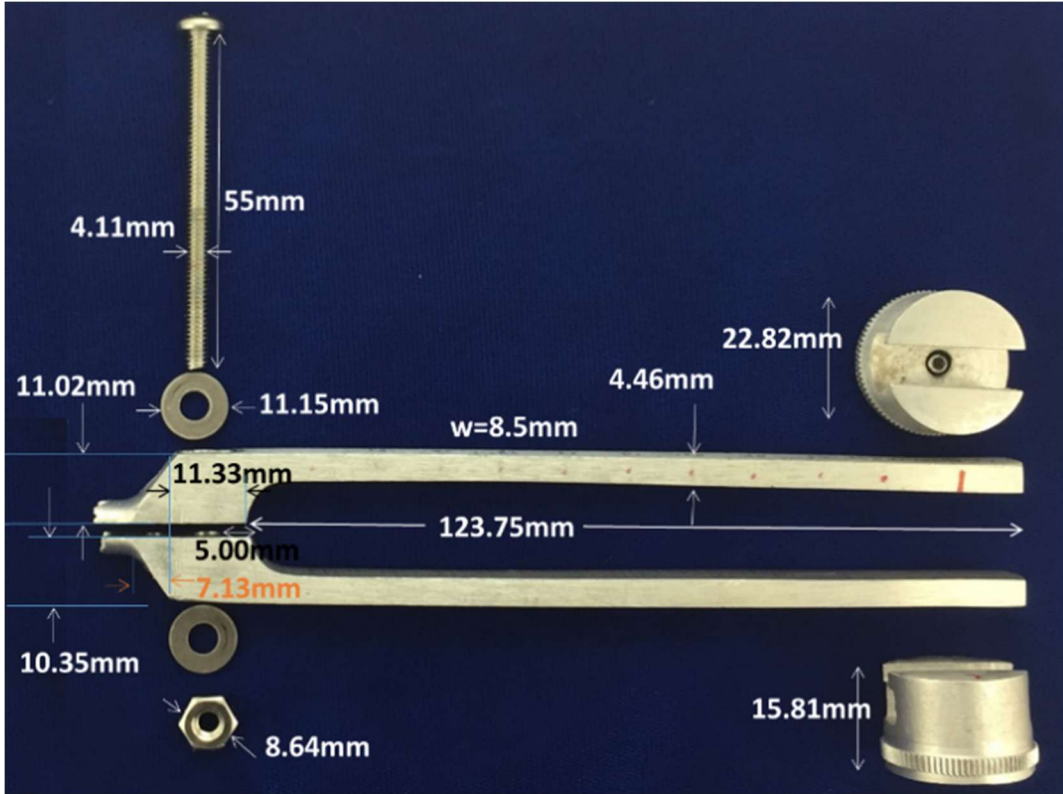


**Figure 5.21:** Effect of cap thickness on  $Q_{Anchor}$ . Increasing cap thickness increases  $Q_{Anchor}$ .

### 5.1.1.3 Experimental verification of the anchor loss reduction in out-of-plane mode by stacking

To verify  $Q_{Anchor}$  improvement by stacking, the structure shown in Figure 5.22 is fabricated and tested. This structure, which is a typical tuning fork, consists of two aluminum layers, which are coupled using a nut and bolt. Two proof masses are also connected to the end of these aluminum layers. Figure 5.22 (a) shows an exploded view of the tested structure, which shows the relationship of assembly of these parts and their sizes. The assembled structure is shown in Figure 5.22 (b).



(a) Parts



(b) Assembled

**Figure 5.22:** (a) Exploded view of various part of the tested structure and their dimensions. (b) Assembled structure.

The resonant behavior of this structure is then tested in two configurations: a) only one resonant layer, and b) two layers are stacked to form a resonator. Figure 5.23 shows these two configurations. Impact hammer modal testing is used to drive these structures in air. Their velocities are then read using LDV. Figure 5.23 shows the ring-down time plot and the fast Fourier transform of these data. As shown in this figure, **stacking increases  $Q$  by more than  $50\times$** . This clearly validates the stacking idea to improve  $Q_{Anchor}$ . For the case of one layer device, the  $Q$  is much less than the stacked case; therefore, its  $Q$  is determined by anchor loss. However, since the resonators are vibrating in air,  $Q_{Fluidic}$  limits their maximum  $Q$ . As a result,  $Q_{Anchor}$  is probably improved much more than  $50\times$ . Nonetheless, this improvement confirms the capability of the stacked resonators to reduce anchor loss significantly.

As discussed before, two layers of a stacked resonator might have different properties and this affects anchor loss. To capture this impact experimentally, some masses are added to the tip of top layer. Figure 5.24 shows this imbalanced mass and its effect on  $Q$ . In this figure, normalized  $Q$ ,  $Q/Q_{non-stacked}$ , is sketched versus normalized imbalanced mass,  $\Delta m/M$ , where  $\Delta m$  is the amount of imbalanced mass and  $M$  is the total mass of the resonator. It is found that mass imbalance between layers increases anchor loss. However, because improvement due to stacking is significant, the reduction in  $Q$  due to mass imbalance is not critical.

In order to bond two device layers different approaches can be used (e.g. using a metal layer between layers). This might reduce coupling between layers. Figure 5.25 shows the effect of material thickness on  $Q$ . In this figure, the thickness of materials is normalized to the total thickness of contacting part of the two layers.

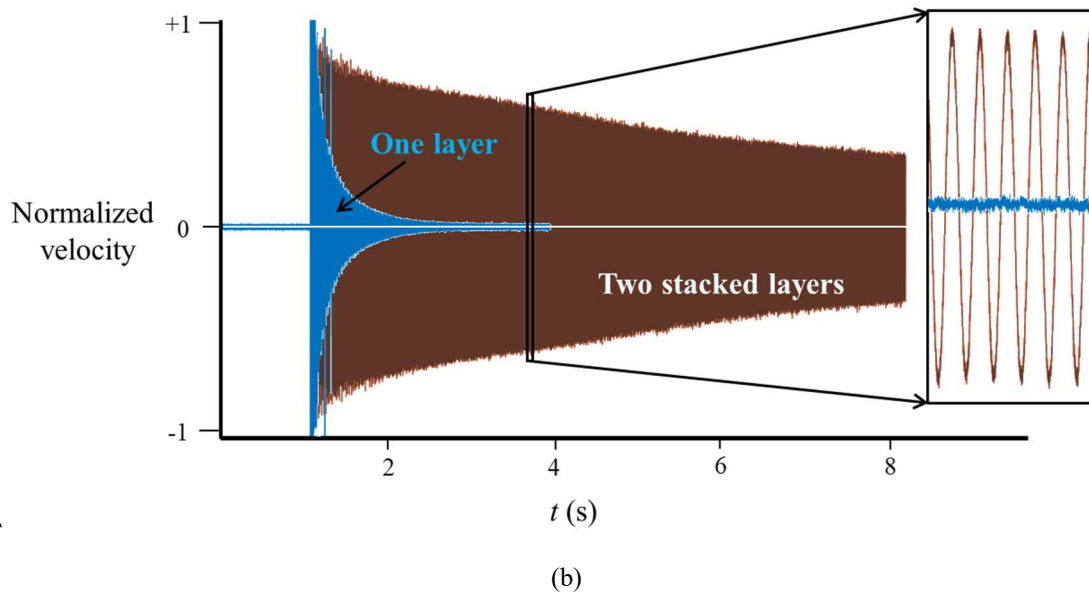
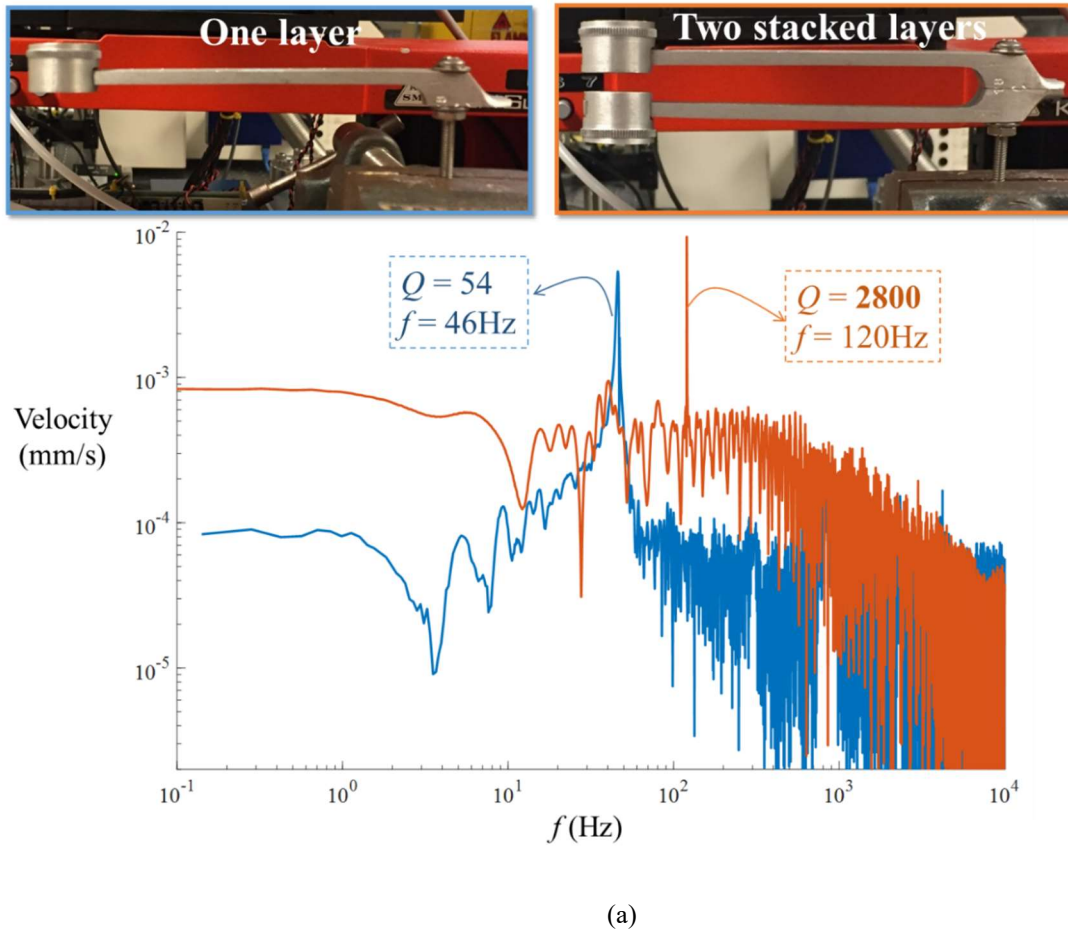


**Figure 5.23:** a) Frequency response of one layer and two stacked layers resonators. Stacking increases  $Q_{Anchor}$  more than  $50\times$ . b) Measured ring-down plot of the one layer and two stacked layers resonators. Stacked resonators shows much larger ring-down time.

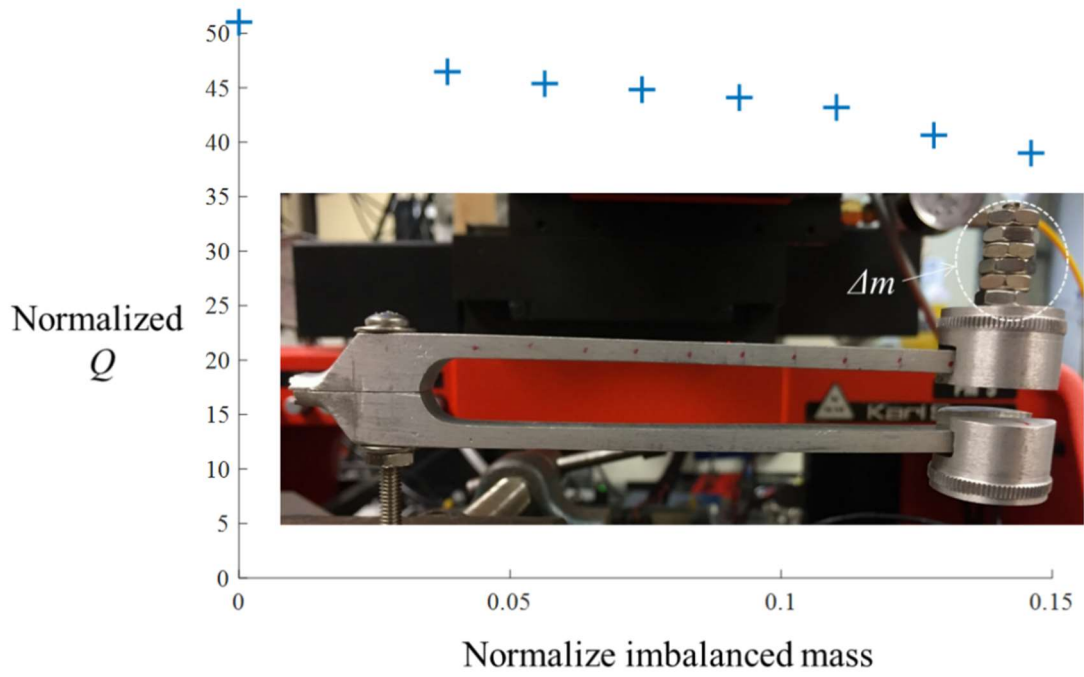


**Figure 5.24:** Effect of mass imbalance between two layers on  $Q$  of a stacked resonator. Mass imbalance between layers decreases  $Q$  slightly.

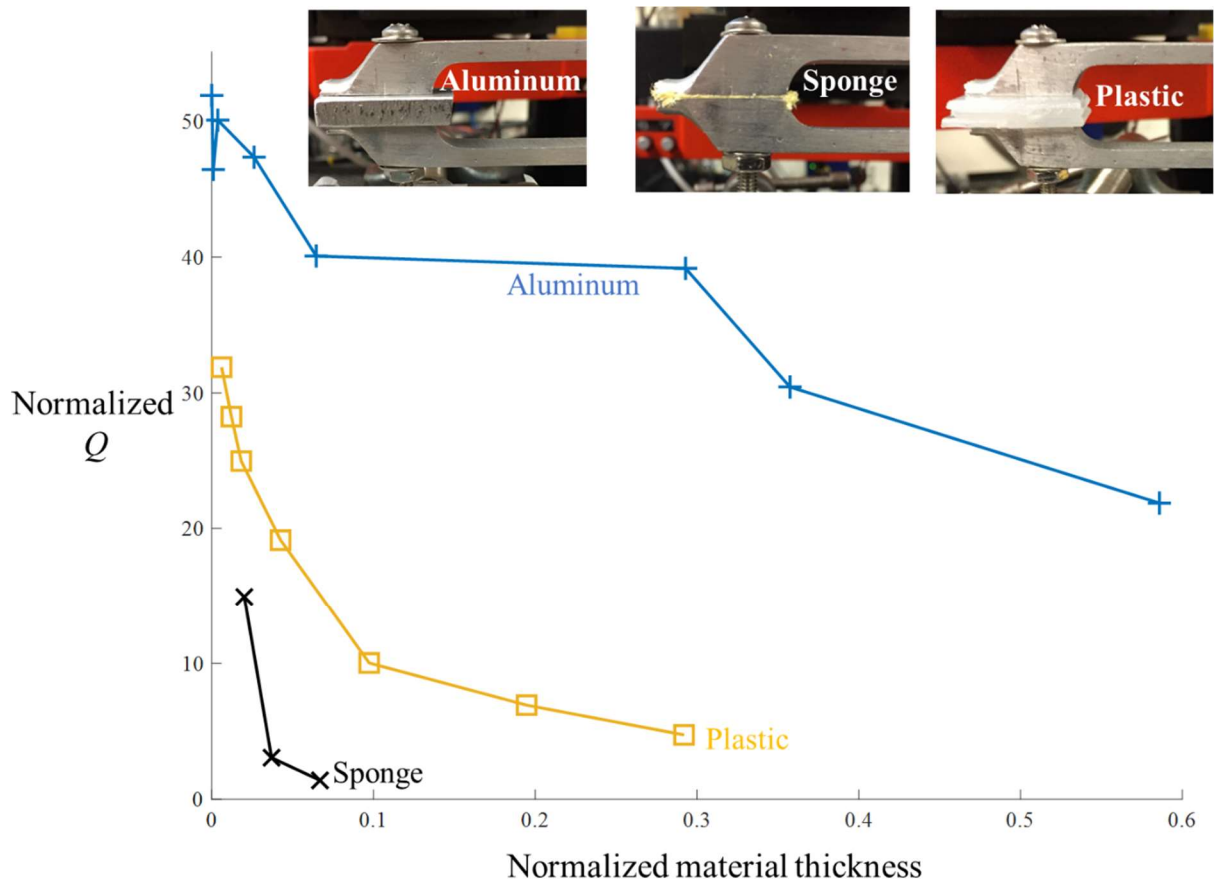


**Figure 5.25:** Normalized  $Q$  versus normalized thickness of material between layers. It is found that increasing thickness reduces coupling between layers and increases anchor loss. Using a material like sponge that disconnects acoustic coupling between devices increases anchor loss significantly. Intrinsic damping of plastic layer causes that the larger amount of the device energy dissipates in the stacked resonators.

The results show that increasing the material thickness reduces coupling between layers and increases anchor loss. Furthermore, a material like plastic that has larger intrinsic dissipation causes larger anchor energy loss in the device. Additionally, using a material like sponge that disconnects acoustic coupling between devices increases anchor loss significantly. In fact, even a thin layer ( $< 2\text{mm}$ ) sponge between device layers decreases  $Q$  to  $Q_{non-stacked}$ . Therefore, it is important to use a bonding material between layers, which does not decouple them acoustically.

During fabrication and bonding of the two layers, there would be misalignments between layers (typically less than  $20\ \mu\text{m}$  in microfabrication process). As discussed in the previous

subsection, linear misalignment increases  $Q$ . Figure 5.26 shows the effects of longitudinal and lateral misalignment on  $Q$ . According to these data, none of the linear misalignments has a major impact on  $Q$ . In fact, during the linear misalignments almost the same amount of forces and moments in opposite direction exerted on the contact area between two layers that cancel out each other; therefore, it should be expected that linear misalignments do not cause a major degradation in  $Q$ .

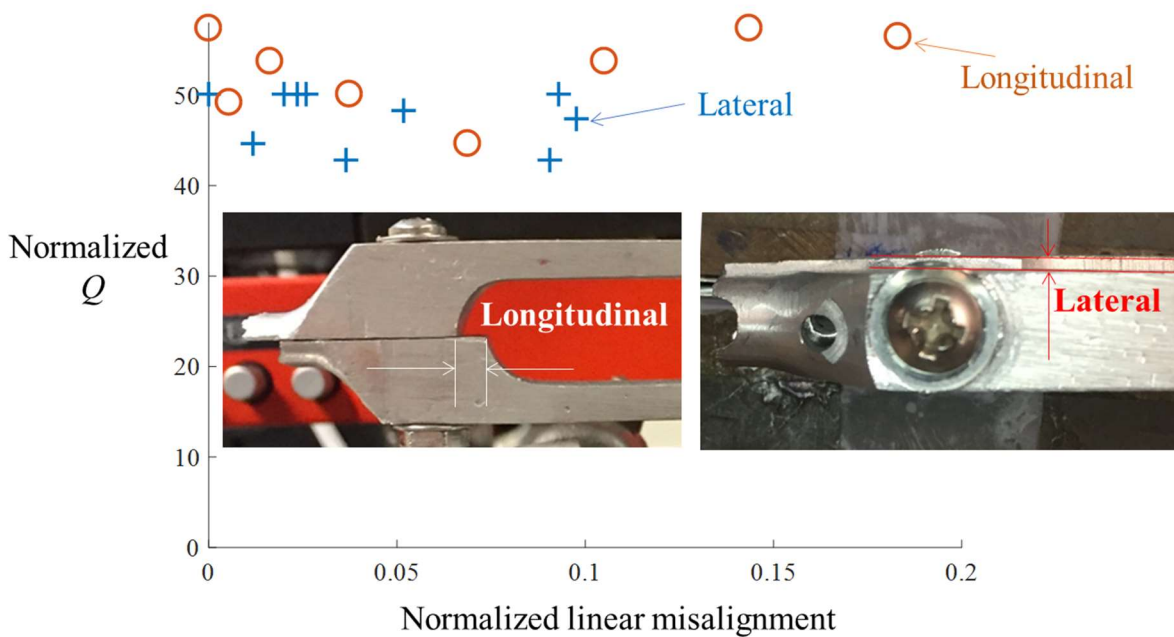


**Figure 5.26:** Effect of linear misalignments on  $Q$  of a stacked resonator. Misalignment values are normalized relative to the length (for longitudinal misalignment) and width (for lateral misalignment) of contact area. It is found that improvement due to the stacking is so good that even with 15% misalignment anchor loss is not dominant dissipation mechanism.

Even though angular misalignment between two layers in microfabrication process is very small, this could happen in the tested structure. As shown in Figure 5.27, this misalignment decreases  $Q$  significantly. There are two reasons for this:

- a) Angular misalignment decreases contact area between two layers, and therefore their coupling.

b) Although two layers exert the same forces in opposite directions in the anchor area that cancel each other out, they exert different moments to the anchored area that are not balanced. These moments create mechanical wave propagation into the substrate, increasing anchor loss.

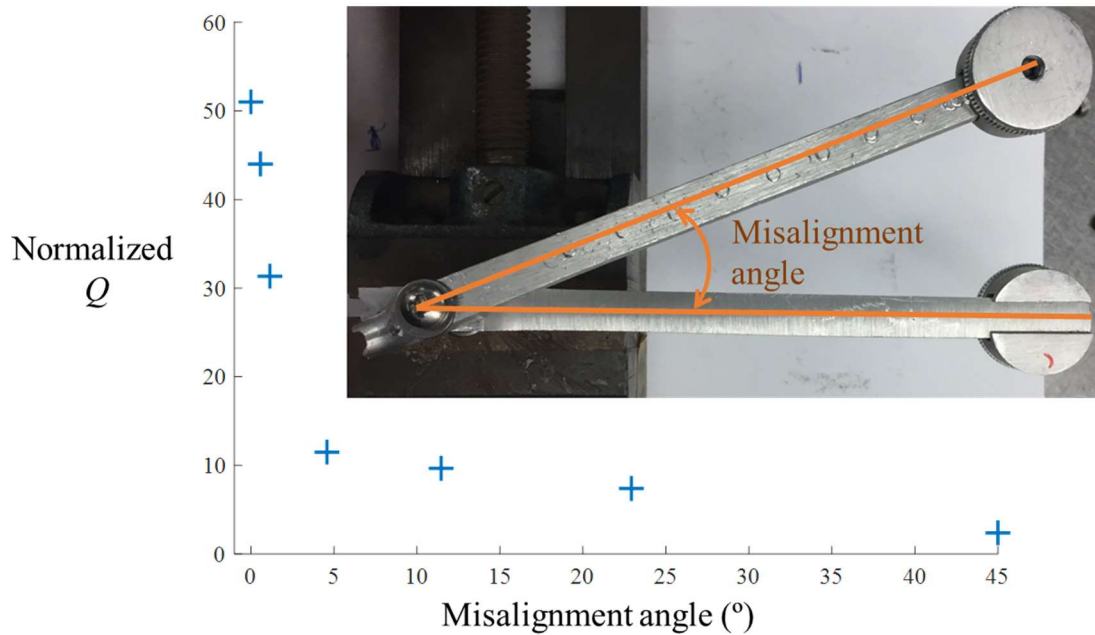


**Figure 5.27:** Effect of angular misalignment on  $Q$  of a stacked resonator. It is found that angular misalignment decreases  $Q$  significantly.

#### 5.1.1.4 Conclusion

Results of this subsection have shown that anchor loss in out-of-plane resonators could be the dominant loss mechanism. However, this loss can be decreased by more than five orders of magnitude by stacking the same resonator that vibrate in the opposite direction of the initial resonator. Anchor loss in the stacked device depends on many parameters. The effective parameters are classified into three categories and a summary of the impact of them on anchor loss presented in Table 5.2.



**TABLE 5.2:** SUMMARY OF THE EFFECTS OF DIFFERENT PARAMETERS ON ANCHOR LOSS OF STACKED RESONATORS.

Category	Effective parameters	Amount of impact	Comments
Device layer	Material	High	<ul style="list-style-type: none"> <li>Increasing the device layers Young's modulus increases anchor loss significantly.</li> <li>Increasing the device layers density decreases anchor loss.</li> <li>Increasing the device layers Poisson's ratio increases anchor loss significantly.</li> </ul>
	Geometry	Moderate	<ul style="list-style-type: none"> <li>Increasing the device layers thickness increases anchor loss significantly.</li> <li>Increasing the suspension beams width increases anchor loss moderately.</li> <li>Increasing the suspension beams length decreases anchor loss significantly.</li> </ul>
	Imperfections	High	<ul style="list-style-type: none"> <li>Geometrical differences between two layers increases anchor loss significantly. It is important that two device layers be made very similarly.</li> </ul>
Bonding	Material	Low	<ul style="list-style-type: none"> <li>Bonding density and Young's modulus do not have a significant effect on anchor loss.</li> <li>Increasing the bonding Poisson's ratio increases anchor loss moderately.</li> <li>Some material such as sponge could decouple two layers and increase anchor loss significantly.</li> </ul>
	Geometry	High	<ul style="list-style-type: none"> <li>Increasing the bonding thickness increases anchor loss moderately.</li> <li>Increasing the bonding length decreases anchor loss significantly.</li> </ul>
	Misalignments	High	<ul style="list-style-type: none"> <li>Linear misalignment between two layers increases anchor loss moderately.</li> <li>Angular misalignment between two layers increases anchor loss significantly.</li> </ul>
Cap	Material	Low	<ul style="list-style-type: none"> <li>Increasing the cap Young's modulus decreases anchor loss.</li> <li>Cap density and Poisson's ratio do not have a significant effect on anchor loss.</li> </ul>
	Thickness	Low	<ul style="list-style-type: none"> <li>Increasing the cap thickness decreases anchor loss slightly.</li> </ul>

### 5.1.2 Thermoelastic dissipation

The next dissipation mechanism in resonators is TED, which was explained in 4.1.2. A geometry shown in Figure 5.28 is considered for calculating  $Q_{TED}$  in out-of-plane resonators. This structure includes a suspended mass that is connected to four folded beams. Through this

subsection, this structure is named SMFB. The mass can move in  $x$  and  $z$  directions. The motion in the  $x$  direction is for driving and the motion in the  $z$  direction is for sensing. Since one-layer and stacked layers resonators with the same geometry produce the same  $Q_{TED}$ , just TED of one-layer device is studied in this part.

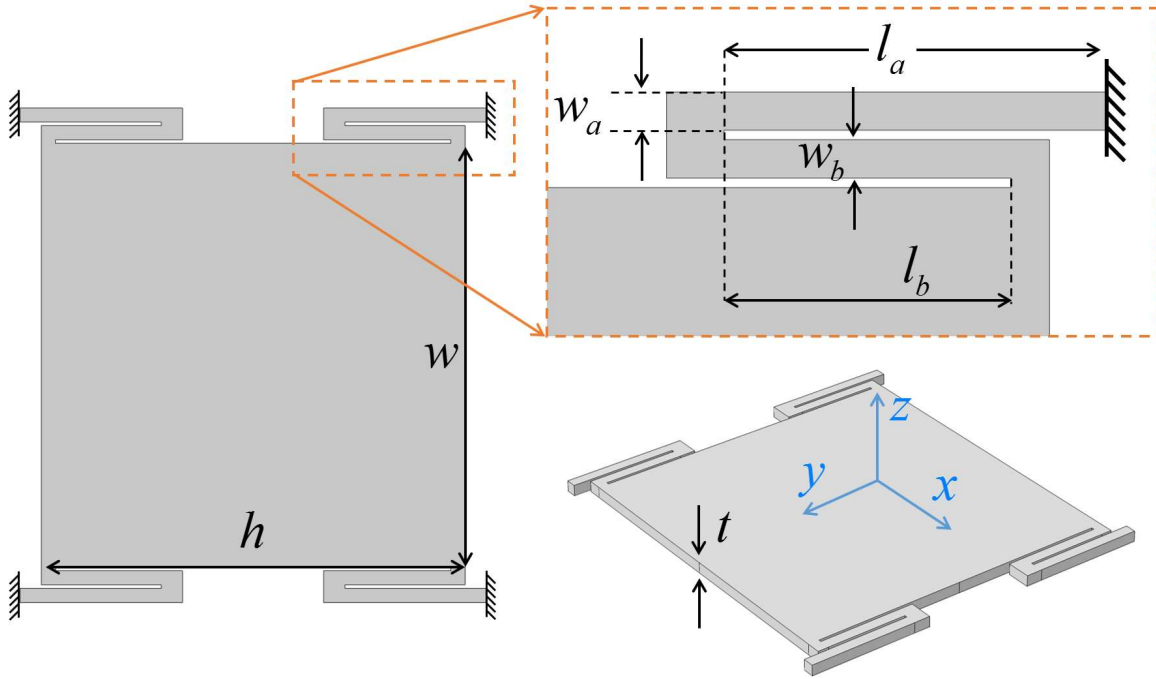


**Figure 5.28:** One layer SMFB resonator that is used for the TED simulation.

COMSOL Multiphysics is used to numerically solve the fully-coupled thermo-mechanical FEM eigenvalue problem for this structure with the dimensions shown in Table 5.3. Silicon is chosen as the reference material, the reason for this will be explained later in this subsection. The material properties are considered as Young's modulus  $E_{Si} = 170$  GPa, Poisson's ratio  $\nu_{Si} = 0.28$ , density  $\rho_{Si} = 2329$  kg/m<sup>3</sup>, thermal conductivity  $k_{Si} = 130$  W/(m·K), specific heat capacity  $C_{SPSi} = 700$  J/(kg·K), and coefficient of thermal expansion  $\alpha_{Si} = 2.6 \times 10^{-6}$  1/K.

**TABLE 5.3:** DIMENSIONS USED FOR SIMULATING TED IN SMFB RESONATORS

Parameter	Value ( $\mu\text{m}$ )
$w$	5000
$h$	5000
$w_a$	150
$w_b$	150
$l_a$	2000
$l_b$	1500
$t$	200

By solving (4.13)–(4.16) numerically at  $T_0 = 293.15$  K, the eigenvector that includes deformations and temperature in each node, and the corresponding eigenvalues are calculated. The simulated temperature deviation distribution in the sensing mode is shown in Figure 5.29. The largest temperature gradients are found at the folded beams.

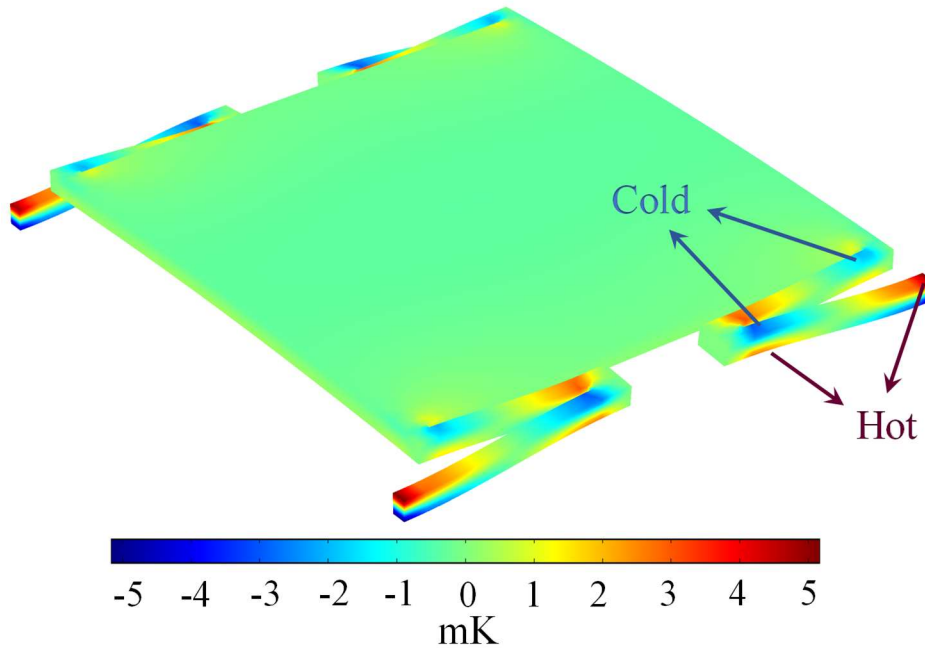


**Figure 5.29:** Temperature deviation distribution of an SMFB resonator in out-of-plane mode.

Figure 5.30 shows that heat can transfer between the hot and cold regions mainly in four different directions:

1. Across the thickness of the beam  $a$ .
2. Across the thickness of the beam  $b$ .
3. Across the length of the beam  $a$ .
4. Across the length of the beam  $b$ .

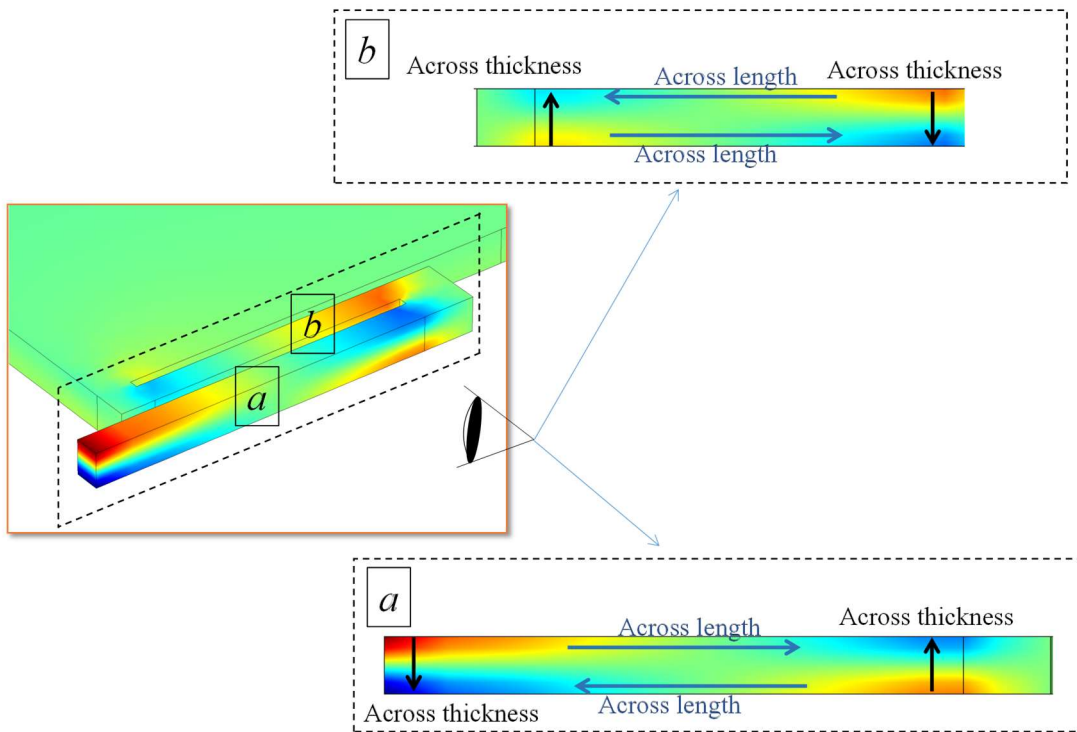


**Figure 5.30:** Thermal paths in a folded beam of an SMFB resonator when it is vibrating in sensing mode. These paths are across the thicknesses and lengths of beams  $a$  and  $b$ .

By using the results of the eigenvalue simulation,  $Q_{TED}$  of the silicon SMFB resonator with the nominal dimensions is found to be 16,691.

As discussed in 4.1.2, for a simple beam resonator, Zener [70, 71] suggested that the  $Q_{TED}$  can be estimated from (5.1):

$$Q_{TED} = \frac{\rho C_{SP}}{E \alpha^2 T_0} \frac{1 + (\omega_{mech} \cdot \tau_{th})^2}{\omega_{mech} \cdot \tau_{th}} \quad (5.1)$$

where  $\tau_{th}$  is the thermal transport time constant of the resonator and can be found from (5.2):

$$\tau_{th} = \frac{b^2}{\pi^2 D} \quad (5.2)$$

where  $b$  is the thickness of the beam in the bending direction. As shown in Figure 5.30, the majority of temperature deviation is happened in the folded beams for an SMFB resonator. In addition, the main paths for heat transfer in these beams are across thickness of the beams; therefore, (5.1) can be used to estimate  $Q_{TED}$  by replacing  $b$  with  $t$ , which results in:

$$Q_{TED} = \frac{\rho C_{SP}}{E \alpha^2 T_0} \frac{1 + \left( \omega_{mech} \cdot \frac{t^2}{\pi^2 D} \right)^2}{\omega_{mech} \cdot \frac{t^2}{\pi^2 D}} \quad (5.3)$$

Eleven different materials are considered for the SMFB resonators with the dimensions shown in Table 5.3 and  $Q_{TED}$  is calculated numerically and analytically; the results are summarized in Table 5.4. Both numerical and analytical approaches predict very similar values for  $Q_{TED}$ . Therefore, this equation can be used for estimating  $Q_{TED}$  of SMFB resonators with a very accurate result.

The result also shows that fused silica is an excellent material for low TED out-of-plane mode resonators. Therefore, we attempted to fabricate these resonators from fused silica. However, during the micromachining process several issues appeared. The main issue was forming tall and precise structures in fused silica. Deep Reactive Ion Etching (DRIE) has been the material of choice for forming thick and vertical structures in silicon. But when used for fused silica, several issues arise. These include the low etch rate of fused silica using DRIE, the inability to etch thick structures in fused silica due to a lack of masking materials, and the larger undercut of masking

material, resulting in non-vertical and rough sidewalls. Because of these issues, another material should be used for increasing  $Q_{TED}$ .

TABLE 5.4:  $Q_{TED}$  OF SMFB RESONATORS WITH DIFFERENT MATERIALS

Material	$E$ (GPa)	$\nu$	$\rho$ (kg/m <sup>3</sup> )	$k$ (W/(m·K))	$\alpha$ (10 <sup>-6</sup> ×1/K)	$C_{SP}$ (J/(kg·K))	$Q$ (FEM)	$Q$ (Analytical model)
SiO <sub>2</sub>	70	0.17	2200	1.4	0.5	730	4.42×10 <sup>7</sup>	5.6×10 <sup>7</sup>
Zerodur	90.3	0.24	2530	1.46	0.02	820	3.52×10 <sup>10</sup>	4.58×10 <sup>10</sup>
Al <sub>2</sub> O <sub>3</sub>	400	0.22	3965	35	6.5	730	1.43×10 <sup>4</sup>	1.7×10 <sup>4</sup>
SiC(6H)	748	0.45	3216	490	4.3	690	1312	581
Si <sub>3</sub> N <sub>4</sub>	250	0.23	3100	20	2.3	700	1.6×10 <sup>5</sup>	1.9×10 <sup>5</sup>
Borosilicate	63	0.2	2230	1.13	3.3	754	1.4×10 <sup>6</sup>	1.8×10 <sup>6</sup>
GaAs	85.9	0.31	5316	33	5.7	550	3.1×10 <sup>4</sup>	3.5×10 <sup>4</sup>
Ge	103	0.26	5323	58	5.9	310	7.6×10 <sup>3</sup>	7.2×10 <sup>3</sup>
InSb	409	0.35	5770	18	5.4	200	4.0×10 <sup>3</sup>	4.9×10 <sup>3</sup>
C[100]	1050	0.1	3515	990	0.8	520	1.6×10 <sup>4</sup>	1.9×10 <sup>4</sup>
Si(c)	170	0.28	2329	130	2.6	700	1.7×10 <sup>4</sup>	1.6×10 <sup>4</sup>

Based on (5.3),  $Q_{TED}$  is equal to the product of  $Q_{mat}$  and  $Q_{freq}$ :

$$Q_{mat} = \frac{\rho C_{SP}}{E \alpha^2 T_0} \quad (5.4)$$

$$Q_{freq} = \frac{1 + \left( \omega_{mech} \cdot \frac{t^2}{\pi^2 D} \right)^2}{\omega_{mech} \cdot \frac{t^2}{\pi^2 D}} \quad (5.5)$$

$Q_{mat}$  depends on the temperature and the material properties of the resonator. As explained, increasing  $Q_{mat}$  causes difficulties in the fabrication process. Therefore, the only way to achieve a high  $Q_{TED}$  is to increase  $Q_{freq}$ .  $Q_{freq}$  is a function of resonant frequency, thermal diffusivity, and resonator thickness and has a minimum value of 2. As a result, it is possible to improve  $Q_{TED}$  of

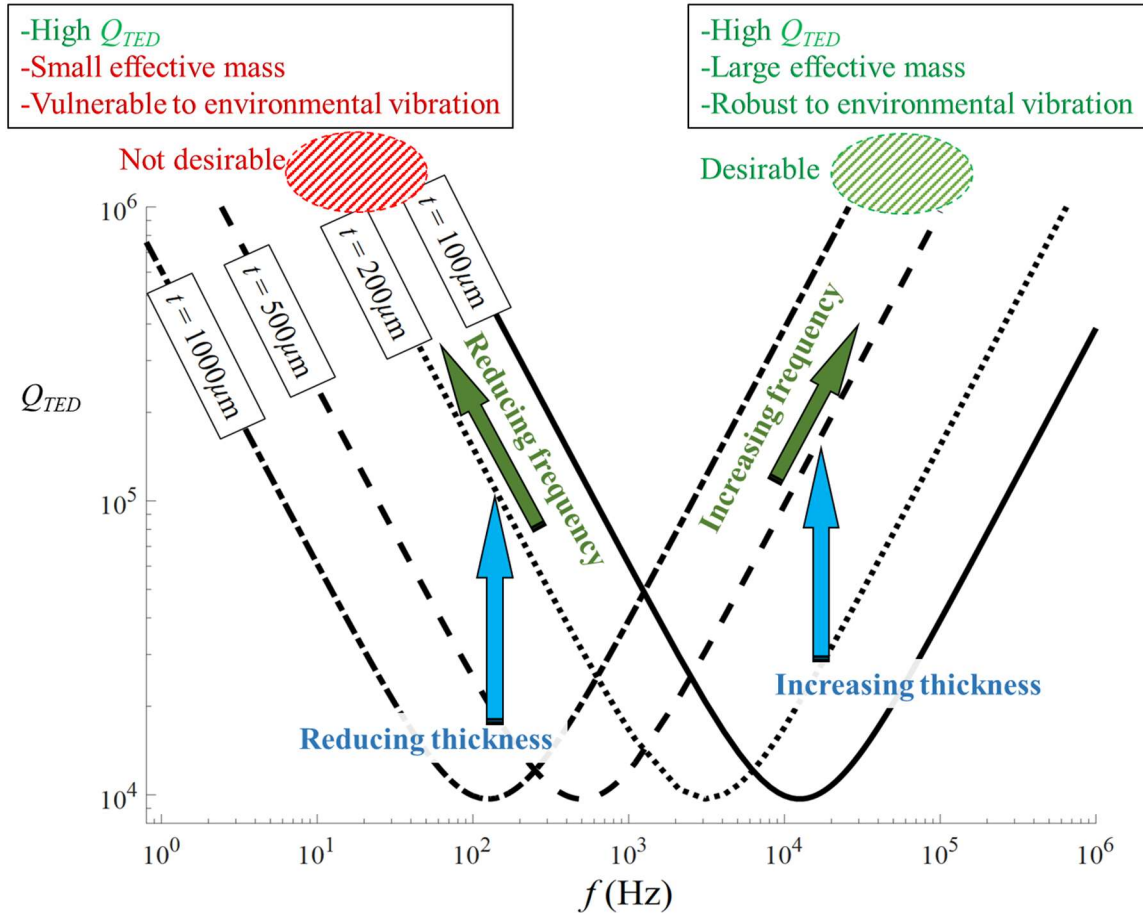
an-out-of-plane resonator fabricated from a non-optimized material by changing thickness and frequency of the device.

Figure 5.31 shows the results of calculating  $Q_{TED}$  using (5.3) for silicon SMFB resonators with four different thicknesses. All four cases have a minimum  $Q_{TED}$  of 9,678.6 that is twice that of  $Q_{mat}$ . This minimum occurs at 12526, 3131.4, 501.02, and 125.25Hz for structures with thicknesses of 100, 200, 500, and 1000 $\mu\text{m}$ , respectively. This value is very small comparing to values for fused silica resonators.

In any case,  $Q_{TED}$  can be increased by changing the designed resonant frequency to be far from this minimum. When resonant frequency is much less than this minimum, the deformation time of the structure is much larger than the thermal transport time (isothermal regime); thus, the structure remains in thermal equilibrium and a very small amount of energy is dissipated through TED. When resonant frequency is much larger than this minimum, the structure deforms so fast that thermal relaxation cannot occur (adiabatic regime); therefore, a small amount of energy is dissipated due to TED.

Furthermore, decreasing the thickness improves the  $Q_{TED}$  in isothermal regime and increasing the thickness in adiabatic regime improves the  $Q_{TED}$ . As a result, to achieve a high  $Q_{TED}$ , silicon SMFB resonators can be used.

Working in isothermal regime results in small effective mass and vulnerability to the environmental effects. Therefore, silicon SMFB resonators should be designed with a **large thicknesses** and **resonant frequencies**. Very thick silicon devices have been successfully fabricated in our group [104]. Therefore, it is possible to achieve a high  $Q_{TED}$  in out-of-plane mode silicon SMFB resonators.



**Figure 5.31:**  $Q_{TED}$  versus resonant frequency of SMFB resonators made from silicon with different thicknesses. All resonators have a same minimum  $Q_{TED}$ . This minimum occurs in lower resonant frequencies for thicker structures.

### 5.1.3 Other dissipation mechanisms

As shown in 4.1.3, by operating micro mechanical resonators in vacuum, fluidic damping can be minimized. If pressure is reduced below  $100 \mu\text{Torr}$ , fluidic damping is no longer the  $Q$ -limiting mechanism in stacked out-of-plane resonators.

As discussed in 4.1.4, phonon interactions become significant in high-frequency resonators and do not have any major impact on total  $Q$  for silicon resonators that operate in the tens of kilohertz range. It is estimated that  $Q_{Phonon}$  for stacked out-of-plane silicon resonators is about 1 billion.



Internal dissipation in resonator material can also be one of the  $Q$ -limiting mechanisms depending on the material. In [105], it is shown that silicon resonators can achieve a  $Q$  higher than 1 billion; therefore, it is unlikely that the  $Q$  of stacked out-of-plane silicon resonators will be limited by internal dissipation.

Surface-to-volume ratio in the proposed stacked layer is small; therefore, it is expected that  $Q_{Surface}$  will be very large. Experimental data published in [95] suggested that increasing the size of single crystalline silicon resonators, increases their  $Q$  due to reduction in Surface-to-volume. As shown in Figure 5.32, it appears that  $Q$  in these resonators is about  $2 \times 10^5 \times dim$  where  $dim$  is the resonator dimension in  $\mu m$ . According to this information,  $Q_{Surface}$  for stacked out-of-plane 500  $\mu m$ -thick silicon resonators is about 100 million. Therefore, surface loss is not the  $Q$ -limiting mechanism in them.

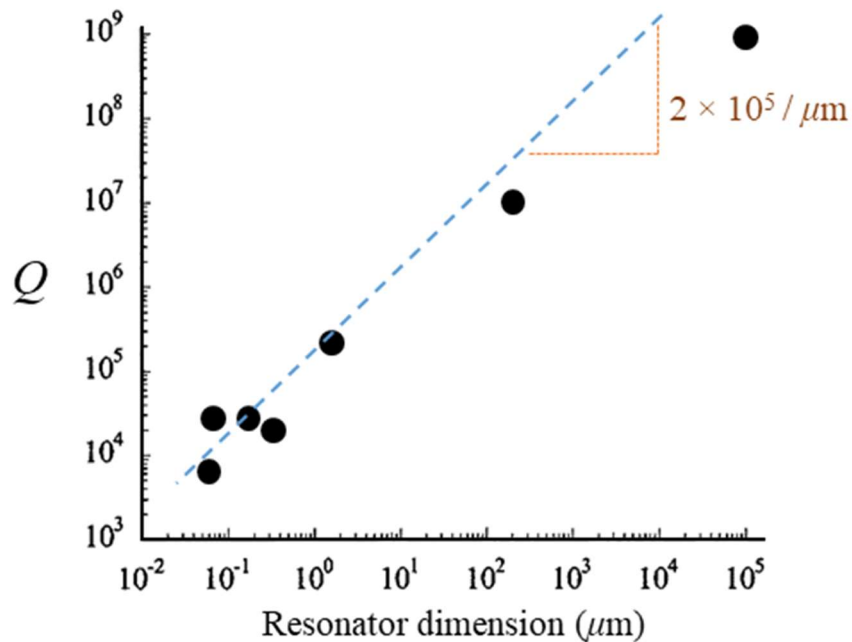


**Figure 5.32:** Effect of silicon resonators dimension on their  $Q$  (original plot is from [95]).

### 5.1.4 Conclusion

All the dissipation mechanisms in out-of-plane mode resonators have been studied. It has been found that anchor loss is the dominant dissipation mechanism in the existing out-of-plane resonators. An innovative idea has been introduced and successfully tested to remove this dissipation. This idea includes creating a virtual nodal point at the contact of the resonator and substrate by stacking two similar resonator and driving them in opposite directions. After removing anchor loss from the system, TED is the most dominant dissipation. To reduce this loss, two approaches can be used: a) using high  $Q_{TED}$  material such as fused silica b) Increasing thickness and frequency of the resonator. Experiment showed that fabricating fused silica is not possible at this moment; therefore, the second approach is suggested to improve  $Q_{TED}$ .

**TABLE 5.5: ESTIMATED VALUES FOR  $Q_S$  OF STACKED SMFB RESONATORS IN OUT-OF-PLANE MODE**

Parameter	Estimated values			
	Silicon	Silicon	Fused silica	Fused silica
Material	Silicon	Silicon	Fused silica	Fused silica
Thickness ( $\mu\text{m}$ )	500	1000	500	1000
Frequency (kHz)	15	23	12	18
$Q_{Anchor}$	$>10^8$	$2.7 \times 10^7$	$>10^8$	$3.1 \times 10^7$
$Q_{TED}$	$1.8 \times 10^5$	$5.5 \times 10^5$	$>10^8$	$>10^8$
$Q_{Fluidic}$	$>10^8$	$>10^8$	$>10^8$	$>10^8$
$Q_{Phonon}$	$>10^8$	$>10^8$	$>10^8$	$>10^8$
$Q_{Internal}$	$>10^8$	$>10^8$	$>10^8$	$>10^8$
$Q_{Surface}$	$10^8$	$>10^8$	$5 \times 10^7$	$10^8$
<b>Total <math>Q</math></b>	<b><math>1.8 \times 10^5</math></b>	<b><math>5.5 \times 10^5</math></b>	<b><math>5 \times 10^7</math></b>	<b><math>3 \times 10^7</math></b>

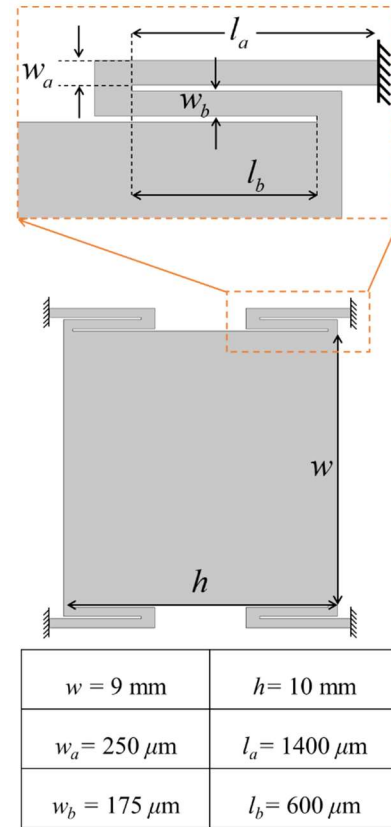


Table 5.5 summarizes estimated values for  $Q$ s of silicon and fused silica stacked SMFB resonators in out-of-plane mode.

Therefore, sensing- $Q$  is successfully optimized for out-of-plane mode resonators. Other important parameters in performance of the  $S^3$  gyroscope will be discussed in the following sections.

## 5.2 Effective Mass

Unlike the shell resonators that have distributed mass with different amplitude of motion, the  $S^3$  gyroscope consists of several springs and two proof masses, and hence its effective mass can be easily estimated with the following equation:

$$M = 2\rho w h t \quad (5.6)$$

For a  $S^3$  resonator with dimensions shown in Table 5.3, this equation estimated the effective mass to be 23.290 mg. It is possible to estimate the effective mass more accurately by numerical simulation using (4.45) and integrate the data for the  $S^3$  gyroscope. Numerical simulation estimates an effective mass of 21.472 mg for out-of-plane mode that is very similar with the theoretical estimation. The reason that the sensing mode has a little lower effective mass is that as the structure deforms vertically some part of the proof mass deformed a little less than the maximum deformation of the system. The large value for the effective mass of the  $S^3$  gyroscope shows a high potential for low noise MEMS gyroscopes. By just making this gyroscope from a  $500\ \mu\text{m}$  thick silicon with proof mass of  $1\text{cm}\times 1\text{cm}$  the effective mass will be more than 150 mg that is much larger than the effective mass of the existing MEMS gyroscopes (the effective mass of the BSR gyroscope is calculated to be less than 1 mg).

### 5.3 Angular Gain

Angular gain is one of the most important parameters in the performance of gyroscopes. Theoretical model for numerical calculation of angular gain was developed in 4.3. It can be shown that if driving and sensing motions are perpendicular to each other as well as to the rotation direction, angular gain is one. This means that all the possible energy can be successfully transferred from the driving mode to the sensing mode due to the Coriolis acceleration.

Figure 5.33 shows the schematic of a perfect  $S^3$  gyroscope. In this case, the deriving and sensing motions and rotation directions are perfectly perpendicular. Therefore, angular gain should be one. In the real  $S^3$  structure such as the one shown in Figure 3.10, some parts of the structure might have different motions. For those cases, numerical simulation should be utilized to predict accurate angular gain. For the  $S^3$  shown in Figure 3.10, angular gain is calculated using (4.58). The result show that **angular gain is 0.986**, which is very close to the maximum possible value.

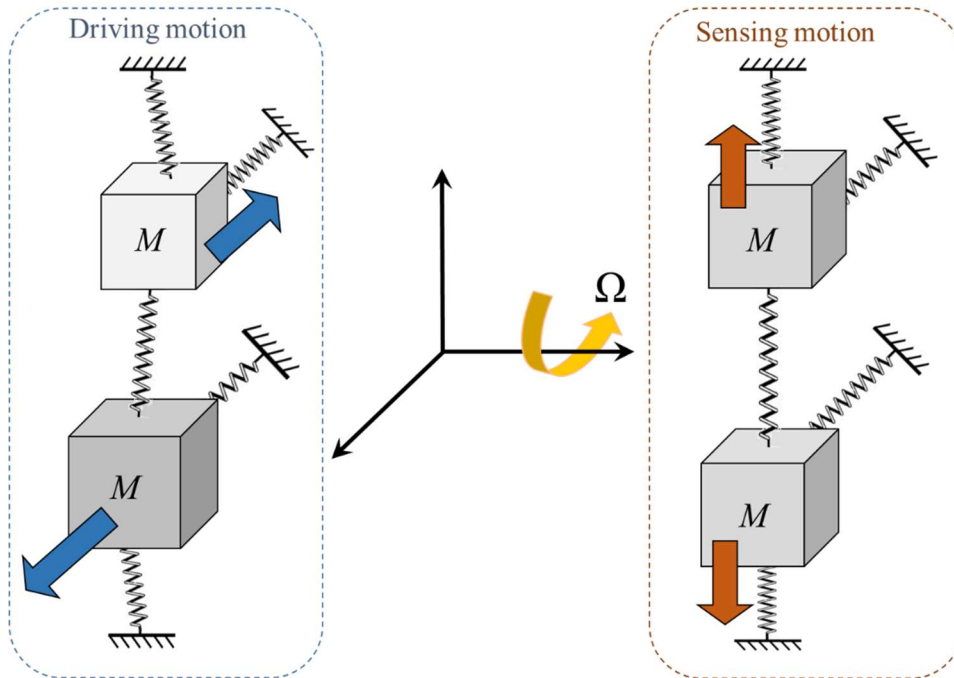


**Figure 5.33:** Schematic of the driving and sensing motion in a  $S^3$  gyroscope. For this schematic, directions of motion in driving and sensing modes are perpendicular to each other as well as to the rotation direction; therefore, angular gain is one.

## 5.4. Resonant Frequency

Resonant frequency of a  $S^3$  gyroscope affects its noise. This section includes an analytical model and numerical simulation for approximating resonant frequencies of  $S^3$  structures and a comprehensive investigation on the effect of different parameters on resonant frequencies of them.

### 5.4.1 Analytical model for resonant frequencies of $S^3$ gyroscope

In this part, simple models are developed for approximating resonant frequencies of the  $S^3$  analytically in sensing and driving directions. To calculate the resonant frequency of the  $S^3$  analytically, it is considered that each layer is a SMFB resonator as shown in Figure 5.28. As shown in Figure 5.34, it is assumed that each folded beam consists of two guided-end beams. This assumption is for estimating the stiffness of each folded beam.

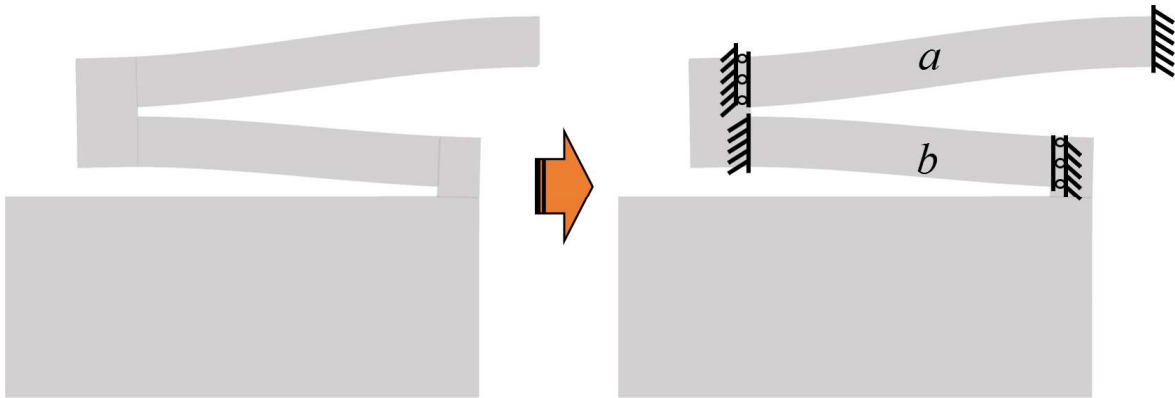


**Figure 5.34:** A folded beam assumed as two guided-end beams.

For a guided-end beam with length  $l$ , stiffness equals:

$$k = \frac{12EI}{l^3} \quad (5.7)$$

where  $I$  is moment of inertia and  $E$  is Young's modulus. Therefore, stiffnesses for beams  $a$  and  $b$  in the  $x$  (driving) direction are

$$k_{ax} = \frac{EtW_a^3}{l_a^3} \quad (5.8)$$

$$k_{bx} = \frac{EtW_b^3}{l_b^3} \quad (5.9)$$

As a result, total stiffness of four folded beams in the  $x$  direction equals:

$$k_x = 4 \times \left( \frac{k_{ax} \times k_{bx}}{k_{ax} + k_{bx}} \right) = 4Et \times \left( \frac{W_a^3 W_b^3}{W_a^3 l_b^3 + W_b^3 l_a^3} \right) \quad (5.10)$$

Stiffnesses in the  $z$  (sensing) direction are:

$$k_{az} = \frac{EW_a t^3}{l_a^3} \quad (5.11)$$

$$k_{bz} = \frac{EW_b t^3}{l_b^3} \quad (5.12)$$

Therefore, the total stiffness of the system in  $z$  direction is:

$$k_z = 4 \times \left( \frac{k_{az} \times k_{bz}}{k_{az} + k_{bz}} \right) = 4Et^3 \times \left( \frac{W_a W_b}{W_a l_b^3 + W_b l_a^3} \right) \quad (5.13)$$

The mass of the system estimated from:

$$m = \rho w h t \quad (5.14)$$

Therefore, resonant frequencies for driving and sensing modes are:

$$f_x = \frac{1}{2\pi} \sqrt{\frac{k_x}{m}} = \frac{1}{\pi} \sqrt{\frac{EW_a^3 W_b^3}{W_a^3 l_b^3 + W_b^3 l_a^3} \frac{1}{\rho w h}} \quad (5.15)$$

$$f_z = \frac{1}{2\pi} \sqrt{\frac{k_z}{m}} = \frac{1}{\pi} \sqrt{\frac{Et^2 w_a w_b}{w_a l_b^3 + w_b l_a^3}} \quad (5.16)$$

To confirm the accuracy of these equations, resonant frequencies of a system with dimensions shown in Table 5.3 are calculated both analytically and numerically and the results are compared. For a silicon  $S^3$  gyroscope with material properties that are considered to be Young's modulus  $E_{si} = 160$  GPa, Poisson's ratio  $\nu_{fs} = 0.28$ , and density  $\rho_{si} = 2329$  kg/m<sup>3</sup>, resonant frequencies are calculated to be:

$$f_x = 7807 Hz \quad (5.17)$$

$$f_z = 10410 Hz \quad (5.18)$$

To obtain resonant frequencies numerically, COMSOL Multiphysics is used to solve the FEM eigenfrequency problem. The results of numerical simulations show that:

$$f_x = 8126 Hz \quad (5.19)$$

$$f_z = 9240 Hz \quad (5.20)$$

The numerical predications are similar to the analytical ones, which confirms the accuracy of the analytical models. Therefore, these analytical models can be used for fast design of the  $S^3$  gyroscopes. However, it should be considered that analytical models are obtained with lots of simplifications; for a more accurate estimation, there is a need for numerical simulation.

#### 5.4.2 Effect of $S^3$ geometry on resonant frequencies

In this section, the effect of the shape characteristics of the  $S^3$  structure on its resonant frequencies is analyzed numerically by changing the geometric properties of the resonator. The results of this analysis are shown in Figures 5.35.

Figure 5.35 shows that increasing the resonator thickness increases the sensing resonant frequency while it does not have a remarkable impact on the driving resonant frequency. Stiffness of beams in the  $x$  direction has a direct relation with the thickness of beams (equation (5.10)). At the same time, the mass of the system has a direct relation with the thickness. Therefore, increasing the thickness should not affect the driving resonant frequency. However, the stiffness of beams in the  $z$  direction has a direct relation to their thickness to the power of three. As a result, increasing the thickness increases the sensing resonant frequency.

This figure also shows that increasing the width or length of the central mass decreases both frequencies. The main reason for this behavior is that increasing each of these parameters increases the mass of the central part, which leads to lower frequencies. On the other hand, as the width of the central mass increases its rigidity decreases in the  $z$  direction that also results in lower resonant frequency in the sensing mode.

Figures 5.35 shows that by increasing the width of the beams will increase resonant frequencies. I increasing the width of the beams increases the moment of inertia of the folded beams. The moment of inertias for a beam with the thickness  $t$  and the width  $w$  in the  $x$  and  $z$  directions are:

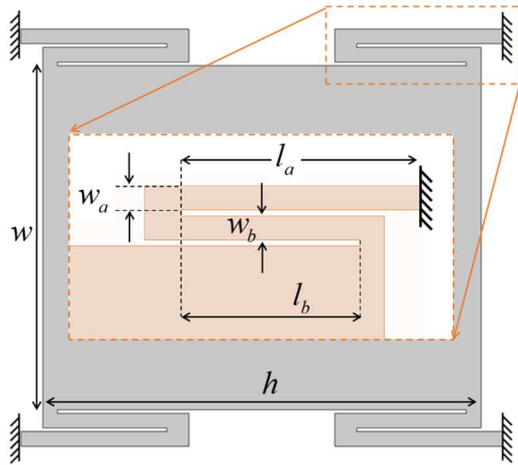
$$I_{xx} = \frac{tw^3}{12} \quad (5.21)$$

$$I_{zz} = \frac{wt^3}{12} \quad (5.22)$$

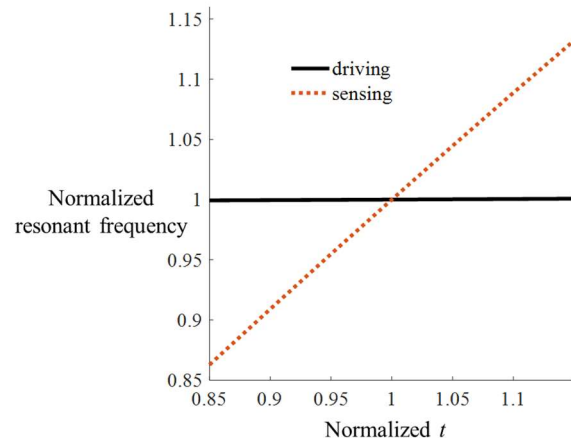
Therefore, increasing the width of beams increases their stiffness, especially in the  $x$  direction. As a result, resonant frequencies increase with increasing the widths, but driving resonant frequency increases more than the sensing.



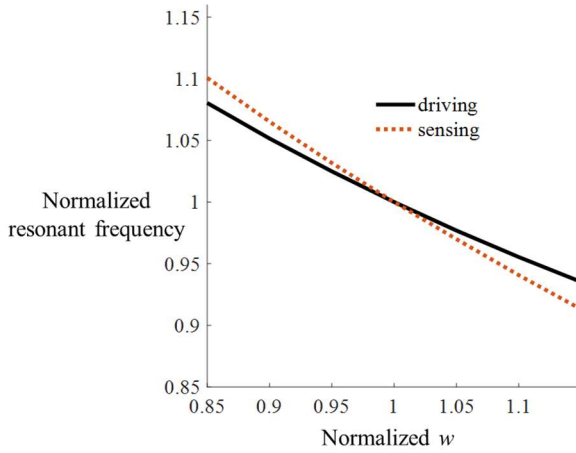
As shown in this figure, increasing the length of the beams reduces resonant frequencies. Stiffness of a beam has an opposite relation to the beam length to the power of three; therefore, increasing the length of folded beams makes them softer thus resonant frequencies decrease.



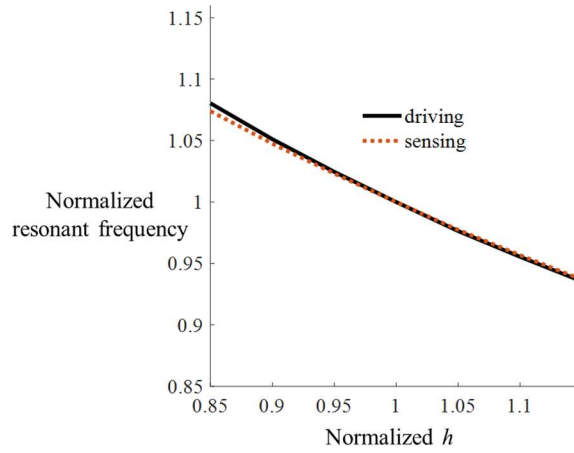
(a)



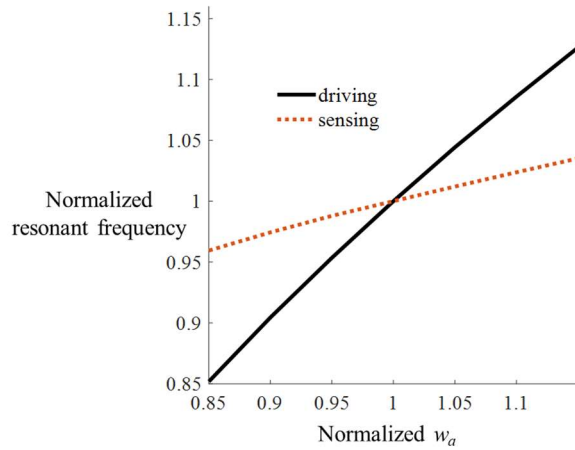
(b)



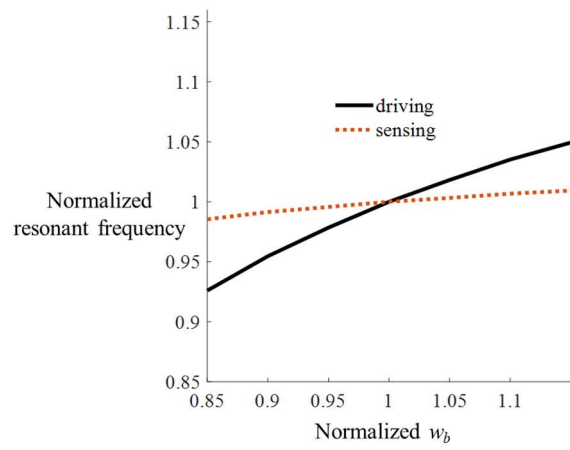
(c)



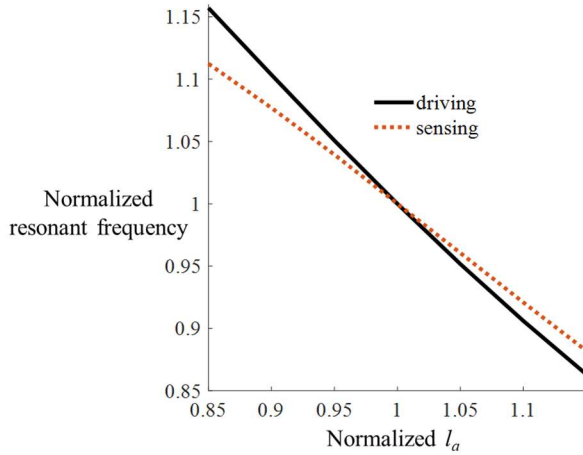
(d)



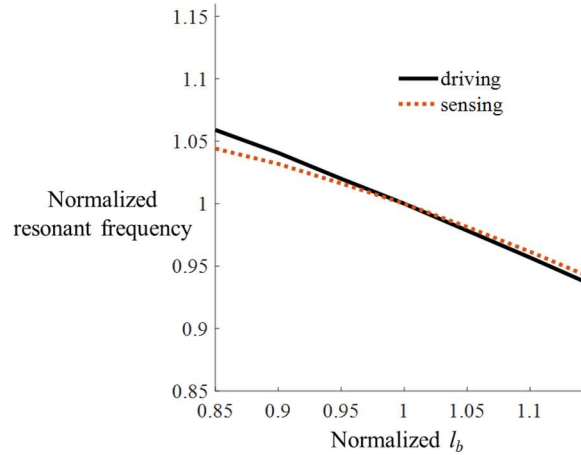
(e)



(f)



(g)



(h)

**Figure 5.35:** Normalized resonant frequencies of driving and sensing mode of a  $S^3$  gyroscope versus its geometrical properties. (b) Effect of thickness of the structure on resonant frequencies. (c) Effect of width of central mass on resonant frequencies. (d) Effect of length of central mass on resonant frequencies. (e) Effect of width of beam  $a$  on resonant frequencies. (f) Effect of width of beam  $b$  on resonant frequencies. (g) Effect of length of beam  $a$  on resonant frequencies. (h) Effect of length of beam  $b$  on resonant frequencies.

### 5.4.3 Effect of temperature on resonant frequencies

As discussed in 5.1, the  $S^3$  gyroscope will be made from silicon. The material properties of silicon are dependent on temperature. The working temperature of the system may change during operation, so the resonant frequency of the structure may vary. It is considered that Young's modulus of silicon changes with temperature by  $-64$  ppm/K (this is just an approximation about the thermal coefficient of Young's modulus (TCE) of silicon, there has been many researches on the effect of temperature on the Young's modulus of silicon). The resonant frequencies of the structure for different operating temperatures are simulated with considering the fact that changing the temperature can cause stress in the system that might lead to a change in resonant frequency. The results are normalized with respect to the resonant frequency at  $293.15$  K and shown in Figure 5.36.

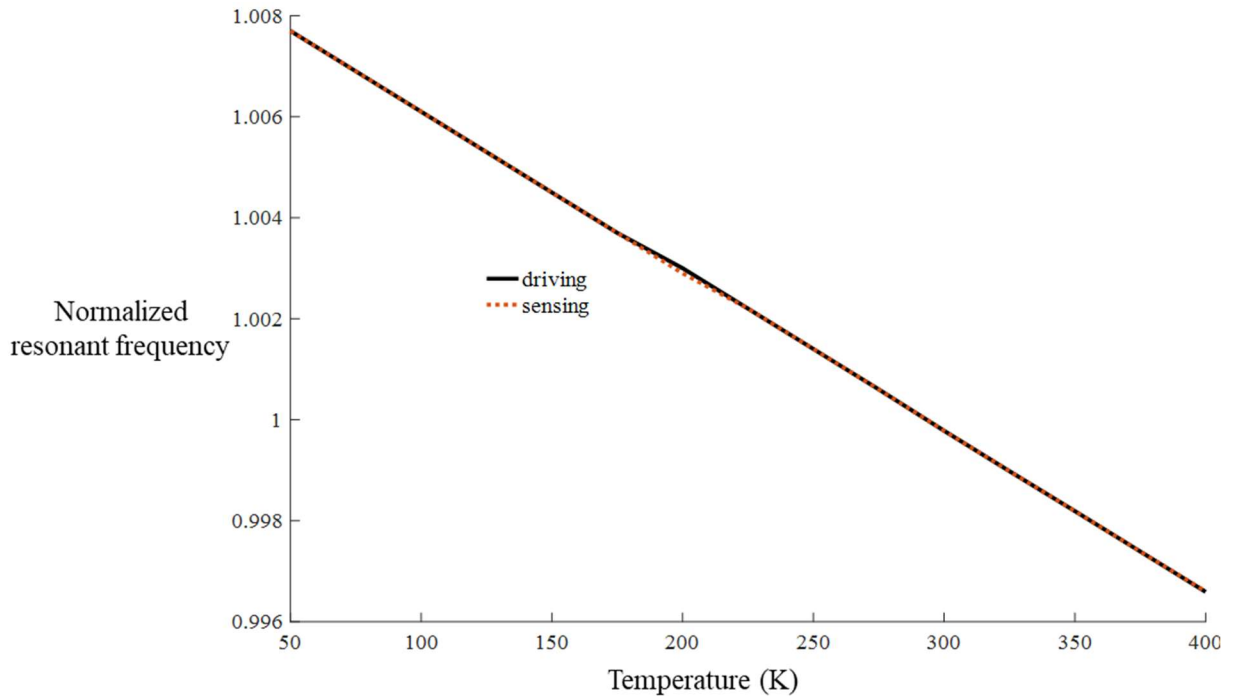


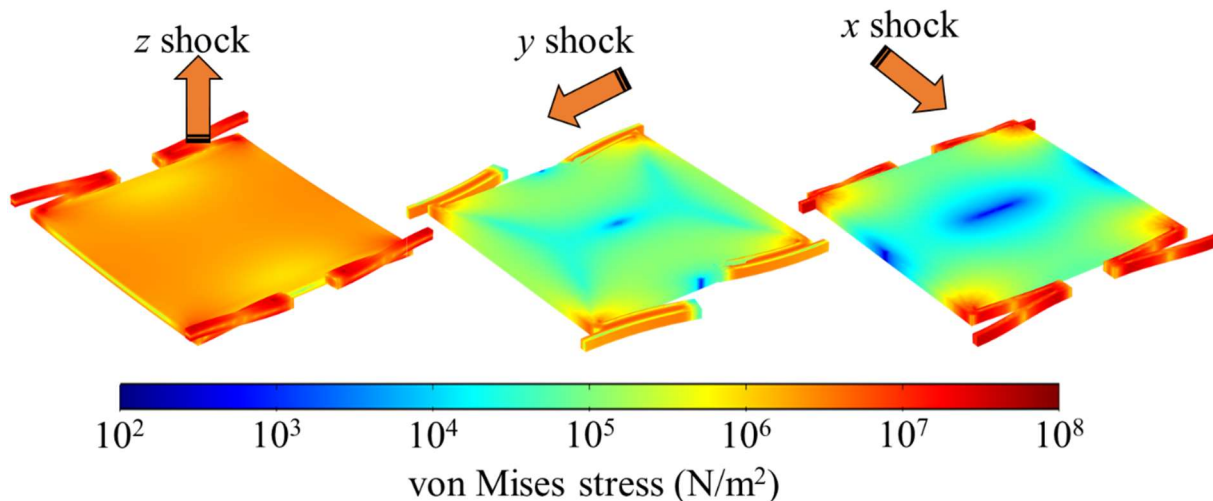
**Figure 5.36:** Effect of operating temperature of the silicon  $S^3$  gyroscope on its resonant frequencies.

Numerical results show that both resonant frequencies change almost in the same manner with respect to temperature.

#### 5.4.4 Effect of shock on resonant frequencies

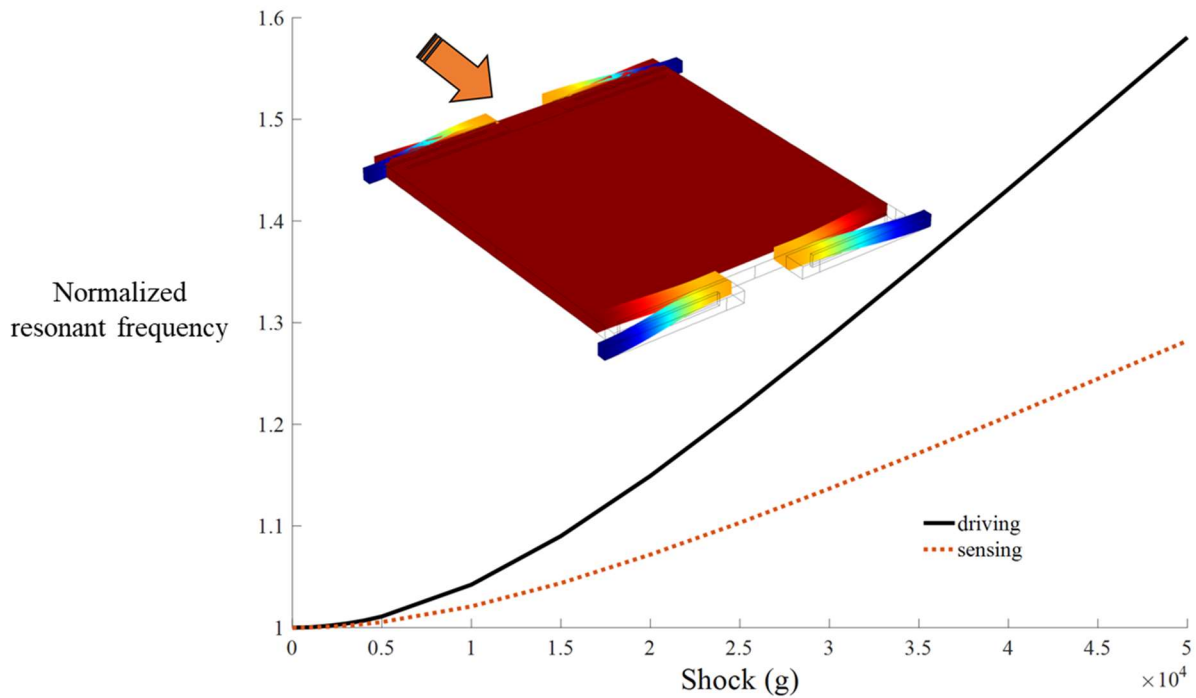
As discussed in 4.4.5, the existence of shock causes stress and deformation in a structure, which can change its resonant pattern. A group of prestressed eigenfrequency simulations is conducted to understand the effects of shock on resonant frequencies of a  $S^3$  resonator. To perform this analysis, the same method that was discussed in the 4.4.5 is utilized.

Figure 5.37 shows von Mises stress distribution in one layer of a  $S^3$  structure under 1,000g shocks. These shocks are exerted in the  $x$ ,  $y$ , and  $z$  directions. This figure shows that all of these shocks create a large stress in the folded beams. Stress on folded beams under  $x$  and  $z$  shocks is larger than  $y$  shock. So, it is expected that these two shocks create larger change in the resonant frequencies.



**Figure 5.37:** von Mises stress in one layer of a  $S^3$  structure under 1,000g shock in different directions. These shocks create a large stress in the folded beams.

The effects of shock on resonant frequencies are depicted in Figures 5.38, 5.39, and 5.40. The amounts of these shocks are changed from 0 to 50,000g. Numerical simulation shows that shock in the  $x$  direction has a large effect on resonant frequencies since it creates a large stress in the folded beams. It is also found that this shock can cause a large amount of frequency split because two modes are not symmetric in the case of a  $S^3$  gyroscope.



**Figure 5.38:** Effect of shock in the  $x$  direction on resonant frequencies. This shock has a significant impact on the resonant frequencies. Additionally, it creates a large frequency split.

Figure 5.39 shows that shock in the  $y$  direction has small effect on resonant frequencies because it does not cause a large stress in the folded beams. Frequency split is also very small in this case.

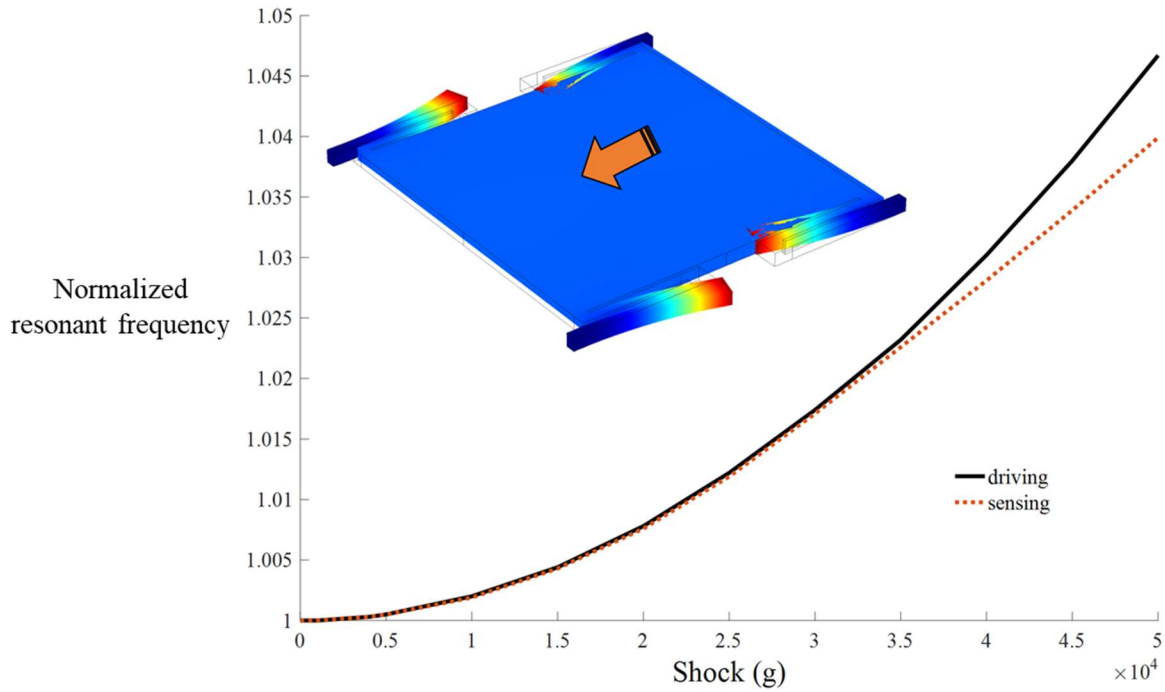


**Figure 5.39:** Effect of shock in the  $y$  direction on resonant frequencies. This shock has a small effect on the resonant frequencies. Furthermore, it does not create a large frequency split.

According to Figure 5.40, shock in the  $z$  direction can cause a relatively large change in resonant frequencies. During a large shock in the  $z$  direction, a relatively large stress is created in the folded beams, which changes the resonant frequencies. In this case, there is a frequency split but not as large as the case of the shock in the  $x$  direction.

#### 5.4.5 Effect of anisotropic behavior of silicon on resonant frequency

All the simulations until now was done be considering that the  $S^3$  gyroscope is made from an isotropic material; however, the most used material for MEMS gyroscopes is the single crystalline silicon, which is an anisotropic material. Material properties of silicon depend on orientation relative to the crystal lattice. For an isotropic material stress-strain relationship can be easily represented by (5.23).

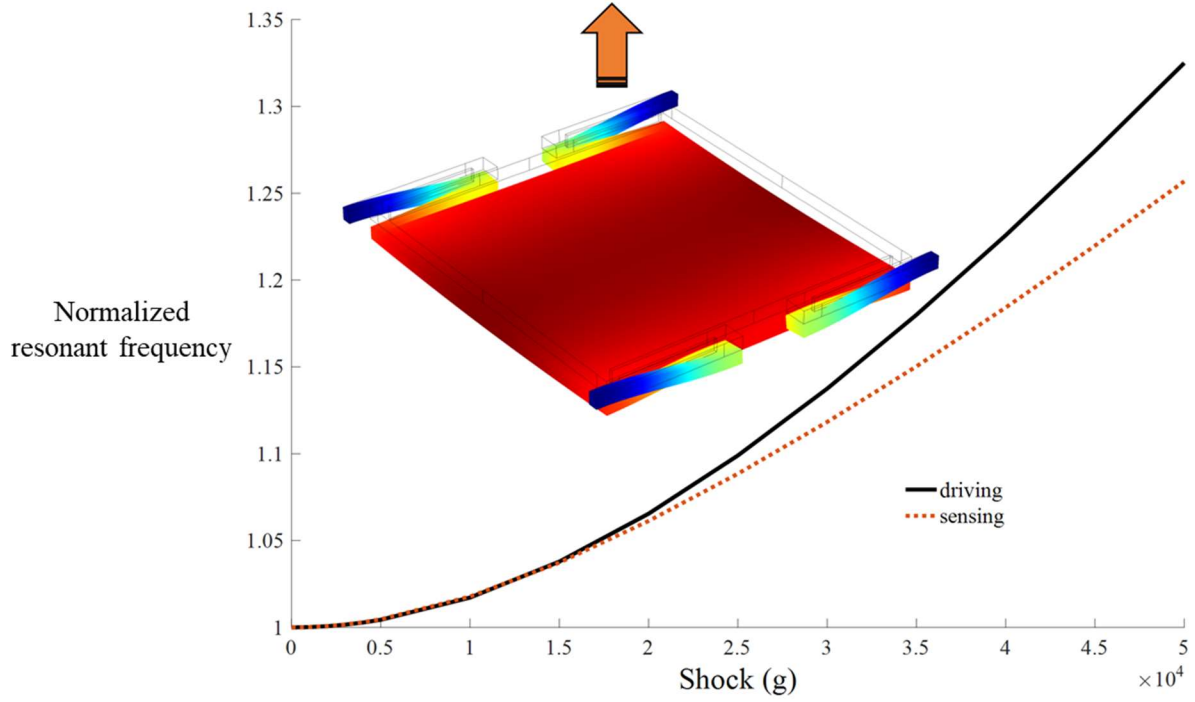


**Figure 5.40:** Effect of shock in the  $z$  direction on resonant frequencies. This shock has a significant impact on resonant frequencies. Additionally, it creates a large frequency split.

$$\sigma = E\varepsilon \quad (5.23)$$

where  $\sigma$  is stress,  $E$  is Young's modulus and  $\varepsilon$  is strain. For an anisotropic material, a fourth rank tensor with 81 terms is required to describe the elasticity by relating the second rank tensors of stress and strain [106]. For silicon, cubic symmetry and the equivalence of the shear conditions reduce this complicated relationship to the following equation:

$$\begin{bmatrix} \sigma_1 \\ \sigma_2 \\ \sigma_3 \\ \sigma_4 \\ \sigma_5 \\ \sigma_6 \end{bmatrix} = \begin{bmatrix} c_{11} & c_{12} & c_{12} & 0 & 0 & 0 \\ c_{12} & c_{11} & c_{12} & 0 & 0 & 0 \\ c_{12} & c_{12} & c_{11} & 0 & 0 & 0 \\ 0 & 0 & 0 & c_{44} & 0 & 0 \\ 0 & 0 & 0 & 0 & c_{44} & 0 \\ 0 & 0 & 0 & 0 & 0 & c_{44} \end{bmatrix} \begin{bmatrix} \varepsilon_1 \\ \varepsilon_2 \\ \varepsilon_3 \\ \varepsilon_4 \\ \varepsilon_5 \\ \varepsilon_6 \end{bmatrix} \quad (5.24)$$

where  $c_{11} = 165.6 \times 10^9$  Pa,  $c_{12} = 63.9 \times 10^9$  Pa and  $c_{44} = 79.5 \times 10^9$  Pa [66].

To quantify the effect of anisotropic behavior of silicon on resonant frequencies of a  $S^3$  gyroscope, COMSOL Multiphysics is used to solve the FEM eigenfrequency problem considering silicon material follows (5.24). Resonant frequencies of a  $S^3$  gyroscope are calculated for a wafer shown in Figure 5.42. It is considered that the  $S^3$  gyroscope can rotate  $\Theta$  ( $^\circ$ ) in this wafer. The results of resonant frequency calculation are normalized to the amount of resonant frequencies when  $\Theta$  is zero. As shown in Figure 5.41, resonant frequencies are different for different directions. This difference can be as much as 10%. Therefore, it is essential for a designer to consider this effect during the designing process.

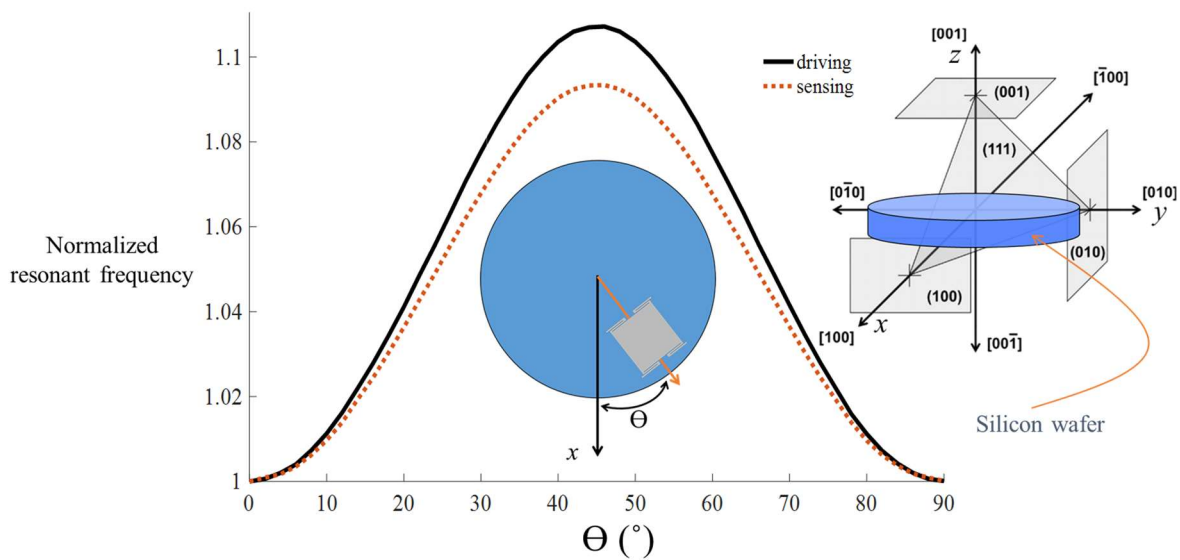


**Figure 5.41:** Effect of location of the  $S^3$  gyroscope on a silicon wafer on its resonant frequencies. This figure also shows a wafer with miller indices in a cubic crystal.

## 5.5 Frequency Split

All the analysis about the resonant frequencies related to a perfectly fabricated  $S^3$  gyroscope; however, during the fabrication there will be some imperfections in the system that lead to frequency split ( $\Delta f$ ) between sensing and driving modes. As shown in Chapter 2,  $\Delta f$  causes



a large performance drop in CVGs. This section talks about the effect of different imperfections on resonant frequencies, and then the electrostatic tuning approach for  $S^3$  gyroscopes will be explained to remove  $\Delta f$ .

### **5.5.1 Effect of geometric imperfections on frequency split**

All of the geometric parameters can be changed during the fabrication process. To understand the effect of change in these parameters on frequency split, each of them are changed and resonant frequency of sensing and driving modes are simulated. Then, the difference between normalized resonant frequencies is calculated and sketched in Figure 5.42 (the frequencies are normalized at their reference frequency for designed structure).

According to Figure 5.42, a change in the thickness of the resonator layer can cause the largest frequency split. This can be a challenge since the thickness of the initial wafers can be as different as 5% that can cause about 5% frequency split. The reason that thickness has this huge impact is that resonant frequency in sensing axis increases linearly with thickness while driving resonant frequency remains almost constant with thickness. This imperfection can be reduced by thinning the thicker wafer to the thickness of the thin one.

The widths of the beam  $a$  and beam  $b$  also can have a large effect on the frequency split. Because these parameters have larger impact on the stiffness in driving direction comparing to the sensing directions. These also can be a challenge because it is likely that the width of beams be different from what is designed due to the over etching of the suspended beams. The lengths of the beams and proof mass dimensions have less of an impact on the frequency split since they have almost the same effect on resonant frequencies of the sensing and driving modes.

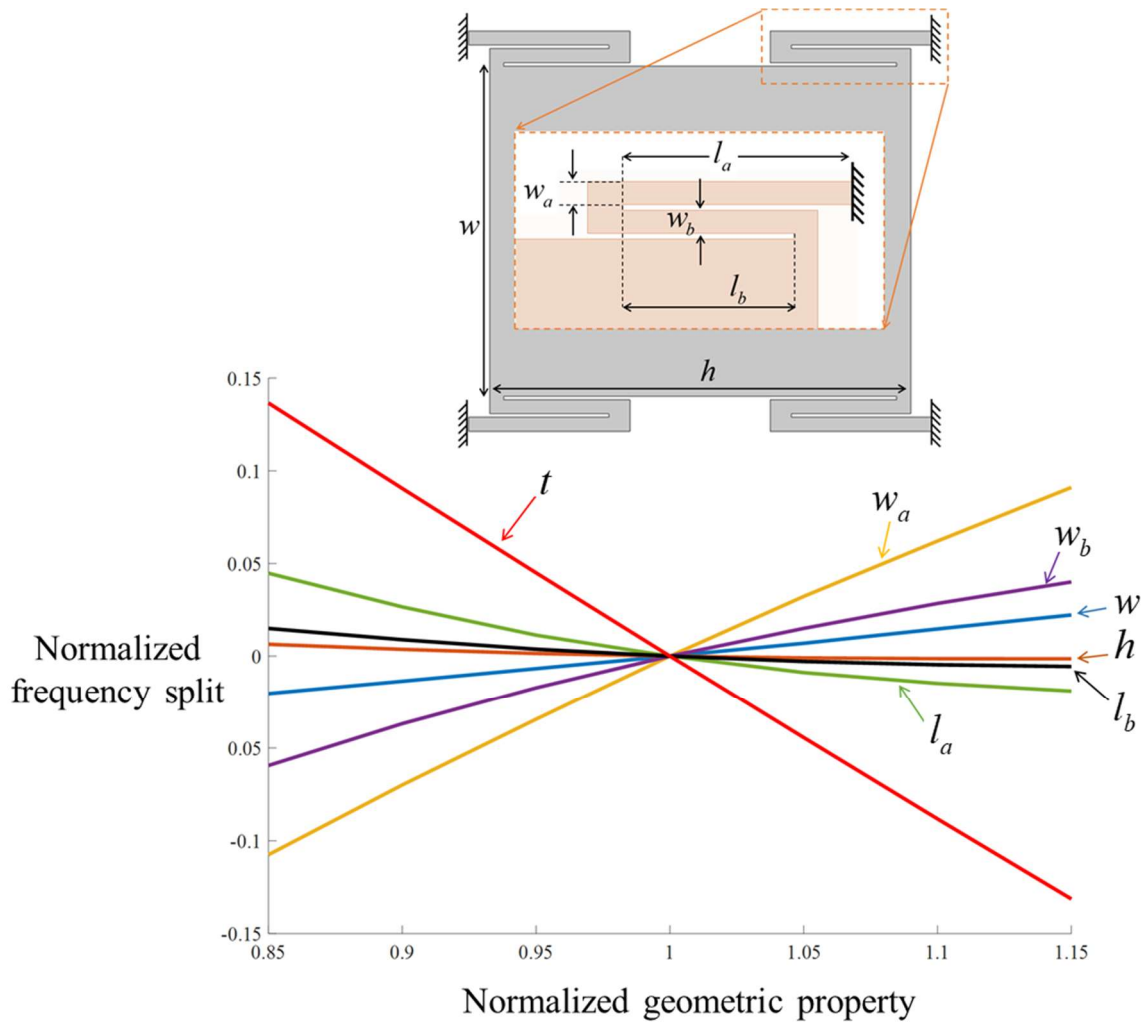


**Figure 5.42:** Effect of imperfections in fabrication of geometric properties of the resonator on split on frequencies. Among all of the parameters, variation in the thickness of the resonator has the largest impact.

### 5.5.2 Effect of imperfection due to anisotropic behavior of silicon on frequency split

As discussed in section 5.4.5, anisotropic behavior of silicon can change resonant frequencies of the designed structure if the device is made in a different direction than designed one. It is possible that during fabrication process the device is made in a different direction, which might cause frequency split. To characterize the amount of this effect, it is considered that the  $S^3$  gyroscope is designed for a  $\Theta$  of zero, so it does not have any frequency split in this location. The

location of the device is changed and resonant frequencies are calculated. The result of the frequency split is shown in Figure 5.43. This imperfection does not have a large impact on the frequency split, unless the location of the device is very off from the designed location, which is very unlikely to happen.

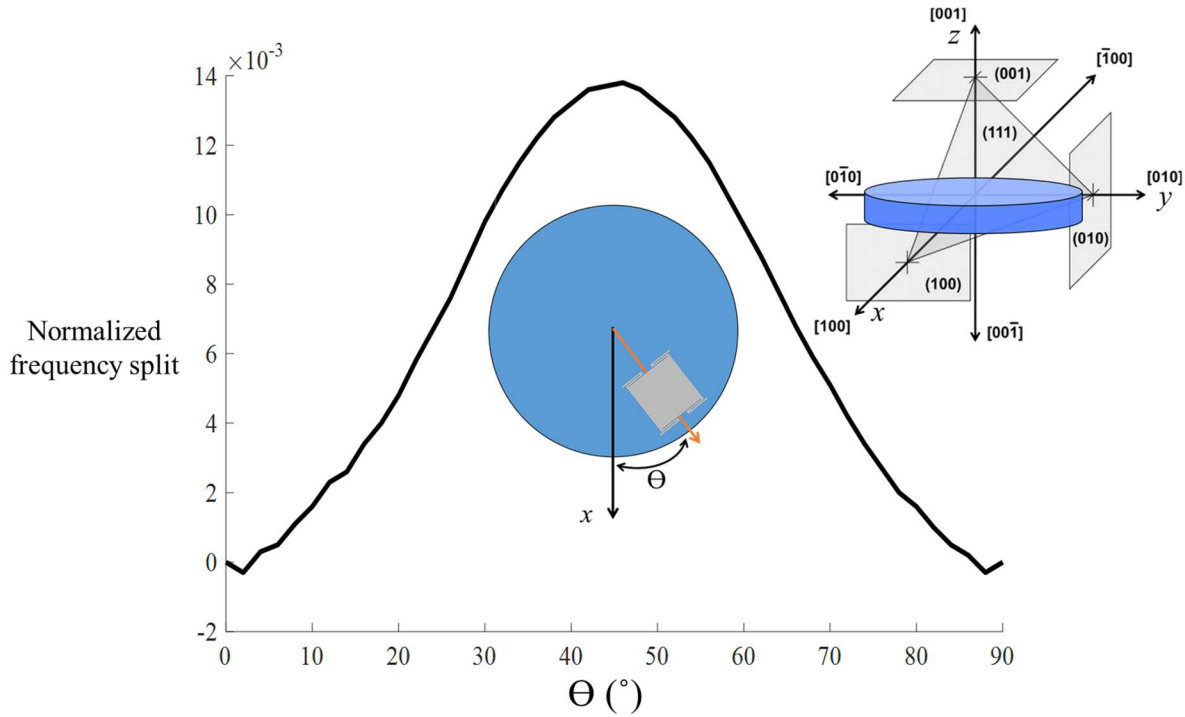


**Figure 5.43:** Effect of location of the  $S^3$  gyroscope on the silicon wafer on its frequency split. It is considered that when  $\Theta$  is zero there is no frequency split.

### 5.5.3 Effect of electrostatic tuning on resonant frequency

Frequency split in the  $S^3$  gyroscope can be removed because DC bias that is applied to the electrodes can change the resonance frequencies. To calculate the effect of this DC voltage ( $V$ ) on resonant frequency, the system of lower mass that is shown in Figure 5.44 is considered.

Electrostatic force that is exerted to this lower mass equals:

$$f_z = -\frac{\varepsilon A}{2(g_0 + z)^2} V^2 = -\frac{\varepsilon A}{2g_0^2 \left(1 + \frac{z}{g_0}\right)^2} V^2 \approx -\frac{\varepsilon A}{2g_0^2} V^2 \left(1 - \frac{2z}{g_0}\right) \quad (5.25)$$

where  $V$ ,  $A$ ,  $g_0$ , and  $\varepsilon$  are voltage, the electrode area, initial gap, and permittivity between the electrodes and resonator, respectively. Newton's second law of motion leads to:

$$m\ddot{z} + k_{2z}z = -\frac{\varepsilon A}{2g_0^2} V^2 \left(1 - \frac{2z}{g_0}\right) \quad (5.26)$$

Therefore:

$$m\ddot{z} + \left(k_{2z} - \frac{\varepsilon A}{g_0^3} V^2\right) z = -\frac{\varepsilon A}{2g_0^2} V^2 \quad (5.27)$$

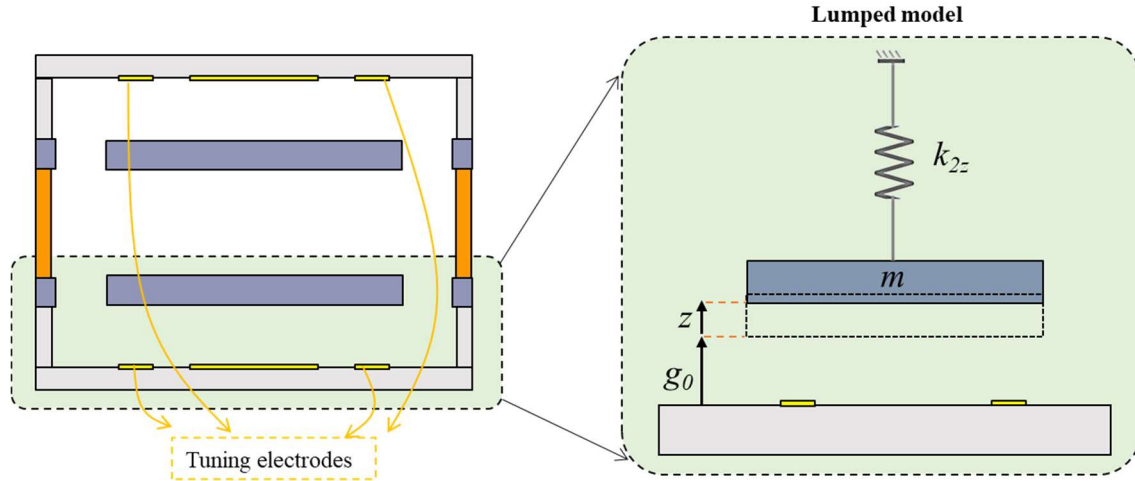


**Figure 5.44:** Schematic of the  $S^3$  gyroscope and a lumped model for the lower mass and tuning electrodes.

As a result, resonant frequency of this system is:

$$f_z = \frac{1}{2\pi} \sqrt{\frac{k_{2z} - \frac{\varepsilon A}{g_0^3} V^2}{m}} = \frac{1}{2\pi} \sqrt{\frac{k_{2z}}{m}} \sqrt{1 - \frac{\varepsilon A}{k_{2z} g_0^3} V^2} \approx f_{z0} \left(1 - \frac{1}{2} \frac{\varepsilon A}{k_{2z} g_0^3} V^2\right) \quad (5.28)$$

where  $f_{z0}$  is resonant frequency of the system without DC voltage. Hence, normalized change in resonant frequency due to the electrostatic force can be obtained from following equation:

$$\frac{\Delta f}{f_{z0}} = -\frac{1}{2} \frac{\epsilon A}{k_{2z} g_0^3} V^2 = -\frac{1}{8\pi^2} \frac{\epsilon A}{m f_{z0}^2 g_0^3} V^2 \quad (5.29)$$

For the  $S^3$  gyroscope where there are two masses, both  $m$  and  $A$  will be multiplied by 2 that leads to the same change in the frequency.

In the case that there is a frequency split between sensing and driving modes, this electrostatic tuning approach can be used for matching the frequencies. As this equation shows, to achieve higher tuning capability area and DC voltage should be as large as possible and gap should be very small. The gap between the cap and device layers is easily controllable and it is expected to get a gap smaller than  $5 \mu\text{m}$ . Area of tuning electrodes is also large. According to calculations, it is expected to get more than 1% tuning range in the  $S^3$  gyroscope.

## 5.6 Gyroscopic Operation

$S^3$  structure with high sensing  $Q$ , extremely large mass, large angular gain, and small  $\Delta f$  is designed. As explained in Chapter 3, two masses in this structure are driven in the in-plane direction. To achieve a low noise in CVGs, driving amplitude should be large.

### 5.6.1 Driving amplitude

Using parallel plate actuation scheme produces a non-linear electrostatic force. In the case of a large driving amplitude (larger than 10% of the driving gap), the device operates in a non-linear regime that reduces its performance. This was shown experimentally for shell gyroscopes

in chapter 4. Two methods can be used to prevent electrical non-linearity in the case of large driving amplitude:

- Designing a very large gap between driving electrodes and the resonator. However, this cannot be used in the design of many types of gyroscopes such as, shell and disk gyroscopes, because by increasing driving gap, the sensing gap also increases. As discussed in chapter 2, a large sensing gap results in a large electronic noise. On the other hand, in  $S^3$  gyroscopes, sensing and driving gaps are independent from each other, so one of them can be small and another can be large. Figure 5.45 shows schematic of a  $S^3$  gyroscope with extremely small sensing gap and large driving gap.
- Using comb-drive actuation instead of parallel plate actuators. Comb-drive actuation is known for its linearity comparing to parallel plate actuators. However, comb-drive is structurally impossible for many types of gyroscopes such as, shell and disk gyroscopes. While, this can be easily done in a  $S^3$  gyroscope.

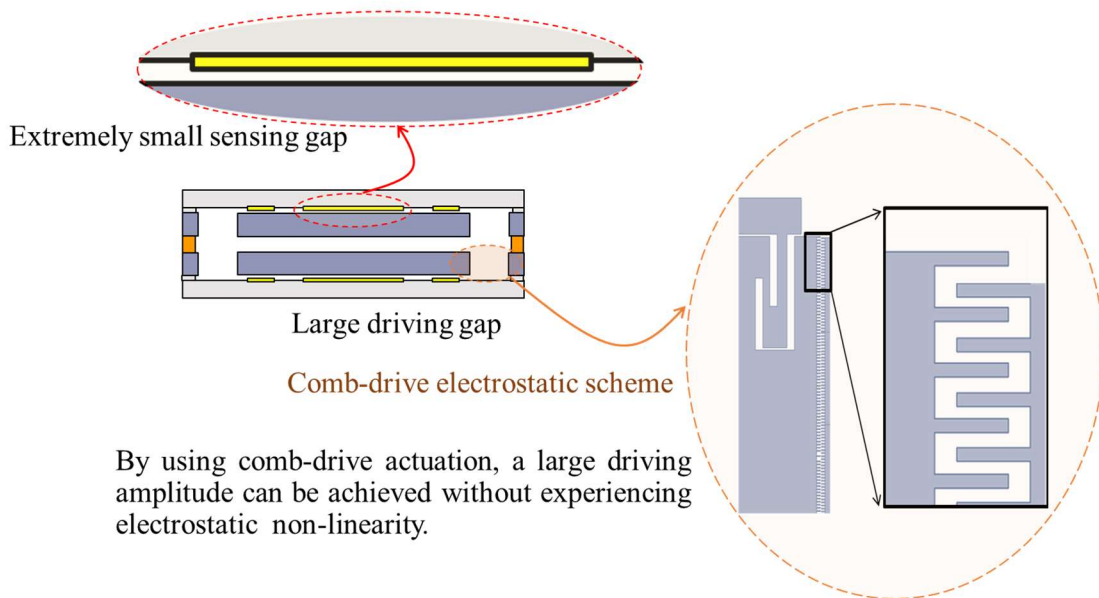


**Figure 5.45:** Schematic of a  $S^3$  gyroscope with extremely small sensing gap and large driving gap. This structure could produce a large driving amplitude and a large sensitivity.

Therefore, driving amplitude in  $S^3$  gyroscope can be very large compared to the majority of existing MEMS gyroscopes.

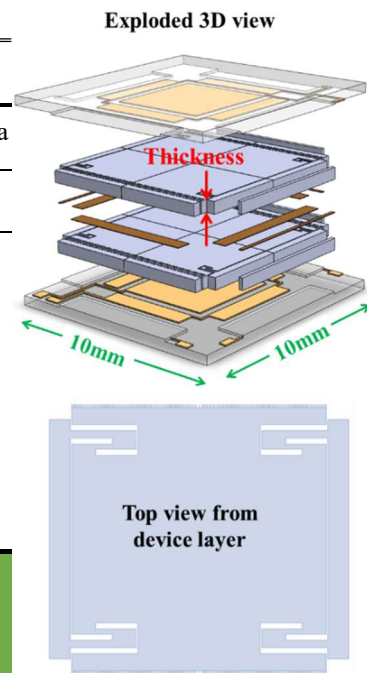
### 5.6.2 Performance

Equation (2.88) very accurately predicted the performance of shell gyroscopes as shown in Figure 4.78. The same equation can be used to estimate ARW of  $S^3$  gyroscopes. Table 5.6 shows the estimated values for the performance of  $S^3$  gyroscopes.

A silicon  $S^3$  gyroscope with 500  $\mu\text{m}$  thickness can achieve **ARW** of about  $1.5 \times 10^{-5} \text{ }^\circ / \sqrt{hr}$  ( $9 \times 10^{-4} \text{ }^\circ / hr / \sqrt{\text{Hz}}$ ). This value is much better than the requirement for inertial navigation (less than  $0.002 \text{ }^\circ / \sqrt{hr}$ ). Furthermore, a fused silica  $S^3$  gyroscope with 1 mm thickness can achieve an **ARW** of about  $7.6 \times 10^{-7} \text{ }^\circ / \sqrt{hr}$ , which is extremely small. However, technology for etching fused silica is not good enough for etching 1 mm substrate at this time.

TABLE 5.6: ESTIMATED ARW OF  $S^3$  GYROSCOPE

Parameter	Estimated values			
	Silicon	Silicon	Fused silica	Fused silica
Material	Silicon	Silicon	Fused silica	Fused silica
Thickness ( $\mu\text{m}$ )	500	1000	500	1000
Sensing $Q$	$1.8 \times 10^5$	$5.5 \times 10^5$	$5 \times 10^7$	$3 \times 10^7$
Effective Mass (mg)	130	260	130	230
Angular gain	0.98	0.98	0.98	0.98
Frequency (kHz)	15	23	12	18
Driving amplitude ( $\mu\text{m}$ )	10	10	10	10
<b>ARW (<math>^\circ / \sqrt{hr}</math>)</b>	<b><math>1.5 \times 10^{-5}</math></b>	<b><math>5 \times 10^{-6}</math></b>	<b><math>1 \times 10^{-6}</math></b>	<b><math>7.6 \times 10^{-7}</math></b>



## 5.7 Conclusion

Pitch or roll gyroscopes need to have a high  $Q$  in out-of-plane mode. However, it is found that  $Q$  of out-of-plane mode is limited by anchor loss in existing resonators. This research has shown that anchor loss can be decreased by more than five orders of magnitude by stacking two resonators that vibrate in the opposite directions. This novel type of resonator can be used in pitch or roll gyroscopes.

CVG design guidelines introduced in chapter 2 have been used to optimize the design of this type of gyroscope. As a result, a silicon MEMS gyroscope with effective mass of 130 mg, angular gain of 0.98, sensing gap of  $5 \mu\text{m}$ , and driving amplitude of  $10 \mu\text{m}$  has been designed. It is estimated that this gyroscope provides an ARW of about  $1.5 \times 10^{-5} \text{ }^\circ/\sqrt{hr}$  ( $9 \times 10^{-4} \text{ }^\circ/hr/\sqrt{\text{Hz}}$ ), which satisfies requirement for navigation.

Using the concept of  $S^3$  gyroscope, it is possible to design a pitch or roll gyroscope, which could achieve an ARW of about  $7.6 \times 10^{-7} \text{ }^\circ/\sqrt{hr}$ . However, this is not feasible with the current technology. Nonetheless, thick silicon  $S^3$  gyroscope could satisfy all the CVGs design parameters (as shown in Figure 5.46) and achieve the performance required for inertial navigation.

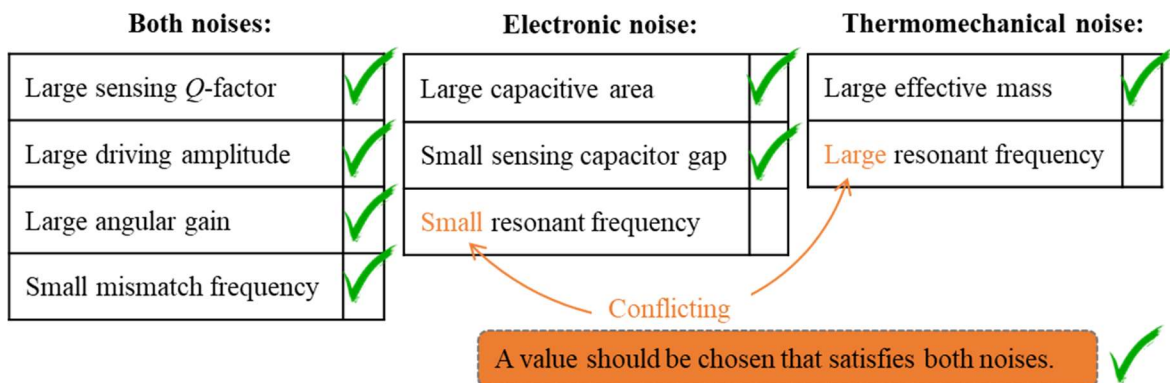


**Figure 5.46:** Checking the  $S^3$  gyroscope design parameters. This novel design structure can satisfy all the required parameters for high performance gyroscopes.



## Chapter 6: Summary, Conclusions, and Future Works

The aim of this research was to identify, analyze, model, and simulate important parameters in performance of MEMS gyroscopes and provide design guidelines for achieving **navigation-grade MEMS gyroscopes for all three axes**. This chapter summarizes the achievements and suggests future research directions.

### 6.1 Summary

It has been shown that the main source of error in inertial gyroscopes is ARW, including thermomechanical and electronic noises. It has been found that by increasing the sensing  $Q$ , effective mass, driving amplitude, sensing area, and angular gain and by reducing the sensing gap and frequency split, ARW decreases.

Shell gyroscopes have been analyzed, redesigned, and optimized to measure rotation rate in yaw direction with very high accuracy. This analysis includes optimizing all the parameters that affect noise.

Energy dissipation mechanisms in shell resonators, including anchor loss, surface loss, fluid damping, phonon interactions, internal dissipation, and TED have been investigated and design guidelines to eliminate or reduce them provided. As a result, miniaturized BSRs with very high  $Q$ s have been designed and fabricated. The highest  $Q$  tested in BSRs is larger than 10 million

that is for an uncoated shell. It has been found that coating the shells decreases their  $Q$ s, which necessitates using thinner coatings.

Angular gain and effective mass of BSRs have been modeled and simulated. The results have shown that for a BSR with a large aspect ratio, angular gain has a good value. However, the effective mass in BSRs is very small.

Resonant frequencies of BSRs and the effect of different parameters, such as shock and temperature, has been investigated comprehensively. It has been found that geometric imperfections can cause a split between the sensing- and driving-mode resonant frequencies. However, this split can be removed by electrostatic tuning.

The  $S^3$  gyroscope has been invented to measure rotation rate in pitch or roll directions. This novel design has solved the main problem of previous pitch and roll gyroscopes, i.e. low  $Q$  in out-of-plane mode.

In the  $S^3$  gyroscope, two similar out-of-plane resonators are stacked on top of each other and move in opposite directions. Since forces from the top and bottom cancel each other out, anchor loss is significantly reduced. This allows using thick resonators, which produces a very small TED, leading to a large  $Q$  in the  $S^3$  gyroscope. Initial testing of a stacked balanced resonator has shown more than **50× improvement in the  $Q$**  of a stacked resonator compared to the same non-stacked resonator.

It has been shown that in addition to  $Q$  improvement, the idea of  $S^3$  gyroscope provides a structure that allows optimization of all other effective parameters in ARW. In fact, a  **$S^3$  gyroscope** has an **extremely large effective mass**, a **very large angular gain**, a **very small sensing gap**, and a **large sensing area**.

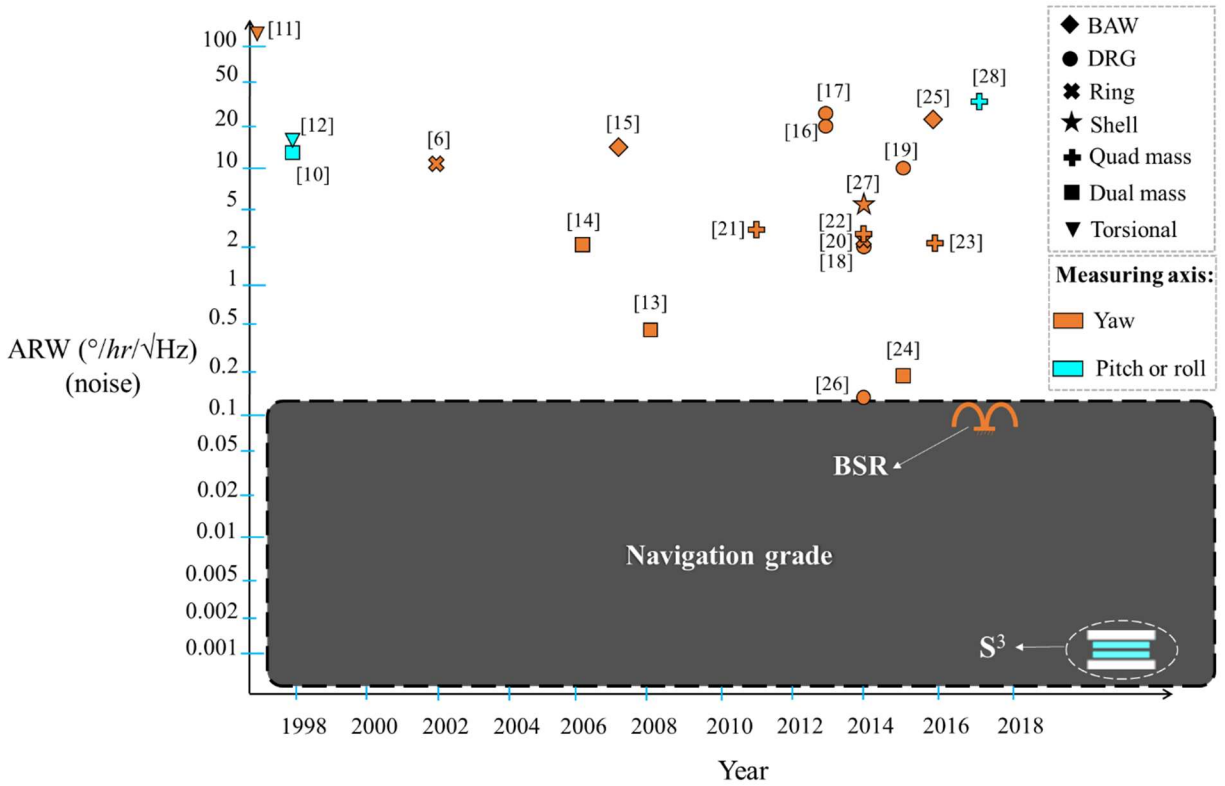


**Figure 6.1:** Summary of the noise performance of the best MEMS gyroscopes. BSR and  $S^3$  gyroscopes could provide required performance for navigation.

## 6.2 Conclusion

Figure 6.1 shows the noise performance of the best MEMS gyroscopes and estimated values for ARW of shell and  $S^3$  gyroscopes. Therefore, it is possible to make navigation-grade MEMS gyroscopes for all navigational directions. In fact, a MEMS BSR gyroscope with a very small ARW ( $<5 \times 10^{-3} \text{ }^\circ/\sqrt{hr}$ ) has been fabricated and tested in our group. In addition, it has been found that the measured noise values are very close to the expected values from theory. This validates the design guidelines provided in this research. Furthermore, it is expected that a  $500 \text{ } \mu\text{m}$

thick silicon  $S^3$  gyroscope achieves ARW of about  $1.5 \times 10^{-5} \text{ }^\circ/\sqrt{hr}$  ( $9 \times 10^{-4} \text{ }^\circ/hr/\sqrt{Hz}$ ), which is much better performance compared to existing pitch or roll gyroscopes.

## 6.3 Future Work

It is possible to improve the performance of the above designs. This section briefly discusses recommendations for improving the shell and  $S^3$  gyroscopes.

### 6.3.1 Shell gyroscopes

The main limiting parameters for performance of shell gyroscopes are their small driving amplitude and small effective mass.

Driving amplitude is limited by the size of the gap between the electrodes and shell (to prevent non-linearity, driving amplitude should be smaller than 10% gap). In the current design, increasing the driving gap size, increases the sensing gap, which results in to a larger electronic noise. Two approach can be implemented to increase driving amplitude:

- Developing a non-linear control system for these gyroscopes, so the non-linear behavior of the gyroscope with large driving amplitude does not reduce its performance.
- Increasing the driving gap and using a different sensing approach: for example using sensing electrodes beneath the shell rim.

The effective mass in shell gyroscopes is small because just a small portion of their structure moves during the device operation. To increase the effective mass, the size of the shell resonator can be increased in the future. Furthermore, designing a shell with a very thick rim could increase the effective mass because the moving part of the shell will have larger mass.

### 6.3.2 S<sup>3</sup> gyroscope

The  $Q$  of out-of-plane mode resonators has been improved significantly, but this  $Q$  can be improved more by decreasing TED. TED can be decreased in the S<sup>3</sup> gyroscope if its resonator is made from fused silica instead of silicon. Currently, technology for etching high aspect-ratio fused silica is not mature. Therefore, developing a large aspect-ratio fused silica etching technology would be beneficial for improving  $Q$ , which will lead to higher performance gyroscopes. In fact, a fused silica S<sup>3</sup> gyroscope with 1 mm thickness can achieve an **ARW** about  $7.6 \times 10^{-7} \text{ }^\circ / \sqrt{\text{hr}}$ , which is an extraordinary value.

## Appendix A: Fabrication of Birdbath Shell Structures

The fabrication process of birdbath shell structures consists of two major steps:

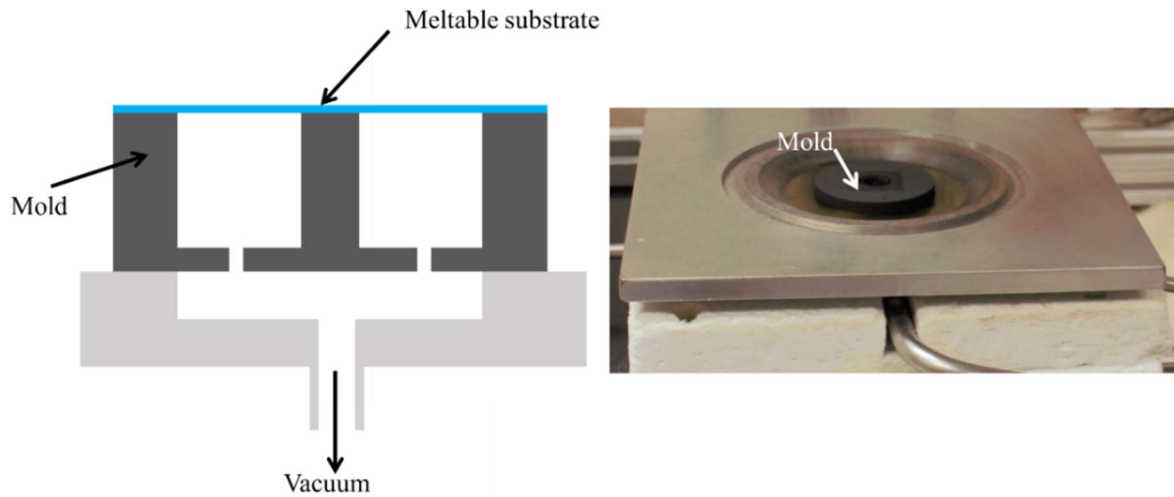
1- Shaping the substrate using blowtorch reflow process (Figure A1):

A substrate is fixed on top a machined graphite mold. Then an oxygen-propane flame reaching temperature  $>1700$  °C is brought to the surface of the substrate. At this temperature, the substrate (if it made from fused silica) starts to reflow into the mold forming a shell in 5–10 seconds.

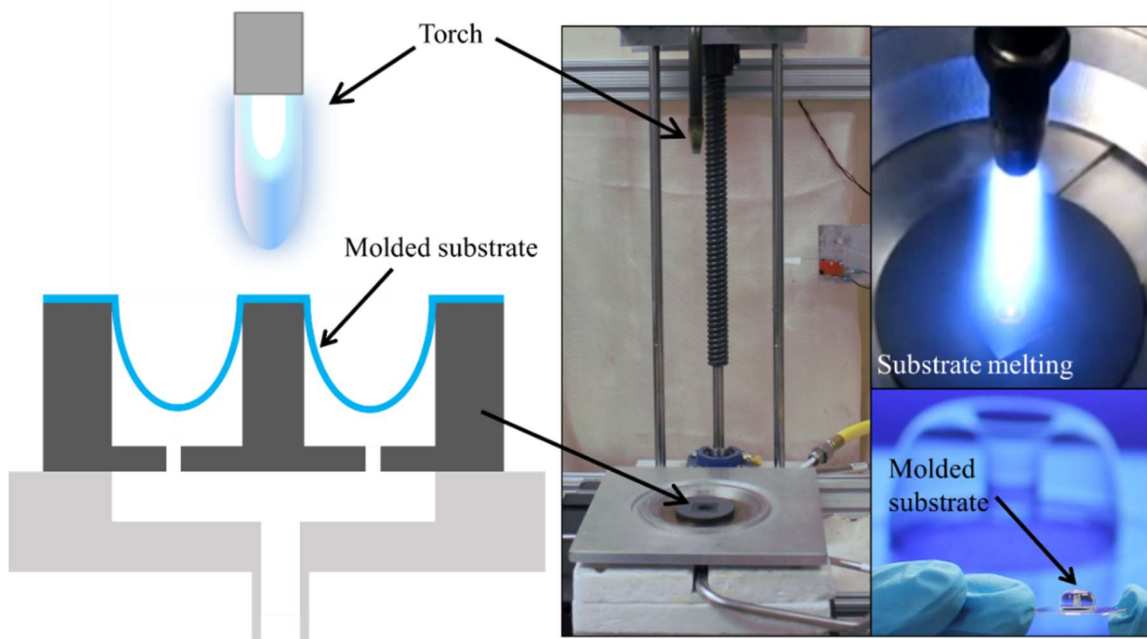
2- Releasing the shell structure from the flat part of the molded substrate (Figure A2):

Molded substrates are set into a thick silicon wafer with holes and surrounded by a protective thermoplastic that rigidly holds the shells in the silicon wafer. As the wafer is lapped, the bottom of the molded structure is removed, isolating the shell from the flat part. The shell rim is then polished with chemical-mechanical polishing/planarization (CMP).

Finally, the thermoplastic is dissolved, and metal is wet-etched to release the shells. Changing blowtorching parameters and the mold design allowed us to fabricate shells with different radii and aspect ratios. In this process, since the shell is fabricated monolithically, the stem is self-aligned. Furthermore, the high temperature flame smooths the shell surface with average roughness of the fabricated shell being less than  $2 \text{ \AA}$ , which could reduce surface loss.

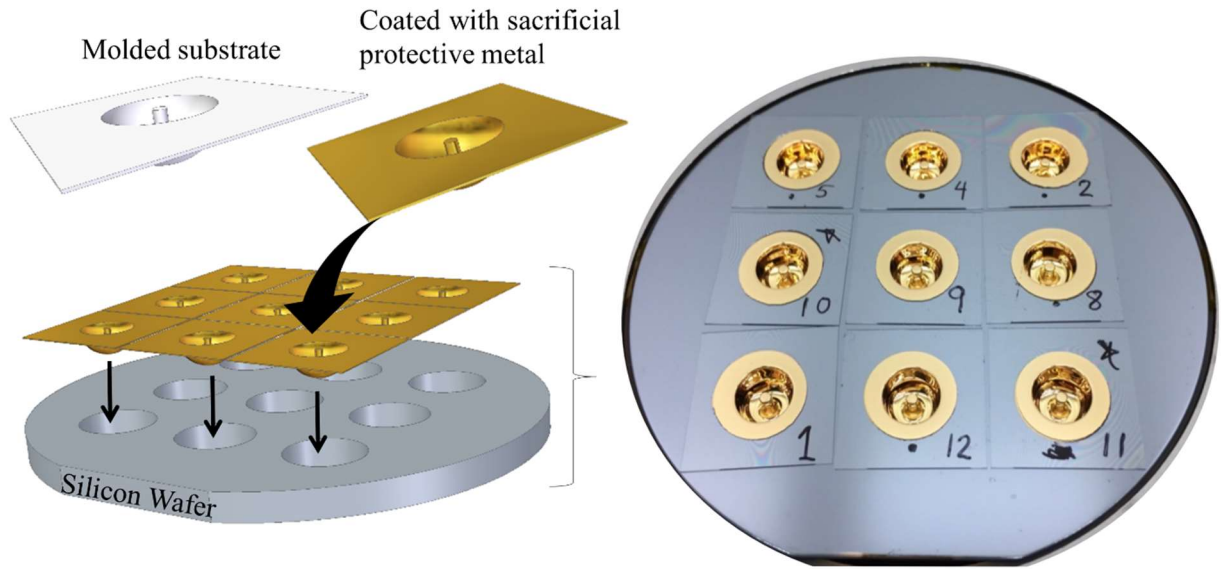


(a)

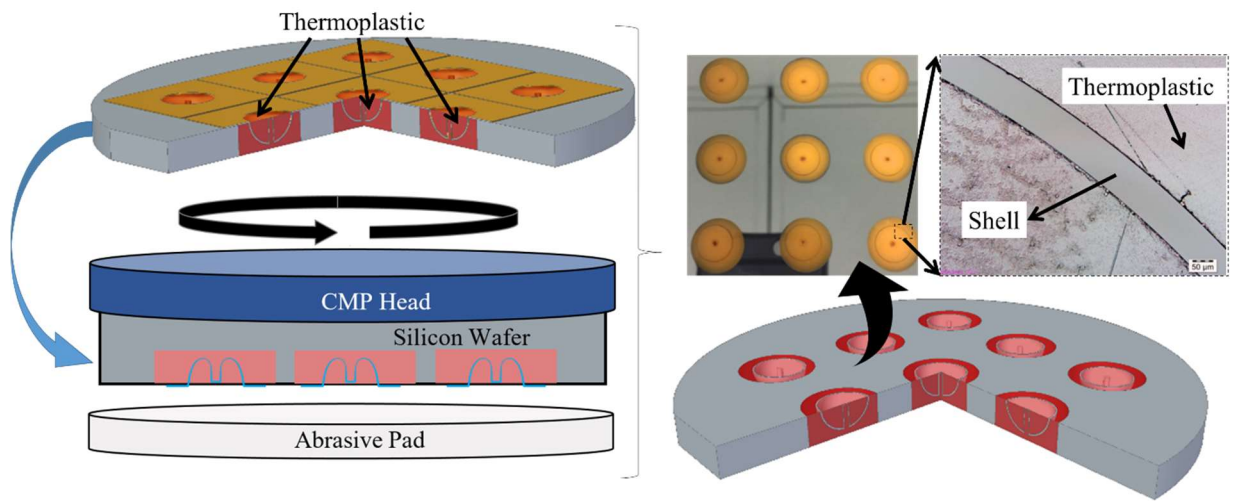


(b)

**Figure A1:** First step in fabrication of micro-scale self-aligned shells. (a) A meltable substrate is placed on a machined mold (in this case graphite). (b) Blowtorch is lowered to heat and soften the substrate until it reflows.



(a)



(b)

**Figure A2:** Second step in fabrication of micro-scale self-aligned shells. (a) Molded structures which are coated with a sacrificial protective metal set into a thick silicon wafer using thermoplastic. (b) The flat portion of the molded substrate is lapped, and the shell rims are polished using CMP. Figures are from [30] and [39].



Figure A3 shows photograph of this type of shells with different sizes. This process initially started by Dr. Jae Young Cho and later has been improved by Dr. Tal Nagourney and Mr. Sajal Singh. For further information, one can read [30], [33], and [39].

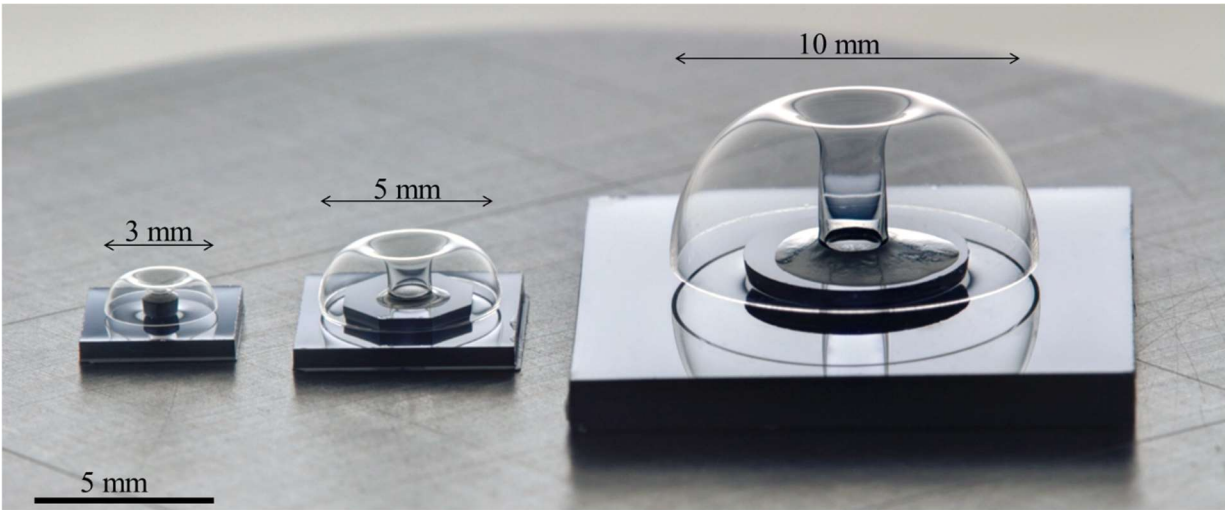


**Figure A3:** Birdbath shell structures with different sizes that are made from fused silica using blowtorch reflow process. Photo used in this figure is courtesy of Dr. Tal Nagourney.

## References

- [1] V. Bhadbhade, N. Jalili, S. Mahmoodi, "A novel piezoelectrically actuated flexural/torsional vibrating beam gyroscope," *J. Sound Vib.*, vol. 311, 2008, pp. 1305–1324.
- [2] S. E. Alper, K. Azgin, and T. Akin, "High-performance SOI-MEMS gyroscope with decoupled oscillation modes," *IEEE Int. Conf. MEMS*, Istanbul, Turkey, 2005, pp. 70–73.
- [3] A. Sharma, M. Zaman, B. Amini, F. Ayazi, "A high-Q in-plane SOI tuning fork device", *IEEE Conf. on Sensors*, 2004, pp. 467–470.
- [4] A. Trusov, G. Atikyan, D. Rozelle, A. Meyer, S. Zotov, B. Simon, and A. Shkel, "Flat is not dead: Current and future performance of Si-MEMS Quad Mass Gyro (QMG) system," *IEEE/ION Position Location and Navigation Symposium (PLANS)*, Savannah, Georgia, USA, 2014, pp. 252–258.
- [5] D. Rozelle, "The hemispherical resonator gyro: From wineglass to the planets," *Proc. 19th AAS/AIAA Space Flight Mechanics Meeting*, 2009, pp. 1157–1178.
- [6] G. He and K. Najafi, "A single-crystal silicon vibrating ring gyroscope," *IEEE Int. Conf. MEMS*, Las Vegas, NV, 2002, pp. 718–721.
- [7] T. H. Su, S. Nitzan, P. Taheri-Tehrani, M. Kline, B. Boser, and D. Horsley, "Silicon MEMS disk resonator gyroscope with an integrated CMOS analog front-end," *IEEE Sensors Journal*, vol. 14, 2013, pp. 3426–3432.
- [8] R. Tabrizian, M. Hojtaba-Shamami, and F. Ayazi, "High-frequency AlN-on-silicon resonant square gyroscopes," *J. Microelectromech. Syst.*, vol. 22, 2013, pp. 1007–1009.

- [9] C. Acar and A. Shkel, "MEMS vibratory gyroscopes—Structural approaches to improve robustness," in MEMS Reference Shelf Series. New York: Springer, 2009, ISBN: 978-0-387-09535-6.
- [10] A. Kourepenis, J. Borenstein, J. Connelly, R. Elliott, P. Ward, and M. Weinberg, "Performance of MEMS inertial sensors," *AIAA GN&C Conf.*, 1998, pp. 1307–1314.
- [11] T. Juneau, A. P. Pisano, and J. H. Smith, "Dual axis operation of a micromachined rate gyroscope," *International Conference on Solid-State Sensors, Actuators and Microsystems (Transducer)*, Chicago, IL, 1997, pp. 883–886.
- [12] W. Geiger, B. Folkmer, J. Merz, H. Sandmaier, and W. Lang, "A new silicon rate gyroscope," *IEEE Int. Conf. MEMS*, Heidelberg, Germany, 1998, pp. 615–620.
- [13] M. Zaman, A. Sharma, Z. Hao, and F. Ayazi, "A mode-matched silicon-yaw tuning-fork gyroscope with sub-degree-per-hour Allan Deviation bias instability," *J. Microelectromechan. Syst.*, vol. 17, 2008, pp. 1526–1536.
- [14] M. Zaman, A. Sharma, and F. Ayazi, "High performance matchedmode tuning fork gyroscope," *IEEE Int. Conf. MEMS*, 2006, pp. 66–69.
- [15] H. Johari and F. Ayazi, "High frequency capacitive disk gyroscopes in (100) and (111) silicon," *IEEE Int. Conf. MEMS*, Kobe, Japan, 2007, pp. 47–50.
- [16] S. Nitzan et al., "Epitaxially-encapsulated polysilicon disk resonator gyroscope," *IEEE Int. Conf. MEMS*, 2013, pp. 625–628.
- [17] T. Su, S. Nitzan, P. Taheri-Tehrani, M. Kline, B. Boser, and D. Horsley, "MEMS disk resonator gyroscope with integrated analog front-end," *IEEE Int. Conf. Sensors*, Baltimore, MD, USA, 2013.
- [18] C. Ahn *et al.*, "Encapsulated high frequency (235 kHz), high-Q (100 k) disk resonator gyroscope with electrostatic parametric pump," *Appl. Phys. Lett.*, vol. 105, 2014, art. no. 243504.

- [19] C. Ahn, E. Ng, V. Hong, J. Huynh, T. Kenny, and S. Wang, "Oxide-coated polysilicon disk resonator gyroscope (DRG) within the wafer-scale encapsulation process," *IEEE International Symposium on Inertial Sensors and Systems*, 2015, pp. 1–2.
- [20] D. Senkal *et al.*, "100 k Q-factor toroidal ring gyroscope implemented in wafer-level epitaxial silicon encapsulation process," *IEEE Int. Conf. MEMS*, San Francisco, CA, USA, 2014, pp. 24–27.
- [21] I. Prikhodko, S. Zotov, A. Trusov, and A. Shkel, "Sub-degree-per-hour silicon MEMS rate sensor with 1 million -factor," *International Conference on Solid-State Sensors, Actuators and Microsystems (Transducer)*, Beijing, China, 2011, pp. 2809–2812.
- [22] A. Trusov, D. Rozelle, G. Atikyan, B. Simon, S. Zotov, A. Shkel, A.D. Meyer, "Force rebalance, whole angle, and self calibration mechanization of silicon MEMS quad mass gyro," *IEEE International Symposium on Inertial Sensors and Systems*, 2014.
- [23] S. Askari, M. Asadian, K. Kakavand, and A. Shkel, "Vacuum sealed and getter activated MEMS Quad Mass Gyroscope demonstrating better than 1.2 million quality factor," *IEEE International Symposium on Inertial Sensors and Systems*, Laguna Beach, CA, 2016, pp. 142–143.
- [24] D. Senkal, A. Efimovskaya and A. Shkel, "Dual Foucault pendulum gyroscope," *International Conference on Solid-State Sensors, Actuators and Microsystems (Transducer)*, Anchorage, AK, 2015, pp. 1219–1222.
- [25] D. Serrano *et al.*, "Substrate-decoupled, bulk-acoustic wave gyroscopes: Design and evaluation of next generation environmentally robust devices," *Microsystems & Nanoengineering*, vol. 2, 2016, art. no. 16015.
- [26] A. Challoner, H. Ge, and J. Liu, "Boeing disc resonator gyroscope," *IEEE/ION Position, Location and Navigation Symposium - PLANS*, Monterey, CA, 2014, pp. 504–514.
- [27] J. Y. Cho, J.-K. Woo, J. Yan, R. Peterson, and K. Najafi, "Fused-silica micro birdbath resonator gyroscope ( $\mu$ -BRG)," *J. Microelectromech. Syst.*, vol. 23, 2014, pp. 66–77.

- [28] H. Wen, A. Daruwalla, F. Ayazi, “Resonant pitch and roll silicon gyroscopes with sub-micron-gap slanted electrodes: Breaking the barrier toward high-performance monolithic inertial measurement units”, *Microsystems & Nanoengineering*, vol. 3, 2017, art. no. 16092.
- [29] <https://www.vectornav.com/support/library/imu-and-ins>
- [30] T. Nagourney, “High-Q fused silica micro-shell resonators for navigation-grade MEMS gyroscopes”, 2018.
- [31] D. Yang, J. Woo, S. Lee, J. Mitchell, A. Challoner and K. Najafi, "A micro oven-control system for inertial sensors," *J. Microelectromech. Syst.*, vol. 26, 2017, pp. 507–518.
- [32] D. M. Yang, K. Najafi, D. F. Lemmerhirt and J. Mitchell, "A micro thermal and stress isolation platform for inertial sensors," *IEEE International Symposium on Inertial Sensors and Systems*, Moltrasio, 2018, pp. 1–4.
- [33] J. Cho, J. Yan, J. A. Gregory, H. Eberhart, R. Peterson, K. Najafi, “3-Dimensional blow torch-molding of fused silica microstructures”, *J. Microelectromech. Syst.*, vol. 22, 2013, pp. 1276–1284.
- [34] J. Cho, J. Yan, J. A. Gregory, H. Eberhart, R. Petrerson, and K. Najafi, “High-Q fused silica birdbath and hemispherical 3D resonators made by blow torch molding,” *IEEE Int. Conf. MEMS*, 2013, pp. 177–180
- [35] J. Cho, T. Nagourney, A. Darvishian, B. Shiari, J. Woo, and K. Najafi, "Fused silica micro birdbath shell resonators with 1.2 million  $Q$  and 43 second decay time constant," *Hilton Head Solid State Sensors, Actuators, and Microsystems Workshop*, Hilton Head Island, SC, 2014.
- [36] D. Senkal, M. Ahamed, M.H. Asadian Ardakani, S. Askari, A. Shkel, “Demonstration of 1 million Q-factor on microglassblown wineglass resonators with out-of-plane electrostatic transduction,” *J. Microelectromech. Syst.*, vol. 24, 2015, pp. 29–37.
- [37] B. Luo, J. Shang, and Y. Zhang, “Hemispherical glass shell resonators fabricated using Chemical Foaming Process”, *IEEE Elec. Comp. C.*, 2015, pp. 2217–2221

- [38] T. Nagourney, J. Cho, A. Darvishian, B. Shiari, and K. Najafi, "130 Second ring-down time and 3.98 million quality factor in 10 kHz fused silica micro birdbath shell resonator," *Hilton Head Solid State Sensors, Actuators, and Microsystems Workshop*, Hilton Head Island, SC, June 2016, pp. 408–411.
- [39] S. Singh, T. Nagourney, J. Cho, A. Darvishian, K. Najafi, and B. Shiari, "Design and fabrication of high-Q birdbath resonator for MEMS gyroscopes," *IEEE/ION Position, Location and Navigation Symposium (PLANS)*, Monterey, CA, 2018, pp. 15–19.
- [40] P. Pai, F. Chowdhury, C. Mastrangelo, and M. Tabib-Azar, "MEMS-based hemispherical resonator gyroscopes," *IEEE Conf. Sensors*, Taipei, Taiwan, 2012, pp. 1–4.
- [41] A. Heidari, M.-L. Chan, H. Yang, G. Jaramillo, P. Taheri-Tehrani, P. Fonda, H. Najar, K. Yamazaki, L. Lin, and D. Horsley, "Micromachined polycrystalline diamond hemispherical shell resonators," *International Conference on Solid-State Sensors, Actuators and Microsystems (Transducer)*, Barcelona, Spain, 2013, pp. 2415–2418.
- [42] P. Shao, C. Mayberry, X. Gao, V. Tavassoli, F. Ayazi, "A Polysilicon Microhemispherical Resonating Gyroscope," *J. Microelectromech. Syst.*, vol. 23, 2014, pp. 762–764.
- [43] P. Shao, V. Tavassoli, L. Chang-Shun, L. Sorenson, and F. Ayazi, "Electrical characterization of ALD-coated silicon dioxide microhemispherical shell resonators," *IEEE Int. Conf. MEMS*, 2014, pp. 612–615.
- [44] J. M. Gray *et al.*, "Hemispherical micro-resonators from atomic layer deposition," *J. Micromech. Microeng.*, vol. 24, 2014, art. no. 125028.
- [45] J. Bernstein, M. Bancu, J. Bauer, E. Cook, P. Kumar, E. Newton, T. Nyinjee, G. Perlin, J. Ricker, W. Teynor, and M. Weinberg, "High Q diamond hemispherical resonators: fabrication and energy loss mechanisms," *J. Micromech. Microeng.*, vol. 25, 2015, art. no. 085006.
- [46] A. Heidari, L. Chan, H. A. Yang, G. Jaramillo, P. Taheri-Tehrani, P. Fonda, H. Najar, K. Yamazaki, L. Lin, D. Horsley, "Hemispherical wineglass resonators fabricated from the microcrystalline diamond", *J. Micromech. Microeng.*, vol. 23, 2013, art. no. 125016.

- [47] P. Shao, V. Tavassoli, C. Mayberry, F. Ayazi, "A 3D-HARPSS polysilicon micro-hemispherical shell resonating gyroscope: design, fabrication and characterization", *IEEE Sensors J.*, vol. 19, 2015, pp. 4974–4985.
- [48] J. Cho, and K. Najafi, "A high-Q all-fused silica solid-stem wineglass hemispherical resonator formed using blow torching and welding," *IEEE Int. Conf. MEMS*, Estoril, Portugal, 2015.
- [49] M. Kanik, P. Bordeenithikasem, D. Kim, N. Selden, A. Desai, R. M'Closkey, and J. Schroers, "Metallic glass hemispherical shell resonators", *J. Microelectromech. Syst.*, vol. 24, 2015, pp.19–28.
- [50] Y. Tao, X. Wu, D. Xiao, X. Xi, Y. Tan, "A novel cupped solid-state wave gyroscope," *Applied Mechanics and Materials*, vols. 110-116, 2012, pp. 715–722.
- [51] Y. Wu, Q. Luan, H. Cui, X. Wu, X. Xi, "Research of a novel combined metal-fused silica resonator for cylinder shell vibrating gyroscopes," *Key Engineering Materials*, vol. 516, 2012, pp. 443–446.
- [52] D. Saito, C. Yang, A. Heidari, H. Najar, L. Lin, and D. Horsley, "Batch-fabricated high Q-factor microcrystalline diamond cylindrical resonator", *IEEE Int. Conf. MEMS*, Estoril, Portugal, 2015, pp. 801–804.
- [53] Y. Pan, D. Wang, Y. Wang, J. Liu, S. Wu, T. Qu, K. Yang, and H. Luo, " Monolithic cylindrical fused silica resonators with high Q factors", *Sensors*, 2016, vol.16, art. no. 1185.
- [54] A. Vafanejad and E. Kim, "Sub-degree angle detection using dome –shaped diaphragm resonator with wine-glass mode vibration," *Hilton Head Solid State Sensors, Actuators, and Microsystems Workshop*, Hilton Head Island, SC, 2014, pp. 391–394.
- [55] T. Nagourney, J. Cho, A. Darvishian, B. Shiari, and K. Najafi, "Micromachined high-Q fused silica bell resonator with complex profile curvature realized using 3D micro blowtorch molding," *International Conference on Solid-State Sensors, Actuators and Microsystem (Transducers)*, Anchorage, Alaska, USA, 2015.

- [56] S. Zotov, A. A. Trusov, and A. M. Shkel, "Three-dimensional spherical shell resonator gyroscope fabricated using wafer-scale glass blowing," *J. Microelectromech. Syst.*, vol. 21, 2012, pp. 509–510.
- [57] P. Prikhodko, S. A. Zotov, A. A. Trusov, and A. M. Shkel, "Microscale glass-blown three-dimensional spherical shell resonators," *J. Microelectromech. Syst.*, vol. 20, 2011, pp. 691–701.
- [58] Z. Hao, A. Erbil, and F. Ayazi, "An analytical model for support loss in micromachined beam resonators with in-plane flexural vibrations," *Sensors and Actuators A*, vol. 109, 2003, pp.156–164.
- [59] J. Judge, D. Photiadis, J. Vignola, B. Houston, and J. Jarzynski, "Attachment loss of micromechanical and nanomechanical resonators in the limits of thick and thin support structures," *J. Appl. Phys.*, vol.101, 2007, art. no. 013521.
- [60] DBindel and S. Govindjee, "Elastic PMLs for resonator anchor loss simulation," *International Journal for Numerical Methods in Engineering*, vol. 64, 2005, pp. 789–818.
- [61] M. Pandey, R. Reichenbach, A. Zehnder, A. Lal, and H. Craighead, "Reducing anchor loss in MEMS resonators using mesa isolation," *J. Microelectromech. Syst.*, vol. 18, 2009, pp. 836–844.
- [62] V. Thakar and M. Rais-Zadeh, "Optimization of tether geometry to achieve low anchor loss in Lamé-mode resonators," *Joint European Frequency and Time Forum & International Frequency Control Symposium (EFTF/IFC)*, Prague, CZ, 2013, pp. 129 -132.
- [63] A. Darvishian, B. Shiari, G. He, K. Najafi, "Effect of substrate thickness on quality factor of mechanical resonators," *International Symposium on Inertial Sensors and Systems*, Hapuna Beach, HI, USA, 2015, pp. 1–4.
- [64] COMSOL. (2012), "Structural mechanics module user's guide," V. 4.3.
- [65] A. Frangi, A. Bugada, M. Martello, and P.T. Savadkoohi, "PML-based models for the evaluation of anchor dissipation in MEMS resonators," *European Journal of Mechanics - A/Solids*, vol. 37, 2013, pp. 256–265.



- [66] COMSOL. (2015). COMSOL Multiphysics Software, V. 5.1. [Online]. Available: <http://www.comsol.com>
- [67] D. Gerrard, E. Ng, C. Ahn, V. Hong, Y. Yang, and T. Kenny, "Modeling the effect of anchor geometry on the quality factor of bulk mode resonators," *International Conference on Solid-State Sensors, Actuators and Microsystems (Transducer)*, Anchorage, Alaska, USA, 2015, pp. 1997–2000.
- [68] S. Johnson, "Notes on perfectly matched layers (PMLs)", Technical report, Massachusetts Institute of Technology, 2007; Available: <http://math.mit.edu/~stevenj/18.369/pml.pdf>
- [69] A. Darvishian, B. Shiari, J. Y. Cho, T. Nagourney and K. Najafi, "Anchor loss in hemispherical shell resonators," *J. Microelectromech. Syst.*, vol. 26, 2017, pp. 51–66.
- [70] C. Zener, "Internal friction in solids I. theory of internal friction in reeds", *Physical Review*, vol. 52, 1937, pp. 230–235.
- [71] C. Zener, "Internal friction in solids II. general theory of thermoelastic internal friction", *Physical Review*, vol. 53, 1938, pp. 90–99.
- [72] R. Lifshitz, M. L. Roukes, "Thermoelastic damping in micro- and nanomechanical systems," *Physical Review B*, vol. 61, 2000, pp. 5600–5609.
- [73] R. Abdolvand, G. Ho, A. Erbil, and F. Ayazi, "Thermoelastic damping in trench-refilled polysilicon resonators," *International Conference on Solid-State Sensors, Actuators and Microsystems (Transducer)*, 2003, pp. 324–327.
- [74] R. Abdolvand, H. Johari, G.K. Ho, A. Erbil, and F. Ayazi, "Quality factor in trench-refilled polysilicon beam resonators," *J. Microelectromech. Syst.*, vol. 15, 2006, pp. 471–478.
- [75] A. Nayfeh, M. Younis, "Modeling and simulations of thermoelastic damping in microplates", *J. Micromech. Microeng.* 14, 2004, pp. 1711–1717.
- [76] R. Candler, A. Duwel, M. Varghese, S. Chandorkar, M. Hopcroft, W. Park, B. Kim, G. Yama, A. Partridge, M. Lutz, and T. Kenny, "Impact of geometry on thermoelastic dissipation in micromechanical resonant beams," *J. Microelectromech. Syst.*, vol. 15, 2006, pp. 927–934.

- [77] A. Duwel, R. Candler, T. Kenny, and M. Varghese, "Engineering MEMS resonators with low thermoelastic damping," *J. Microelectromech. Syst.*, vol. 15, 2006, pp. 1437–1445.
- [78] J. Lake, A. Duwel, R. Candler, "Particle swarm optimization for design of slotted MEMS resonators with low thermoelastic dissipation", *J. Microelectromech. Syst.*, vol. 23, 2014, pp. 364–371.
- [79] B. Kim, M. Hopcroft, R. Candler, C. Jha, M. Agarwal, R. Melamud, S. Chandorkar, G. Yama, and T. Kenny, "Temperature dependence of quality factor in MEMS resonators," *J. Microelectromech. Syst.*, vol. 17, 2008, pp. 755–766.
- [80] S. Ghaffari and T. Kenny, "Thermoelastic dissipation in composite silicon MEMS resonators with thin film silicon dioxide coating," *MRS Proceedings*, vol. 1426, 2012, pp. 193–198.
- [81] S. Ghaffari, C. Ahn, E. Ng, S. Wang, and T. Kenny, "Crystallographic effects in modeling fundamental behavior of MEMS silicon resonators", *Microelectronics Journal*, vol.44, 2013, pp. 586–591.
- [82] A. Darvishian, B. Shiari, J. Cho, T. Nagourney, and K. Najafi, "Investigation of thermoelastic loss mechanism in shell resonators," *ASME International Mechanical Engineering Congress & Exposition*, Montreal, Canada, 2014, IMECE2014-39331.
- [83] S. Ghaffari, E. Ng, C. Ahn, Y. Yang, S. Wang, V. Hong, and T. Kenny, "Accurate modeling of quality factor behavior of complex silicon MEMS resonators", *J. Microelectromech. Syst.*, vol. 24, 2015, pp. 276–288.
- [84] L. Sorenson, P. Shao, and F. Ayazi, "Bulk and surface thermoelastic dissipation in Micro-hemispherical shell resonators", *J. Microelectromech. Syst.*, vol. 24, 2015, pp. 486–502.
- [85] A. Darvishian, T. Nagourney, J. Cho, B. Shiari, and K. Najafi, "Thermoelastic dissipation in micromachined birdbath shell resonators," *J. Microelectromech. Syst.*, vol. 26, 2017, pp. 758–772.
- [86] Schott Inc. Zero Expansion Glass Ceramic, accessed on 2016. [Online]. Available: [http://www.schott.com/advanced\\_optics](http://www.schott.com/advanced_optics)

- [87] Schott Inc. TIE-43: Properties of ZERODUR, accessed on 2016. [Online]. Available: [http://www.schott.com/advanced\\_optics/technical\\_information](http://www.schott.com/advanced_optics/technical_information)
- [88] Momenive Inc. Thermal Properties of Fused Quartz, accessed on 2016. [Online]. Available: <http://www.momentive.com>
- [89] National Institute of Standards and Technology (NIST) Property Data Summaries, accessed on 2016. [Online]. Available: <http://srdata.nist.gov>
- [90] R. Tabrizian, M. Rais-Zadeh, and F. Ayazi, "Effect of phonon interactions on limiting the fQ Product of micromechanical resonators," *International Conference on Solid-State Sensors, Actuators and Microsystems (Transducer)*, 2009, pp. 2131–2134.
- [91] S. Ghaffari *et al.*, "Quantum limit of quality factor in silicon micro and nano mechanical resonators," *Sci. Rep.*, vol. 3, 2013, art. no. 3244.
- [92] G. Sosale, S. Prabhakar, L. Fréchet, and S. Vengallatore, "A microcantilever platform for measuring internal friction in thin films using thermoelastic damping for calibration," *J. Microelectromech. Syst.*, vol. 20, 2011, pp. 764–773.
- [93] P. Mohanty *et al.*, "Intrinsic dissipation in high-frequency micromechanical resonators", *Phys. Rev. B*, vol. 66, 2002, art. no. 085416.
- [94] A. Ageev, B. C. Palmer, A. De Felice, S. D. Penn, and P. R. Saulson, "Very high quality factor measured in annealed fused silica," *Class. Quantum Gravity*, vol. 21, 2004, pp. 3887–3892.
- [95] K. Yasumura, T. Stowe, E. Chow, T. Pfafman, T. Kenny, B. Barry, C. Stipe, and D. Rugar, "Quality factors in micron- and submicron-thick cantilevers," *J. Microelectromech. Syst.*, vol. 9, 2000, pp. 117–125.
- [96] B. Shiari and K. Najafi, "Surface effect influence on the quality factor of microresonators", *International Conference on Solid-State Sensors, Actuators and Microsystems (Transducer)*, Barcelona, Spain, 2013, pp. 1715–1718.

- [97] M. Ahamed, D. Senkal, and A. Shkel, "Effect of annealing on mechanical quality factor of fused quartz hemispherical resonator," *International Symposium on Inertial Sensors and Systems*, Laguna Beach, CA, USA, 2014, pp. 1–4.
- [98] S. Penn, "Update on mechanical loss studies in fused silica," 2006.
- [99] P. Paolino and L. Bellon, "Frequency dependence of viscous and viscoelastic dissipation in coated micro-cantilevers from noise measurement," *Nanotechnology*, vol. 20, 2009, art. no. 405705.
- [100] T. Li and L. Bellon, "Dissipation of micro-cantilevers as a function of air pressure and metallic coating," *Europhys. Lett.*, vol. 98, 2012, art. no. 14004.
- [101] F. Forster, K. Koster, "Elasticity and damping in relation to the state of the material", *The Engineer*, 1938, pp. 626–628.
- [102] T. Nagourney, J. Cho, A. Darvishian, B. Shiari, and K. Najafi, "Effect of metal annealing on the Q-factor of metal-coated fused silica micro shell resonators," *IEEE International Symposium on Inertial Sensors and Systems*, Hapuna Beach, HI, 2015, pp. 1–5.
- [103] C. Boyd, J. Woo, J. Cho, T. Nagourney, A. Darvishian, B. Shiari, and K. Najafi, "Effect of drive-axis displacement on MEMS Birdbath Resonator Gyroscope performance," *IEEE International Symposium on Inertial Sensors and Systems*, Kauai, HI, 2017, pp. 1–2.
- [104] Y. Tang, A. Sandoughsaz, K. Owen, and K. Najafi, "Ultra deep reactive ion etching of high aspect-ratio and thick silicon using a ramped-parameter process," *J. Microelectromech. Syst.*, vol. 27, 2018, pp. 686–697.
- [105] D. McGuigan, C. Lam, R. Gram, A. Hoffman, D. Douglas, and H. Gutche, "Measurements of the mechanical Q of single-crystal silicon at low temperatures," *J. Low Temp. Phys.*, 30, 1978, art. no. 621.
- [106] M. Hopcroft, W. Nix, and T. Kenny, "What is the Young's modulus of silicon?," *J. Microelectromech. Syst.*, vol. 19, 2010, pp. 229–238.